The Onset of Secular Evolution in the Universe

Determining the Cosmic Epoch of Bar Formation with Integral Field Spectroscopy

Camila de Sá Freitas

München 2023

The Onset of Secular Evolution in the Universe

Determining the Cosmic Epoch of Bar Formation with Integral Field Spectroscopy

Camila de Sá Freitas

Dissertation
der Fakultät für Physik
der Ludwig-Maximilians-Universität
München

vorgelegt von
Camila de Sá Freitas
aus Volta Redonda, Rio de Janeiro – Brazil

München, den September 6th, 2023

Erstgutachter: PD. Dr. Klaus Dolag
Zweitgutachter: Prof. Dr. Simon White
Tag der mündlichen Prüfung: October 25th, 2023

"Mire, Daniel. El destino suele estar a la vuelta de la esquina. Como si fuese un chorizo, una furcia o un vendedor de lotería: sus tres encarnaciones más socorridas. Pero lo que no hace es visitas a domicilio. Hay que ir a por él."

La Sombra del Viento

Carlos Ruiz Zafón

Contents

List of Figures

List of Tables

Abstract

Disc galaxies build up their mass in a two-phase scenario. At higher redshifts, external processes dominate the evolution of the galaxy. With the expansion of the Universe and the decrease in the frequency of interactions, these external processes give place to the internal development of the galaxy, including disc formation and settling. However, it is unclear when this transition occurs in the Universe. Once the disc settles, at least partially, it is often prone to developing a non-axisymmetric structure, namely the bar. One of the immediate effects due to the presence of the bar is the gas inflow towards central parts of the galaxy, leading to central star formation and the building of a new rotationally-supported stellar structure, i.e., the nuclear disc. Therefore, we can estimate the cosmic epoch of bar formation (and thus the transition time in the two-phase scenario) by deriving the star formation history of the nuclear disc. In this thesis, we present the first generally applicable methodology to derive the time of bar formation for a sizeable sample of galaxies and, additionally, we share the first results from applying this methodology to 19 galaxies observed with the MUSE integral field spectrograph on the VLT (mostly from the TIMER survey).

Our methodology consists in carefully isolating the contribution of the nuclear disc to the observed spectra, in order to derive its star formation history free of contamination from other co-spatial stellar structures. To ascertain the uncertainties involved, particularly of a systematic nature, we run a thorough series of tests, leading to realistic error estimates. Among our main results, we find a wide range of values of disc-settling epochs ($0 \leq z \leq 6$), which indicates this is an ongoing process in the Universe that has commenced substantially earlier than previously thought. Analysing the current stellar mass of the bar-hosting galaxy, we find no correlation with the bar age. This contradicts the downsizing scenario that predicts that the more massive galaxies assembled their mass first, forming their bars first. Regarding secular evolution, we find evidence that bars can grow over time (relative to the host galaxy). In addition, by analysing the evolution of the light fraction enclosed in the bar over time, we find evidence of angular momentum exchange across the galaxy, with the trapping by the bar of stars from the galaxy disc, which can explain the bar growth.

This methodology allows us, for the first time, to test theoretical predictions regarding bar-driven evolution from an observational perspective, opening new lines of research in the near future.

Zusammenfassung

Scheibengalaxien entwickeln ihre Masse in zwei Phasen. Bei hohen Rotverschiebungen dominieren externe Prozesse die Entwicklung der Galaxie. Durch die Ausdehnung des Universums und die Abnahme der Interaktionshäufigkeit verschiebt sich die Entwicklung zu internen Prozessen, wie zum Beispiel der Entstehung und Absetzung einer Scheibe. Der genaue Zeitpunkt dieses Übergangs ist jedoch unklar. Sobald sich die Scheibe zumindest teilweise absetzt, entwickelt sich oft kurz darauf eine nicht achsensymmetrische Struktur: der Balken. Dieser ermöglicht Gasströme in Richtung des Zentrums der Galaxie, was zu zentraler Sternentstehung und der Entstehung einer neuen rotationsunterstützten Sternstruktur führt: die zentrale Sternscheibe. Durch die Entwicklung der Sternentstehung in der zentralen Sternscheibe können wir die Entstehungsepoche des Balkens abschätzen (und dadurch auch den Überganszeitpunkt der zwei Phasen). In dieser Arbeit stellen wir die erste allgemein anwendbare Methodik zur Bestimmung des Zeitpunkts der Balkenentstehung für eine große Galaxienstichprobe vor. Zusätzlich präsentieren wir erste Ergebnisse für 19 Galaxien, die mit dem MUSE Integralfeldspektrograf am VLT beobachtet wurden (hauptsächlich aus der TIMER Durchmusterung).

Unsere Methodik isoliert sorgfältig den Beitrag der zentralen Sternscheibe zum beobachteten Spektrum, um die Entwicklung der Sternentstehung frei von Kontamination anderer stellarer Strukturen zu bestimmen. Für eine realistische Fehlerabschätzung, insbesondere der Systematiken, sorgt eine Vielzahl an Tests. Eines unserer wichtigsten Ergebnisse ist eine breite Zeitspanne für die Absetzung des Scheibenmaterials (0 <= z <= 6). Dies deutet auf einen kontinuierlichen Prozess hin, mit einem früheren Beginn als bisher angenommen. Wir finden keine Korrelation des Balkenalters mit der aktuellen stellaren Masse der Galaxie. Dies widerspricht dem Downsizing-Szenario, welches vorhersagt, dass schwere Galaxien ihre Masse zuerst ansammeln und der Balken zuerst entsteht. Bezüglich säkularer Evolution zeigen wir, dass Drehimpuls durch die gesamte Galaxie ausgetauscht wird, wobei Sterne aus der galaktischen Scheibe im Balken eingefangen werden. Dies kann das Wachstums des Balken erklären.

Diese Methodik ermöglicht erstmals die Überprüfung theoretischer Vorhersagen bezüglich der Entwicklung von Galaxien durch Balken basierend auf Beobachtungen und eröffnet neue Forschungsrichtungen in der Zukunft.

1

Introduction

1.1 Galaxies throughout history

Galaxies have been intriguing societies and filling their imagination for centuries, especially our galaxy, the Milky Way. Many different cultures had their myths to explain the milky white stream in the sky. The term "*Milky Way*" is the translation of "*Via Lactea*" from Latin, which in turn comes from the Greek for "*galaxias kuklos*" (milky circle). Among the different myths to explain the nomenclature in ancient Greek society, is the one in which Zeus places his mortal son, Heracles, to be breastfed by Hera, who is sleeping. By doing this, Heracles would gain immortality. However, once Hera woke up, she pushed the unknown baby away, spilling the milk into the skies[1][2]. Beyond the Greeks, other societies built myths around the bright path as well. For some Tupi-Guarani tribes, present in many South American countries, the Milky Way contrasts between light and dark patches gave place to myths and constellations. The Milky Way is often called "*Tapi'i rapé*" ("*Path of the Tapir*" in Guarani, an indigenous South America animal), due to the Tapir constellation[3][4], which is located in the stream. The Tapir constellation rises in the sky in the second half of September. This coincides with the transition between cold and warm seasons for indigenous people in the south of Brazil and between draught and rain for the ones in the north. Additionally, the guarani people called the Large and Small Magellanic Clouds as "*Tapi'i Huguá*" ("*Tapir Drinking Fountain*") and "*Coxi Huguá*" ("*Wild Pig Drinking Fountain*"). In the south of Australia, the Kaurna people – an aboriginal Australian tribe – considered the Milky Way as the river in the sky world (named "*Wodliparri*") with campfires along it and creatures hidden in the dark patches – "*Yurakauwe*", which means monster water[5].

However, it was only at the turn of the 20th century that we began to understand the nature of galaxies. In 1920, the Smithsonian Museum of Natural History hosted what was known as the "Great Debate". Astronomers Harlow Shapley and Heber Curtis met to debate about the size of the Milky Way, the size of the Universe, and the nature of the so-called "spiral nebulae". Shapley argued that the Milky Way was big enough to encompass all these newly discovered objects. From the visual aspect of the spiral nebulae, a possible explanation for their nature, that was put forward at that time, was that they were collapsing into planetary systems[6], like our Solar System. On the other hand, Curtis argued that spiral nebulae are independent sources similar to the Milky Way, and external to it, as also proposed by philosopher Immanuel Kant with the "island universes". In that scenario, the Universe would have to be bigger than the accepted by the time, at least 10^8 light-years. It was only in 1925 that Hubble was able to settle the debate. By measuring the distance of Cepheids in the spiral nebulae – applying the methodology

[1] http://judy-volker.com/StarLore/Myths/MilkyWay1.html
[2] https://books.google.de/books?id=YJawuz5Q1vEC&pg=PA44&redir_esc=y#v=onepage&q&f=false
[3] https://revistacienciaecultura.org.br/?artigos=mitos-e-estacoes-no-ceu-tupi-guarani
[4] http://www.telescopiosnaescola.pro.br/indigenas.pdf
[5] https://able.adelaide.edu.au/humanities/kaurna-warra-pintyanthi-kwp-team
[6] "The Cosmic Evolution of Galaxy Structure", Christopher J. Conselice

proposed by Henrietta Leavitt –, he inferred their distances. His results demonstrated that these objects were extragalactic sources (Hubble, 1925), similar to the Milky Way. This marked the beginning of Extragalactic Astrophysics research as we know it.

Almost 100 years after Hubble's discovery, our understanding of galaxies has increased considerably. We have developed classification systems, multiple evolutionary models, and tools to investigate, in-depth, the history of these objects. However, many questions remain. In this Chapter, I will briefly summarise some of our knowledge around these objects, and the gaps in which this Thesis contributes to further build our understanding of galaxies.

1.2 Emergence of the Hubble sequence

Shortly after we learned the extragalactic nature of spiral nebulae, one aspect captured the attention of astronomers: their diverse morphology and how it emerges. Hubble (1926) was one of the pioneers in creating a classification system based on the visual structures of galaxies in the optical bands, known as the *Hubble Tunning Fork* (see Fig. 1.1), which is still broadly applied today. In this system, galaxies are classified mainly between three classes: ellipticals, lenticulars, and spirals – the latter splitting between barred and unbarred. Hubble also classified ellipticals/lenticulars as "early-type" and spirals/irregulars as "late-type", because he assumed an evolutionary sequence from left to right. In fact, as we now know, this left-to-right sequence does not correspond to how galaxies form and evolve, but notwithstanding, the nomenclature of "early" and "late"-type galaxies is still in use today. Additionally, galaxies that do not fall in any of these classes were considered irregulars. This classification was later expanded and followed by different systems (e.g., Morgan, 1958; De Vaucouleurs, 1959; van den Bergh, 1960; Sandage, 1961). De Vaucouleurs (1959) introduced an important parameter of galaxy morphology, the "Hubble T-type", which is a numerical classification that ranges from -6 to 10, corresponding to the early and late-type morphologies.

Morphological classification systems, a priori, were not tailored to relate to galaxy physical properties or evolution histories. Nevertheless, many intrinsic properties relate to morphological type. Simien & De Vaucouleurs (1986) demonstrated that the fraction of light in the bulge correlates well with the galaxy T-type, in which the smaller the T-type, the more prominent the spherical structure in the galaxy. This is to a large degree expected since the prominence of the central structure component in disc galaxies is one of the criteria in the Hubble classification scheme. Additionally, Roberts & Haynes (1994) summarized how the morphological classification relates to the blue luminosity, the galaxy size and mass, the atomic hydrogen mass, the mass surface density, and the colour. Nowadays, it is well-accepted that galaxy morphology is intrinsically linked to underlying physical properties. Furthermore, since the morphology of a galaxy describes the internal stellar mass distribution, it relates to the stellar mass assembly history to some degree. Hence, to understand how the Hubble sequence of the Local Universe emerged, it is necessary to

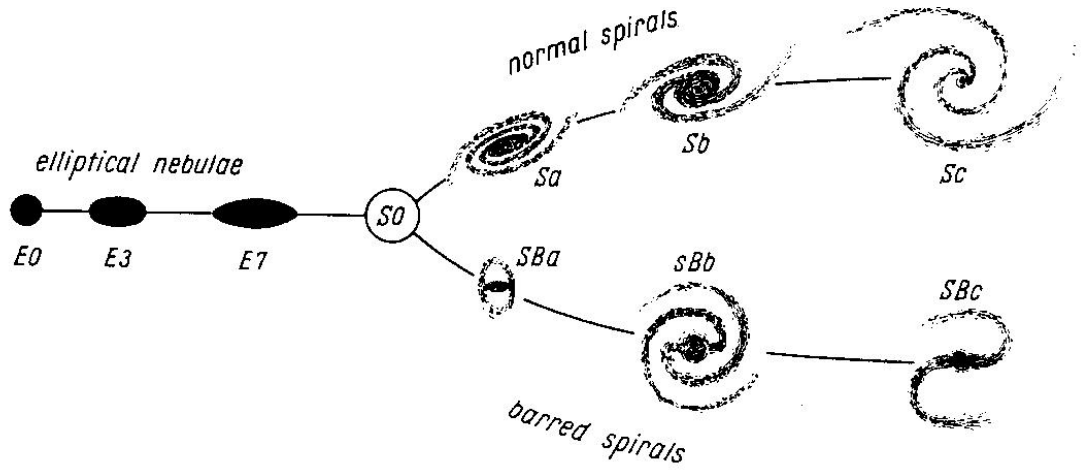

Figure 1.1: Hubble Tunning Fork illustration (Hubble, 1936).

understand how galaxies formed and evolved in a cosmological context.

The current standard cosmological model, Lambda Cold Dark Matter (ΛCDM), has three main components; a cosmological constant, denoted by the Greek letter Λ, which is associated with dark energy and the observed accelerated expansion of the Universe; cold dark matter, associated with structure formation; and baryonic matter, associated with visible structures (i.e., galaxies, stars, planets). In this cosmological paradigm, the Universe is flat and its energy density distribution consists of approximately 75% of dark energy, 21% of cold dark matter, and 4% baryonic matter (e.g., Davis et al., 1985; Garnavich et al., 1998; Perlmutter et al., 1999; de Bernardis et al., 2000). Although the nature of dark energy and dark matter remains unknown, they play an important role in the formation and evolution of structure in the Universe. Dark matter accumulates in clumps, called haloes, which grow through mergers, with large structures forming through consecutive accretion/mergers of smaller progenitors (e.g., White & Rees, 1978), in what is called the hierarchical formation. These dark matter halos provide gravitational wells in which baryonic matter falls, and galaxies form and evolve (e.g., White & Rees, 1978; White & Frenk, 1991).

By investigating our own Galaxy, Eggen et al. (1962) proposed a unique scenario to describe how different galaxy morphologies form, known as the "monolithic collapse" scenario. In this scenario, galaxies form from the collapse of a slowly rotating gas cloud. The main difference between the formation histories of spiral and elliptical galaxies is how the gas collapses and how it dissipates gravitational energy. If, while the cloud is collapsing, it is entirely converted into stars, this collapse will be approximately dissipationless and the product will be a system of stars with random motions, providing a possible explanation for the formation of elliptical galaxies and classical bulges. On the other hand, if the gas is not mostly converted into stars during its collapse, gravitational energy can be dissipated via shocks and radiative cooling of the remaining gas, and the gas cloud shrinks until it

is supported by angular momentum in a flat shape, leading to disc galaxies. Nevertheless, numerical simulations struggled to explain the formation of observed ellipticals (e.g., Larson 1974, 1975), which in reality are not as flat as predicted and show either little or no rotation (e.g., Bertola & Capaccioli, 1975; Illingworth, 1977). Additionally, the monolithic collapse scenario does not take into consideration the existence of dark matter halos, at the time not part of the cosmological paradigm. Although this scenario does not successfully describe elliptical galaxy formation, the idea of disc galaxies forming through mechanisms of gas dissipation was further explored (e.g., Sandage et al., 1970; Gott III & Thuan, 1976; Larson, 1976). Gott III & Thuan (1976) proposed that the key factor to form either disc or elliptical galaxies is the ratio between the star formation timescale and the collapse time of the protogalaxy, which was related to the initial perturbations in the early Universe. Larson (1976), on the other hand, proposed that, to form a disc galaxy, its pristine gas would mainly be diffuse, inhibiting the star formation process. Lastly, Fall & Efstathiou (1980) developed further the disc formation scenario considering also extended dark matter halos. The authors find that the halo assembly happens first, followed by the gas infall. The residual gas, in turn, dissipates the energy and settles in a rotating disc (in agreement with White & Rees, 1978).

Using a numerical simulation, Toomre & Toomre (1972) demonstrated for the first time that the merger of galaxies can create peculiar observed structures, such as tidal arms, and possibly lead to elliptical galaxies. The authors defended a scenario in which most elliptical galaxies would be merger remnants if not all. Later, studies found that major and minor mergers can build dispersion-dominated structures – i.e., spheroids (e.g., Toomre, 1977; Gerhard, 1981; Farouki & Shapiro, 1982; Hernquist, 1993; Bournaud et al., 2005; Naab et al., 2009; Naab et al., 2014; Athanassoula et al., 2016; Semenov et al., 2023a). Additionally, depending on the mass ratio of the merger, the gas fraction, and feedback properties, the remnant of the merger can be a central spheroid, called "classical bulge", or an elliptical galaxy (e.g., Bournaud et al., 2005; Springel et al., 2005; Schawinski et al., 2014; Nogueira-Cavalcante et al., 2018). In this picture, both stellar structures are dynamically pressure-supported, i.e., kept together by the high-velocity dispersion of their stars, relative to their rotation around the centre of the system. In addition, the classical bulge could be seen as a mini elliptical galaxy surrounded by a rotationally supported stellar disk, which forms from gas infall. Nonetheless, the mass-size relation of classical bulges is different from that of elliptical galaxies, indicating, at least to some extent, different formation processes (e.g., Gadotti, 2009; Laurikainen et al., 2010). As the Universe expands and becomes less dense, interactions and mergers become less frequent as well – affecting how galaxies evolve. That is, at higher redshifts, external processes such as mergers and interactions have an important impact on how galaxies evolve (e.g., Schreiber et al., 2006; Genzel et al., 2008; Law et al., 2009; Dekel et al., 2009, Oser et al., 2010) and, later on, internal processes begin to play an important role in the evolution of galaxies (Kormendy & Kennicutt, 2004).

More recently, Ferreira et al. (2022b) employed James Webb Space Telescope (JWST) data, investigating the optical rest-frame morphological evolution of around 4000

galaxies, between redshifts $1.5 \leq z \leq 8$. Among many interesting results, the authors find that the Hubble sequence was already in place since $z \sim 6$ for galaxies with masses below $10^{9.5}$ $M_{\odot}$. That is, the fractions of disc, spheroids, and peculiar galaxies are approximately constant between $1.5 \leq z \leq 6$ for lower mass galaxies. Additionally, investigating the fraction of stellar mass for different morphologies (disc, peculiar, spheroidal, and other), they find that disc galaxies dominate the fraction of stellar mass since $z \sim 4.5$, and already contribute to almost 70% of the total stellar mass in $z = 1.5$. When it comes to the fraction of star formation rate (SFR), spheroidal galaxies only contribute significantly to the formation of stars at higher redshifts ($z > 6$), decreasing over time. On the other hand, the contribution to star formation from spiral galaxies increases with time, reaching almost 60% at $z = 1.5$. Ferreira et al. (2022b) provides insightful findings regarding the cosmological evolution of morphologies and relative contributions. Since disc-like galaxies are already dominant at $z \sim 4.5$, it is crucial to understand how these galaxies form in order to develop a fuller picture of galaxy evolution.

1.3 Disc formation within the Universe

At early times in the life of the Universe, galaxy mergers and interactions are common, and as such external processes dominate over the evolution of galaxies. However, at later times, external processes become less frequent, and internal processes begin to play a leading role in the evolution of galaxies. Due to that, the formation and evolution history of a disc galaxy is expected to be a combination of external and internal processes (e.g., Cook et al., 2010; Oser et al., 2010; Kraljic et al., 2012). However, it is not clear when this transition takes place in the Universe, and which factors determine when it happens.

Due to our privileged perspective of the Milky Way galaxy, it is possible to derive its mass assembly and chemo-dynamical histories in detail, deriving the formation epoch of different structures, such as the thick and thin discs (see illustration of the Milky Way disc structure in Fig. 1.2 – e.g., Gilmore et al., 1989; Snaith et al. 2014, 2015; Haywood et al. 2015, 2016; Belokurov & Kravtsov, 2022; Conroy et al., 2022; Rix et al., 2022; Semenov et al., 2023a). More specifically, studies find that the Milky Way disc assembled in three different stages: the (*i*) protogalaxy phase, in which stars in the halo are very metal poor ([Fe/H] ≤ -1.5) and dispersion dominated, indicating they formed during early epochs, with large contribution of mergers (e.g., Renaud et al., 2021 find $\sim 20 - 30\%$ of increase in the stellar mass from mergers); the (*ii*) spin-up of the thick disc, in which stars are more metal-rich ($-1.5 \leq$[Fe/H] ≤ -1.0) and already show rotation support motion, with velocities of 150 km.s^{-1} (e.g., Belokurov & Kravtsov, 2022; Conroy et al., 2022); and (*iii*) the settling-down to a thin disc, that hosts most of the current star formation ([Fe/H]> -1), with lower dispersion and higher rotational velocities (220 km.s^{-1}). The last stage is considered the disc-settling that corresponds to when the galaxy achieves a constant SFR and an equilibrium rotating disc. Due to the advent of high-resolution integral field spectroscopy, it is now possible to carry out similar analysis on nearby edge-

on galaxies and investigate their mass assembly history (e.g., Pinna et al., 2019; Martig et al., 2021). However, since it requires observations of inclined discs with high spatial resolution data, it not yet[7] possible to perform such analysis on a large number of galaxies, deriving their disc assembly.

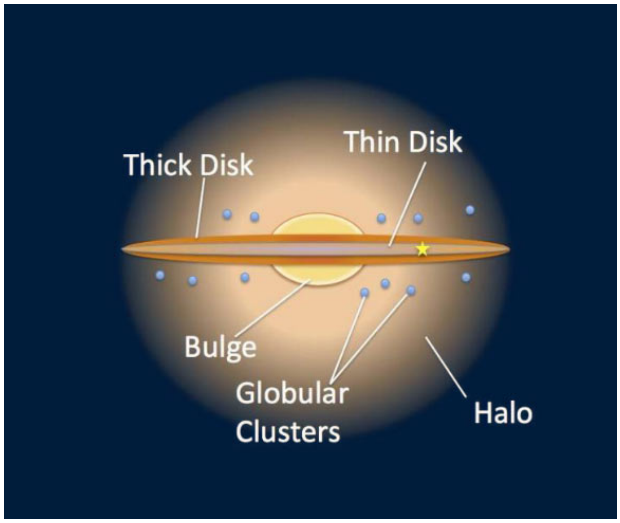

Figure 1.2: Artistic representation of Milky Way's disc structure, highlighting the thin and thick discs, the halo, bulge and other structures (credits: NASA / JPL Caltech / R.Hurt / SSC.)

Early simulations that attempted to model disc formation within the cosmological context (e.g., Navarro & Benz, 1991; Katz, 1992; Navarro & White, 1994; Sommer-Larsen et al., 1999) faced what was known as the "angular momentum catastrophe". In this scenario, most of the angular momentum of the galaxy is lost during its assembly, resulting in compact discs and spheroids. A solution to the "angular momentum catastrophe" was found in the form of energetic stellar feedback, which, when introduced in the simulations, was able to create extended discs (e.g., Brook et al., 2004; Agertz et al., 2011). More recently, Stern et al. (2021) find that, for a Milky-Way-like galaxy, in order to settle its disc, the circumgalactic medium (CGM) plays an important role. The authors argue that the virialization of the inner parts of the CGM enables cooling flows, which settles the disc. Additionally, once the disc settles, its star formation rate evolves from a "bursty" behaviour to a "steady" one. Lastly, simulations show that the onset of the disc formation is only possible in the absence of violent mergers, which would reset the process (e.g., Rosas-Guevara et al., 2020; Stern et al., 2021; Semenov et al. 2023a,b).

To investigate when discs arise in the history of the Universe, we can analyse the morphology of galaxies at different redshifts. Studies based on observations from the Hubble Space Telescope (HST), on the UV rest-frame band, found that irregular and clumpy morphologies dominate at $z > 2.5$ (e.g. Elmegreen et al., 2007; Conselice et al., 2008; Guo et al., 2015), creating the expectation that discs only emerged in the Universe $z \approx 1 - 2$. Nevertheless, since different wavelength bands probe different underlying physical properties and stellar populations, the morphology and structural parameters of

[7]Nevertheless, as I discuss in the closing chapter of this Thesis, the large Very Large Telescope (VLT) program GECKOS (Generalising Edge-on galaxies and their Chemical bimodalities, Kinematics, and Outflows out to Solar environments; van de Sande et al., 2023) was recently accepted and will make possible such direct comparisons soon.

galaxies are highly dependable on the rest-frame wavelength (e.g., Kuchinski et al., 2000; Lauger et al., 2005; Buta et al., 2010; Vika et al., 2015; Kennedy et al., 2015). Kuchinski et al. (2000) showed how nearby disc galaxies can also appear to have clumpy morphologies when observed in UV rest-frame bands. With the inauguration of the ALMA facilities, it became possible to probe the interstellar medium (ISM) at higher redshifts, revealing cold rotational supported discs up to $z \approx 6$ (e.g., Smit et al., 2018; Neeleman et al., 2020; Rizzo et al., 2020; Lelli et al., 2021; Posses et al., 2023). More recently, JWST observations are finding that disc galaxies exist at least since $z \approx 8$, when the Universe was younger than 1 Gyr old (e.g., Ferreira et al. 2022a,b; Nelson et al., 2022; Jacobs et al., 2023). Even though there is mounting evidence of the existence of discs at higher redshifts, indicating that disc galaxies settle earlier than previously thought, studies find that these discs are usually turbulent and thick (e.g., Elmegreen & Elmegreen, 2006; Cresci et al., 2009; Newman et al., 2013). However, it is worth noting that other studies find evidence for cold discs already at these high redshifts (e.g. Rizzo et al. 2020 and Lelli et al., 2023). Therefore, despite significant leaps forward over the last few years, the issue of when and how galactic discs settled in the Universe remains one of the most pressing questions in galaxy formation and evolution.

1.4 The formation and evolution of bars

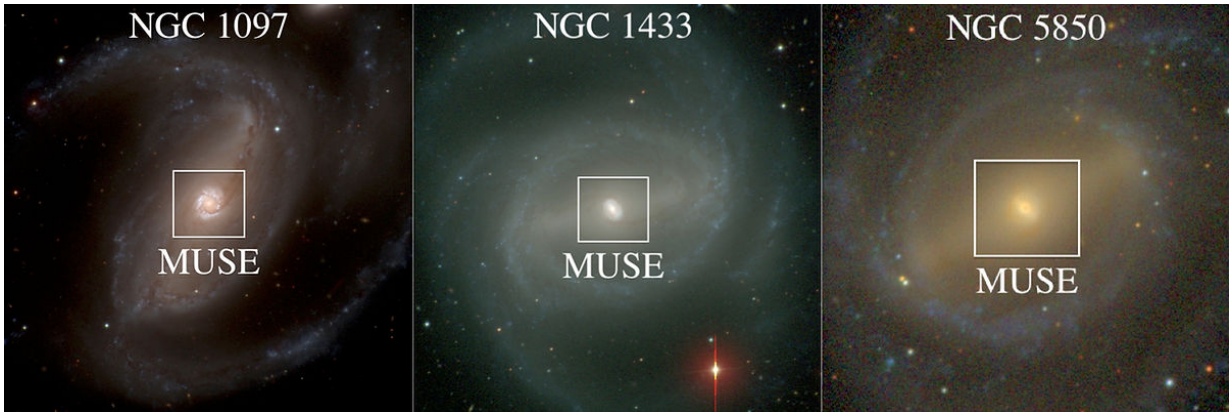

Figure 1.3: Example of barred galaxies from the Time Inference with MUSE in Extragalactic Rings survey (TIMER – Gadotti et al., 2019). Coulored images are from the Carnegie-Irvine Galaxy Survey (Ho et al., 2011) with the Multi Unit Spectroscopic Explorer (MUSE) field of view in white squares.

A large number of disc galaxies display an elongated structure, named a bar, in different redshifts (see example in Fig. 1.3[8]). Studies find that the fraction of barred galaxies increases with time (e.g., Sheth et al., 2008; Cameron et al., 2010; Melvin et al., 2014; Simmons et al., 2014; Simmons et al., 2014; Rosas-Guevara et al., 2020) and, for the

[8]Image credit and details: https://www.muse-timer.org/science

Local Universe, over two-thirds of disc galaxies have either a strong or a weak bar (e.g., Eskridge et al., 2000; Menéndez-Delmestre et al., 2007; Barazza et al., 2008; Sheth et al., 2008; Aguerri et al., 2009; Nair & Abraham, 2010; Buta et al., 2015; Erwin, 2018).

Theoretical works have proposed that bars form when its host galaxy's disc is self-gravitating with differential rotation, and rotationally supported with relatively low-velocity dispersion (e.g., Toomre, 1963; Hohl, 1971; Ostriker & Peebles, 1973; Combes & Sanders, 1981; Gerin et al., 1990; Combes & Elmegreen, 1993; Athanassoula, 2002; Kraljic et al., 2012). Therefore, the formation of a bar within its host galaxy will in general coincide, or follow shortly after, the formation of its stellar disc. Using cosmological zoom-in simulations, Kraljic et al. (2012) find that the bar formation takes place coincidentally with the disc settling, specifically when the thin disc forms – at least partially. This is in agreement with findings for the Milky Way as well, whose thin disc formed around 8 Gyr ago (e.g., Haywood et al., 2013; Conroy et al., 2022), coincident with the proposed time of bar formation for the Milky Way (e.g., Wylie et al., 2022; Sanders et al., 2022). Recently, Ghosh et al. (2023) systematically investigated in hydrodynamical simulations the roles of the thin and thick discs in the bar formation. The authors find that all the models with thin and thick discs form bars in both components, in which the thick disc bar is always weaker than the thin disc one. Additionally, their models with only thick discs can indeed form bars, but they heavily depend on the disc scale length and height. In other words, even though some specific models without a thin disc can form bars, they tend to be weak. When it comes to analysing the disc dynamical properties that allow or suppress bar formation, most numerical simulations consider one stellar disc component instead of two, finding that dynamically hot discs are stable against bar formation (e.g., Toomre, 1964; Binney & Tremaine, 2008), either suppressing or delaying it (e.g., Aumer & Binney, 2017).

Numerical simulations and theoretical work propose that bars form due to disc instabilities, where even small perturbations can trigger the global bar formation (e.g., Toomre, 1964; Hohl, 1971; Noguchi, 1987; Gerin et al., 1990). There are different channels for said instabilities, mainly differentiating between internal (e.g., Debattista & Sellwood, 2000; Athanassoula, 2003; Berentzen et al., 2007; Okamoto et al., 2015) or external triggers (e.g., Noguchi, 1987; Gerin et al., 1989; Miwa & Noguchi, 1998; Peschken & Łokas, 2019; Łokas, 2021.). Regarding internal disc instabilities, Toomre (1964) introduced the *Toomre's stability criterion*, which describes a disc's stability against unstable modes within its plane. The criterion for a stellar disc to be locally stable against axisymmetric instabilities can be described as:

$$Q_{\rm star} \equiv \frac{\sigma_{\rm R}\kappa}{3.36{\rm G}\Sigma} > 1, \tag{1.1}$$

where $\sigma_{\rm R}$ is the radial velocity dispersion, κ is the epicyclic frequency, G is the gravitational constant, and Σ is the surface density. If the disc is locally stable everywhere, global

axisymmetric stability can be reached (e.g., Kalnajs, 1976). However, this does not ensure the disc is stable against nonaxisymmetric modes, like the bar. Toomre (1964) argued that to keep the disc stable against bar formation, the random motions parallel to the plane must be sufficiently large, that is, the disc should be thick and dynamically hot. In the case this is not met, the bar is "spontaneously" formed once the disc settles into a low-dispersion system (e.g., Combes & Sanders, 1981; Polyachenko, 2013).

External disc instability triggers, on the other hand, can be minor mergers (e.g., Noguchi, 1987; Goz et al., 2015), close interactions with other galaxies (also known as flybys – e.g., Gerin et al., 1990; Lang et al., 2014; Łokas et al., 2014; Łokas, 2018), or even interactions with the dark matter halo substructures (e.g., Romano-Díaz et al., 2008). The parameter space needed to characterise encounters between galaxies is large, and includes not only the individual galaxies' properties but also the interaction properties that have to be taken into account, such as mass ratio, encounter speed, centre of mass distance, relative inclination of the two galaxies, and relative rotation (e.g., Gerin et al., 1990; Romano-Díaz et al., 2008; Lang et al., 2014; Łokas et al. 2015, 2016; Peschken & Łokas, 2019). In fact, some studies show that different interaction configurations can either induce bar formation or delay the process and destroy existing bars (e.g., Beckman & Mahoney, 1999; Debattista et al., 2006; Romano-Díaz et al., 2008; Méndez-Abreu et al., 2012; Zana et al., 2018; Ghosh et al., 2021). Lastly, it is not clear if bars which formed through different channels present long-lasting properties that would allow us to determine how they formed (e.g., Miwa & Noguchi, 1998; Berentzen et al., 2004; Łokas, 2021), although some studies show that tidally-induced bars tend to form longer than those formed through internal instabilities (e.g. Holley-Bockelmann et al., 2005).

Considering the different ways of triggering bar formation, simulations show that bars form relatively easily. Additionally, recent works describe bars to be long-lived and robust structures, that are not easily destroyed (e.g., Shen & Sellwood, 2004; Athanassoula et al., 2005). Thus, the question remains as to why some disc galaxies in the Local Universe remain bar-less and if some of these galaxies ever hosted a bar that was destroyed – even if unlikely. Numerical works find that different characteristics can suppress bar formation. In the presence of a central mass concentration, bar formation is delayed (e.g., Pfenniger & Norman, 1990; Bournaud & Combes, 2002; Shen & Sellwood, 2004; Athanassoula et al. 2005, 2013; Saha & Elmegreen, 2018), although studies find that a large amount of mass is necessary to affect bar formation, possibly being unrealistic (e.g., Athanassoula et al., 2005); furthermore, gas-rich, turbulent discs and/or massive dark matter halos can also play a role delaying bar formation (e.g., Toomre, 1964; Ostriker & Peebles, 1973; Athanassoula, 2003; Binney & Tremaine, 2008). Nevertheless, it remains unclear which properties of nearby galaxies are responsible for maintaining them bar-less.

1.4.1 Resonant Orbital Families

Once the bar forms from the stars already present in the galaxy disc, it rotates as a solid body with an angular frequency, often called the pattern speed ($\Omega_{\rm bar}$). In the rotating frame of reference, it is possible to identify different resonant orbits, both in the bar and in the disc (e.g., Contopoulos & Papayannopoulos, 1980; Contopoulos & Grosbol, 1989; Binney & Tremaine, 2008). While there are many different bar orbital families, we will briefly describe the two that are thought to be most important for characterising the bar and the bar-built structures that are relevant for this Thesis: the x_1 and x_2 families. The x_1 family is considered the *backbone* of the bar, that is, stars following these orbits sustain the bar elongated structure. The orbits are elongated parallel to the bar and can have different shapes depending on their energies, from pure ellipses to ellipses with cusps and/or loops at the extremities. The x_2 family is elongated perpendicular to the bar and is constrained to the central-most regions of the galaxy (see the example from Sellwood, 2014 in Fig. 1.4). Additionally, the x_2 family is thought to be associated with the formation of bar-built central structures, called the nuclear disc and nuclear ring (further discussed in Sect. 1.5.3).

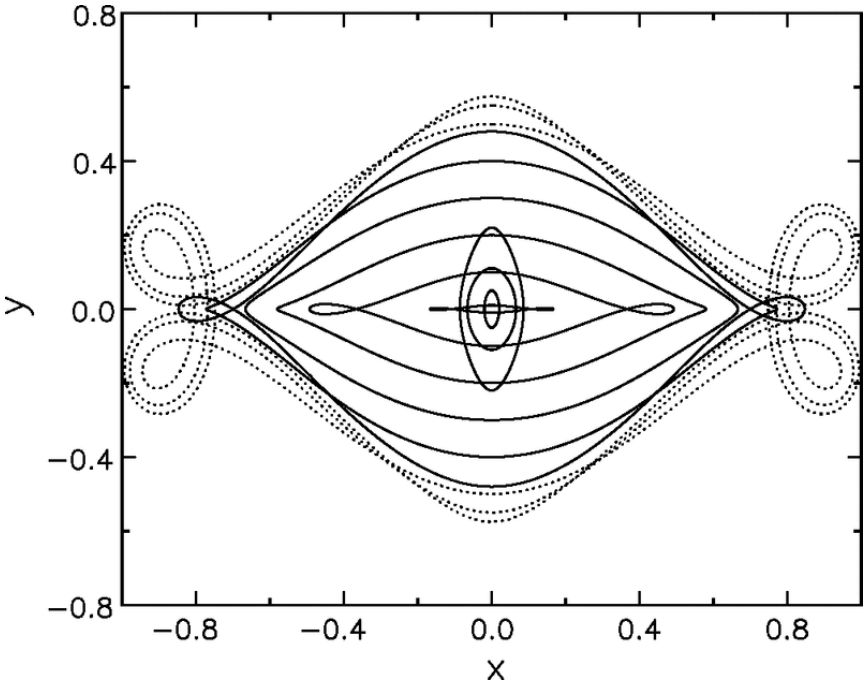

Figure 1.4: Examples or periodic orbits in the bar rest-frame (fig. 11 from Sellwood, 2014). The solid lines represent the periodic orbit families x_1 and x_2, where the first is parallel to the bar (horizontal), while the second is confined to the central regions and are aligned perpendicular to the bar and perpendicular to the first. The dotted lines are 4:1 resonant orbits – which can also contribute to the bar structure and morphology.

Furthermore, due to the influence of the bar exerted on stars in the disc, some disc

orbits will also be in resonance with the bar as well. A star with an angular frequency of Ω, and a radial frequency κ orbits in planar resonance with the bar if it follows the relation (Binney & Tremaine, 1987):

$$l\kappa + m(\Omega - \Omega_{\rm bar}) = 0 \tag{1.2}$$

where m and l are integers that, in the bar rest-frame, represent the radial oscillations and revolutions around the centre, respectively (e.g., Binney & Tremaine, 2008; Sellwood, 2014). Orbits with $\Omega = \Omega_{\rm bar}$, are in *corotation resonance* (CR) with the bar, and these are associated with the corotation radius. Theoretical work by Contopoulos (1980), showed that the corotation radius is a limiting radius to how long a bar can be, i.e. the bar cannot extend beyond corotation. Additionally, solutions for $l = -1, +1$ and $m = 2$ define the *inner* and *outer Lindblad resonances* (ILR and OLR), respectively. Typically, for strong bars, the concept of the ILR is expanded to the x_2 orbital family, i.e. the presence of x_2 orbits signal the existence of an ILR in the galaxy (e.g., Athanassoula, 1992a). Numerical works show that these three resonances are trapping resonances, that is, they trap gas and stars over time (e.g., Athanassoula 2002, 2003; Ceverino & Klypin, 2007). Often, they are associated with the formation of structures within the galaxy, such as nuclear discs/rings such as nuclear discs/rings (ILR), inner rings (CR), and outer rings (OLR – see example in Fig. 1.5[9] – e.g., Buta, 1995; Buta & Combes, 1996)

Figure 1.5: Example of a barred galaxy with rings, NGC 1398 (image credit Mark Hanson). On the right, I illustrate the rings present in this galaxy: the nuclear disc/ring, associated to the ILR (1 - blue circle); the bar (2 - white ellipse); the inner ring, associated to the CR (3 - green circle); and the outer ring, associated to the OLR (4 - yellow circle).

[9]Image credit: https://apod.nasa.gov/apod/ap230712.html

1.4.2 Angular momentum exchange

In an isolated galaxy, the total angular momentum must be conserved, thus, different regions of the galaxy will either absorb or emit angular momentum, in equilibrium. Angular momentum exchange plays a major role in the bar evolution. Theoretical works find that the bar loses angular momentum, growing stronger, longer, and slower (e.g., Athanassoula, 2003). Athanassoula (2003) argues that there are mainly three ways a bar can shed angular momentum: (*i*) by trapping disc starts outside the bar region, changing their former quasi-circular orbit into an elongated one. In this way, the newly trapped stars will compose the outer parts of the bar which, in turn, will grow longer and stronger; (*ii*) by making the orbits of stars that belong to the bar more elongated, the bar becomes thinner; and (*iii*) by decreasing its pattern speed and slowing down. Of course, these processes can happen simultaneously. For example, as the bar becomes slower, the CR radius moves outwards, allowing space for newly-trapped stars. These exchanges take place at the resonances, such as the ILR, CR, and OLR (e.g., Athanassoula 2002, 2003; Ceverino & Klypin, 2007). Mapping the angular momentum exchange (i.e., gain or lost) for N-body simulated galaxies, Athanassoula (2003) finds that, in the disc, ILR is the main resonance that emits angular momentum, while the CR absorbs it. This agrees with Lynden-Bell & Kalnajs (1972) results in which the galaxy loses angular momentum outwards. On the other hand, the spheroid components absorb angular momentum, at the resonances. Additionally, Athanassoula (2003) measured the net angular momentum for different structures – disc, halo, and spheroid – over time, finding that the disc component loses angular momentum while the halo and spheroid gain it. The angular momentum exchanged between different components is closely related to the capacity of these structures to emit/or absorb and their limitation factors, such as associated velocity dispersion, the mass in the resonant regions, and if the dark matter halo is rigid or not (see e.g. Combes & Sanders, 1981, Athanassoula, 2003; Halle et al., 2015, Fragkoudi et al., 2017)

1.4.3 Observational properties of bars

The knowledge regarding bar orbit periodic families and resonances comes mainly from numerical simulations, since observationally we can not trace temporal changes in galaxies. However, they do create counterparts that can be measured observationally: bar length, strength, and pattern speed. Below, I briefly summarize different techniques to measure such bar properties.

Measuring bar length

Measuring bar lengths is not straightforward, both for mock and real galaxies. Since the bar is located in a disc, many times with a prominent bulge and spiral arms, determining the end of a structure and the beginning of another is not a simple task. Throughout the literature, many different strategies have been proposed, and not always converged.

The simplest approach to measure bar length is by visual inspection (e.g., Martin

& Roy, 1995; Díaz-García et al., 2016) or considering a manual bar-shaped mask (e.g., Masters et al., 2021). A more sophisticated possibility is to perform a photometric structure decomposition of the galaxy and derive radial surface brightness profiles. With this, it is possible to model the light distribution using parametric functions – such as the Sérsic profile for bulges and bars, exponential disc, modified Ferrer's ellipsoid for bars, and others (e.g., de Jong, 1996; Prieto et al., 1996; Gadotti, 2011; Salo et al., 2015; Kruk et al., 2017). Other studies use isophote ellipse fitting, considering different parameters as the bar length delimiter, such as the radius in which the position angle changes after the ellipticity increases (e.g., Sheth et al., 2003; Erwin, 2005), or the radius in which the ellipticity is maximum (e.g., Wozniak et al., 1995; Erwin, 2005; Aguerri et al., 2009). Applying Fourier decomposition, one can consider $m = 2$ as the mode related to bi-symmetric structures, like the bar. Due to that, studies consider the radius in which the $m = 2$ mode drops to a fraction of its peak value to indicate the bar length (e.g., Fragkoudi et al., 2021; Ghosh et al., 2023). Lastly, from a dynamically motivated perspective, some studies model the galactic potential, including the bar, to locate the position of the maximum extent of the most stable x_1-orbit (e.g., Petersen et al., 2023) or trapped bar orbits (e.g., Lucey et al., 2023).

In the face of so many different approaches to measuring bar length, it is necessary to understand the strengths and weaknesses of each method and which methods result in consistent estimates. For a sample of around 600 face-on galaxies (drawn from the S^4G survey – Sheth et al., 2010), Díaz-García et al. (2016) analyzed different bar properties, including the length, using different estimators. The authors compared bar length estimations from different methods, such as visual inspection, ellipse fitting – considering the radius of maximum ellipticity –, the radius of maximum torque, and the radius of maximum $m = 2$ mode, obtained through Fourier decomposition. All methods correlate positively and, compared to visual inspection, some approaches underestimate the bar size, while others produce an overstimate. Nonetheless, several studies have found that the semi-major axis of maximum ellipticity tends to underestimate the bar length (e.g., Wozniak et al., 1995; Laurikainen et al., 2002; Athanassoula, 2002; Erwin & Sparke, 2003). More recently, Ghosh & Di Matteo (2023) compared different methods for measuring bar length, considering a $N-$body model of a barred galaxy with a live dark matter halo that evolves. Briefly, all the methods considered in that work are also positively correlated, however, some over/underestimate the size of the bar in different evolutionary moments and/or in the presence of spiral arms. For example, the method that considers the radius in which $m = 2$ drops to 70% of the peak value seems to be reliable only in the absence of spiral arms, otherwise it overestimates the bar length in $\sim 5 - 15\%$. In conclusion, different methods will have different systematic problems and which method is the most reliable is still an open question.

Measuring bar strength

Intuitively, the bar strength can be associated with the bar potential, since the deeper the gravitational potential the more robust and stable the bar is. Along with that, a deep potential will also allow the bar to trap more stars in x_1-orbits, increasing the fraction of light enclosed in the bar – when compared to the disc. However, the quantitative measurement of bar strength is not uniquely defined and different approaches exist in the literature, such as the ratio between the maximum value of the surface brightness in the bar compared to the minimum in the inter-bar region (e.g., Elmegreen & Elmegreen, 1985; Regan & Elmegreen, 1997); the minor and major axis ratio and bar length (e.g., Martin, 1995; Martinet & Friedli, 1997; Chapelon et al., 1999); and the ratio between the amplitude between the Fourier components $m = 2$ and $m = 0$ (e.g., Aguerri et al. 1998, 2000; Debattista & Sellwood, 2000; Athanassoula, 2003). In addition, simulations show that, as bars evolve and become stronger, their morphology becomes boxier as well (e.g., Athanassoula, 2002). Due to that, Gadotti (2011) introduced a new parameter to measure strength in bars, the product between ellipticity and boxiness, finding a positive correlation with the normalized bar size. By characterizing galaxies in the S^4G, Díaz-García et al. (2016) also compared three different approaches to measuring bar strength: the gravitational torque, the normalized amplitude of the Fourier $m = 2$ component, and the isophotal ellipticity (from Herrera-Endoqui et al., 2015), finding that the three proxies correlate positively and depend on the galaxy T-type. In summary, there are different ways of characterizing bar strength that rely on different properties, however, there is not a unified definition of bar strength so far.

Measuring bar pattern speed

The bar pattern speed ($\Omega_{\rm bar}$), as already mentioned in Section 1.4.1, is the angular velocity at which the bar rotates around the centre of the galaxy as a solid body and, the radius where $\Omega = \Omega_{\rm bar}$ defines the corotation radius. A classical method used to measure $\Omega_{\rm bar}$ is the Tremaine-Weinberg method (TW – Tremaine & Weinberg, 1984), which is model-independent and requires the galaxy kinematics and physical parameters, such as inclination and position angle. Briefly, the TW method consists of measuring the line-of-sight velocity in slits parallel to the galaxy's major axis position angle and follows:

$$\Omega_{\rm bar} sin(i) = \frac{\langle v \rangle}{\langle x \rangle}, \tag{1.3}$$

where $\langle v \rangle$ is the light-weighted average line-of-sight velocity in the slit and $\langle x \rangle$, is the light-weighted average distance of the slit to the centre. Although it is considered a simple method, Zou et al. (2019) demonstrated, by using a simulated galaxy, that the main source of uncertainty for the TW method is the position angle of the galaxy, in agreement with Garma-Oehmichen et al. (2022). Additionally, Williams et al. (2021) showed that different

tracers (i.e., stars, ionized gas, molecular gas) can derive different $\Omega_{\rm bar}$ for the same galaxy, highlighting how measuring the bar pattern speed is not trivial.

Additionally to the pattern speed, Elmegreen (1996) introduced the $\mathcal{R}$ parameter, defined as the ratio between the corotation radius and the bar length ($\mathcal{R} = {\rm R_{CR}}/{\rm R_{bar}}$). With this, bars are commonly categorized as fast if $1 \leq \mathcal{R} \leq 1.4$ and slow if $\mathcal{R} \geq 1.4$. That is bars with a given length and rotation curve, which have different corotation radii (and therefore $\Omega_{\rm bar}$) rotate faster ($\mathcal{R} < 1.4$) or slower ($\mathcal{R} > 1.4$) for shorter and longer corotation radii, respectively, and this definition is made as to normalise the bar pattern speed to be compared between different galaxies. $\mathcal{R}$ is often called the "bar rotation rate". As discussed above, as bars slow down they also get longer and then one could ask how the bar rotation rate would change at all. It is thus important to point out that theoretical work (e.g., Debattista & Sellwood, 2000) suggests that, through dynamical friction with the dark matter halo, the corotation radius grows more significantly than the bar. Lastly, since the corotation radius limits the bar length, $\mathcal{R}$ must be above 1 for all galaxies (although, see discussion regarding "ultra-fast bars" – e.g., Cuomo et al., 2019).

1.5 Bar-driven evolution

Stellar bars are understood as one of the most important internal drivers of secular evolution. Bars efficiently redistribute angular momentum, as well as stars, gas and dark matter, across the galaxy (e.g. Lynden-Bell & Kalnajs, 1972; Combes & Gerin, 1985; Athanassoula, 2003; Munoz-Tunón et al., 2004; Sheth et al., 2005; Romero-Gómez et al., 2007; Di Matteo et al., 2013; Halle et al., 2015; Fragkoudi et al. 2016, 2017). Additionally, bars have been linked to a global quenching of star formation in galaxies (e.g. Masters et al., 2012; Schawinski et al., 2014; Haywood et al., 2016; Géron et al., 2021), while linked with inducing bursts of star formation in central regions (e.g. Ishizuki et al., 1990; Ellison et al., 2011; Coelho & Gadotti, 2011). In this Section, I briefly describe some of the evolutionary consequences of a galaxy hosting a bar.

1.5.1 Bar quenching

In comparison to unbarred galaxies, galaxies hosting bars are typically redder with lower current SFR (e.g., Masters et al., 2011; Vera et al., 2016; Kruk et al., 2018), which can be associated to a "bar quenching". In other words, bars can be responsible for quenching the star formation of their host galaxy by sweeping the gas available in the disc toward its central parts, causing significant bursts of central star formation that deplete the gas content. It is not trivial, however, to disentangle which processes in barred galaxies are due to the presence of the bar or not. For example, it is not clear if bars form preferentially in already red and quiescent galaxies or if they are the inducers of the quench and gas consumption (e.g., Villa-Vargas et al., 2010; Algorry et al., 2017). To disentangle the bar-driven processes, Fraser-McKelvie et al. (2020) analysed a Mapping Nearby Galaxies at

APO (MaNGA) sample of galaxies, with unbarred counterparts matched for both mass and morphology. The authors find that barred galaxies are, in general, more metal-rich, less dust-obscured, and with older stellar populations than their unbarred counterparts. They argue that the differences in SFH can explain the current properties of both groups, that is, barred galaxies peak their star formation and assemble most of their stellar mass before unbarred galaxies. Furthermore, barred galaxies quench earlier than their unbarred counterpart.

Even though bar quenching can explain the described differences, it remains a debate if that is indeed the case. These properties can be due to two facts: either bars drive galaxy quenching or bars are more likely to form in galaxies that already started to quench (in agreement with theoretical findings from Berentzen et al., 2007; Athanassoula et al., 2013; Seo et al., 2019). To appropriately constrain the bar-quenching contribution to galaxy evolution, it is necessary to derive the age of the bars simultaneously with the period in which the galaxy started to quench, which was not yet achieved by the community.

1.5.2 Box/peanut bulge formation

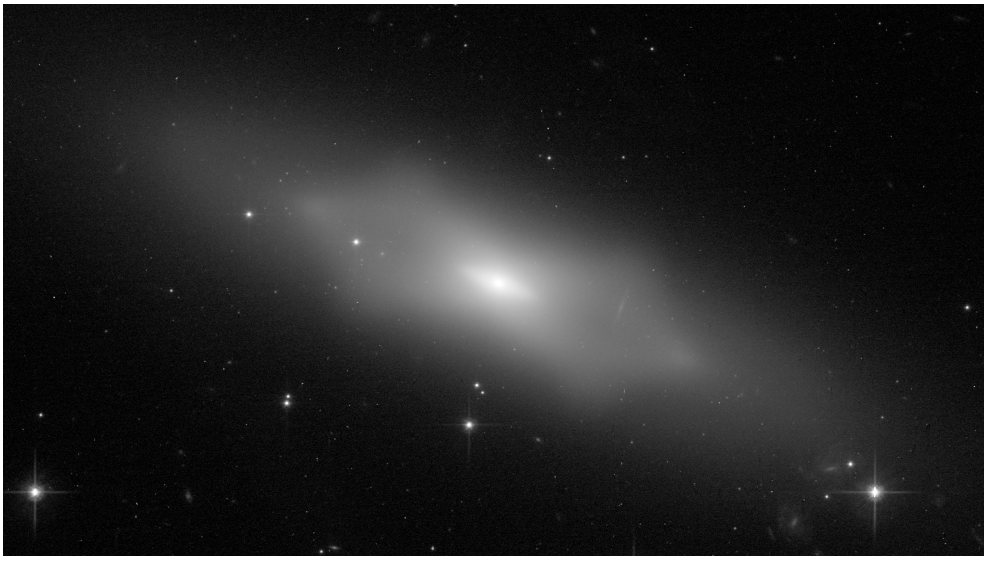

Figure 1.6: Edge-on galaxy NGC 1175 captured by the Hubble Space Telescope (HST), a clear example of Box/Peanut/X-shape bulge structure.

Box/peanut bulges (also referred as X-shaped, b/p's, or box/peanuts) are structures that extend vertically above and/or below the plane of the disc of galaxies (see example Fig. 1.6[10]). These structures are detected in nearly half of the edge-on galaxies in the Local Universe (e.g., De Souza & Dos Anjos, 1987; Lütticke et al., 2000), including the Milky Way (e.g., Weiland et al., 1994; Howard et al., 2009; Ness & Lang, 2016).

[10]Image credit: https://www.esa.int/ESA_Multimedia/Images/2019/12/Hubble_s_celestial_peanut

Numerical studies find that the box/peanut bulges are linked to the bar evolution, more precisely the bar buckling – that is, vertical orbital instabilities that cause the inner part of the bar to puff out of the plane of the disc (e.g., Binney, 1981; Pfenniger & Friedli, 1991; Skokos et al., 2002), and form relatively shortly after the bar formation itself ($1 - 2$ Gyr – e.g., Combes et al., 1990; Martinez-Valpuesta et al., 2006). Considering high-resolution N-body simulations, Martinez-Valpuesta et al. (2006) investigated the effects of the initial buckling on the bar, finding its height can nearly double while its length shrinks by half. Additionally, the authors find that within the bar lifetime, recurrent buckling is possible. By mapping the contribution of different structures in the centre of the Milky Way, studies find that most of what is commonly denominated as "classical bulge" is actually the b/p (e.g., Shen et al., 2010; Ness et al. 2012, 2013; Wegg & Gerhard, 2013; Di Matteo et al., 2014; Fragkoudi et al. 2017, 2018). Lastly, regarding the effects on star formation, the box/peanut formation has been associated with both an enhancement (e.g., Pérez et al., 2017) in star formation and a decrease of gas inflow (e.g., Fragkoudi et al., 2016) through the bar towards the central parts. By analysing CALIFA data and comparing it to numerical simulations, Pérez et al. (2017) find that the bar buckling can increase star formation in the central regions. On the other hand, Fragkoudi et al. (2016) analysed hydrodynamic simulations and found that the vertical instabilities decrease the gas inflow and subsequent star formation.

1.5.3 Formation and evolution of nuclear discs

One of the immediate effects that follow bar formation – and the ensuing onset of tangential forces in the disc – is the gas inflow to the central parts of the galaxy. This gas inflow builds the rotation-supported structures known as nuclear discs/rings (see example in Fig. 1.7[11]). Simulations and theoretical studies find that, after the bar forms, it only takes $\sim 10^8$ yrs to form the nuclear disc (ND; see example in Fig. 1.8 – e.g. Athanassoula 1992a,b; Lin et al., 2013; Emsellem et al., 2015, Seo et al., 2019; Baba & Kawata, 2020). Many galaxies in the Local Universe, including the Milky Way (e.g., Sormani et al., 2020, 2022), host nuclear discs and/or rings (e.g., Comerón et al., 2010; Sheth et al., 2010; Gadotti et al., 2015; Erwin et al., 2015), which can vary in properties such as size, SFR, and gas and dust content. Considering an SDSS sample of ~ 1000 galaxies and performing 2D image decompositions, Gadotti (2009) found that 32% of disc galaxies with photometric bulges actually host a nuclear disc. The Atlas of Images of NUclear Rings (AINUR – Comerón et al., 2010) shows that 20% of the disc galaxies in the Local Universe host a star-forming nuclear ring. The TIMER survey (Gadotti et al., 2019) finds that for a sample of 21 massive, strongly barred galaxies, morphologically selected as hosting nuclear rings, at least 19 clearly host a rapidly rotating nuclear disc. Nevertheless, it is not clear how common these structures are for different morphologies, masses, and redshifts, and how accurate the different detection methods are.

Nuclear discs, which in the past were also referred to as "pseudo-bulges" (e.g.

[11]Image credit and details: https://www.eso.org/public/images/eso0438d/

Figure 1.7: Example of barred galaxy, NGC 1097 (image credit ESO). On the right, I illustrate important structures for this Thesis: the bar (1 – white ellipse); one of the dust lanes (2 – black line); and the nuclear disc/ring (3 – blue circle).

Kormendy & Kennicutt, 2004), can be differentiated from "classical bulges" by using photometry since they display exponential surface density profiles, characteristic of discs (e.g., Gadotti et al., 2020 and references therein). For that reason, they also have been called "discy-bulges" and other denominations, to differentiate these structures from classical dynamically-hot bulges (Athanassoula, 2005). Even though these structures can be identified through photometry, results from the TIMER survey (Gadotti et al., 2019, 2020) argue that the chances of misclassification of nuclear discs can be high when the physical spatial resolution is not suitable, and the best way to find and characterize these structures is through high spatial resolution integral field spectroscopy, with the derivation of the spatial distributions of stellar kinematics and population properties. In agreement, Méndez-Abreu et al. (2018) find no correlation between photometric and kinematic properties of bulges in a sample of 28 lenticular galaxies from the Calar Alto Legacy Integral Field Area survey (CALIFA, Sánchez et al., 2012).

By measuring the high spatial resolution kinematic properties of nuclear discs, Gadotti et al. (2020) found that the nuclear disc kinematic size is well correlated with the bar length, (in qualitative accordance with Shlosman et al., 1989; Knapen, 2005; Comerón et al., 2010), where, typically, longer bars host larger nuclear discs. The kinematic size is defined by the place in which the radial profile of stellar velocity over velocity dispersion (V/σ) is maximum. Additionally, some recent simulations suggest that as the bar grows

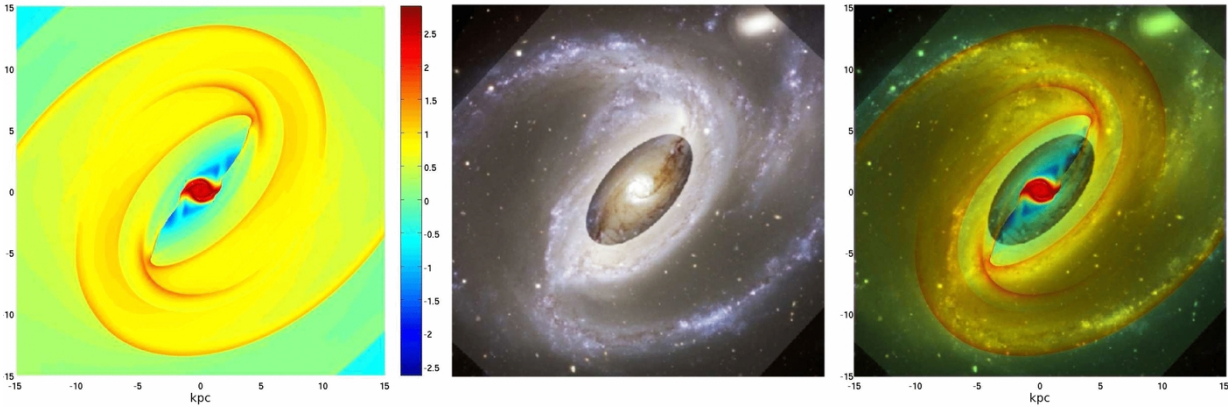

Figure 1.8: Hydrodynamical simulation of NGC 1097, from Lin et al. (2013). In the left panel is the simulation gas surface density distribution (in logarithmic scale in units of $M_{\odot}.pc^{-2}$), in which it is possible to identify the bar, the dust lanes and the nuclear disc – as illustrated in Fig. 1.7. The central panel is the same as in Fig. 1.7, but with different brightness enhancements and, in the right panel, the authors show the superposition of both images.

longer, the nuclear disc also increases in size (e.g., Seo et al., 2019). This indicates a possible co-evolution between the bar and the nuclear disc. This co-evolution can be explained by the place in which the gas stops moving inwards and forms the nuclear disc. Even though the exact location in which it happens is unclear, some works suggest it can be associated with bar properties, directly or indirectly. Early work indicates that the gas moving inwards stops at the Inner Linbald Resonance (ILR) and forms the nuclear disc (e.g., Athanassoula, 1992a, 1992b). As the bar grows and evolves, the ILR moves outwards, building the nuclear disc inside-out. With this, we expect the nuclear disc evolution to be linked with the bar evolution, where the nuclear disc is built inside-out (e.g., Bittner et al., 2020, de Sá-Freitas et al., 2023). However, it remains unclear if bars grow with time and if the co-evolution with nuclear discs is real since nuclear discs can also grow independently of the bar (e.g., Athanassoula, 1992). Lastly, different works suggest that nuclear rings are the outer rim of the nuclear disc, which is currently forming stars (e.g., Cole et al., 2014; Bittner et al., 2020). Gadotti et al. (2020) and Bittner et al. (2020) demonstrated that nuclear discs and nuclear rings have the same kinematic properties and should not be differentiated.

In addition to building nuclear discs, gas inflows via the bar have been associated with providing a gas reservoir for super massive black holes (SMBH) at the centres of galaxies, triggering active galactic nuclei (AGN – e.g., Davies et al., 2014; Audibert et al., 2021). Studying a sample of Seyfert galaxies (that is, galaxies with nuclear activity related to the central supermassive black hole – SMBH), Simkin et al. (1980) found that nuclear activity is preferentially seen in barred galaxies with inner rings or pseudorings (in agreement with e.g. Arsenault, 1989; Shlosman et al., 1989; Friedli & Benz, 1993; Heller & Shlosman, 1994;

Moles et al., 1995). Considering a sample of 186 Seyfert/AGN galaxies, Moles et al. (1995) found that 95% of these galaxies hosted bars and rings. On the other hand, however, Ho et al. (1997) analysed a sample of 500 galaxies, concluding that bars do not necessarily correlate with AGN activity. Even though bars can funnel gas from kiloparsec scales to central regions, the gas might be stalled in the ILR, forming nuclear discs instead of moving further to the SMBH. Due to that, additional mechanisms have been proposed to bring the gas from the nuclear disc to the inner regions, such as nuclear bars (e.g., Shlosman et al., 1989; Hopkins & Quataert, 2010). More recently, Kolcu et al. (2023) proposed a new technique to identify coherent structures funnelling gas inside the nuclear disc/ring, such as nuclear spiral arms. Using integral field spectroscopy data (from TIMER survey – Gadotti et al., 2019) and analyzing the differences in velocities of Hα and [NII]λ6583, the authors detect funnelling spirals in NGC 1097, part of the Composite Bulges survey (Erwin et al., 2023 – in prep.). Coelho & Gadotti (2011) found that in a sample of relatively low mass galaxies, "35% of barred galaxies are AGN, whereas this fraction drops to only 16% when one considers unbarred galaxies. In the high mass bin, 55% of barred galaxies are AGN, whereas 34% of unbarred galaxies are AGN." In line with these results, Silva-Lima et al. (2022) and Garland et al. (2023) find that AGN are preferentially found in barred galaxies, although the degree of statistical significance of the results is varied (but see also Zee et al., 2023). Therefore, while bars are not a sufficient nor a necessary condition for triggering AGN, a consensus emerges in that bars help building a reservoir of gas near the SMBH, which is then further moved inwards via other physical processes.

1.6 Goals of this Thesis

To fully understand when and how bars form, and the subsequent evolutionary processes they drive within their host galaxies, we first need to determine the ages of bars. These can also be used as a lower limit to estimate when discs settle in the Universe. However, it is not trivial to derive the bar formation time. One approach to determining when bars emerged, is by investigating the fraction of bars at different redshifts. However, there are limitations involved in this approach, as finding bars at high redshifts can be challenging due resolution issues, sensitivity limitations and band-shifting. For example, with HST, galaxies above redshift $1-2$ can only be probed at a rest-frame wavelength that corresponds to the bluest part of the optical spectrum or the UV, where bars are harder to detect due to their old stellar populations. Furthermore, measuring the bar length for nearby well-resolved galaxies is already a challenge and, for high-redshift galaxies, the uncertainties are significantly larger. Even though simulations predict that bars can exist since $z \approx 1-2$ (e.g., Kraljic et al. 2012; Rosas-Guevara et al. 2020; Fragkoudi et al. 2020, 2021), only recently were bars above $z = 2$ observed, thanks to the higher sensitivity and wavelength coverage offered by JWST (Guo et al., 2023). To overcome these instrumental limitations, one can use archaeological data from nearby barred galaxies to estimate when their bars have formed.

Since bars form from stars that were previously in the galaxy disc, the age of the stellar population in the bar is not the so-called dynamical age of the bar, i.e., the time since the bar formed. Different studies have attempted to time when the bar formed for a handful of galaxies using different approaches. Gadotti et al. (2015) analysed stellar populations in the nuclear disc of NGC 4371 using high-quality Multi Unit Spectroscopic Explorer (MUSE) data, and found a bar age of about 10 Gyrs. Pérez et al. (2017) used the formation of the boxy/peanut-shaped bulge, which originated from instabilities of the bar, to estimate the age of the bar in NGC 6032 as 10 Gyrs. de Lorenzo-Cáceres et al. (2019) analysed the star formation histories (SFHs) of nuclear structures, including inner bars, and found that the inner bars in NGC 1291 and NGC 5850 must have formed at least 6.5 Gyrs and 4.5 Gyrs ago, respectively. However, until this Thesis, there was not a systematic methodology that could be applied generally to a large number of galaxies.

The main goal of this Thesis is to measure, for the first time, the ages of bars in a sample of barred galaxies in the local Universe, to provide a temporal benchmark on bar formation and evolution. To do that, I will first present the first broadly applicable methodology to derive bar ages for galaxies in the nearby Universe. I then apply this method to a sample of galaxies in the nearby Universe, as well as reporting on the serendipitous discovery of the smallest and youngest nuclear discs to date.

In Chapter 2, I present in detail the newly developed methodology to estimate bar ages based on the nuclear disc formation – since it takes place in 10^8 yr following the bar formation, the formation of the nuclear disc is a good proxy for the dynamical age of the bar (e.g., Athanassoula 1992,a; Emsellem et al., 2015; Seo et al., 2019; Baba & Kawata, 2020). That is, by deriving the star formation history (SFH) of the nuclear disc one can derive the age of the bar (Gadotti et al., 2015). I start by disentangling the light of the nuclear disc from other structures in the central region of the galaxy since the observed light carries tangled information about the nuclear disc with the underlying main disc – and possibly other structural components that were already present when the nuclear disc formed. With the independent spectra information, I am able to derive the nuclear disc SFH and its onset, estimating the bar formation epoch as well. I present pilot results for NGC 1433, one of the galaxies in the TIMER survey (Gadotti et al., 2019). The TIMER survey consists of a VLT@MUSE, high-quality data survey, covering the central few kiloparsec of 24 face-on nearby galaxies – of which, to date, 21 galaxies were observed. The sample was selected from the Spitzer Survey of Stellar Structure in Galaxies (S^4G – Sheth et al., 2010), and all galaxies host bars with a range of bar strength and show prominent central structures. In addition, all TIMER galaxies are part of the local 40 Mpc volume and are more massive than 10^{10} $M_\odot$. Lastly, the approach was tested on simulated galaxies, ensuring a reliable criterium to measure the formation of the bar linked to the nuclear disc SFH and perform tests to constrain the statistical and systematic errors in the derived bar age.

In Chapter 3, I present the serendipitous discovery of the smallest extragalactic

nuclear discs, kinematically confirmed, with sizes similar to the nuclear disc hosted by the Milky Way. Additionally, applying the methodology presented in Chapter 2, I derive the corresponding bar ages, finding relatively young bars with ages of 0.7 and 4.5 Gyr. These are the only external nuclear discs with sizes similar to that of the Milky Way's nuclear disc, and their relatively young ages fit well in our theoretical understanding of bar and nuclear disc formation and evolution, as will be discussed in detail further below.

Following, in Chapter 4, I applied this methodology to 17 galaxies from the TIMER survey (Gadotti et al., 2019) and, together with the 2 galaxies with newly discovered nuclear discs and the Milky Way, present the largest selection of barred galaxies with derived bar ages – individual results for the TIMER galaxies can be found in Appendix A. With this sample, I am thus able, for the first time, to observationally test time-related theoretical predictions on the evolution of bars and their host galaxies. Additionally, this work enables new lines of investigation and new inputs on galaxy and bar evolution.

Finally, in Chapter 5 I summarize the findings of this Thesis, tracing the outlook plan for possible future work.

2

A new method for age-dating the formation of bars in disc galaxies

The TIMER view on NGC1433's old bar and the inside-out growth of its nuclear disc

Camila de Sá-Freitas; F. Fragkoudi; D. A. Gadotti; J. Falcón-Barroso; A. Bittner; P. Sánchez-Blázquez; G. van de Ven; R. Bieri; L. Coccato; P. Coelho; K. Fahrion; G. Gonçalves; T. Kim; A. de Lorenzo-Cáceres; M. Martig ; I. Martín-Navarro; J. Mendez-Abreu; J. Neumann; M. Querejeta

A&A, 671 (2023a)

The epoch in which galactic discs settle is a major benchmark for testing models of galaxy formation and evolution but remains largely unknown. Once discs settle and become sufficiently self-gravitating, stellar bars are able to form; therefore, determining the ages of bars can shed light on the epoch of disc settling, and on the onset of secular evolution. Nevertheless, timing when the bar formed has proven challenging. In this work we present a new methodology for obtaining the bar age, using the star formation history of nuclear discs. Nuclear discs are rotation-supported structures, built by gas pushed to the centre via bar-induced torques, and their formation is thus coincident with bar formation. In particular, we used integral field spectroscopic data from the TIMER survey to disentangle the star formation history of the nuclear disc from that of the underlying main disc, which enables us to more accurately determine when the nuclear disc formed. We demonstrate the methodology on the galaxy NGC 1433 – which we find to host an old bar that is $7.5^{+1.6}_{-1.1}(\mathrm{sys})^{+0.2}_{-0.5}(\mathrm{stat})$ Gyr old – and describe a number of tests carried out on both the observational data and numerical simulations. In addition, we present evidence that the nuclear disc of NGC 1433 grows in accordance with an inside-out formation scenario. This methodology is applicable to high-resolution integral field spectroscopic data of barred galaxies with nuclear discs, making it ideally suited for the TIMER survey sample. In the future we will thus be able to determine the bar age for a large sample of galaxies, shedding light on the epoch of disc settling and bar formation.

2.1 Sample and data description

In order to present the methodology we have developed – which separates the light of NDs from the underlying population – we select NGC 1433 for the pilot study (de Sá-Freitas et al., 2023), since it has a ND with similar properties to most NDs in the TIMER sample (e.g. Gadotti et al., 2020, Bittner et al., 2020 – which will be future targets of study). Also, we ensure that our methodology does not produce artificial bar ages for unbarred galaxies by applying it to two control bar-less galaxies: NGC 1380 and NGC 1084 (see Section 2.3.1).

Buta et al. (2015) classified NGC 1433 morphologically as strongly barred with a nuclear ring/lens and a nuclear bar. In addition, the galaxy is at a distance of 10 Mpc, has an inclination of 34°, and stellar mass of 2×10^{10} $M_{\odot}$ (see references in Gadotti et al., 2019). Following Gadotti et al. (2020), the radius of the ND is defined as the peak in the v/σ radial profile, which is 440 pc (see Fig. 2.3). We used data from the TIMER project: the observations were carried out using the MUSE instrument at the European Southern Observatory Very Large Telescope (ESO-VLT), in Period 97, from 2016 March to October, in Wide Field Mode. Considering the point spread function full width at half maximum, the spatial resolution of these observations is about 50 pc. Further details on the observations and data reduction can be found in Gadotti et al. (2019).

In Fig. 2.1 we display colour composites of our target along with maps of stellar kinematics and population properties: stellar velocity and velocity dispersion, the higher-order moments of the line of sight velocity distribution h_3 and h_4, stellar age, metallicity, and $\alpha-$enhancement, which were produced applying the GIST pipeline (Bittner et al., 2019) to the TIMER MUSE data (more details on the following section). One can see that NGC 1433 has clear signatures of a ND, that is, a rapidly rotating structure detached from the MD and coincident with a drop in velocity dispersion and mean ages. In addition, it also shows an anti-correlation between velocity and h_3, and an increase in h_4, as expected for NDs. These results are all in agreement with the findings in Gadotti et al. (2020) and Bittner et al. (2020), respectively.

2.2 Methodology

In this section we describe our methodology step-by-step, as illustrated in Fig. 2.2. We describe how we create the underlying stellar population contribution (Sect. 2.2.1) and how we isolate the SFH of the ND (Sect. 2.2.2). In Sect. 2.2.3 we describe the details in our data analysis and our criterion for obtaining the time of bar formation. In Sect. 2.2.4 we test our methodology by applying it to a simulated barred galaxy.

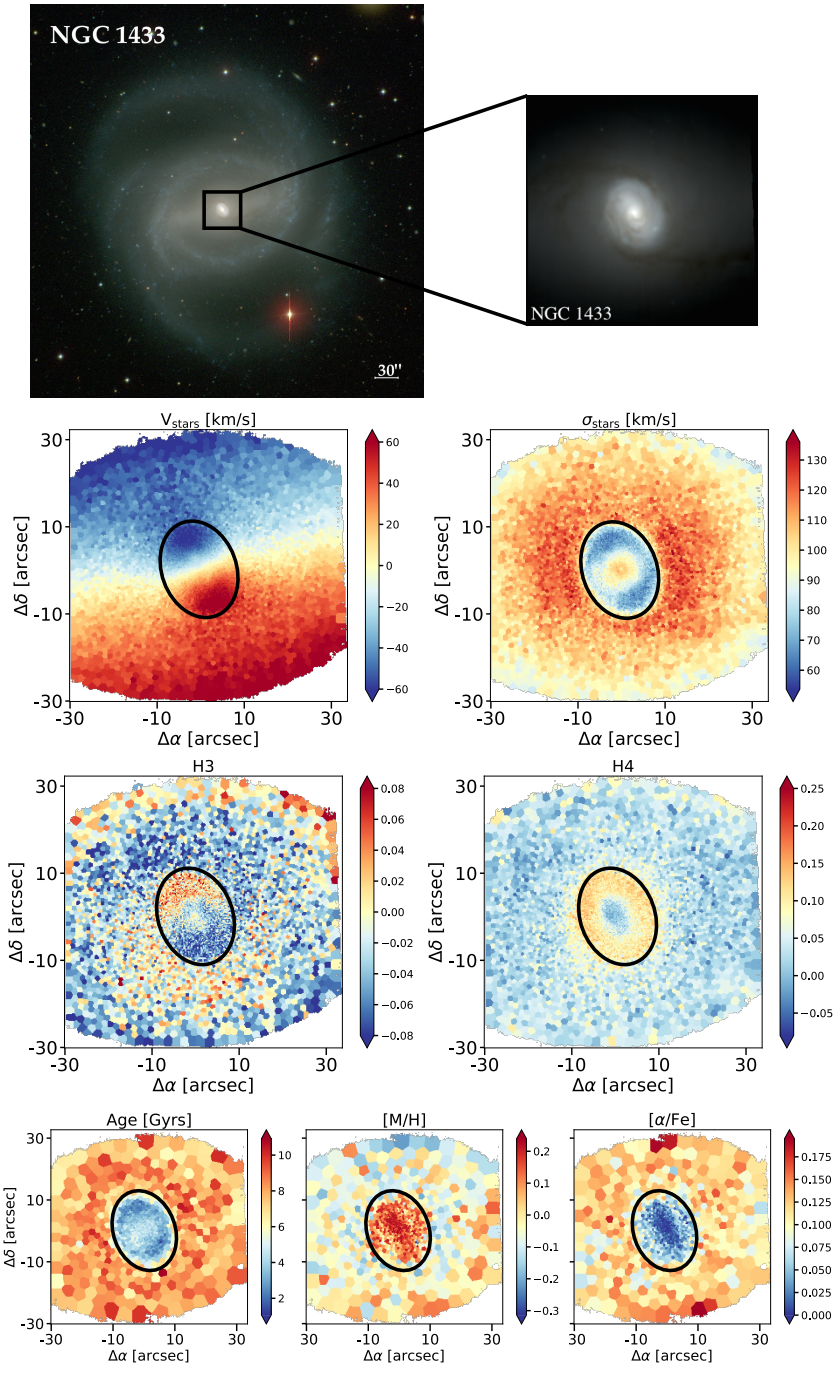

Figure 2.1: **NGC1433 data and derived maps:** The top two images are the colour composites of NGC 1433 from the Carnegie-Irvine Galaxy Survey (top left; Ho et al., 2011) and TIMER (top right; Gadotti et al., 2019). Below are maps that show (from left to right and top to bottom) the stellar kinematics and population properties derived from the TIMER data using GIST: stellar velocity, velocity dispersion, h_3, h_4, age, metallicity, and α enhancement. The ND radius is shown with a solid black contour and displays a faster rotation, a drop in velocity dispersion, an anti-correlation between velocity and h_3, and an increase in h_4. In addition, the same region corresponds to a drop in mean age and α enhancement and an increase in metallicity. It is clear that NGC 1433 hosts a younger ND with more rotational support in the central region than the underlying population, in agreement with Gadotti et al. (2020) and Bittner et al. (2020).

Figure 2.2: Illustration of the methodology described in Sect. 2.2 for a galaxy that hosts a ND. In the top left we highlight the field of view from MUSE in the centre of the galaxy and the position of the representative region just outside the ND. The position of the representative ring is chosen taking the v/σ radial profile into consideration. From it we derive the representative spectrum used to build the MD. In the bottom left we display the output from the light disentangling: the original data cube (red), the ND data cube (blue), and the representative MD data cube (green). All three data cubes have spaxels corrected to $v = 0$ km/s and $\sigma = \sigma_{\max}$ km/s. Lastly, we collapse each data cube into a mean spectrum (as illustrated) and derive SFHs for each one. The steps in our methodology are described to the right.

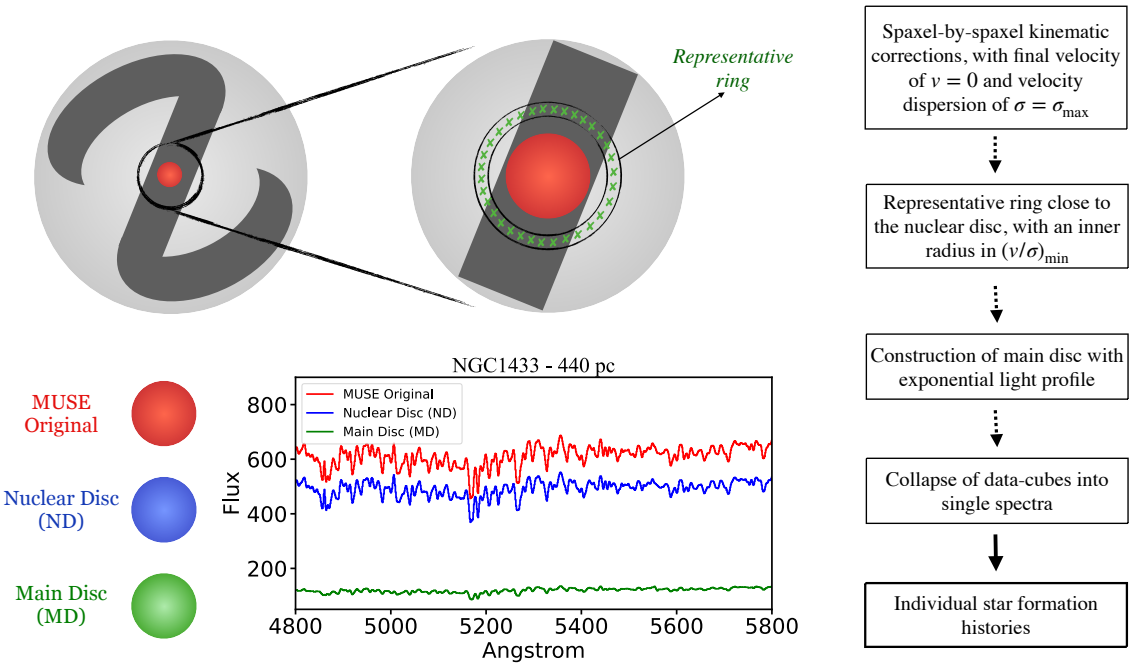

2.2.1 Building the underlying population contribution and disentangling the nuclear disc light

Recent studies deriving radial profiles of stellar ages found that galaxies hosting NDs display a drop in average ages towards the centre. This drop in average ages is coincident with the radius of the peak in stellar v/σ (e.g. Falcón-Barroso et al., 2002, Bittner et al., 2020), which implies that these galaxies have a central stellar structure that is younger than the main underlying population. This agrees with the scenario whereby NDs are structures formed by a relatively late gas inflow induced by stellar bars (e.g. Gadotti et al., 2015; Gadotti et al., 2019; Bittner et al., 2020). Hereafter, we consider the 'underlying main disc' to be every stellar population that was present before the formation of the ND. Since the observed light carries combined information of the younger ND and other underlying central

structures, the ages derived for the central region of the galaxy can only be considered as an upper limit to the mean stellar age of the ND.

In this section we describe a new strategy to build the underlying MD and disentangle the light of it from that of the ND. In summary, this methodology consists of deriving a spectrum that represents the main underlying disc (hereafter referred to as the 'representative spectrum'), using it to build a representative MD data cube, and later subtract it from the observed data. We make two hypothesis: (1) the MD extend all the way to the centre, and its surface brightness profile follows an exponential law and (2) the stellar populations of the MD do not change significantly in the inner regions and, therefore, we can assume is similar to the spectrum extracted from an aperture surrounding the nuclear ring. The result from this subtraction is expected to be the isolated ND. A step-by-step outline and an illustration of our methodology are shown in Fig. 2.2.

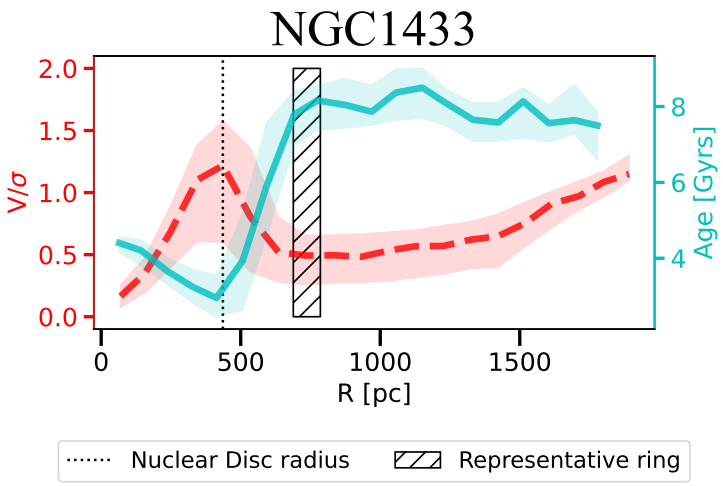

Figure 2.3: v/σ radial profile, displayed in dashed red contours (values in the left-axis), and light-weighted average age, in solid blue contours (values in the right axis) for NGC 1433. We display the median values together with the first and third quartiles. The vertical dotted black line marks the ND radius and the hatched area the representative ring. Note that the representative ring is placed in the first v/σ minimum outside the ND, which matches the oldest mean age.

Before building the MD, we treated the original data cube, taking the kinematic properties into consideration. We first used the data analysis pipeline (DAP) from the PHANGS-MUSE survey (Emsellem et al., 2022) for the original data cube, deriving kinematic and line emission properties. DAP is a module-based pipeline based on the Galaxy IFU Spectroscopy Tool (GIST; Bittner et al., 2019) able to extract properties from data cubes such as kinematic information, emission lines fluxes and more. For the emission lines fitting, DAP uses `pPXF` (Cappellari, 2012), considering emission lines as extra gaussian elements added to the stellar continuum. We measured the kinematic maps for Voronoi-binned (Cappellari & Copin, 2003) data with signal to noise of 100 and emission lines spaxel-by-spaxel, between the wavelengths 4800 and 7000 Å, employing the E-MILES simple stellar population (SSP) model library (Vazdekis et al., 2016) to remove the stellar continuum. From the results, we have kinematic properties such as stellar velocity and velocity dispersion and emission line fluxes. Applying the kinematic information, we shift all spectra to

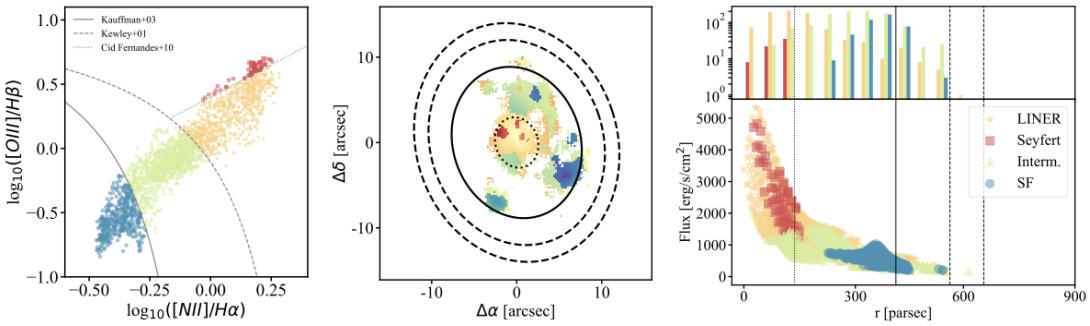

Figure 2.4: **NGC1433 BPT classification**: **Left:** BPT diagram (Baldwin et al., 1981) classification of each spaxel for the ND in NGC 1433. The BPT classification is continued in the **middle** and **right** panels, which display the physical position of the different spaxels and the light radial profile, respectively. We also display the radius of the inner mask dominated by AGN contributions (dotted contours), the radius of the ND (solid contours), and the representative ring (dashed contours).

have a final velocity of $v = 0$ km/s, accounting for both the galaxy recession velocity and internal kinematics. In addition, we also convolved the original data to ensure that every spectra has $\sigma = \sigma_{\rm max}$, where the latter is the highest velocity dispersion in the central region of the original data cube. For NGC 1433, $\sigma_{\rm max}$ is 122 km/s. We point out that we verified that the convolved data and the original data result in the same stellar population, so such a procedure does not affect our results. Our aim in doing so is to ensure we do not create artificial wings or artificial emission/absorption lines when subtracting the spectra (see below). Once the original data were shifted to $v = 0$ km/s and $\sigma = \sigma_{\rm max}$ km/s, we built our underlying MD.

The first step is to define the representative region from which we will extract the representative spectrum. This region is chosen as a ring surrounding the ND – from now on referred to as the 'representative ring'. The representative ring is expected to be as close as possible to the ND without being contaminated by its light. For galaxies hosting a ND, such as NGC 1433, we take into consideration the stellar v/σ radial profile (Fig. 2.3). We define the inner radius of the representative ring as the first minimum point outside the ND. That is the radius outside of which we expect the light from the MD to start dominating and, as expected, it is also the radius with the oldest mean age (see Fig. 2.3). Nevertheless, we tested different positions for the representative ring to assess the systematic error linked to this decision (see Section 2.3.1). In addition, the representative ring has a width of 2", so one does not expect strong age and flux gradients inside of it. Nonetheless, we performed tests with widths between 1" and 4" with little variation in the outcome.

Secondly, we aim to mask spaxels dominated by active galactic nucleus (AGN) emission, based on the Baldwin, Phillips & Tervelich (BPT) diagram classification (Baldwin et al., 1981), with AON $\geq$ 20. We used the emission lines Hα, Hβ, [OIII], and [NII] extracted by DAP, as described above, to build the BPT diagram in Fig. 2.4.

In the third step, we normalise the flux in each spaxel of the representative ring to account for the radial flux increase in the MD towards the centre. We normalised each spectra to $r = 0$ pc, assuming that the disc light profile follows the exponential function

$$I(r) = I_0 \times e^{-r/h}, \tag{2.1}$$

where h is the disc scale-length, r is the distance of a given spaxel from the centre (corrected for inclination effects), and I_0 is the flux at $r = 0$ pc. The value of h taken for NGC 1433 comes from Salo et al. (2015) and is 3100 pc. Considering we have $I(r)$ for each spaxel in the representative ring, we divided it by $e^{-r/h}$, extrapolating the observed flux to the centre of the galaxy. We derived the representative spectrum as the mean flux per wavelength of all spectra from the representative ring with $v = 0$ km/s, $\sigma = \sigma_{\max}$ km/s and the corresponding flux at $r = 0$ pc. Finally, to re-construct a data cube of the MD, we extrapolated the representative spectrum back to a range of radii, again taking an exponential light profile into account for the MD. Although the MD is often described with an exponential light profile, recent studies show that discs may not follow an exponential light profile all the way to the centre (e.g. Zhu et al., 2018; Breda et al., 2020; Papaderos et al., 2022). In light of this, we tested the implications of assuming an exponential profile in Section 2.3.1, by applying the same methodology to a flat light profile MD. We show that the choice of a profile for the main underlying population does not affect the results noticeably.

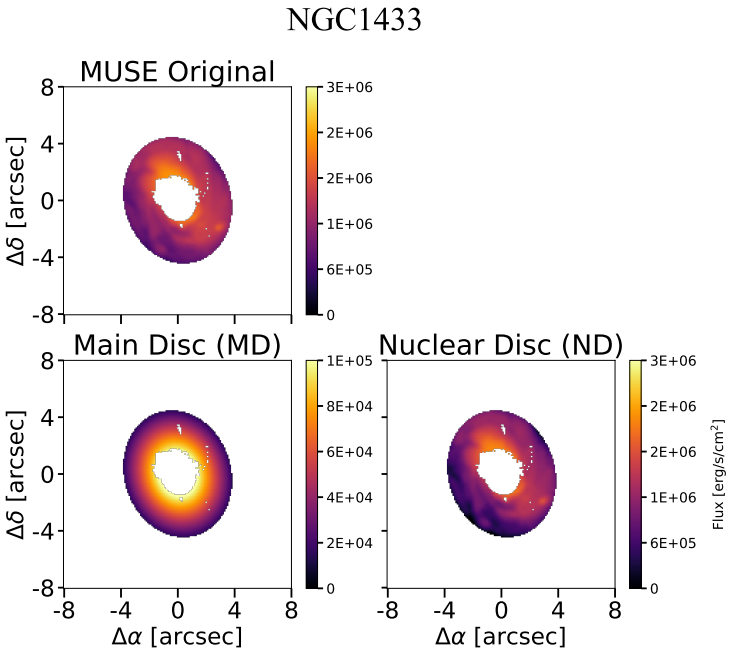

Figure 2.5: Illustration of different data products derived from the methodology described in Sect. 2.2. We display the sum of the original MUSE fluxes between 4800 and 5800 Å (top row), and the derived representative MD (bottom row, left) and the ND data (bottom row, right), which is the result of subtracting the representative MD from the original data cube. For the representative MD, it is possible to notice the exponential increase in flux towards the centre. All data cubes were masked for AGN contributions with AON ≥ 20.

Next, we subtracted the reconstructed MD from the original data. As mentioned,

in order to prevent the creation of artificial wings from the subtraction, we also used the original data convolved and shifted to $v = 0$ km/s and $\sigma = \sigma_{\rm max}$ km/s. With that, we can disentangle our original data into the MD and the ND data cubes, as exemplified in Fig. 2.5. Lastly, we collapse each data cube into a single mean spectra, deriving SFHs for each one. To assure that the collapsed spectra is the correct description of the central region for the three data cubes, we masked contributions from the AGN in the centre. Using the BPT classification (with AON $\geq$ 20) together with the light radial profile (Fig. 2.4, right), we delimited a central region to be masked of around 140 pc (15 spaxels), since it is dominated by AGN emission and can contaminate the total flux of the ND.

Due to the high quality of the TIMER data (Gadotti et al., 2019), the decision to collapse the data cube is not motivated by the increase of signal-to-noise ratio. Instead, we collapse the data cube to save computational time and guarantee low statistical errors. Nevertheless, we applied the same methodology for the non-collapsed data cube and the bar age is not strongly affected (see Section 2.3.1).

2.2.2 Deriving star formation histories and mass assembly

For each collapsed spectrum – MUSE original, MD, and clean ND data – we ran the GIST pipeline (Bittner et al., 2019) to derive stellar population properties and SFHs. To guarantee consistency in our analysis with previous TIMER work, we used the same GIST configuration as in Bittner et al. (2020). Firstly, GIST employs an un-regularised run of `pPXF` (Cappellari & Emsellem, 2004; Cappellari, 2017) to derive stellar kinematic properties. We also include a low-order multiplicative Legendre polynomial in the fit to account for small differences between the shape of the continuum templates and the observed spectra. Next, GIST employs `pyGandALF` (see Bittner et al., 2019) to model emission lines as Gaussians, simultaneously fitting the stellar continuum while the stellar kinematics remains fixed from the previous step. With this, we obtain the emission-subtracted spectra. Lastly, GIST performs a regularised `pPXF` run in the emission-subtracted spectra, in order to fit a combination of stellar populations and derive mean properties. Since metallicity and stellar velocity dispersion can both be responsible for absorption line broadening, causing possible degeneracies (e.g. Sanchez-Blazquez et al., 2011), we keep the stellar kinematics fixed from previous steps. In addition, to account for extinction and continuum mismatch effects, we apply an eighth-order multiplicative Legendre polynomial in the fit. For the last step, we employ the MILES library (Vazdekis et al., 2015), light-weighted, with [M/Fe] between -1 and $+0.4$, ages in the range 0.03–14 Gyr, and [α/Fe] enhancements of $+0.0$ and $+0.4$. Lastly, we use the regularisation error value of 0.15 derived for TIMER data by Bittner et al. (2020). As described in Cappellari (2017), the regularisation of the SFHs allows one to derive the smoothest and still physically meaningful result. To assess how much our final bar age relies on the regularisation error, we tested different values in Section 2.3.1. For further details on the data analyses, we refer the reader to previous TIMER papers (e.g. Bittner et al., 2020).

Lastly, pPXF also estimates different weights for SSPs with different ages, allowing us to build a non-parametric SFH. Each weight represents the fraction of the light formed in the different SSPs. In order to convert the light-weighted SFHs to mass-weighted SFHs, we consider the distance to the galaxy to derive the intrinsic luminosity. We then use the mass-to-light ratios[1] predicted from the BaSTI isochrones (Pietrinferni et al., 2004, 2006, 2009, 2013) to convert luminosity into stellar mass. The mass-to-light ratios assume a Kroupa revised initial mass function (Kroupa, 2001), and the MILES template library (Vazdekis et al., 2015) with [α/Fe] enhancements of +0.0 and +0.4. These mass-to-light ratios depend on the age, metallicity and [α/Fe] enhancement that best describe the observed data, and account for both stellar and remnants masses.

2.2.3 Age-dating bar formation

Considering the scenario in which the ND is formed from a late gas inflow due to the bar, in an ideal case, one could expect the original SFH characterised by an older star formation event followed by a later burst. Once we are able to disentangle the MD and the ND, we can expect the former's SFH to map the oldest star formation event and the latter's to map the youngest burst.

If we could perfectly disentangle the light of the ND from the underlying MD, one could simply use the first peak in the ND SFH as the formation time of the ND and, consequently, the bar. However, due to gradients in the stellar population properties, the region around the ND that we use to obtain the SFH of the MD might not be identical to the real SFH of the main underlying disc within the ND region. Thus, it might not fully remove the contamination of the MD from the ND light. With that in mind, and by testing our methodology on N-body+hydrodynamic simulations (see Sect. 2.2.4), we employed a criterion to time the bar formation epoch as the moment when the ND dominates the star formation, as a signature of the bar bringing gas towards the centre. That corresponds to the first time in which the ratio between the star formation in the ND and that in the MD, ND/MD, rises above 1, with a positive slope towards younger ages. In order to verify whether this is a reliable criterion, we test our methodology using an N-body+hydrodynamic simulation of a barred galaxy below.

2.2.4 Testing the method using hydrodynamic simulations

In order to test the robustness of the methodology developed here and some of the assumptions employed, we used an N-body and hydrodynamic simulation of an isolated Milky-Way-like disc galaxy, which forms a bar and a ND self-consistently (the simulation is part of a suite of models developed to study the evolution of barred galaxies; Fragkoudi & Bieri, in prep.).

[1] http://research.iac.es/proyecto/miles/pages/predicted-masses-and-photometric-observables-based-on-photometric-libraries.php

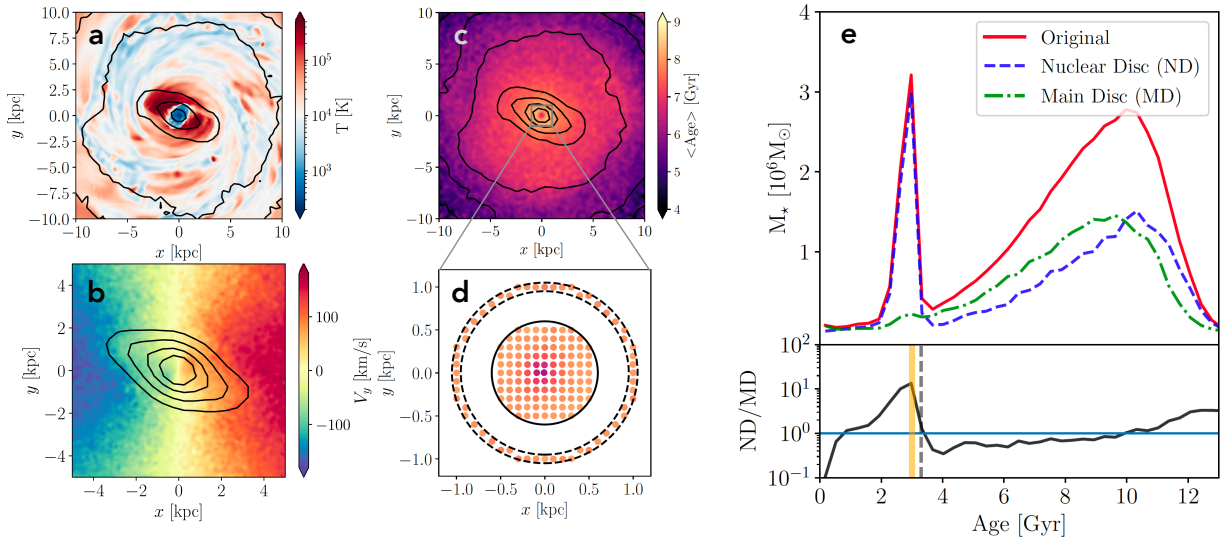

Figure 2.6: Testing the methodology using hydrodynamic simulations. **a:** Face-on projection of the gas temperature. The dust lanes on the leading edge of the bar and the gaseous ND are clearly visible as low temperature regions. **b:** Kinematic map showing the velocity of stars in the y direction with stellar isodensity contours over plotted, which outline the shape of the bar (note the different scale compared to panel *a*). A highly rotating stellar component in the central kiloparsec (i.e. the ND) is clearly evident in the kinematic map. **c:** Age map of all the stars in the simulated galaxy. The grey box shows the inset that is represented in panel *d*. **d:** Zoomed-in view around the ND region. The inner and outer dashed lines denote the region used to obtain the SFH of the 'representative disc region'. The solid black line denotes the radius within which the SFH of the ND is estimated. The scatter points indicate the locations of the pixels used for deriving the SFHs in panel *e*. The points are colour-coded by the mean age in the pixel. **e:** The top panel shows the SFHs of the original ND region (solid red), of the representative SFH of the MD (dot-dashed green), and of the ND with the representative SFH subtracted (dashed blue). The bottom panel shows the ratio of the subtracted SFH to the representative SFH. The vertical orange line indicates the time of bar formation in the simulation (3 Gyr), and the vertical dashed line indicates the time at which ND/MD is above 1 (3.3 Gyr).

Description of the hydrodynamic simulations

The simulation used in this Section has both a collisionless (stellar disc and dark matter halo) and collisional (gaseous disc) component, which is able to form stars that subsequently return mass, energy, and metals to the interstellar medium via supernova feedback, and is part of a suite of isolated disc simulations developed to study the evolution of barred galaxies (these will be presented in detail in Fragkoudi & Bieri, in prep.). Here we describe the main properties of the simulation that are relevant for this study. The simulation is run using the adaptive mesh refinement (AMR) code RAMSES (Teyssier, 2002). The AMR grid is refined using a quasi-Lagrangian strategy, and has seven refinement levels, with the maximum resolution reached in the simulation being 10 pc. The initial conditions of the model are created with the Markov chain Monte Carlo code DICE (Perret et al., 2014; Perret, 2016). The total mass of the system is $M_{\rm tot} = 2 \times 10^{12} {\rm M}_{\odot}$, with 98.5%, 1.425% and 0.075% of this distributed in the dark matter, stellar and gaseous components, respectively. The dark matter and stellar components have particles with masses $3.7 \times 10^4 {\rm M}_{\odot}$ and $4.3 \times 10^5 {\rm M}_{\odot}$, respectively. The dark matter halo has a Navarro-Frenk-White profile (Navarro et al., 1997) with a scale-length of 3 kpc, while the stars (gas) are modelled as an exponential disc, with a scale-length of 3 kpc (4 kpc) and a scale-height of 150 pc (50 pc). Gas in the simulation cools via atomic and metal-dependant cooling processes.

Star formation is modelled as a Schmidt law,

$$\dot{\rho}_{\star} = \epsilon_{\star} \rho_{\rm gas} / t_{\rm ff}, \tag{2.2}$$

where $\dot{\rho}_{\star}$ is the local star formation rate, and $t_{\rm ff} = \sqrt{3\pi/(32 G \rho_{\rm gas})}$ is the free-fall time. Star formation is triggered when the gaseous density $\rho_{\rm gas}$ is larger than $1\,{\rm cm}^{-3}$ and the temperature is less than 100 K, with an efficiency of $\epsilon_{\star} = 1\%$. Core-collapse supernova feedback is implemented by assuming that a fraction of the stellar population, $\eta_{\rm SN} = 0.2$, will explode as supernovae. The explosion itself is modelled using the mechanical feedback implementation presented in Kimm & Cen (2014) and Kimm et al. (2015). In this implementation, the supernova explosion is injected into the surrounding interstellar medium according to the phase of the explosion (energy conserving or momentum conserving); in other words, it is injected as momentum or thermal energy, depending on whether the cooling radius is resolved. More details on the feedback implementation can be found in (Kimm & Cen, 2014; Kimm et al., 2015).

Age-dating the simulated bar

The described simulation is evolved for a total of 3.3 Gyr. The axisymmetric stellar disc that is in place at the start of the simulation (which we refer to as the 'old stellar component') rapidly forms a bar after $\sim$0.3 Gyr (we define the bar as being fully formed when the $m = 2$ Fourier mode of the surface density, A_2>0.3). During and after the formation of the bar, gas piles up at the leading edges of the bar, where it shocks, loses angular momentum, and is funnelled to the centre, where it forms a dense gaseous ND (see panel

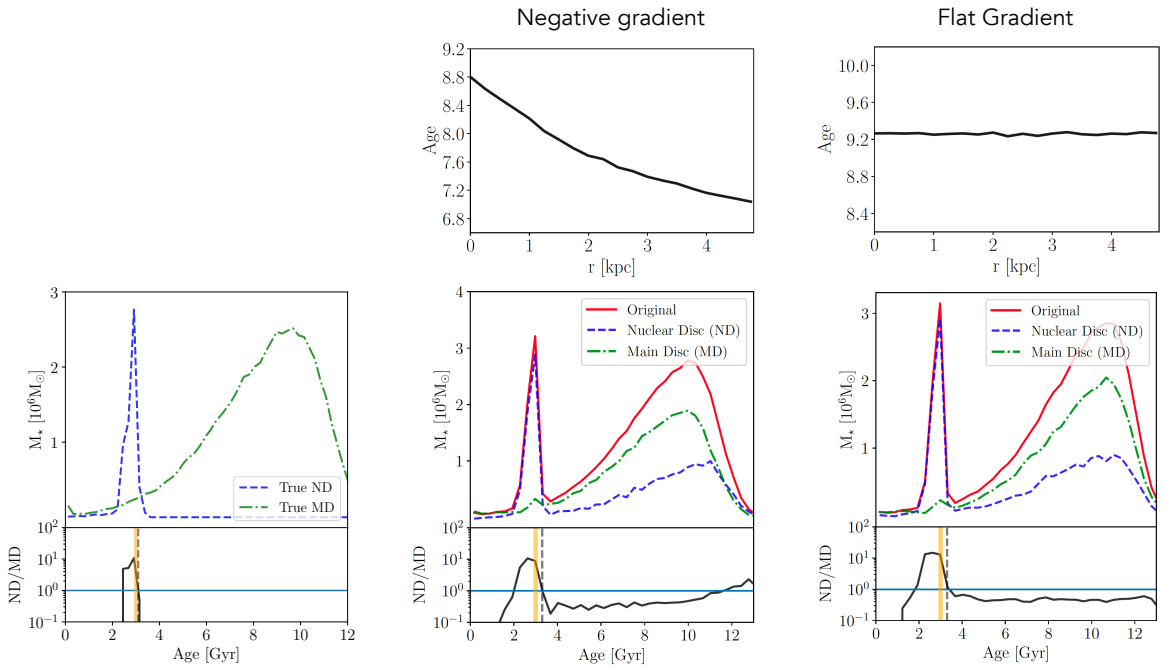

Figure 2.7: Testing the bar age criterion and how the age gradient in the underlying MD affects our methodology for a simulated galaxy. In the left panel we show the 'true' SFH of the ND and MD. The true SFH of the ND is defined as the SFH of all stars formed from the gas pushed to the centre after the bar forms within the ND radius, $r_{\rm ND}$. The true SFH of the MD is defined as the SFH of all the 'old' stars in the disc that were present before the bar and ND formed in the disc, within the same radius (i.e. $r_{\rm ND}$). As one can see, in the bottom panel, the bar age criterion – the first moment at which ND/MD is above 1 with a positive slope towards younger ages (the vertical grey dashed line) – successfully times the moment the bar is formed (given by the vertical orange line). By comparing this and Fig. 2.6 we see that the methodology we present in this paper – which involves using a representative region around the ND to model the MD – is able to recover the SFH of the ND and, therefore, the bar age. In the middle and right panels we explore how the age gradient of the old underlying MD affects our methodology: in the middle panels we show a case where there is a negative age gradient applied to the underlying MD, while in the right panels we show the effects of a flat age gradient on the obtained results. The top panels show the average age gradient as a function of radius, and the bottom panels show how this affects the SFHs of the original ND region (red), of the representative SFH of the underlying MD (green), and of the cleaned ND (blue), and the lower panels show the ND/MD ratio.

(a) of Fig. 2.6), which proceeds to form stars. These new stars – formed out of gas pushed to the centre by the bar – form a highly rotating stellar ND (see panel **(b)** of Fig. 2.6), whose size is set by the bar orbits in the inner regions (see Athanassoula 1992b), similar to those observed in the local barred galaxies (e.g. Gadotti et al., 2020).

We highlight that, while the new stars formed out of the gas have self-consistent ages – according to when they are formed in the simulation–, the old stellar component can have any SFH we assign to it. In order to model the age gradient often found in galaxies, we assigned ages to the old stellar component at the initial snapshot such that a negative age gradient was obtained [2] (i.e. with older stars in the centre and younger stars at the edge of the disc). This old underlying population, together with the new stars formed out of the gas in the simulation, give rise to the age map of the galaxy at the end of the simulation shown in panel **(c)** of Fig. 2.6.

We can now extract the SFH for a given 'pixel' in the ND region – as we do in the observations – which will contain stars born from gas pushed to the centre by the bar, as well as old stars that were present before the bar formed. We also extract the SFH for pixels in the region just outside the ND, which give us the representative SFH of the underlying main stellar disc (MD). Therefore, as in the methodology used for the observations, we can extract the SFH of both the ND region and the MD. We then subtract the SFH of the MD from the SFH in the ND region, in order to obtain the SFH of the 'clean' ND itself. These SFHs are shown in panel **(e)** of Fig. 2.6, with solid red for the original total SFH within the ND region, dot-dashed green for the SFH of the main underlying disc, and dashed blue lines for the clean ND SFH. This can be compared to the 'true' SFHs of the ND and MD, which are shown in the left panel of Fig. 2.7.

We find that due to the age gradient in the underlying disc as well as the gradient in the light profile, there can be a contamination of the 'old component' in the subtracted ND SFH, which cannot be fully removed by subtracting the underlying MD (see Fig. 2.7, where we show how assuming a negative age gradient versus a flat age gradient affects the methodology). The extent to which there is 'contamination' by the oldest stars in the ND will depend on both how steep the age gradient is, and on the location of the ring used to obtain the SFH of the MD (see also Fig. 2.14). This indicates that we cannot simply use the oldest peak in the subtracted SFH (ND) in order to obtain the time at which the ND formed, but we rather should use the comparison between the subtracted ND and the representative SFH of the MD (i.e. ND/MD). In practice, this is the time when the SFH of the ND increases above that of the MD (i.e. when ND/MD rises above 1), with a positive slope towards younger ages.

As can be seen from panel **(e)** of Fig. 2.6, this method allows us to recover the time at which the bar formed (which in the simulation occurs at $t_{\rm lookback} \sim 3\,{\rm Gyr}$), which is

[2] In practice, this is done by sampling from Gaussian distributions at each radius, with a decreasing mean value for the age.

marked with the vertical solid orange line, while the ratio of the ND over the representative MD SFH (ND/MD) gives a bar age of $t_{\rm lookback}$=3.3 Gyr. Therefore, we find that, even with the contamination of older ages in the subtracted spectrum, we can recover the time of bar formation, as the first time at which ND/MD rises above one, with an accuracy that will depend on the width of the age bins in the SFHs. The main limitation in obtaining the bar age using this methodology therefore stems from uncertainties in deriving stellar ages – and therefore the SFH – which are typically of the order of $\sim$ 1 Gyr (see e.g. Bittner et al. 2020).

2.3 Results

After following the methodology to disentangle SFHs described in Sect. 2.2, we present our results for our pilot study galaxy, NGC 1433. We remind the reader that the chosen criterion to time bar formation epoch is the first moment when the ratio ND/MD increases above 1 with positive slope towards younger ages.

Figure 2.8 shows our main results: the mass of stars formed with different age bins of the stellar templates – analogous to SFHs – for the MUSE original (solid-red line), the MD (dot dashed green line) and the ND (dashed blue line) for NGC 1433, together with the ratio ND/MD in the bottom panel. The age is related to the SSP template combination that best fits the observed spectra and can be understood as a 'look-back time' (i.e. $t = 0$ is the present time).

We measure the bar formation epoch of NGC 1433 to occur $7.5^{+1.6}_{-1.1}(\mathrm{sys})^{+0.2}_{-0.5}(\mathrm{stat})$ Gyrs ago, corresponding to a redshift of $z \approx 1$. In order to quantify the statistical error of the methodology, we perform 100 Monte Carlo runs for each of the collapsed spectra (original data, ND data and representative spectra) to derive variations on the bar age. We use the noise information to sample a distribution of fluxes for each wavelength, creating 100 artificial spectra. We then run pPXF on each of these spectra, to obtain the different SFHs and the subsequent bar ages. This is shown in Fig. 2.8 as the shaded area of each SFH. From it, we derive a statistical uncertainty corresponding to $^{+0.2}_{-0.5}$(stat) Gyr. The statistical error is subdominant, since, by collapsing the data cubes into single spectra, we achieve signal-to-noise values over 2000. To further quantify uncertainties in the derived bar age, which can be introduced due to various aspects of the methodology, we perform multiple tests with different configurations (see Section 2.3.1): different locations for the representative ring, different light profiles to describe the increase in density of the main underlying population towards the centre, and different regularisation errors for the `pPXF` run that results in the derivation of the SFHs. From these tests, we find that there is a systematic uncertainty in our measurements of the bar age of the order of $^{+1.6}_{-1.1}$(sys) Gyr, which we quote in addition to our statistical errors.

From the SFHs, we can derive estimates of the total stellar mass in the isolated ND and the underlying MD within the ND radius, by summing the mass formed through time

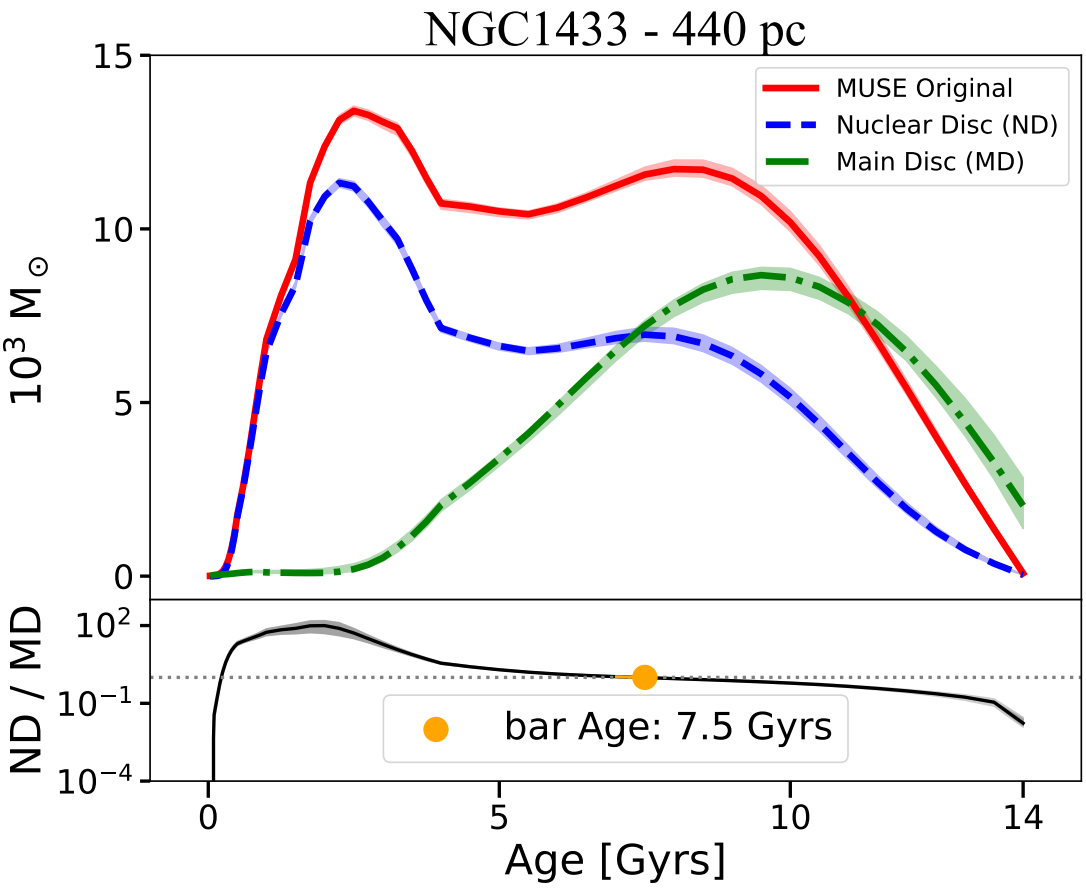

Figure 2.8: Mass-weighted SFHs for NGC 1433 from collapsed spectra of the MUSE original data, ND data, and representative MD data, as illustrated in Fig. 2.2. The y-axis corresponds to the mass formed, in solar masses, for each age bin and the x-axis to the age in Gyr, that is, the look-back time. The original data are shown with a solid red line, the subtracted data with a dashed blue line, and the representative spectrum with the dot-dashed green line. The lines are the SFHs derived from the data, while the shaded regions are results from 100 Monte Carlo runs. In the bottom panel we display ND/MD in black, and highlighted with an orange circle is the age where ND/MD rises above one for the first time, together with the statistical uncertainty: $^{+0.2}_{-0.5}$(stat) Gyr.

following each curve. However, if NGC 1433 has significant age gradients within the central kiloparsec, the very oldest population in the underlying disc may still be partly present in the isolated ND, as discussed above. Therefore, these would be, respectively, an upper limit to the mass of the ND, and a lower limit to the mass of the underlying population within the ND region. For NGC 1433, we measure the underlying MD mass within the ND radius as 2.95×10^8 $M_\odot$ and the 'cleaned' ND mass as 4.05×10^8 $M_\odot$. To explore whether these values are in agreement with the literature, we extrapolate the underlying MD mass to obtain the total mass of the galaxy assuming an exponential function, following Eq. 2.3:

$$M_h = 2\pi \int_0^\infty \Sigma(r) r dr = 2\pi \Sigma_0 h^2, \tag{2.3}$$

where Σ_0 is the mass density at the centre and h is the disc scale-length. Using the mass of the underlying MD within the ND radius, we measure the mass density as 512 $M_\odot/pc^2$. This value gives the extrapolated mass for the entire galaxy of 2.74×10^{10} $M_\odot$, which is consistent with the total stellar mass of 2×10^{10} $M_\odot$ derived by Muñoz-Mateos et al. (2015), considering the uncertainties involved. This indicates that our measurements for the total stellar mass of the ND and the underlying main population are reliable. In addition, this also shows that the methodology described above to disentangle the light of the nuclear and underlying discs is trustworthy. Interestingly, our mass estimates indicate that the ND dominates the stellar mass budget in the central region, with the ND being ∼40% more massive than the underlying MD in the same region.

In addition, we analyse the SFH in different radial bins inside the ND region for the original data (left panel; Fig. 2.9) and the ND cleaned data (right panel; Fig. 2.9). At the top of each panel we display the mean age for each radius, colour-coded according to distance from the centre. As one can see for the cleaned ND results, the SFH and the mean ages gradually get younger at larger radii, in agreement with the inside-out growth scenario (Bittner et al., 2020). We discuss the implications of these findings further in Sect. 2.4.2.

2.3.1 Constraining systematic errors in the methodology

Control galaxies: NGC 1380 and NGC 1084

In order to assess whether our methodology creates spurious results for galaxies that do not host a ND, we applied the same methodology for two control galaxies: NGC 1380 and NGC 1084.

Considering NGC 1380, Gao et al. (2019) describe the galaxy as an inclined system with a classical bulge and no clear presence of a bar. The galaxy is at a distance of 21.2 Mpc with inclination of 47° (see references in Sarzi et al., 2018 and Gao et al., 2019). We consider the effective radius of the bulge to be 1080 pc (12.1 arcsec) from the photometric decomposition performed in Gao et al. (2019) instead of the ND radius. The data for

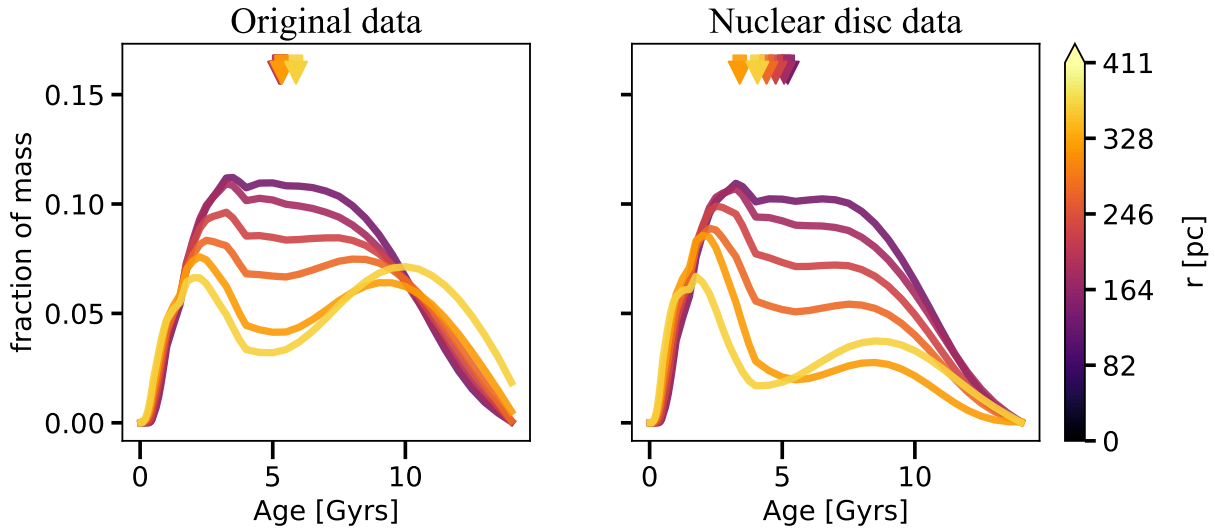

Figure 2.9: SFHs for NGC 1433 in different galactocentric radii for the original data (**left**) and the ND data (**right**). In the y-axis we display the fraction of mass formed. In the upper part of each panel we use arrows to display the mean age for each SFH, following the same colour coding with respect to the distance to the centre. For both data cubes, it is clear that the farther from the centre, the younger the SFH is (with the exception of the last curve), meaning that the fraction of younger stars increases. This is shown even more strikingly with the subtracted data cube: it is clear that the outskirts of the ND are in fact younger, in accordance with the inside-out growth scenario of Bittner et al. (2019).

NGC 1380 comes from the ESO archive, PI: Sarzi, M., programme ID 296.B-5054, using MUSE in Wide Field Mode. Further details about the galaxy and the observations can be found in Sarzi et al. (2018).

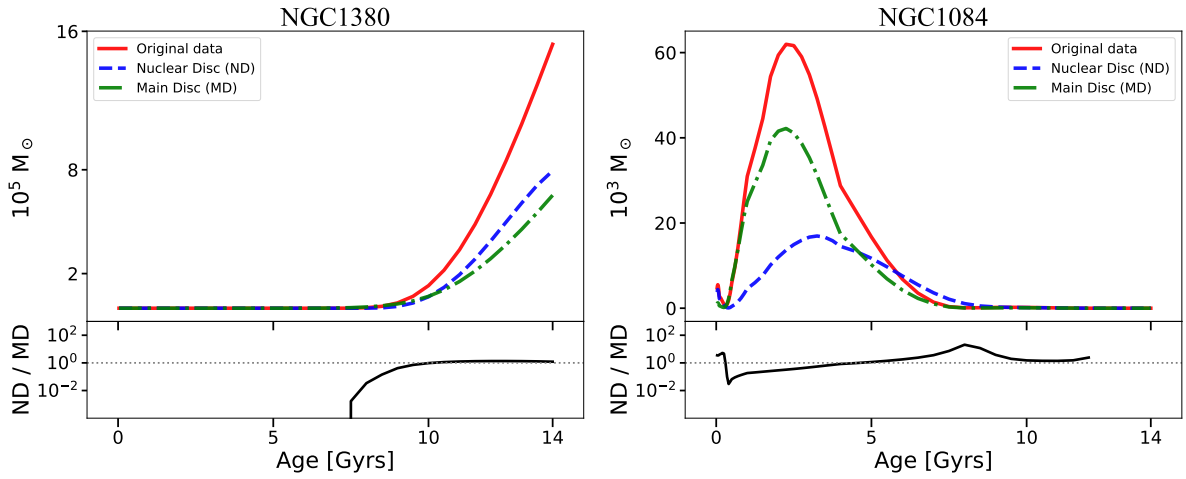

Figure 2.10: Same as Fig. 2.8 but for NGC 1380 (top) and NGC 1084 (bottom). It is clear that for both galaxies neither the representative MD nor the 'cleaned' data show important deviations in their SFHs.

As a second control galaxy, NGC 1084 is a bar-less galaxy (Gao et al., 2019) with inclination[3] of 49.9° that also does not host a ND. Gao et al. (2019) also describe its morphology with a broken inner disc and a bulge with effective radius of ≈ 150 pc (4.3 arcsec). The data for NGC 1084 comes from the ESO archive, PI: Carollo, C. M., programme ID 099.B-0242, using MUSE in Wide Field Mode.

Figure 2.10 shows the outcome of these tests. It is clear that the subtracted spectra show SFHs similar to those in the original spectra. Therefore, our methodology does not artificially produce differences in the SFHs of the regions where the nuclear and main underlying discs dominate, which would wrongly be attributed to the formation of the bar.

The location of the representative ring

Ideally, the representative ring should be located immediately after the end of the ND so that it is not contaminated by light from it and represents, as closely as possible, the underlying population in the region where the ND dominates. However, the end of the ND is not trivial to pinpoint, as this structure may gradually fade into the MD. If the region is too close to the ND, it may be affected by its young star formation, but if it is too far, it may not map the underlying MD old star formation. Our methodology used the physical justification based on kinematic maps to select the representative region. Nevertheless, to constrain how much the position of the representative ring could affect our final result,

[3]See http://leda.univ-lyon1.fr/ledacat.cgi

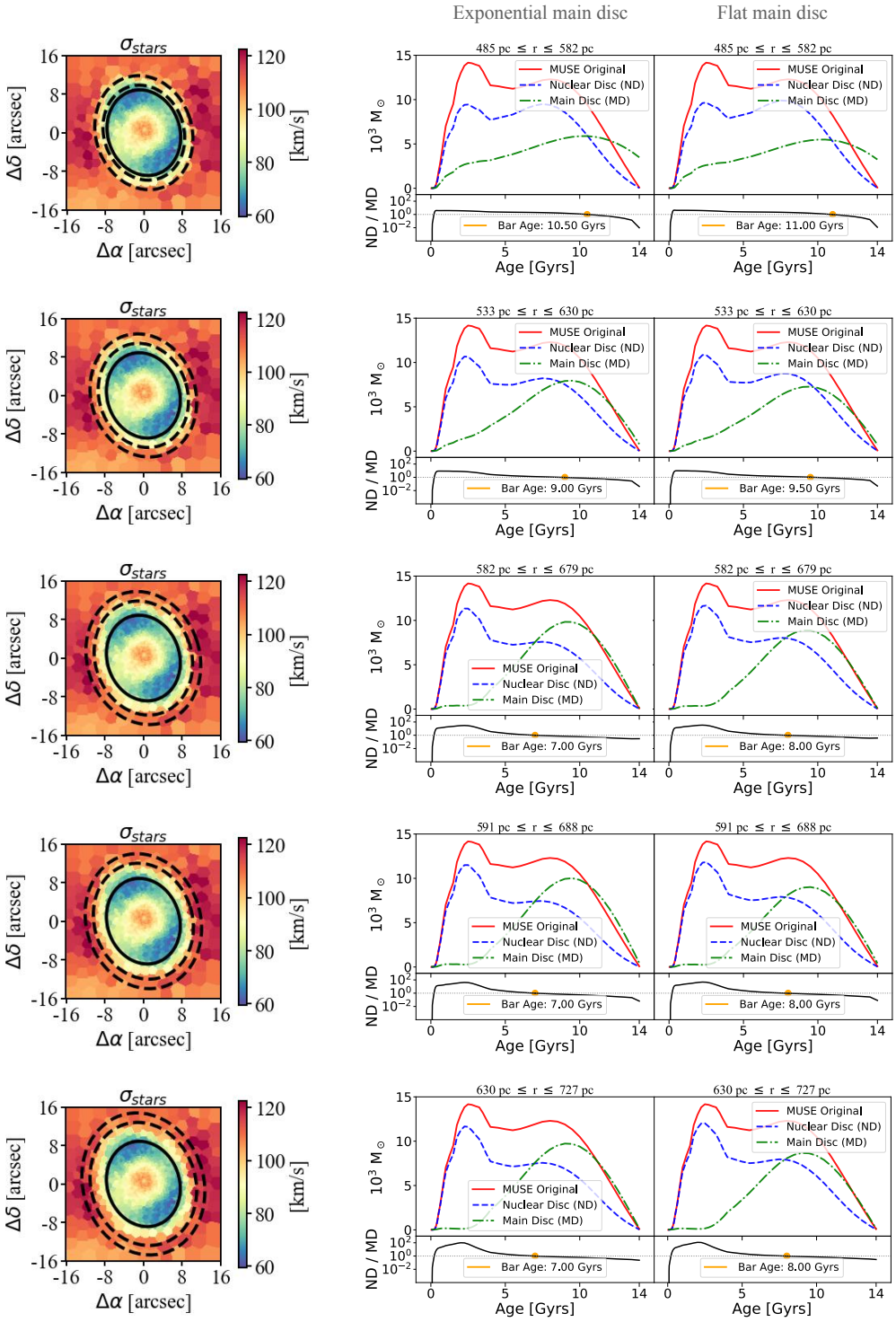

Figure 2.11: Results for different configurations in the methodology presented in Sect. 2.2, varying the position of the representative ring (row by row) and the assumed light profile of the main underlying disc. To be continued on the next page.

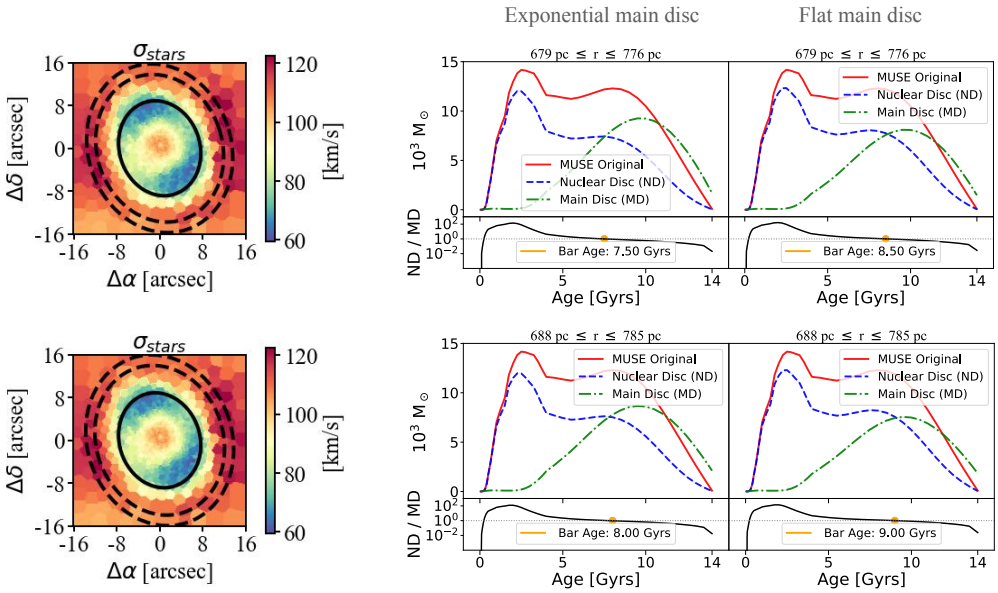

Figure 2.11: Results for different configurations in the methodology presented in Sect. 2.2, varying the position of the representative ring (row by row) and the assumed light profile of the main underlying disc. In the first column, we display the stellar velocity dispersion map, indicating the representative ring position with the dashed lines (the solid line corresponds to the peak in v/σ at the outskirts of the ND). In the middle and left columns we display results for exponential and flat light profiles, respectively. One can see that the different configurations result in bar ages in the range 7.0–9.5 Gyr, with the exception of the representative ring closest to the centre. The middle panel of the bottom row corresponds to the standard configuration of our methodology. We note that the mask used that the mask used for the representative ring is slightly different than the one used for the main result. With this, the bar age is slightly older, 8 Gyrs.

we produce a number of tests with the representative ring at different positions closer to the centre than the position we employed. The results are summarised in Fig. 2.11 (center column). We note that the mask used that the mask used for the representative ring of Fig. 2.11 is slightly different than the one used in the main result. For this case, we masked all spaxels with AGN contribution, with no threshold for AON (as opposite of AON $\geq$ 20 used for the main result). With this, the bar age is slightly older, 8 Gyrs (Fig. 2.11, last row, center). With this test we aim to assess the relative systematic error due to the location of the representative ring, therefore this does not affect the conclusions. We further note that the change in bar age due to the different mask is well within the systematic error uncertainties.

With the exception of the most central representative ring, for underlying MDs following an exponential light profile, the derived bar ages are constrained to the range 7–9 Gyr.

Different main disc profiles: flat versus exponential

In order to build the underlying MD, one has to assume a light profile that describes it. Although galaxy discs are usually assumed as having exponential light profiles, recent studies demonstrate that some cases may follow a flat light profile (e.g. Zhu et al., 2018; Breda et al., 2020; Papaderos et al., 2022). In order to assess how much such a decision may affect our final result, we compared exponential and flat profiles as extreme possible cases. The results are summarised in Fig. 2.11 (right column).

For each representative ring position, one sees that the final bar age derived using a flat profile is 0.5-1.0 Gyr older than that derived with an exponential profile (with the exception of the most central representative ring).

Considering the light profile choice together with the position of the representative ring, the derived bar ages vary between 7.0-9.5 Gyr.

Spaxel-by-spaxel analysis

Considering the elevated signal-to-noise ratio in the TIMER data (Gadotti et al., 2019), it would be possible to run the same methodology spaxel-by-spaxel, deriving spatially resolved SFHs, and then obtaining a mean SFH for each data cube. This would be in contrast to our regular methodology, in which the individual spectra in the data cubes are collapsed into a single spectrum, to then proceed to the derivation of the SFH. The disadvantages of doing so spaxel by spaxel are that the statistical uncertainties for each SFH would be larger and the computational time would increase significantly. Since our goal is to apply the same methodology for the whole TIMER sample, it is too detrimental to require substantial computational time for the analysis of an individual galaxy. Nevertheless, to verify that the results do not differ significantly with the different approaches, we applied the alternative methodology using our data for NGC 1433. For the spatially resolved

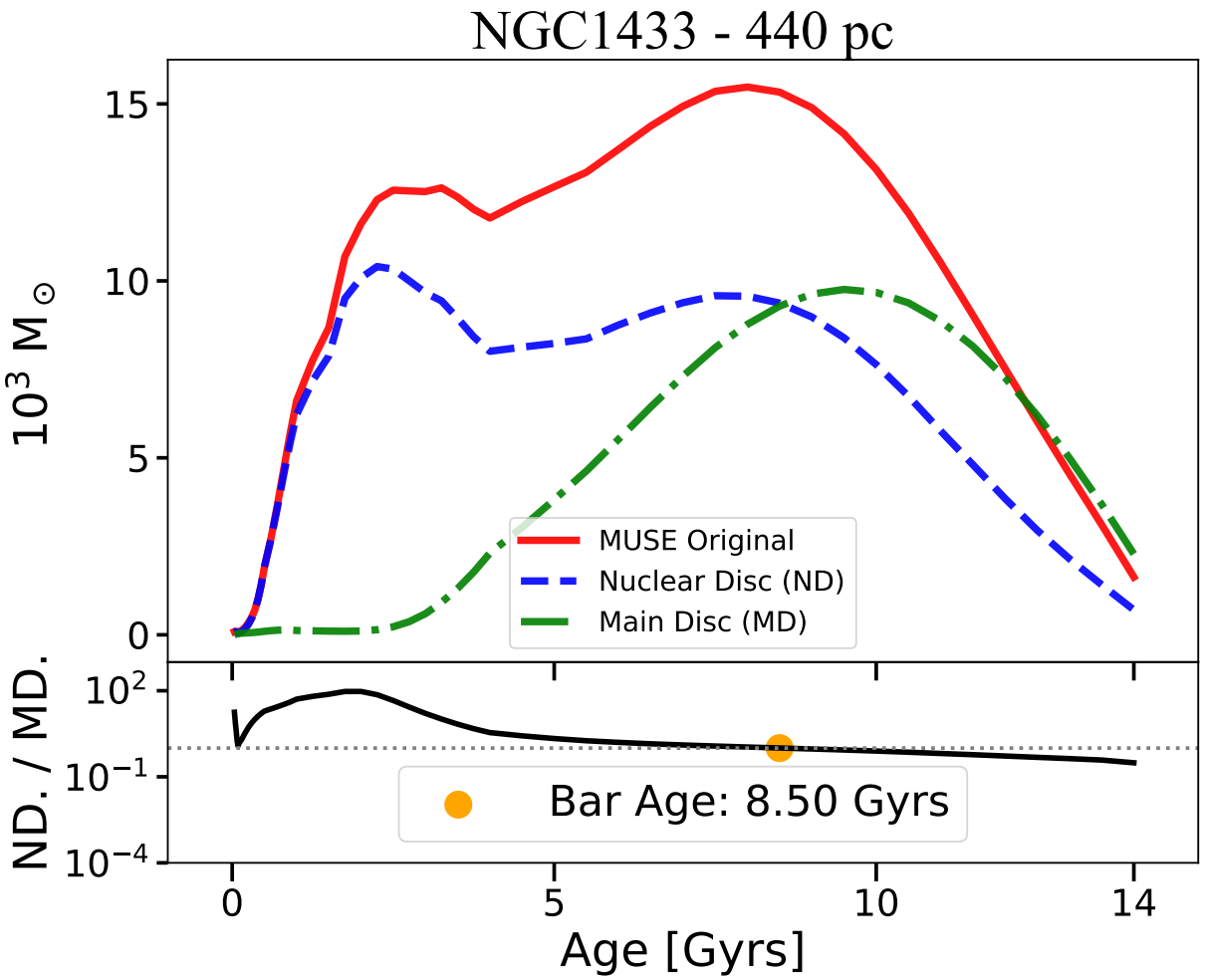

Figure 2.12: Same as Fig. 2.8, but for the test with spaxel-by-spaxel SFHs instead of a single collapsed spectrum produced for each data cube. The presented SFHs are mean SFHs calculated over all spaxels.

products, we considered the mean SFHs to measure the bar age. The result is shown in Fig. 2.12 and, as one can see, the derived bar age is not substantially different; in fact, the difference is within typical uncertainties in the derivation of stellar ages. With that in mind, we decided to keep our regular methodology employing collapsed spectra to ensure smaller statistical errors and lower computational requirements.

pPXF regularisation

As described in Cappellari (2017), regularisation allows one to have the smoothest SFH solution, without affecting the physical reality of it. In our methodology, we used the `regul_err` value of 0.15 derived by Bittner et al. (2020) for the TIMER sample following the procedure developed by McDermid et al. (2015). Nevertheless, in order to assess how

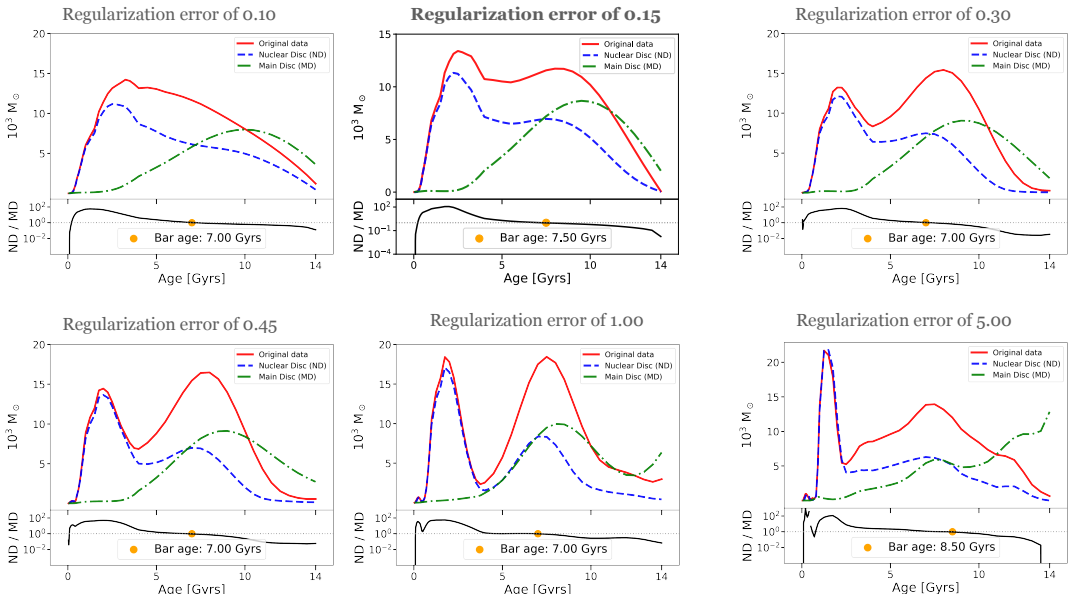

Figure 2.13: Same as Fig. 2.8 but for different values of the regularisation error parameter applied by `pPXF`. The original configuration uses a regularisation error of 0.15. The systematic effect of employing different regularisations is constrained to 0.5 Gyr.

much our final result depends on it, we produce tests with values of `regul_err` in the range 0.1-5.0. The results are summarised in Fig. 2.13. Since `regul = 1/regul_err`, the larger the regularisation error, the less regularised the solution is. As one can see, by changing the regularisation error parameter our bar age has variations of ± 0.5 Gyr.

Considering the variations due to the representative ring position and the MD light profile, this leaves us with systematic errors of $^{+1.6}_{-1.1}$ Gyr, after summing in quadrature the maximum variations we find with the four tests on systematic effects.

Interestingly, the regularisation error of 1.00 leads to a SFH that looks similar to that of the simulation presented in Fig. 2.6 (panel **e**), which could lead to the incorrect interpretation that the first peak ($\sim$ 8 Gyrs) is a contamination of the MD and the second peak ($\sim$ 5 Gyrs) is the real bar formation. We point out however that, even though they might look similar at a first glance, one should expect that contamination from the MD would be from the oldest stars, as showed from the different tests for the simulated galaxies (Section 2.3.1). Since the oldest peak of the ND is younger than the one from the MD, we do not expect this to be a sign contamination. In addition, this feature is not a well converged feature (as it is not evident for regularisation errors of 0.45 and 5) and is particular to a singular regularisation error. As noted in the main body of the paper, the peak at younger ages could arise through a number of mechanisms that induce gas inflow, such as the formation of the boxy/peanut bulge (e.g. Pérez et al. 2017) as well as through an interaction or flyby that removes angular momentum from gas in the disc, causing a

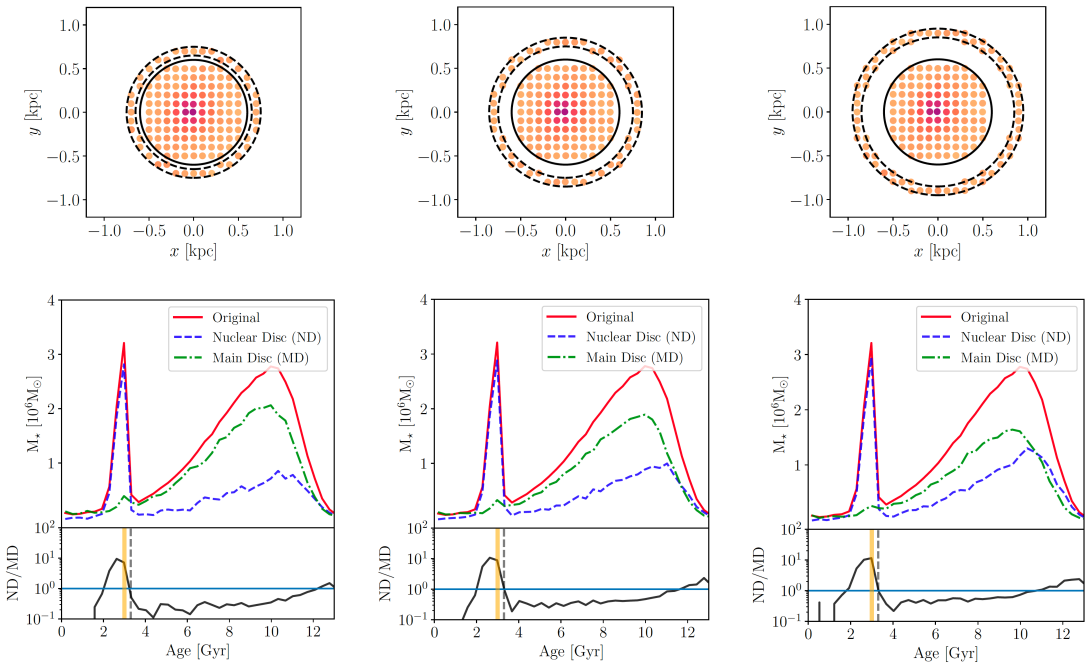

Figure 2.14: Testing the effects of ring location on the methodology for a simulated galaxy. From left to right we show cases where the ring used to reconstruct the representative SFH of the underlying MD is placed at larger radii, in a case where the model has a negative age gradient in the underlying MD. The top rows show the locations of the rings with respect to the ND region, and the bottom panels show the SFHs. We see that when the ring is placed at larger radii, the representative SFH of the MD does not fully match the ND region at the oldest ages.

burst in gas inflow to the central regions through the bar.

Testing the methodology with hydrodynamic simulations

In this section we describe some of the tests carried out on the simulations that allowed us to assess the effects of some of the assumptions in our methodology. In particular, we tested how an assumed underlying age gradient of the old disc, as well as how the location of the ring used to obtain the representative spectrum, affected the results.

In the left panel of Fig. 2.7, we show what are the true SFHs of the ND and the underlying MD in the simulations. Then, we show that we can accurately reproduce the time the bar formed using these two values and our chosen criterion for the time of bar formation (i.e. the first moment when the ratio of ND/MD increases above 1 with positive slope towards younger ages; see Sect. 2.2). We define the true SFH of the ND as the SFH of all stars formed from the gas pushed to the centre after the bar forms within the radius corresponding to the ND ($r_{\rm ND}$). The true SFH of the MD is defined as the SFH of all the

'old' stars that were present before the bar and ND formed in the MD, within the same radius $r_{\rm ND}$. As we can see, the bar age is well constrained by the moment when ND/MD is above 1 with positive slope towards younger ages for the first time. We can compare true SFHs to the recovered SFHs from our methodology in Fig. 2.6, where we see that the SFH of the ND is well recovered, apart from at the oldest ages.

In addition, we test how the underlying age gradient of the MD in the galaxy can affect the determination of the bar age. In the right panel of Fig. 2.7, we show a case where there is no age gradient in the underlying MD of the galaxy. By subtracting the main underlying disc (as obtained from the representative ring around the ND) from the original data, we obtain a peak in ND/MD that corresponds to the time of bar formation, while before this peak, ND/MD is consistently below < 1. When a negative age gradient is added to the old disc in the simulation (middle panel), we find similar results, with the difference that, at old ages, ND/MD rises again above one. This happens because there are old stars that are present in the ND region, which are not present in the 'representative' MD region which is at larger radii. Therefore, due to the age gradient, there is a lack of old stars in the ring, which leads to a rise in ND/MD for the oldest populations. This effect will be larger, the larger the age gradient (which will vary from galaxy to galaxy). Due to this, for our criterion of determining the bar age, we explicitly require that ND/MD be above 1 with a positive slope towards younger ages (rather than simply ND/MD > 1, as this could occur at old ages due to a strong age gradient in the inner galaxy).

In Fig. 2.14 we test how the location of the ring affects our methodology, in a case where there is a negative age gradient (if there is no age gradient, the location of the ring does not have a significant effect on the methodology, as long as the SFH of the MD is appropriately rescaled to take into account the higher surface density in the centre of the galaxy, due to its exponential profile). When the ring is placed at larger radii, the representative SFH will be lacking more of the old stars that are present at smaller radii, which can be seen by the increase in ND/MD > 1 for old ages, as we move to larger radii (i.e. the middle and right panels of Fig. 2.14). Therefore, the representative ring should not be placed at too large radii from the ND, as the farther away it is placed, the more different the stellar populations will be from those of the underlying MD within the ND region. As described in Sect. 2.2, we therefore select the radius just outside the ND, where the average age is oldest (see Fig. 2.3). This ensures we select a region outside the influence of the ND itself, but without going to larger radii where the stellar population properties of the representative region will be significantly different from those of the underlying MD in the ND region.

We also note that we applied our methodology to other simulations with the same initial conditions, but with modifications in the star formation and stellar feedback prescriptions, and we were able to recover the bar age reliably also with these changes (i.e. the methodology does not depend on the details of the star formation and stellar feedback prescriptions in the simulation).

2.4 Discussion

In this section we discuss the results from applying our methodology to the galaxy NGC 1433 and what they reveal about the formation and evolution of bars and NDs.

2.4.1 The old bar in NGC 1433

Applying the methodology described in Sect. 2.2 and considering our chosen criterion, we find a bar age of $7.5^{+1.6}_{-1.1}(\mathrm{sys})^{+0.2}_{-0.5}(\mathrm{stat})$ Gyr for NGC 1433, which hosts a ND with a radius of 440 pc (e.g. Gadotti et al., 2019; Bittner et al., 2020). This corresponds to a redshift $z \approx 1$ and is consistent with other observational studies, such as Simmons et al. (2014), who also find massive galaxies with bars at $z \approx 2$. In addition, Gadotti et al. (2015) and Pérez et al. (2017) also inferred similar bar ages for other local galaxies, using independent methodologies. Furthermore, this is comparable to predictions from cosmological simulations, which also find bars that form between redshifts $1 - 2$ and that survive down to $z = 0$ (e.g. Kraljic et al. 2012; Fragkoudi et al. 2020). Our results indicate that NGC 1433 hosts an old and long-lived bar, which is in accordance with several observed characteristics of this galaxy and our current understanding of bar formation and bar-driven evolutionary processes.

As the bar evolves, the shape of its light profile may change. Kim et al. (2015) suggested that the bar Sérsic index (n_{bar}) evolves from an exponential ($n_{\mathrm{bar}} \approx 1 - 2$) to a flat ($n_{\mathrm{bar}} \approx 0.2$) profile (but see also Anderson et al., 2022). They also measured n_{bar} for 144 local galaxies from the S^{4}G sample and found that the oldest bars have a n_{bar} index close to 0.2. In addition, simulations demonstrate that, as the bar grows older, it becomes more elongated and stronger (e.g. Athanassoula et al., 2013), which can be measured by the bar length, $\mathrm{R_{bar}}$, and the A_2 index. The latter is the second component of the Fourier light/mass distribution in the galaxy and is associated with the bar non-axisymmetry. Lastly, the bar-to-total (Bar/T) luminosity ratio also increases as the bar grows longer and more massive, and the bar morphology evolves to a more rectangular or boxy shape (e.g. Kim et al., 2015). The bar morphology is measured by the index c, where $c = 2.0$ represents a perfect ellipse and $c \geq 2.7$ a strongly boxy bar (see Gadotti, 2011). In summary, an old bar is expected to have a flat light profile ($n_{\mathrm{bar}} \leq 0.7$), high strength ($A_2 \geq 0.4$), a strongly boxy shape ($c \geq 2.7$), relatively large bar-to-total ratio (Bar/T ≥ 0.09) and bar length normalised by the disc scale-length $\mathrm{R_{bar}}/h \geq 1.5$. Apart from A_2, these values are the median values of the corresponding distributions as found in Gadotti (2011) for a sample of about 300 massive barred galaxies.

NGC 1433 has $n_{\mathrm{bar}} = 0.3$, $A_2 = 0.56$, a deprojected, normalised bar length of 1.2, a boxy shape with $c = 2.9$, and lastly, a Bar/T $= 0.08$ (see Kim et al., 2014 and Díaz-García et al., 2016). Most of these characteristics are consistent with the expectation of an old bar, also in accordance with our bar age estimate of $7.5^{+1.6}_{-1.1}(\mathrm{sys})^{+0.2}_{-0.5}(\mathrm{stat})$ Gyr. Lastly, NGC 1433 has similar characteristics as NGC 4371, which was studied by Gadotti et al. (2015) also

using the archaeological evidence present on its ND. The authors investigated the oldest stars in the ND to estimate a bar age of ≈ 10 Gyr. In addition, NGC 4371 has $n_{\rm bar} = 0.2$, $A_2 = 0.62$, deprojected normalised bar length of 1.3, $c = 2.7$, and Bar/T = 0.08 (see Gadotti et al., 2015 and Díaz-García et al., 2016). Both the age and the characteristics of NGC 1433 and NGC 4371 are very consistent with each other and with the scenario whereby they are amongst the first galaxies to form bars.

The conditions to form a bar are connected with the MD properties, and depend on the galaxy assembling enough mass and settling in more ordered motion. With this in mind, one can expect that the more massive galaxies will reach the necessary conditions first, following a downsizing picture (e.g. Sheth et al., 2012). Despite that, another plausible possibility is the one where early interactions and/or minor mergers, which happened after the disc has settled, could have triggered the bar formation (e.g. Noguchi, 1987; Gerin et al., 1990; Miwa & Noguchi, 1998; Peschken & Łokas, 2019; Łokas, 2021). Gadotti et al. (2015) argued how this could be possible for NGC 4371, which is member of the Virgo cluster. Similarly, NGC 1433 is part of the Dorado group (Maia et al., 1989). Following the pre-processing picture, galaxies enter clusters with already some level of processing due to earlier interactions (Haines et al., 2015) while in groups, which could also be responsible for early bar formation ~ 7.5 Gyrs ago. Méndez-Abreu et al. (2010) and Méndez-Abreu et al. (2012) found that galaxies in the Coma and Virgo clusters that host bars are mainly massive ($10^9 \leq {\rm M/M_\odot} \leq 10^{11}$).

2.4.2 The inside-out scenario for the growth of nuclear discs

Bittner et al. (2020) showed that in the TIMER sample, the derived age profiles of NDs follow a negative gradient, with the outer parts of the ND being younger. This is in accordance with an inside-out growth scenario, in which one can have a growing gaseous ND that forms stars, and/or star formation concentrated in rings of increasing size, on the external borders of the ND, as shown by Hα maps (Bittner et al., 2020). In this scenario, the gas funnelled by the bar towards the centre piles up near the inner Lindblad resonance of the bar. As the bar grows longer, the radius of the inner Lindblad resonance increases, which leads to the buildup of a ND in an inside-out fashion.

In order to test this scenario, we analyse the SFHs of the subtracted ND in different radial bins, as shown in Fig. 2.9, and derive the mean ages at each radius (shown as arrows on the top part of the panels). For the original data, the inside-out evidence is subtle, with little change in the mean ages in each radial bin. Nonetheless, with the subtracted data, the inside-out growth of the disc becomes strikingly evident, since in the outer part of the ND the older stellar populations are almost completely absent from the clean ND. This is reflected in the mean age at different radii for the subtracted ND, in which there is a clear gradient towards younger ages at larger radii. This result is also testament that the methodology we develop to subtract the underlying disc component is robust. It shows that the ND of NGC 1433 is consistent with the inside-out growth picture for NDs. This

highlights how inner structures such as NDs might be assembled in a self-similar way to the corresponding larger-scale structure of the MD.

Finally, we note that Fig. 2.9 shows a prominent peak in the SFHs at all radii at young ages ($\sim$ 2.5 Gyr), which is also evident in Fig. 2.8: there is a late burst of star formation, which occurs at younger ages than the first burst associated with the formation of the ND at $\sim$ 7.5 Gyr. This implies an event that leads to a renewed inflow of gas at late times, which gives rise to such a burst of star formation. Various mechanisms could give rise to such a late gas inflow event through the bar, such as mechanisms that remove angular momentum from gas, for example an interaction or flyby, or – interestingly for this galaxy – this late inflow could be related to the buckling of the bar and the formation of the boxy/peanut bulge (e.g. Pérez et al., 2017).

2.5 Summary and concluding remarks

In this Chapter we have developed and presented a new method for dating the bar formation epoch of observed disc galaxies. We summarise our findings as follows:

- We present a new methodology that allows us to disentangle the light from NDs, which are formed by the bar, from the underlying MDs of galaxies, using high-resolution integral field spectroscopic data from MUSE on the VLT. This allows us to find the time at which the ND formed, by isolating the moment when its star formation starts to dominate over the star formation in the underlying population. As NDs are formed due to bar-driven inflow – which is concurrent with the formation time of the bar – this allows us to determine the age of the bar.

- We performed a number of tests of our methodology, both on observed data and on a hydrodynamic simulation of a barred galaxy (which self-consistently forms a ND), in order to validate the robustness of the methodology.

- As a pilot study, we applied our methodology to the barred galaxy NGC 1433 from the TIMER survey (Gadotti et al., 2019) and find a bar age of $7.5^{+1.6}_{-1.1}(\mathrm{sys})^{+0.2}_{-0.5}(\mathrm{stat})$ Gyr. This implies that NGC 1433 has an old bar that formed around $z \sim 1$. This aligns with a number of observational characteristics of the galaxy, such as its mass, bar strength, and light profile (see Sect. 2.4.1 for a more detailed discussion on this). Our results are consistent with other studies in the literature that find old bars (e.g. Simmons et al. 2014; Gadotti et al. 2015), as well as with results from cosmological simulations (e.g. Kraljic et al. 2012; Fragkoudi et al. 2020) that imply that bars can be old, long-lived structures.

- By examining the SFH of the ND of NGC 1433 at different radii, we find that the disc grows inside out, with younger stars forming at progressively larger radii and the youngest stars forming at the edge of the ND (i.e. at the location of the nuclear

ring). This is in agreement with an inside-out growth scenario for NDs (see Bittner et al. 2020, and Sect. 2.4.2).

We will apply the methodology presented here to the full TIMER sample of barred galaxies, which will provide, for the first time, robust age determinations for bars in a sizeable sample of disc galaxies. This will enable us to compare the age of bars with various galaxy properties, such as the total mass, the bar length, and the pattern speed, enabling us to place important constraints on the evolution of dynamical properties of disc galaxies with time, the epoch of disc settling, and the effects of bar-driven evolution.

3

Disc galaxies are still settling

The discovery of the smallest nuclear discs and their young stellar bars

Camila de Sá-Freitas; D. A. Gadotti; F. Fragkoudi; L. Coccato; P. Coelho; A. de Lorenzo-Cáceres; J. Falcón-Barroso; T. Kolcu; I. Martín-Navarro; J. Mendez-Abreu; J. Neumann; P. Sanchez Blazquez; M. Querejeta; G. van de Ven

A&A (in press, 2023b)

When galactic discs settle and become massive enough, they are able to form stellar bars. These non-axisymmetric structures induce shocks in the gas, causing it to flow to the centre where nuclear structures, such as nuclear discs and rings, are formed. Previous theoretical and observational studies have hinted at the co-evolution of bars and nuclear discs, suggesting that nuclear discs grow "inside-out", thereby proposing that smaller discs live in younger bars. Nevertheless, it remains unclear how the bar and the nuclear structures form and evolve with time. The smallest nuclear discs discovered to date tend to be larger than $\sim$ 200 pc, even though some theoretical studies find that when nuclear discs form they can be much smaller. Using MUSE archival data, we report for the first time two extragalactic nuclear discs with radius sizes below 100 pc. Additionally, our estimations reveal the youngest bars found to date. We estimate that the bars in these galaxies formed $4.50^{+1.60}_{-1.10}(\mathrm{sys})^{+1.00}_{-0.75}(\mathrm{stat})$ and $0.7^{+2.60}(\mathrm{sys})^{+0.05}_{-0.05}(\mathrm{stat})$ Gyr ago, for NGC 289 and NGC 1566, respectively. This suggests that at least some disc galaxies in the Local Universe may still be dynamically settling. By adding these results to previous findings in the literature, we retrieve a stronger correlation between nuclear disc size and bar length and we derive a tentative exponential growth scenario for nuclear discs.

3.1 Sample and data description

In this section, we describe the galaxies hosting these small nuclear discs, NGC 289 and NGC 1566, together with the data description and observing program details.

NGC 289 is a weak barred spiral galaxy (T-type 4 – Sheth et al., 2010) with the presence of rings (e.g., de Vaucouleurs et al., 1991; Muñoz-Mateos et al., 2013; Buta et al., 2015), with stellar mass measurements varying between 3.2×10^{10} $M_\odot$ (López-Cobá et al., 2022) and 4×10^{10} $M_\odot$ (Sheth et al., 2010, Muñoz-Mateos et al., 2015), and inclination of 43°[1]. Considering the redshift-independent distance measurements distribution from the NASA/IPAC Extragalactic Database (NED[2]), we derive a median distance of 18 Mpc. At that distance, the measured deprojected bar size of 18.4 ± 0.4" from Muñoz-Mateos et al. (2013) corresponds to 1.62 ± 0.35 kpc. Lastly, NGC 289 has an interacting companion, the dwarf galaxy Arp 1981 (e.g., Bendo & Joseph, 2004). We use ESO archive data[3] from the MUSE Atlas of Disks program (MAD – Erroz-Ferrer et al., 2019), PI: Carollo, M. C., program ID 096.B-0309, using the MUSE Wide Field Mode. The galaxy was observed on the 15^{th} of October 2015, for a total integration time of 2400 seconds, with a point spread function (PSF) with full width at half-maximum (FWHM) of 0.6″. More details regarding the galaxy, observation, and calibration can be found in Erroz-Ferrer et al. (2019).

NGC 1566 is classified as a weakly barred galaxy (T-type 4 – Sheth et al., 2010; de Vaucouleurs et al., 1991), with rings – nuclear and outer – and spiral arms. The galaxy has stellar mass measurements between 3.8×10^{10} $M_\odot$ (Sheth et al., 2010, Muñoz-Mateos et al., 2015) and 6×10^{10} $M_\odot$ (Leroy et al., 2021), with an inclination of 32° (Salo et al., 2015), and it is at a median distance[2] of 7.3 Mpc. At that distance, the measured deprojected bar size of 40.5 ± 2.5" from Muñoz-Mateos et al. (2013) corresponds to 1.4 ± 0.1 kpc. Lastly, NGC 1566 belongs to the Dorado group and has a dwarf elliptical companion, NGC 1581 (e.g., Kendall et al., 2015). We use ESO archive data[3] from the MAD program (Erroz-Ferrer et al., 2019), PI: Carollo, M. C., program ID 0100.B-0116, using the MUSE Wide Field Mode with adaptive optics. The galaxy was observed on the 23^{rd} of October 2017, for a total integration time of 3600 seconds, with a PSF FWHM of 1.0″. More details regarding the galaxy, observation, and calibration can be found in Erroz-Ferrer et al. (2019).

3.2 Analysis and methodology

3.2.1 Finding nuclear discs

We expect most of the nuclear discs to form by gas infall due to the onset of a non-axisymmetric potential, such as the one produced by stellar bars. Within this scenario,

[1] http://leda.univ-lyon1.fr
[2] https://ned.ipac.caltech.edu
[3] http://archive.eso.org

there are common properties that one can expect nuclear discs to present.

Firstly, the stars formed by the gas will form the stellar nuclear disc, which will present higher rotational velocities than the stars already present in the central region of the galaxy. In addition, since the nuclear disc is a rotationally-supported structure, we expect low values of velocity dispersion. Once the nuclear disc forms, we have at least two structures co-existing: a cold, rapidly rotating system (the nuclear disc) and a more slowly rotating system of stars that were already present (the main disc). Considering they had different formation histories, epochs, and time scales, each structure rotates independently, that is, they have different dynamical properties. Since the light from the nuclear region carries information about both these structures, the absorption lines will not be perfect Gaussians, but display deviations. We can measure these deviations considering the Gaussian-Hermite higher-order moments h_3 and h_4 (Van Der Marel & Franx, 1993), which measure asymmetric and symmetric deviations, respectively. A negative h_3 indicates an excess of stars rotating slower than the average system velocity, while a positive h_3 indicates the opposite, an excess of stars rotating faster than the average velocity. This explains why in the presence of a fast-rotating nuclear disc, there is an anti-correlation between stellar velocity and h_3: the region in which the nuclear disc is fastly approaching the observer (blue-shifted velocities), there is also the main disc approaching us slower, hence negatives values of h_3. The opposite is also true. On the other hand, a positive h_4 indicates the presence of two rotating systems with different velocity dispersion, generating a pointy Gaussian distribution. For more details about the Gaussian-Hermite higher-order moments, see fig. 3 on Gadotti & de Souza (2005). In summary, the expected kinematic properties for the presence of a nuclear disc are (*i*) an increase in rotational stellar velocity, which is the line-of-sight velocity corrected for inclination, (*ii*) a drop in stellar velocity dispersion, (*iii*) an anti-correlation between stellar velocity and h_3, and (*iv*) an increase in h_4 (e.g., Gadotti et al., 2020).

The same formation scenario also predicts mean stellar population characteristics. Since the nuclear disc is formed by a gas inflow that only takes place once the bar potential is in place, its stars are expected to be younger than the stars from the main disc in the same region. Additionally, the gas brought inwards by the bar is likely to be already metal-enriched when forming the stars of the nuclear disc. Hence, the metallicity ([M/H]) of the nuclear disc is expected to increase and be higher than the surroundings. Nevertheless, depending on the metallicity gradient of the galaxy, the origin of the gas, and the star formation history of the nuclear disc, one can find different metallicity behaviours within the nuclear disc (e.g., Bittner et al., 2020). Lastly, since the nuclear disc evolution is due to long secular evolution processes, it is slowly built with continuous star formation. Because of that, depending on the strength of ongoing star formation, we expect the nuclear disc to present lower α-enhancement values ([α/Fe]) than the surroundings – at least for most nuclear discs. In summary, among the stellar population properties we expect the nuclear disc to present when compared to its surroundings are (*v*) younger median stellar ages, (*vi*) higher [M/H], and (*vii*) lower [α/Fe] (e.g., Cole et al., 2014; Bittner et al., 2020). Hence,

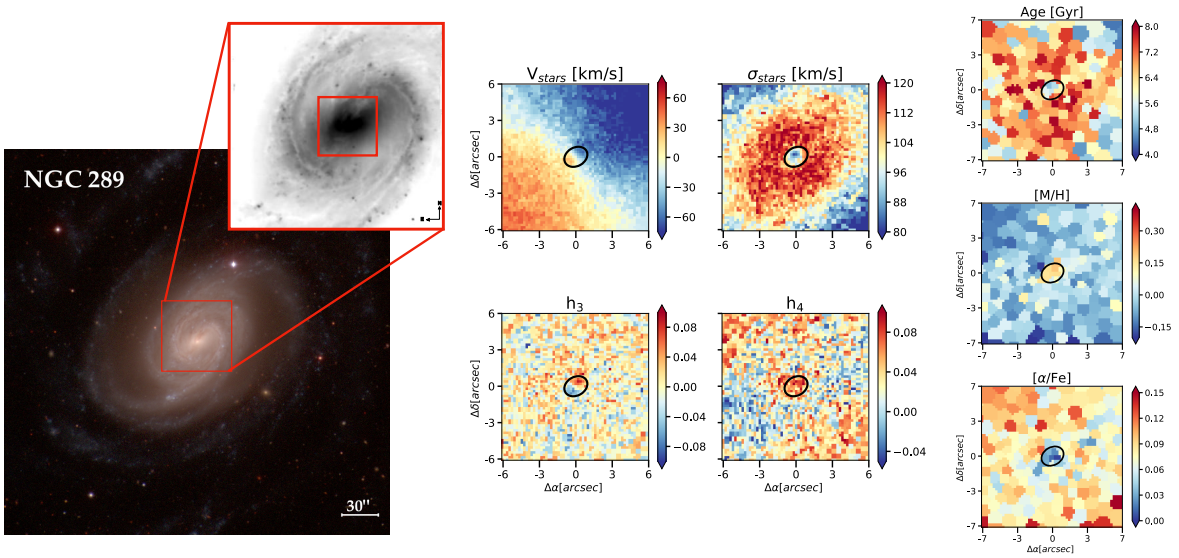

Figure 3.1: ***NGC 289 data and derived maps***. On the left, we display the colour composites of NGC 289 from the Carnegie-Irvine Galaxy Survey (CGS – Ho et al., 2011) together with the black and white image from MUSE ESO archival data (MAD – Erroz-Ferrer et al., 2019). We highlight the central region from which we derive the kinematic and stellar population maps. On the right, we display the seven spatial maps with derived kinematic and stellar population properties: stellar velocity (V_{stars}), stellar velocity dispersion (σ_{stars}), the Gauss-Hermite higher-order moments h_3 and h_4 (Van Der Marel & Franx, 1993), mean age, metallicity ([M/H]), and α elements enhancement ([α/Fe]). Together with the spatial maps, we display the limit of the nuclear disc in a black solid ellipse. We find a nuclear disc with a radius size of 90 pc. Within the limits of the ellipse, one can notice all the expected properties of a nuclear disc: increase in stellar velocity, decrease in stellar velocity dispersion, anti-correlation between h_3 and the stellar velocity, increase in h_4, decrease in mean ages, increase in [M/H], and decrease in [α/Fe].

to unmistakably identify the presence of nuclear discs in galaxies and their origin, one has to derive kinematic and stellar population properties from data cubes.

To derive the kinematic and stellar population properties of the galaxies in our sample, we use the `Galaxy IFU Spectroscopy Tool` (GIST – Bittner et al., 2019). GIST is a module-based pipeline that allows us to derive physical properties from fully reduced data cubes. To ensure consistency with previous works, we followed the analysis described in Gadotti et al. (2020), Bittner et al. (2020) and de Sá-Freitas et al. (2023), in two independent runs.

In the first run, we aim to derive the kinematic properties of the galaxy. Firstly, GIST employs an unregularised run of `pPXF` (Cappellari & Emsellem, 2004; Cappellari, 2012), considering the wavelength range between $4800-8950$ Å. The data is binned following the Voronoi binning procedure (Cappellari & Copin, 2003) to achieve a signal-to-noise of 40. Additionally, we include a low-order multiplicative Legendre polynomial to account for differences between the observed spectra and the shape of the continuum templates. From this run, we retrieve spatial maps of stellar velocity, stellar velocity dispersion, h_3, and h_4.

In the second run, we aim to derive the stellar population properties of the galaxy. We repeat the first step of the unregularised `pPXF` run, but considering a wavelength range of $4800-5800$ Å and Voronoi-binning our sample to achieve a signal-to-noise of 100. This choice is due to the fact that a higher signal-to-noise is more reliable when it comes to retrieving stellar population properties and avoiding spurious results between adjacent bins, as demonstrated in Bittner et al. (2020). Next, GIST employs `pyGandALF`, which is a `python` version of the `Gas and Absorption Line Fitting` (`gandALF` – Sarzi et al., 2006; Falcón-Barroso et al., 2006). This step consists of the modelling and removal of emission lines as Gaussians, resulting in the emission-subtracted spectra. In the last step, GIST employs a regularised run of `pPXF` in the emission-subtracted spectra, fitting different templates of stellar populations and enabling us to derive mean properties. We consider the MILES simple stellar population models library (Vazdekis et al., 2015), with [M/H] values between -1 and $+0.4$, ages between 0.03 and 14 Gyr, and [α/Fe] enhancements of $+0.0$ and $+0.4$. We normalise the MILES templates for each mean flux, deriving light-weighted properties. In addition, since both metallicity and velocity dispersion can be responsible for broadening the absorption lines (e.g., Sanchez-Blazquez et al., 2011), we fixed the stellar kinematics from the unregularised `pPXF` run. Lastly, we use the regularisation error value of 0.15 (Bittner et al., 2020) and apply an 8th order multiplicative Legendre polynomial – to account for possible extinction and continuum mismatches between the templates and the observed spectra. From the second run, we retrieve spatial maps of light-weighted mean values of stellar age, [M/H], and [α/Fe]. Lastly, we would like the reader to keep in mind that for that specific wavelength, the dominant α element is magnesium (Mg) and our analysis refer to it.

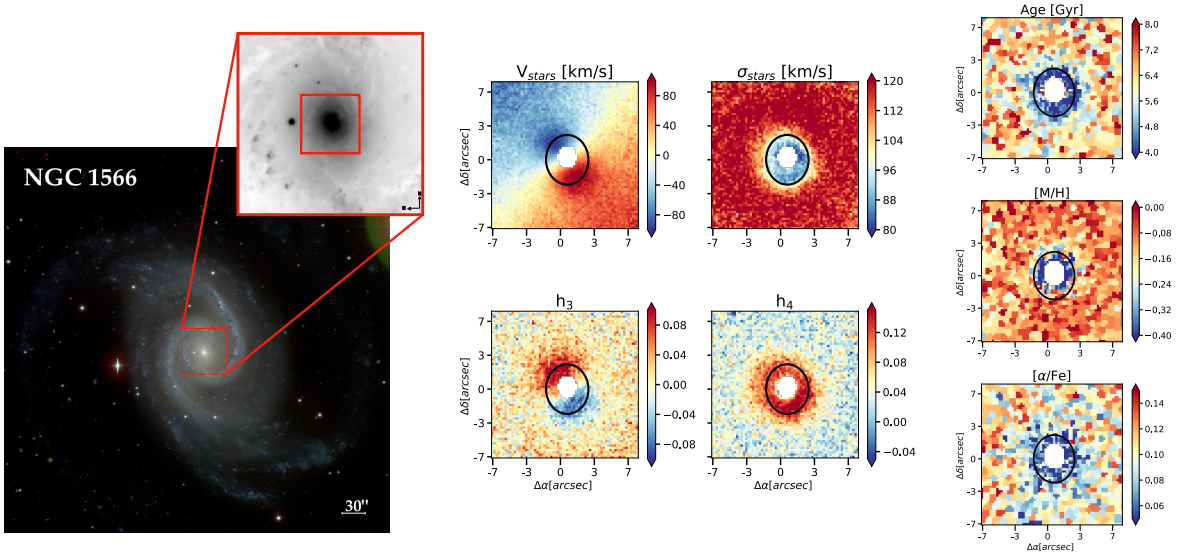

Figure 3.2: ***NGC 1566 data and derived maps***. Same as Fig. 3.1. With the spatial maps, we display the limit of the nuclear disc measured considering the peak in the V/σ radial profile, in a black solid ellipse. We find a nuclear disc with a radius size of 77 pc. Within the limits of the ellipse, one can notice most of the properties expected for a nuclear disc: increase in stellar velocity, decrease in stellar velocity dispersion, anti-correlation between h_3 and the stellar velocity, increase in h_4, decrease in mean ages, and decrease in [α/Fe]. The only property that differs from expected is the [M/H], which also decreases. This behaviour can be related to the original properties of the in-falling gas. Lastly, we mask the central region which presented strong emission lines, characteristic of AGN.

3.2.2 Estimating bar ages using nuclear discs

Numerical simulations have shown that when a bar forms, a nuclear disc forms within 10^8 yr, which is relatively short compared to the bar lifetime (which is of the order of a few 10^9 yr – Athanassoula, 1992a, 1992b; Emsellem et al., 2015; Seo et al., 2019; Baba & Kawata, 2020). Considering that, one can derive the bar formation epoch measuring the ages of the stars in the nuclear disc. However, deriving such properties is not a trivial task, since the observed light from the nuclear disc also carries tangled information from stars that were already present when it formed – that is, the main disc. With that in mind, we developed a methodology to disentangle the independent information from the nuclear disc and the main disc and, subsequently, estimate the time of the bar formation. For more details on the methodology, we refer the reader to Chapter 2. In what follows we briefly summarise the different steps of the method: **first**, we convolve and shift all spectra in the data cube, ensuring the same velocity dispersion and velocity zero for all spaxels; **second**, we mask all spaxels classified as AGN using the BPT classification with amplitude over noise (AON) above 20 (Baldwin et al., 1981); **third**, we select a ring region around the nuclear disc to derive the spectrum of the underlying main disc, hereafter denominated *representative ring/spectrum* – for this sample of small nuclear discs, we placed the representative ring region at 1.2" from the nuclear disc radius; **fourth**, using the representative spectrum and assuming an exponential light profile, we model the main disc data cube – we use disc scale-lengths values derived in Salo et al. (2015); **fifth**, we subtract the main disc from the original data cube – shifted to velocity zero and convolved to maximum velocity dispersion – and consider the difference as the light from the nuclear disc isolated; as an extra step, we collapsed each data cube into a average spectrum; **lastly**, we employ GIST as described in Section 3.2.1 for the second run, deriving mean stellar populations for each collapsed spectrum (MUSE original, main disc, and nuclear disc).

During the fit of the emission-subtracted spectra, `pPXF` estimates different weights for different simple stellar populations (SSPs), differing in age, [M/H], and [α/Fe]. These weights represent the fraction of the light due to the different SSPs. Considering the different weights for different SSPs, we are able to build light-weighted non-parametric SFHs for each collapsed spectrum (MUSE original, nuclear disc, and main disc). Finally, to convert the SFHs from light- to mass-weighted, we apply the mass-to-light ratios[4] predictions from the MILES models (Vazdekis et al., 2015), considering the BaSTI isochrones (Pietrinferni et al., 2004, 2006, 2009, 2013), converting luminosity into mass. The mentioned mass-to-light ratios assume a Kroupa revised IMF (Kroupa, 2001) with [α/Fe] enhancements of +0.0 and +0.4. Additionally, the ratios account for both stellar and remnants masses and depend on age, [M/H], and [α/Fe] that best describes the observed spectra. As a result, we can derive independent mass-weighted SFHs for the nuclear disc and main disc.

Finally, we consider that shortly after the bar forms the stellar mass built by the

[4]http://research.iac.es/proyecto/miles/pages/predicted-masses-and-photometric-observables-based-on-photometric-libraries.php

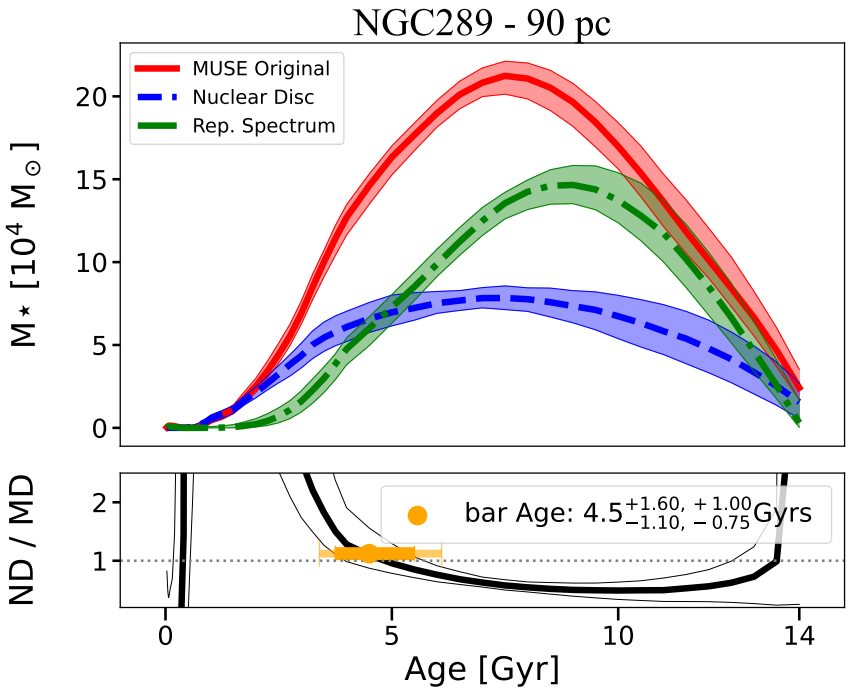

Figure 3.3: ***NGC 289 bar age measurement.*** On the top panel, we display star formation histories – stellar mass built over time – of the original data (red-solid line), the modelled main disc (green-dot-dashed line), and the nuclear disc isolated (blue-dashed line). With each SFH, we display the results from the 100 MC runs (shaded regions), considering the 1^{st} and 9^{th} quantiles. On the bottom panel, we display the ratio between the nuclear disc and the main disc SFHs as a function of time (black-solid line), with the range of values from the 100 MC runs (grey-shaded region). We consider the moment of bar formation when ND/MD > 1 towards younger ages. This moment is highlighted by the orange dot and marks an age of $4.5^{+1.60}_{-1.10}(\mathrm{sys})^{+1.00}_{-0.75}(\mathrm{stat})$ Gyr. Further discussion of the measurement of the presented errors can be found in Sect. 3.3.2.

nuclear disc increases above the stellar mass built by the main disc and, therefore, the ratio between the nuclear disc and the main disc rises above 1, with a positive slope towards younger ages (see Chapter 2). This takes into account that it is possible to have residuals of old stellar populations in the nuclear disc, which is expected since the representative spectrum might not be as old as the underlying main disc. For more details on some of the tests carried out to test our methodology, as well as its caveats, we refer the reader to Chapter 2.

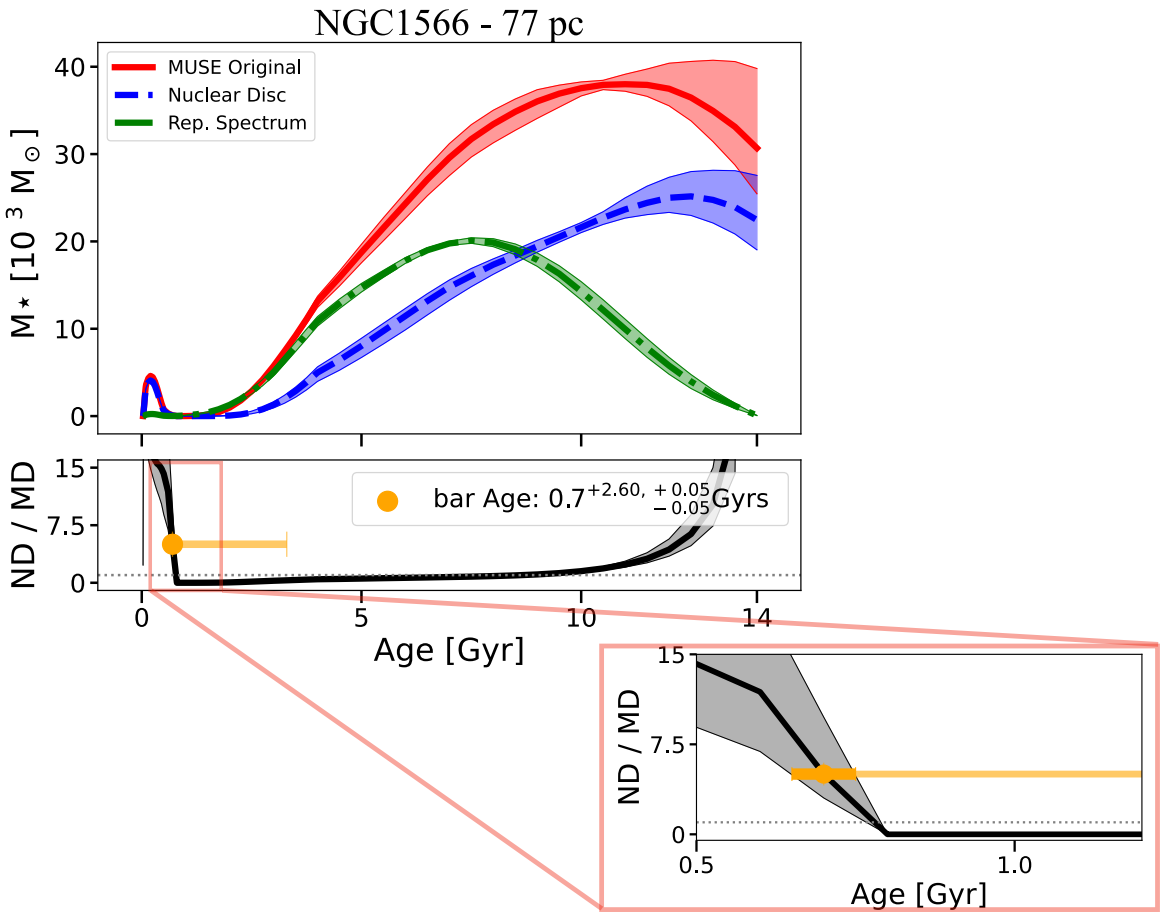

Figure 3.4: ***NGC 1566 bar age measurement.*** Same as Fig. 3.3. The criterion of ND/MD > 1 is highlighted by the orange dot and marks an age of $0.7^{+2.60}$(sys)$^{+0.05}_{-0.05}$(stat) Gyr for the bar hosted by NGC 1566. Additionally, we display a zoom-in of a region of the bottom panel, highlighting the variations due to the 100 MC runs (grey-shaded regions).

3.3 Results

3.3.1 Evidence of small nuclear discs

In this Section, we describe our results on the presence of nuclear discs on NGC 289 and NGC 1566. Figures 3.1 and 3.2 display, for each galaxy, the object coloured-image from the Carnegie-Irvine Galaxy Survey (CGS - Ho et al., 2011), the MUSE field of view, and the spatial maps of the kinematic and stellar population properties. The individual analysis and further discussion are below.

NGC 289 – Since the spatial resolution of the data is limited, we can not derive a meaningful radial profile of V/σ within the nuclear disc, nor identify the position of its maximum value. Because of this, we determine the radius size of the nuclear disc visually, considering only the spatial maps in Fig. 3.1. We find the nuclear disc radius to be 1", which corresponds to a physical radius size of 90 pc. This radius is very consistent across all seven assessed maps. Considering the 1^{st} and 3^{rd} quartiles of the distribution of distance measurements from NED, the nuclear disc radius size error is 90^{+16}_{-8} pc. Despite the apparent small size of the nuclear disc, the expected characteristics are still clear. Following the kinematic maps, we found an increase in the stellar velocity and a drop in the stellar velocity dispersion. Furthermore, considering the Gauss-Hermite higher-order moments h_3 and h_4, we identify an anti-correlation with V for the former and an increase for the latter. All these kinematic properties indicate the presence of a second independent rotationally-supported structure, i.e., the nuclear disc. Additionally, the stellar population properties agree with the scenario that the nuclear disc was formed by gas inflow following the formation of the bar. The nuclear disc presents younger average ages than the surrounding regions, an increase in the [M/H], and a decrease in [α/Fe] enhancements. We would like to stress how the powerful resolution of MUSE allows us to identify nuclear discs even in extreme cases such as the one of NGC 289.

NGC 1566 – the results for NGC 1566 are presented in Fig. 3.2. We mask the central region due to the presence of broad emission lines, characteristic of AGNs. Considering the V/σ radial profile, we find a nuclear disc with an apparent radius of 2.2" corresponding to a physical radius size of 77 pc. Considering the 1^{st} and 3^{rd} quartiles of the distribution of distance measurements from NED, the nuclear disc size error is 77^{+47}_{-2} pc. As NGC 289, NGC 1566 displays most of the characteristics of a young nuclear disc, when compared to the main disc: increase in stellar velocity rotation, decrease in stellar velocity dispersion, $h_3 - V$ anti-correlation, increase in h_4, younger average stellar ages, and increase in [α/Fe] enhancements. The only unexpected characteristic is the decrease in [M/H], where the opposite is expected for most bar-built nuclear discs. Nevertheless, Bittner et al. (2020) found the same trend for 3 nuclear discs and 8 nuclear rings in a sample of 17 galaxies. This behaviour can be related to the original properties of the in-falling gas.

In summary, the two galaxies present the kinematic characteristics of a nuclear disc

and most of the expected stellar population properties. Even though the [M/H] values of NGC 1566 are not necessarily consistent with most of the nuclear disc characteristics (e.g., Bittner et al., 2020), the two nuclear discs display younger stellar ages in comparison to the surroundings, which is expected for bar-driven gas inflow. Lastly, it is worth it highlighting that the nuclear disc radius sizes of NGC 289 and NGC 1566 may not be consistent with each other, since we did not derive them following the same methodology. As noticeable in Fig. 3.2, the characteristic kinematic radius size, based on the peak of V/σ, can be underestimating the nuclear disc size of NGC 1566 when compared to NGC 289.

3.3.2 Timing bar formation

In this Section, we describe the measured ages for the bars hosted by NGC 289 and NGC 1566 following the methodology presented in the Chapter 2. In Figs. 3.3 and 3.4 we present the Star Formation Histories – stellar mass built over time – for the original data, the nuclear disc, and the main disc for NGC 289 and NGC 1566, respectively. We also display the ratio between the stellar mass of the nuclear disc and the main disc for every given SSP age, with a highlight on the bar age. As described in Chapter 2, we constrain possible errors in our results, considering mainly two sources: data statistical errors and methodology systematic errors. We measured the data statistical error by performing 100 Monte Carlo runs in the collapsed data of each data cube – MUSE original, nuclear disc, and main disc. We consider the noise at each wavelength to sample a random distribution of fluxes, creating 100 artificial spectra. Following that, we repeat the methodology from Sec. 3.2.2 for each of the 300 artificial data cubes, deriving a distribution of SFHs and bar ages, which we consider as the statistical error.

On the other hand, the measurement of systematic errors consists of quantifying how the configuration of our methodology can affect the final bar age. This includes different galactocentric distances of the representative ring, the light profile assumed to model the main disc (exponential or flat), the measured age for collapsed and non-collapsed versions of the data cubes, and the adopted regularisation value in the final `pPXF` fit. Each different configuration results in a somewhat different bar age. We consider the difference from our main configuration to each test as a systematic error value. To quantify the final systematic error, we add all systematic errors in quadrature. In this Chapter, we vary the position of the representative ring, and the assumed model profile (exponential or flat), and consider the collapsed and non-collapsed configurations. For the regularisation value, we assume the error of 0.5 Gyr depending on the chosen regularisation value, found in Chapter 2.

NGC 289 – We find an age of 4.50 Gyr for the bar hosted by NGC 289 (see Fig. 3.3). Additionally, from the Monte Carlo runs, we measure a statistical error of $^{+1.00}_{-0.75}$ Gyr, considering the 1^{st} and 9^{th} quantiles of the distributions of SFHs. Compared to the statistical error we find for the bar in NGC 1433 ($^{+0.2}_{-0.5}$ – Chapter 2), NGC 289 errors are $1.5 - 5$ times larger. This is expected due to the fact that the nuclear disc present in

Galaxy	Stellar mass ($M_\odot$)	Reference	Method
NGC 289	4.3×10^{10}	Sheth et al. (2010)	3.6μm
	4.0×10^{10}	López-Cobá et al. (2022)	SSP analysis
	4.6×10^{10}	This work	SSP analysis and extrapolation of exponential disc
NGC 1433	2.0×10^{10}	Sheth et al. (2010)	3.6μm
	7.4×10^{10}	Leroy et al. (2021)	3.4μm
	2.62×10^{10}	Chapter 2	SSP analysis and extrapolation of exponential disc
NGC 1566	3.8×10^{10}	Sheth et al. (2010)	3.6μm
	6.2×10^{10}	Leroy et al. (2021)	3.4μm
	8.3×10^{10}	This work	SSP analysis and extrapolation of exponential disc
NGC 4371	3.2×10^{10}	Sheth et al. (2010)	3.6μm
	6.3×10^{10}	Gallo et al. (2010)	g_0 and z_0 bands
Milky Way	$6.1 \pm 1.14 \times 10^{10}$	Licquia & Newman (2015)	Hierarchical Bayesian combination of previous measurements from the literature

Table 3.1: Total stellar masses for the galaxies considered in Fig. 3.5, as derived in different studies and with different methods, as indicated.

NGC 1433 is much larger and better resolved. In that sense, the original data occupies more spaxels when compared to NGC 289. Thus, once we collapse the data cube, we achieve a signal-to-noise close to 2000 for NGC 1433. On the other hand, the collapsed spectrum of NGC 289 has a signal-to-noise of around 200. Additionally, we constrained a systematic error of +1.6 on the bar age by varying the configurations on our methodology – the position of the representative ring, modelled main disc light profile, running the analysis on a spaxel by spaxel basis rather than collapsing the data cube, and regularisation. Lastly, in Chapter 2 we demonstrated that placing the representative ring closer to the nuclear disc can result in younger bar ages. More specifically, we found a systematic error of 1.1 Gyr younger for bar ages. Since the data on NGC 289 intrinsically has a low physical spatial resolution, we originally placed the representative ring the closest allowed by observational constraints, that is, 1.2" of distance determined by the seeing. Due to that, we can not explore the systematic error of placing the representative ring closer to the nuclear disc and opted to adopt the systematic error of 1.1 Gyr younger for NGC 289 as well. In summary, we find that NGC 289 hosts a bar with an age of $4.50^{+1.60}_{-1.10}(\mathrm{sys})^{+1.00}_{-0.75}(\mathrm{stat})$ Gyr.

NGC 1566 – We find an age of 0.70 Gyr for the bar hosted by NGC 1566 (see Fig. 3.4). For this galaxy, when applying our methodology we find an excess of old stellar populations in our nuclear disc. As discussed in Chapter 2, this is likely due to the negative age gradient in the galaxy. Our method of obtaining the bar age is robust against biases introduced due to this old stellar population residual. From the Monte Carlo runs, we measure a statistical error of ± 0.05 Gyr, considering the 1^{st} and 9^{th} quantiles, considerably smaller than NGC 289. The low statistical error for NGC 1566 is mainly due to two facts: (*i*) the signal to noise achieved by the collapsed data cube is over 1000 and (*ii*) the particular shape of the SFHs and the sudden peak in young ages is similar in the 100 MC runs. Nevertheless, we also present a zoomed-in region in Fig. 3.4 to highlight the differences from the 100 MC runs. In addition, we find systematic errors of +2.60 Gyr. The systematic errors are due to the differences between the collapsed and non-collapsed results and the regularisation error adopted from Chapter 2. Because NGC 1566 is a nearby galaxy (7.3 Mpc) and the observations were carried out with adaptative optics, the resolution is sufficient to test how varying the distance of the representative ring will affect our results, which is one of our main systematic uncertainties. However, the bar age retrieved for different representative rings distances remains the same, that is, 0.70 Gyr. In summary, we find a bar age of $0.70^{+2.60}(\mathrm{sys})^{+0.05}_{-0.05}(\mathrm{stat})$ Gyr for NGC 1566.

3.3.3 Integrating the SFHs – a consistency check

Assuming our decomposition of the central light in the two discs is correct and, taking into account their relative brightness, we can calculate their contribution to the mass integrating their SFH (see also de Sá-Freitas et al., 2023 – Chapter 2). For NGC 289 we measure 6.4×10^7 $\mathrm{M}_\odot$ and 4.4×10^7 $\mathrm{M}_\odot$ for the main and nuclear disc, respectively. In that sense, the recently formed nuclear disc accounts for $\sim 41\%$ of the total mass budget within the central 90 pc. On the other hand, for NGC 1566 we measure the main disc mass

of 2.9×10^7 $M_\odot$ and the nuclear disc mass of 3.8×10^7 $M_\odot$, where the nuclear disc accounts for $\sim 56\%$ of the central mass budget within 77 pc. The measured masses for the nuclear discs are in good agreement with the findings in Seo et al. (2019), in which the authors find masses for recently formed nuclear discs of 4×10^7 $M_\odot$ for Milky-Way-like galaxies, with stellar masses of $4.5 - 5 \times 10^{10} M_\odot$.

Furthermore, considering the surface mass density of the main disc, we are able to extrapolate the results above to estimate the total stellar mass of the galaxy assuming an exponential function following:

$$M_\star = 2\pi \int_0^\infty \Sigma(r) dr = 2\pi \Sigma_0 h^2, \tag{3.1}$$

where Σ_0 is the central surface density and h is the disc scale-length – we consider 1.7 kpc and 2.6 kpc for NGC 289 and NGC 1566, respectively (Salo et al., 2015). We find extrapolated total stellar masses of 4.6×10^{10} $M_\odot$, for NGC 289, and 8.3×10^{10} $M_\odot$, for NGC 1566. With these estimates for the total stellar mass of the galaxy, we can compare it to measurements that apply different methods, to do a consistency check of our structure disentanglement. In Table 3.1 we summarise the different stellar masses measured for different galaxies, including NGC 289 and NGC 1566. We find extrapolated masses close to the literature, especially in the case of NGC 289. On the other hand, the extrapolated mass for NGC 1566 is larger than the ones measured by the S^4G (Sheth et al., 2010) and PHANGS (Leroy et al., 2021) teams. Nevertheless, the values from both works also vary greatly, demonstrating that measuring the stellar mass content is not a trivial task.

3.4 Small nuclear discs and young bars in the context of secular evolution

In this Section, we discuss our results on the smallest nuclear discs reported and what insights they bring for galaxy secular evolution. We would like to stress that the results achieved by this work were only possible due to the incredible resolving power of state-of-the-art IFUs. Our results illustrate how we can uncover relatively compact structures, their kinematics, and their stellar population properties.

3.4.1 The smallest nuclear discs discovered – what does this tell us?

In this Chapter, we report the smallest kinematically confirmed nuclear discs, as well as the youngest bar, ever discovered, to the best of our knowledge. The nuclear discs hosted by NGC 289 and NGC 1566 have respective sizes of 90^{+16}_{-8} and 77^{+47}_{-2} pc. In Sect. 3.3.1 we present the characteristics of each nuclear disc, together with spatial maps of the kinematic and stellar population properties. Both galaxies show all the kinematic characteristics

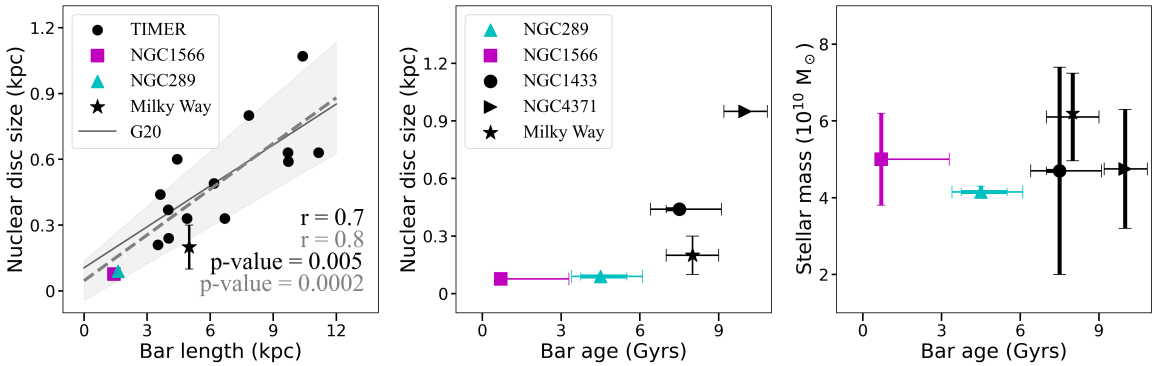

Figure 3.5: ***The smallest nuclear disc and their young bars in context.*** **In the left**, we show the relation of nuclear disc size with bar length from the TIMER sample (Gadotti et al., 2020 – black circles), together with the two galaxies from this paper – NGC 289 (cyan triangle), and NGC 1566 (magenta square) – and values for the Milky Way (black star). For the nuclear disc size for the Milky Way, we consider $\sim 100 - 300$ pc (Sormani et al., 2020,2022) and for the bar length, 5.0 ± 0.2 kpc (Wegg et al., 2015). We also display the linear regression for the TIMER sample alone (solid black line) and considering this work, with the two new galaxies (dashed grey line). With the galaxies in this Chapter, the Pearson correlation coefficient between nuclear disc size and bar length is strengthened from 0.73 (TIMER only) to 0.82 (this work). We do not consider the Milky Way for linear regression. The two galaxies from this work host considerably smaller nuclear discs than the ones in the TIMER sample. **In the centre**, we show the relation of nuclear disc size with bar age. We consider the values for NGC 1433 (de Sá-Freitas et al., 2023), NGC 4371 (Gadotti et al., 2015, 2020), the Milky Way (Sormani et al., 2020, 2022; Wylie et al., 2022; Sanders et al., 2022) and the two galaxies from this work, NGC 289 and NGC 1566. The error bars of NGC 289 and NGC 1566 are the statistical and systematic errors, measured in this Chapter; for NGC 1433, we considered the statistical and systematic errors from Chapter 2; for the Milky Way, we considered the different values from the literature, and for NGC 4371, we considered the measured errors from Gadotti et al. (2015). It is clear that the bar ages measured for NGC 289 and NGC 1566 are the youngest, even when considering the error bars. **In the right**, we display the values of the total stellar mass as a function of bar age. For stellar mass values, we consider the mean value of different literature references (see Table 3.1). We do not consider the extrapolated values for total stellar mass from this work. With the information from the 5 galaxies, we find no correlation. This could indicate that downsizing is not sufficient to determine bar formation, although more data is needed to achieve robust results.

expected for the presence of a second ordered fast-rotating structure in the centre of the galaxy, the nuclear disc. Additionally, the stellar population properties of both galaxies are those expected if the nuclear disc is formed by gas infall due to the presence of the bar. When compared to the surroundings, both nuclear discs have younger mean stellar ages and lower [α/Fe] values. These properties indicate the late formation of the nuclear disc when compared to the main disc that was already present. Also, the lower values of [α/Fe] indicate a continuous star formation, the opposite of a sudden starburst driven by mergers, which would present higher values of [α/Fe] enhancement. Additionally, NGC 289 presents higher values of [M/H] in the nuclear disc when compared to the surroundings, which is also expected in the bar-built scenario. Lastly, on the contrary, NGC 1566 presents lower values of metallicity, which is not expected for the bar-built scenario of the nuclear disc. However, Gadotti et al. (2019) report a similar case in the TIMER survey, NGC 1097, in which the nuclear ring also presents low values of [M/H], indicating the lack of pre-processing. As in NGC 1097, NGC 1566 has signs of a recent interaction and a low-mass satellite companion, NGC 1581, which could explain the origin of the low-metallicity gas. Also, Bittner et al. (2020) find similar radial trends for 3 nuclear discs and 8 nuclear rings out of 17 galaxies. Since the metallicity values are intrinsically connected to the origin and history of the gas brought inwards – which we do not know and is beyond the scope of this work – it is possible that the original gas was not enriched for unknown reasons, and can still be in agreement with the bar-built scenario of nuclear discs.

When compared to known nuclear discs, such as the ones reported by the TIMER collaboration (left panel in Fig. 3.5 – Gadotti et al., 2019), the nuclear discs we find are the smallest reported. Interestingly, both galaxies also have smaller bars than the TIMER sample, with sizes comparable to nuclear bars (Erwin, 2004). However, there is no evidence of longer bars in both cases, and we therefore consider these to be the main bar of the galaxy, albeit with lengths that are at the low end of the observed distribution. In fact, Erwin (2005) finds that the mean main bar size in late-type disc galaxies (Sc-Sd) is 1.5 kpc, very close to the bars in both galaxies studied here (although note that both are Sbc galaxies). This makes them interesting objects to investigate further the evolutionary link between bars and nuclear discs. There is growing evidence that supports that bars and nuclear discs can evolve simultaneously, both from simulations and observations (e.g., Shlosman et al., 1989; Knapen, 2005; Comerón et al., 2010; Seo et al., 2019; Gadotti et al., 2020). From observations, Gadotti et al. (2020) show a clear relation between the kinematic nuclear disc size and the bar length (see left panel in Fig. 3.5), which can imply a possible co-evolution. Furthermore, studies indicate that the nuclear disc grows inside-out with time (e.g., Bittner et al., 2020; de Sá-Freitas et al., 2023 – Chapter 2), in agreement with simulations (Seo et al., 2019). In fact, Seo et al. (2019) predict that, for Milky-Way galaxies, bar-built nuclear discs can form as small as 40 pc – depending on properties such as gas fraction and dynamics –, which is in agreement with our findings. Adding the two galaxies from this work, the correlation between nuclear disc size and bar length is strengthened from a Person-coefficient of 0.72 to 0.83, with a *p-value* of 2×10^{-4} (see Fig. 3.5, left panel). This is consistent with the scenario in which the nuclear disc

growth is connected to the bar length, although the correlation itself does not necessarily imply causality. Nonetheless, exactly which mechanisms are responsible for defining the size of the nuclear disc and how are still debated (see, e.g., Sormani et al., 2018).

Finally, in this Chapter, we find the first kinematically confirmed extragalactic nuclear disc as small as the one in our Galaxy, which has a size of $100 - 200$ pc (e.g., Launhardt et al., 2002). The differences in the size of the nuclear disc from the Milky Way to extragalactic can be either real, in the sense that our Galaxy hosts a small nuclear disc, or artificial, due to different measurement methods. Although we cannot rule out that the differences can arise from different measurement methods, our findings show that small nuclear discs (~ 100 pc) exist and can be found in other galaxies as well.

3.4.2 Bars are still forming and discs are still settling

A number of theoretical and observational studies find that bars are robust, long-lived structures, and once formed, cannot be easily destroyed (e.g., Athanassoula, 2003; Athanassoula et al., 2005; Kraljic et al., 2012; Gadotti et al., 2015; Pérez et al., 2017; de Lorenzo-Cáceres et al., 2019; Rosas-Guevara et al., 2020; Fragkoudi et al., 2020, 2021; de Sá-Freitas et al., 2023). Additionally, by studying how the fraction of barred galaxies evolves with redshift, it becomes clear that bars exist at least since $z \leq 1 - 2$ (e.g., Sheth et al., 2008; Melvin et al., 2014; Guo et al., 2023), and the fraction increases with time (e.g., Sheth et al., 2008; Cameron et al., 2010; Melvin et al., 2014; Zhao et al., 2020). In fact, in the Local Universe, bars are common structures and are present in $30\% - 70\%$ of the galaxies (e.g., Eskridge et al., 2000; Menéndez-Delmestre et al., 2007; Barazza et al., 2008; Aguerri et al., 2009; Nair & Abraham, 2010; Buta et al., 2015; Erwin, 2018). Although it is not completely clear what are the fundamental properties of galaxies to lead them to form and sustain a bar, analytical and numerical works indicate that the moment of bar formation is linked to the dynamical settlement of the disc (e.g., Kraljic et al., 2012). That is, galaxies can only form and sustain a bar once their discs are massive enough and sufficiently dynamically cold, at least partially. Due to that, massive galaxies are expected to achieve a minimum mass to settle first, following the downsizing scenario (e.g., Cowie et al., 1996; Thomas et al., 2010; Sheth et al., 2012). In that scenario, one could expect a relation between galaxy mass and bar age, where the oldest bars would be found in massive galaxies and, on the other hand, young bars in less massive galaxies.

Following the methodology presented in Chapter 2, we measure the bar ages of NGC 289 and NGC 1566 of $4.50^{+1.60}_{-1.10}(\mathrm{sys})^{+1.00}_{-0.75}(\mathrm{stat})$ Gyr and $0.7^{+2.60}(\mathrm{sys})^{+0.05}_{-0.05}(\mathrm{stat})$ Gyr, respectively. To the best of our knowledge, these are the youngest bars for which we have a robust estimate of their ages. Since bar formation is associated with disc settling, our findings indicate that the discs in these galaxies recently settled or are still partially settling. Additionally, analysing photometric and kinematic properties following Erwin & Debattista (2017) and Méndez-Abreu et al. (2008, 2019), respectively, we did not find any evidence of a presence of a box/peanut bulge. More specifically, we looked for 'spurs'

signatures in S^{4}G images and analysed the h_4 along the bar major axis. For both analyses, we did not find signs of the presence of a box/peanut bulge. For more details regarding the photometric analysis, we refer the reader to Erwin & Debattista (2017) and, for the kinematic analysis, to Méndez-Abreu et al. (2008, 2019). Since it is expected that bars take $\sim 3-4$ Gyr to develop a box/peanut bulge (e.g., Pérez et al., 2017), this is in line with the fact that these bars are young and recently formed. Considering the scenario in which bars form nuclear discs, it is not surprising that the smallest nuclear discs are hosted by young bars. In fact, this is expected in the bar-driven and inside-out growth scenarios. That is, recently formed bars would host small nuclear discs (e.g., Seo et al., 2019). In summary, the measured bar ages together with the nuclear disc sizes from our work support scenarios of co-evolution between the bar and nuclear disc, and the inside-out growth of the nuclear disc itself, even if provisionally.

Analysing our sample in the context with other findings, for the first time we can start to investigate the relationship between nuclear disc size and bar age (see Table 3.2 and Fig. 3.5 – middle panel), which will allow us to understand how nuclear discs grow in size in the future once we derive more bar ages using the full TIMER sample. Considering the current sample of galaxies for which we do have the measured bar age – NGC 1433 (7.5 Gyr – de Sá-Freitas et al., 2023; Chapter 2); NGC 4371 (10 Gyr – Gadotti et al., 2015); and the Milky Way (8 Gyr – Wylie et al., 2022; Sanders et al., 2022), in addition to NGC 289 and NGC 1566 –, we show a tentative exponential growth scenario for nuclear discs in galaxies with similar stellar masses (see Table 3.1). Whereupon the nuclear disc, at first, hardly shows a development until $\sim$ 6 Gyr, followed by fast growth. Despite our small sample, this scenario is in qualitative agreement with theoretical expectations (e.g. Seo et al., 2019), that find that young nuclear discs form small and are repetitively destroyed by their own star formation. This can also explain the lack of small nuclear discs discovered. Once they accumulate enough mass and the bar grows long enough, the nuclear disc can effectively grow. However, Seo et al. (2019) find this transition to happen after $\sim$ 2 Gyr, depending on the simulation configurations. Nevertheless, this is a preliminary result and a larger sample is needed to robustly understand how nuclear discs grow, which is one of the TIMER collaboration goals for the future. In addition, more simulations are needed, in particular simulations employing a cosmological setting, to better understand the formation and growth of nuclear discs.

Finally, we also investigate how our sample fits the downsizing scenario (see Fig. 3.5 – right panel), in which massive galaxies are expected to host older bars. To investigate this scenario, we considered different mass measurements in the literature, summarised in Table 3.1. Contrary to the expected, our galaxies that host young bars have similar stellar masses of galaxies with bars as old as 10 Gyr. This indicates that the downsizing scenario may not be sufficient to explain bar formation, but other processes may also be needed. In other words, even if galaxies have enough mass, other factors can be limiting bar formation, and further investigation is needed. In fact, bars can also form due to tidal interactions, including interactions with satellite galaxies, and this mechanism of bar formation may

Galaxy	R_{bar} [Kpc]	R_{ND} [Kpc]	Bar age [Gyr]	Reference
NGC 289	1.62	0.090	$4.5^{+1.60}_{-1.10}(\text{sys})^{+1.00}_{-0.75}(\text{stat})$	This work
NGC 1566	1.40	0.077	$0.7^{+2.60}(\text{sys})^{+0.05}_{-0.05}(\text{stat})$	This work
NGC 1433	3.63	0.380	$7.5^{+1.60}_{-1.10}(\text{sys})^{+0.2}_{-0.5}(\text{stat})$	Chapter 2
NGC 4371	5.20	0.950	10.0 ± 0.8	Gadotti et al. (2015)
Milky Way	5.00	0.200	8.0	Wylie et al. (2022), Sanders et al. (2022)

Table 3.2: Properties of galaxies considered in Fig. 3.5 derived from different studies. The bar lengths (R_{bar}) for NGC 289 and NGC 1566 are from Muñoz-Mateos et al. (2015), NGC 1433 from Kim et al. (2014), and NGC 4371 from Herrera-Endoqui et al. (2015). The kinematic nuclear disc sizes (R_{ND}) for NGC 1433 and NGC 4371 are from Gadotti et al. (2020). Finally, R_{ND} and R_{bar} values of the Milky Way are from Launhardt et al. (2002) and Wegg et al. (2015).

be independent of the galaxy mass (see, e.g., Noguchi, 1987; Gerin et al., 1990; Łokas, 2021). This could be the case of NGC 289 and NGC 1566 since both galaxies have close companions and signs of recent interactions. Nevertheless, from Table 3.1, it is clear that stellar mass measurement is not trivial, and different methods can result in masses differing by a factor ~ 3. Additionally, we present here a small sample and a tentative result. In the near future, we will analyse the same properties for the entire TIMER sample (Gadotti et al., 2019), which will enable us to derive a more robust scenario.

3.5 Summary and conclusions

In this Chapter, we report the smallest kinematically confirmed nuclear discs observed to date. Additionally, applying the methodology from Chapter 2, we measure their respective bar ages, and find that their bars are also the youngest bars to date for which there are bar age estimates. We summarise our findings as follows:

- We report evidence for the serendipitous discovery of nuclear discs with sizes of 90^{+16}_{-8} and 77^{+47}_{-2} pc in NGC 289 and NGC 1566, respectively. We analysed spatially resolved kinematic and stellar population properties for both galaxies. Both galaxies present all the kinematic characteristics of a secondary fast-rotating central structure, the nuclear disc. In addition, their nuclear discs present most of the average stellar population properties expected for a bar-driven formation. These properties follow

the scenario in which the nuclear disc is formed by gas inflow triggered by the bar formation (Section 3.3.1).

- We measured the ages for both bars hosting the nuclear discs and find ages of $4.50^{+1.60}_{-1.10}(\mathrm{sys})^{+1.00}_{-0.75}(\mathrm{stat})$ and $0.7^{+2.60}(\mathrm{sys})^{+0.05}_{-0.05}(\mathrm{stat})$ Gyr for NGC 289 and NGC 1566, respectively. This is in agreement with the bar-driven and inside-out growth scenarios, in which young bars form small nuclear discs, and, as the bar grows longer, the nuclear disc grows larger (Section 3.3.2).

- Analysing the bar length and nuclear disc size relation together with the TIMER sample (Gadotti et al., 2019), we find that our sample agrees with the correlation. In fact, by adding our two galaxies, the correlation is strengthened from r = 0.73 to 0.82 with a *p-value* of 2×10^{-4}. This is in agreement with the nuclear disc growing inside out with time (Section 3.4.1).

- Analysing the bar age with nuclear disc size relation, together with 3 galaxies from the literature (NGC 1433, NGC 4371, and the Milky Way), we find a suggestive exponential relation. In that scenario, nuclear discs would take longer to effectively grow. This is in qualitative agreement with theoretical works (e.g. Seo et al., 2019) which suggest that nuclear discs grow in time (Section 3.4.2).

- Analysing the bar age with the galaxy stellar mass relation together with 3 galaxies from the literature (NGC 1433, NGC 4371, and the Milky Way), we do not find a correlation between the bar age with the galaxy stellar mass. Although this finding might challenge the downsizing scenario for bar formation, whereby more massive galaxies would host older stellar bars, we also point out that our sample size is still rather limited. Nevertheless, we emphasise that measuring stellar mass is not trivial, and different methods find different masses (Section 3.4.2).

These results provide further intriguing evidence of the interplay between nuclear discs and the formation and evolution of bars. By applying the methodology presented in the Chapter 2 to the entire TIMER sample (Gadotti et al., 2019) we will be able to increase our sample size, thus enabling us to probe the role played by downsizing on bar formation and the intricate interplay between bar formation and nuclear disc evolution.

4

A TIMER tale

First results on bar ages for nearby galaxies

Camila de Sá-Freitas; and TIMER team

in prep.

The settlement of the galaxy disc marks a transition in its evolution: external processes give place to internal operations as the protagonist of galaxy evolution. However, constraining this epoch is not straightforward and different efforts are in the making. One way to measure it is by age-dating the bar formation on nearby galaxies.[1]. This was not possible before the methodology presented in Chapter 2 and a suitable data set like TIMER. We present for the first time the – preliminary – achievement of the *TIMER tale*: measuring bar ages and disc settling, for a sample of 20 galaxies. Among our results, we find bar ages between $\sim 1-12.5$ Gyr, indicating disc settling has been taking place since at least $z \approx 6$, and it is an ongoing process in the Universe. Furthermore, we find no relation between bar ages and galaxy stellar mass, contradicting the predictions of downsizing that the most massive galaxies would host older bars. We reveal indications of angular momentum exchange between the bar and the main disc, in that bars capture stars from the disc. Lastly, our results agree with the scenario in which nuclear discs, in general, grow from the inside out. This work will allow further investigation from an observational point of view of secular evolution, such as bar length growth, bar-induced quenching, angular momentum exchange, the evolution of the bar pattern speed, and the evolution of the nuclear disc.

---

[1]This Chapter will be submitted to A&A in the future.

4.1 Sample and data description

To better constrain how galaxies evolve, especially in later stages, one needs to be able to derive bar ages for a large sample, since it plays a major role on driving secular evolution. To apply our methodology described in Chapter 2 to more galaxies, we need high spatial resolution integral-field spectroscopy from the central part of the galaxies, that is, the bar-built nuclear disc. The Time Inference with MUSE in Extragalactic Rings (TIMER – Gadotti et al., 2019) survey was specially designed with these characteristics. In this Chapter, we apply our methodology to the TIMER sample to better understand when bars formed in nearby galaxies and how galaxies evolve.

TIMER is a high-quality data survey of the central region of 24 nearby galaxies observed using the MUSE-VLT instrument. Among the main goals of the survey, are *i*) estimating the cosmic epoch in which disc galaxies settled, hence formed the bar; and *ii*) test if the downsizing scenario applies to the formation of bars. The sample was selected from the Spitzer Survey of Stellar Structure in Galaxies (S^4G – Sheth et al., 2010) considering several morphological and observable characteristics. From the S^4G, the TIMER survey focuses on massive galaxies ($\sim 10^{10}$ M$\odot$), with prominent bars, and inner structures. Additionally, the selected galaxies are not highly inclined ($i < 60°$) and are observable from the Paranal Observatory – where the VLT is located – that is, DEC $< +25°$. Considering these constraints, the TIMER survey consists of 24 galaxies, with distances within 40 Mpc.

The MUSE-VLT instrument consists of an integral field spectrograph, with a field of view of $1' \times 1'$ and a scale-plate of $0.2''$/spaxel, which corresponds to approximately $90,000$ spectra per pointing. The TIMER observations were carried during Period 97, 2016 from March to October, for $\sim$ 3840s on average on each source, resulting in a high signal-to-noise ratio (SNR) per pixel (typically above 100 at the centre). The average sky resolution is $0.8' - 0.9'$ and the data was reduced using the MUSE pipeline (version 1.6). For more details on the survey and data reduction analysis, we refer to Gadotti et al. (2019).

We consider kinematic properties of the TIMER galaxies as derived in Gadotti et al. (2020)) to select the ones with a distinguishable nuclear disc kinematic radius (R_{kin}). R_{kin} is the galactocentric distance in which V/σ peaks and, although it does not necessarily delimit a sharp end of the nuclear disc, it can be considered a characteristic dynamical radius. Additionally, we considered the stellar population properties (age, metallicity and alpha abundance) and star formation rate map morphology from Bittner et al. (2020) that classified the TIMER nuclear discs between star-forming (SF), non-star-forming (NSF), and peculiar (P). Finally, we also included the galaxies from Chapter 3, NGC 289 and NGC 1566. With that, the final sample considered in this Chapter consists of 20 galaxies that are listed in Table 4.1, together with key properties.

Table 4.1: **Sample of galaxies used in this Chapter**. The columns are (1) the object designation, (2) the morphological/structural type according to Buta et al. (2015), (3) the median distance from NASA Extragalactic Database (NED), (4) the inclination with respect to the plane of the sky, (5) the stellar mass from the S^{4}G survey (Sheth et al., 2010), considering observations in the 3.6μm, (6) the HI mass (Gadotti et al., 2019), (7) the semi-major axis considering the S^{4}G 25.5 AB mag arcsec^{-2} isophote at 3.6μm, (8) R_{kin} from Gadotti et al. (2020), (9) the R_{ND} radius determined in this Chapter, and (10) the bar length (Kim et al., 2014; Herrera-Endoqui et al., 2015).

Galaxy	Type	dist	inc	M$\star$	M_{HI}	$R_{25.5}$	R_{kin}	R_{ND}	R_{bar}
		(Mpc)	(deg)	(10^{10} M$_\odot$)	(10^{10} M$_\odot$)	(Kpc)	(Kpc)	(Kpc)	(Kpc)
(1)	(2)	(3)	(4)	(5)	(6)	(7)	(8)	(9)	(10)
Non-star-forming									
IC 1438	R_1SAB$_a$(r´1,nl)0/a	33.8	24	3.1	0.12	12.7	0.60	0.820	4.43
NGC 1300	(R)SB(s,bl,nrl)b	18.0	26	3.8	0.22	17.9	0.33	0.520	6.70
NGC 1433	(R´$_1$)SB(r,p,nrl,nb)a	10.0	34	2.0	0.07	12.7	0.38	0.440	3.63
NGC 4371	(L)SB$_a$(r,bl,nr)0$^{0/+}$	16.8	59	3.2	0.08	15.2	0.95	1.009	5.2
NGC 4643	(L)SB(rs,bl,nl)0$^{0/+}$	25.7	44	10.7	0.03	20.5	0.50	0.620	7.3
NGC 5248	(R´)SAB(s,nr)bc	16.9	41	4.7	0.40	17.3	0.49	0.820	1.4
NGC 5850	(R´)SB(r,bl,nr,nb)ab	23.1	39	6.0	0.11	20.8	0.80	1.000	7.84
NGC 7140	(R´)SAB$_x$(rs,nrl)ab	37.4	51	5.1	1.29	25.8	0.63	0.980	11.16
NGC 7755	(R´)SAB(rs,nrl)bc	31.5	52	4.0	0.65	11.0	0.47	0.760	3.5
Star-forming									
NGC 613	SB(rs,bl,nr)b	25.1	39	12.2	0.47	23.4	0.59	0.830	9.72
NGC 1097	(R´)SB(rs,bl,nr)ab pec	20.0	51	17.4	0.91	35.1	1.07	1.360	10.40
NGC 3351	(R´)SB(r,bl,nr)a	10.1	42	3.1	0.09	12.4	0.24	0.390	4.02
NGC 4303	SAB(rs,nl)bc	16.5	34	7.2	0.45	18.1	0.21	0.400	3.52
NGC 4981	SAB(s,nl)bc	24.7	54	2.8	0.35	13.5	0.14	0.480	2.7
NGC 4984	(R´R)SAB$_a$(l,bl,nl)0/a	21.3	53	4.9	0.03	19.0	0.49	0.765	6.18
NGC 5236	SAB(s,nr)c	7.0	21	10.9	1.95	19.3	0.37	0.475	4.4
NGC 7552	(R´$_1$)SB(rs,bl,nr)a	17.1	14	3.3	0.21	21.4	0.33	0.500	4.90
Peculiar									
NGC 5728	(R_1)SB(r´1,bl,nr,nb)0/a	30.6	44	7.1	0.19	20.5	0.63	1.190	9.7
Chapter 3									
NGC 289	(R´,R´L)SAB(rs,rs)ab	18.4	43	4.0	–	11.0	–	0.090	18.4
NGC 1566	(R´$_1$)SAB(rs,rs)b	7.3	32	3.8	–	9.3	–	0.077	1.4

4.2 A complementary approach on deriving bar ages

Since the current methodology described in Chapter 2 demands a considerable computational time – especially on shifting and convolving the spaxel-by-spaxel spectra – and our goal in this Chapter is to derive the bar ages for a larger sample, we decided to test a complementary approach to derive bar ages, keeping the same strategy: we use a representative ring to model the main disc and subtract it from the original data. The difference lies in the fact that instead of working with spectra – which demands convolving, shifting, and normalizing (described in detail in Chapter 2) –, we work with the star formation histories. In other words, we derive the SFHs spaxel-by-spaxel for the original data cube and proceed with disentangling the nuclear disc from the main underlying disc directly on the SFHs, instead of applying this process on the spectra.

First, we run GIST as described in Section 2.2.2 for the entire original MUSE datacube (for details on configuration, see Sections 2.2.2 and 3.2.2). Considering the different regularization errors presented for NGC 1433 (Section 2.3.1, Fig. 2.13) and how it does not affect the final result drastically, we proceeded to apply a regularization error of 0.45 for all galaxies. With the light-weighted results and considering the mass-to-light ratios predicted from BaSTI isochrones[2] (Pietrinferni et al., 2004, 2006, 2009, 2013), we derive mass-weighted SFHs spaxel-by-spaxel. Second, we select the regions of the nuclear disc and the representative ring, masking AGN-dominated spaxels. Third, to model the main disc SFHs spaxel-by-spaxel, we consider the mea SFHs from the representative ring and extrapolate it to the nuclear disc region exponentially, considering the disc scale-length from Salo et al. (2015) and the galactocentric distance. After building normalised, spatially-distributed SFHs for the main disc within the nuclear disc region, we subtract them from the original ones, deriving the nuclear disc clea SFHs spaxel-by-spaxel. Finally, we measure the mea SFH of each of the components – MUSE original, main disc, and nuclear disc. To derive the bar age, we consider the same criterion as described in Section 2.2.2, that is, the bar age corresponds to the first time that the ratio ND_{SFH}/MD_{SFH} is above 1 towards younger ages. We will refer to this new approach from now on as the *SFH-based approach*, and an illustration of it can be seen in Fig. 4.1.

We tested the SFH-based approach for the 3 galaxies from Chapters 2 and 3: NGC 1433, NGC 1566, and NGC 289. The comparisons between approaches are in Fig. 4.2 and, as can be seen, both result in similar bar ages for three galaxies – considering the measurement errors. To ensure consistency, we repeated the same configurations of nuclear disc size, representative ring position and width, exponential profile modelling for the main disc, and central masking. The only difference in configuration for the new approach was for NGC 1566, in which the AGN-dominated spaxels were not masked. This decision was made because, otherwise, it would not be possible to derive any bar age with the SFH-approach. Additionally, we consider NGC 1566 an extreme case with the smallest nuclear

[2]http://research.iac.es/proyecto/miles/pages/predicted-masses-and-photometric-observables-based-on-photometric-libraries.php

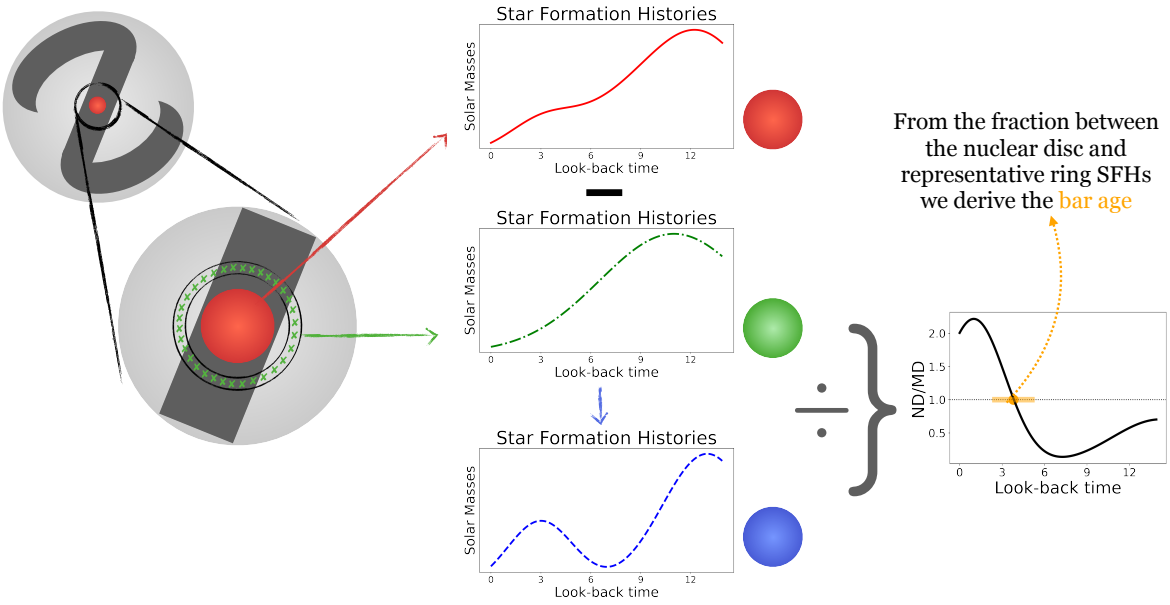

Figure 4.1: Illustration analogous to Fig. 2.2, for the SFH-based approach described in Section 4.2.

disc ever detected, which is not the case for most of the TIMER galaxies. In light of that, we decided to proceed applying the SFH-based approach for the rest of the TIMER sample.

Applying the SFH-based approach to derive bar ages has a clear advantage on computational time: each run lasts about a day instead of about a week. This is mainly because convolving/shifting the spaxel-by-spaxel spectra and collapsing the data cubes into mean spectra, demands computational time. On the other hand, we are not able to derive the statistical errors using Monte Carlo runs, since they are performed in the spectra phase considering observational noise (see Chapter 2 for more details). In light of that, we decided to consider the roughly estimated error of ± 1.5 Gyr based on the statistical and systematic errors from Chapters 2 and 3 and plan to better assess our measurement errors in the future.

Additionally, for all the galaxies in the sample, we determined a new nuclear disc size (Table 4.1, column 9). R_{kin} is a characteristic radius, dynamically motivated. However, in many cases it is possible to notice star-forming rings that belong to the nuclear disc but are placed outside of R_{kin}. Because of that, we visually estimated a new nuclear disc size, R_{ND}, based on the SFR and mean age maps. The R_{ND} is usually larger than R_{kin} and, as can be seen in Appendix A, also enclosures the star-forming rings. Nevertheless, we applied the SFH-based methodology considering both radii to assess if this affects our final result drastically, and found similar bar ages. Finally, we placed the representative ring $2''$ away from the nuclear disc, considering a ring with $2''$ width, and consider an exponential profile for the main disc, for all galaxies. This is close to the approaches in Chapters 2

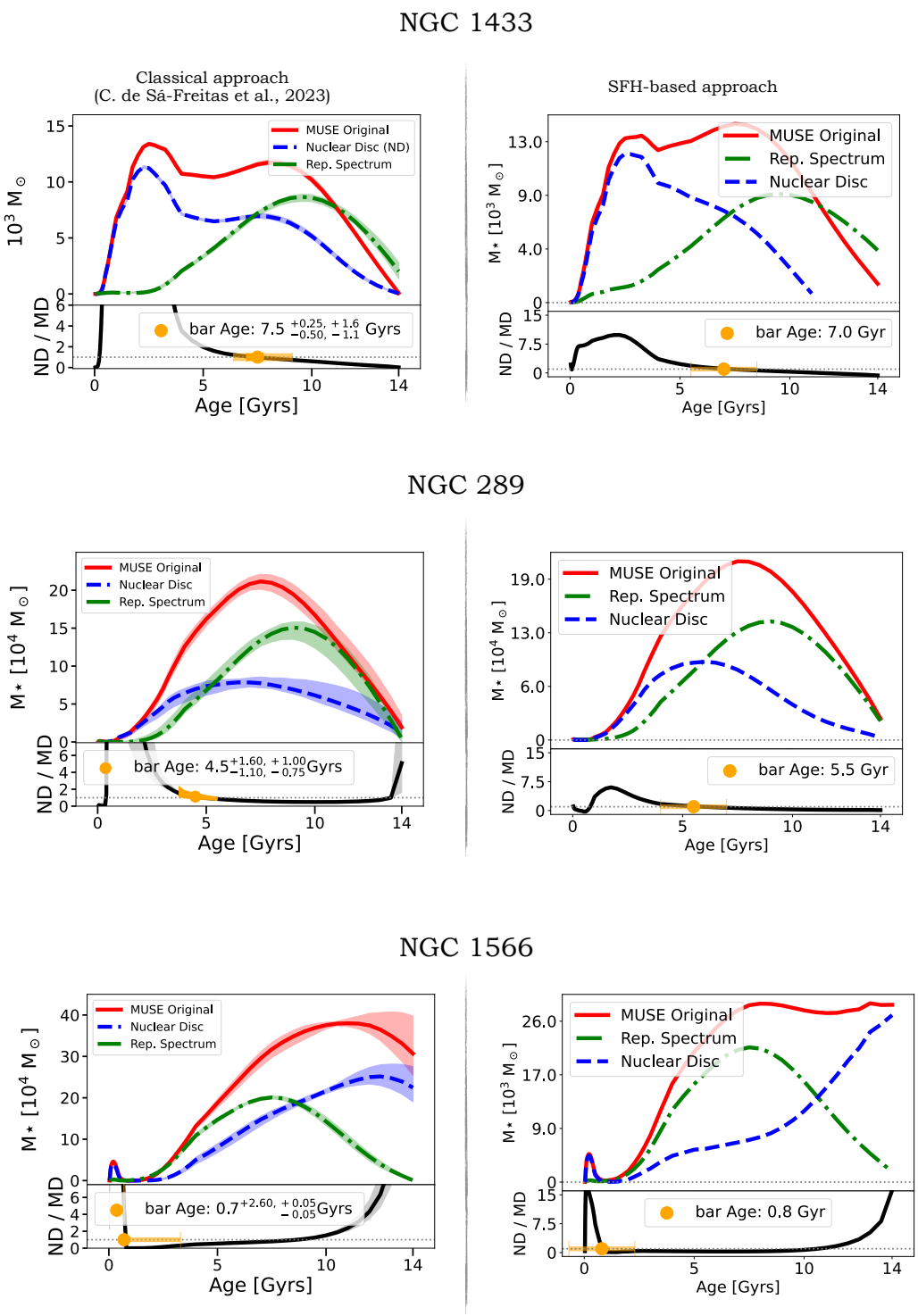

Figure 4.2: Comparison between the classical approach to determine bar ages (as developed in Chapter 2), and the SFH-based approach, described in this Chapter, for galaxies from Chapters 2 and 3 – NGC 1433, NGC 289, and NGC 1566. Most of the configurations were kept the same: the nuclear disc radius, the galactocentric distance and the width of the representative ring, the exponential modelling of the main disc, and the central masked regions. For NGC 1566, the AGN-dominated spaxels were not masked. Considering the measurement errors, both approaches result in consistent bar ages.

and 3, except in the fixed distance of the representative ring. In Chapter 2, we considered the minimum in the V/σ profile, while in Chapter 3, we used a fixed distance of $1.2''$. Nevertheless, considering the tests performed in Chapter 2, varying the position of the representative ring does not affect the final bar age significantly.

4.3 Results

4.3.1 Derived bar ages

We applied the SFH-based approach described in Section 4.2 to all TIMER galaxies that had a discernible nuclear disc size, listed in Table 4.1. The individual results can be found in Appendix A and are listed in Table 4.2. From all the listed galaxies, the only one we were not able to derive a bar age for was NGC 4981, in which the criterion was never met (see results in Appendix A). However, this galaxy is a complex case since its data has the lowest resolution in the sample and the smallest nuclear disc derived in Gadotti et al. (2020). Nevertheless, we successfully derived bar ages for the remaining 17 galaxies, finding a wide range of formation epochs between $1.0 - 12.5$ Gyr (Fig. 4.4). Considering the nuclear disc classification from Bittner et al. (2020), we notice that the SF nuclear discs are hosted by younger bars, with ages varying between $1 - 6$ Gyr, whereas the NSF nuclear discs are hosted by a wide range of different bars, with a majority of bars with ages greater than 6.0 Gyr.

For each galaxy, we provide individual results, such as Fig. 4.3, in Appendix A. We display, in the top panel, the spatial maps of V/σ, mean light-weighted stellar age, and star formation rate (SFR). Additionally, we show the contours we considered in this chapter, that is, R_{kin} (Gadotti et al., 2020), R_{ND}, and the position of the representative ring. Lastly, we mask in the SFR map the regions that are AGN dominated, accordingly to the BPT classification (Baldwin et al., 1981). In the middle panel, we display the mea SFH of the original data, the main disc, and the clean nuclear disc (after the subtraction), together with the ratio ND/MD and the bar age. We display the mean SFH of the clean nuclear disc, the mean stellar ages, and the median of the mean stellar ages, colour-coded for different radii. Lastly, in the bottom panel, we show the radial fraction of mass for different age bins for the original data and the clean nuclear disc. Following, we will summarize the individual results for each galaxy, highlighting the interesting features. These results are shown in the figures in the Appendix A. Finally, for each galaxy, we used the NED cone search tool[3] to search for possible interacting galaxies. We considered the sky distribution of galaxies within $10'$ and with close redshift values, and we highlight the galaxies in which we find candidates of companions.

IC 1438 – IC 1438 has a NSF nuclear disc with a nuclear/inner bar (TIMER collaboration, in prep.), that is, the nuclear disc developed a bar that has similar properties

[3]https://ned.ipac.caltech.edu/conesearch

Table 4.2: We summarize the main results of this Chapter together with different galaxy and bar properties. The columns are (1) the object designation, (2) the derived bar age following the SFH-based approach, described in Section 4.2, (3) and (4) the values of A_2 and Q_B derived in Díaz-García et al. (2016), while (5), (6), and (7) are the Bulge/Tot, Disc/Tot, and Bar/Tot fractions derived from Salo et al. (2015), respectively. We separate the sample between *Non-star-forming*, *Star-forming*, and *Peculiar*, following the classification of Bittner et al. (2020), and added the results from Chapter 3 on NGC 289 and NGC 1566.

Galaxy	**Bar age**	**A_2**	**Q_B**	**Bulge/Tot**	**Disc/Tot**	**Bar/Tot**
(1)	(2)	(3)	(4)	(5)	(6)	(7)
Non-star-forming						
IC 1438	10.00	0.838	0.178	0.288	0.521	0.191
NGC 1300	8.00	0.603	0.580	0.073	0.562	0.198
NGC 1433	9.00	0.560	0.366	0.140	0.746	0.114
NGC 4371	11.00	0.618	0.234	0.234	0.617	0.148
NGC 4643	12.50	0.813	0.272	0.253	0.534	0.214
NGC 5248	2.75	0.324	0.138	0.206	0.795	0.000
NGC 5850	12.50	0.742	0.327	0.188	0.678	0.134
NGC 7140	5.50	0.805	0.399	0.142	0.789	0.069
NGC 7755	5.00	0.841	0.401	0.161	0.761	0.078
Star-forming						
NGC 613	3.50	0.903	0.489	0.130	0.746	0.124
NGC 1097	3.75	0.709	0.254	0.240	0.562	0.198
NGC 3351	5.00	0.513	0.227	0.147	0.755	0.098
NGC 4303	4.50	0.550	0.535	0.091	0.909	0.000
NGC 4981	–	0.093	–	0.118	0.882	0.000
NGC 4984	3.75	0.836	0.176	0.382	0.372	0.246
NGC 5236	3.50	0.467	0.472	0.080	0.872	0.048
NGC 7552	1.00	1.060	0.358	0.339	0.378	0.283
Peculiar						
NGC 5728	10.00	1.149	0.387	0.263	0.389	0.348
Chapter 3						
NGC 289	4.50	–	–	0.044	0.651	0.305
NGC 1566	0.70	–	–	0.017	0.918	0.064

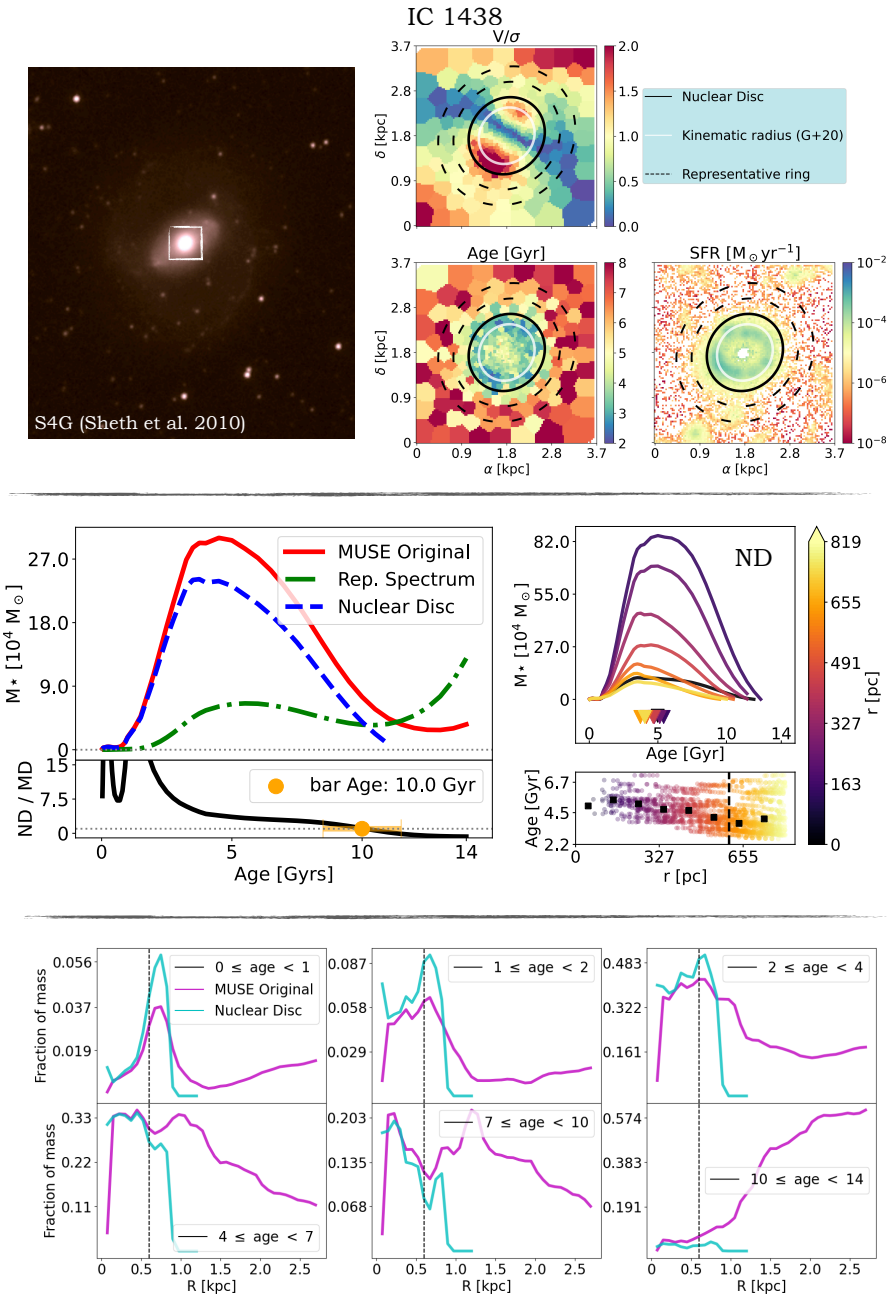

Figure 4.3: Individual results for IC 1438. **Top row**: in the left, we show the S^{4}G image of the galaxy, with the region of the nuclear disc for which we show spatial properties (on the right). The properties we show are the V/σ, the mean light-weighted stellar age, and the SFR map, masked for AGN-dominated spaxels. We also show the contours for R_{kin} (white-solid contours), the R_{ND} (black-solid contours), and the representative ring (black-dashed contours). **Middle row:** main results from our analysis: in the left, we show the SFHs for the original data within the nuclear disc region, the modelled main disc, and the clean nuclear disc (after subtraction), together with ND/MD and the derived bar age; in the right, we show the mean nuclear disc SFHs colour-coded for radius, together with the radial profile of the mean age. **Bottom row:** radial fraction of mass for different age bins, both for the original data (magenta) and the clean nuclear disc data (cyan), the dotted line marks R_{kin}.

and evolution of main disc bars (de Lorenzo-Cáceres et al., 2019; Bittner et al., 2021).

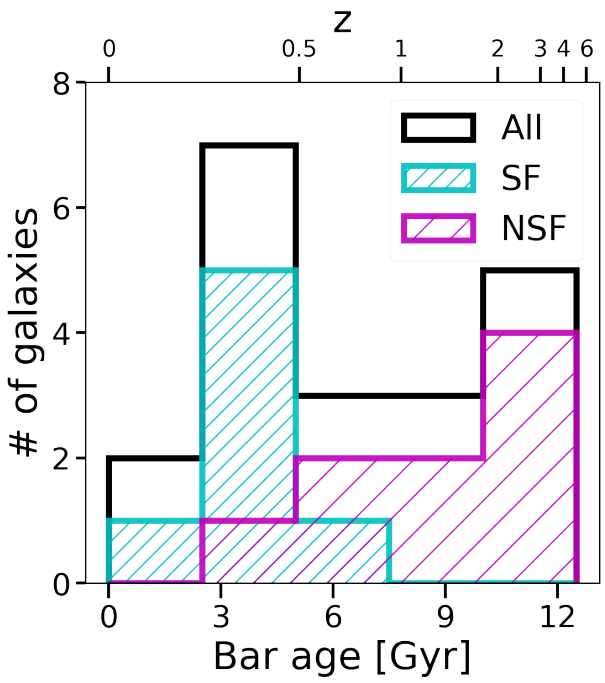

Figure 4.4: Bar age distribution for all galaxies listed in Table 4.2 (black contour), for the SF (cyan double-hatched contour), and NSF (magenta hatched contour) sub-samples. As can be seen, we find bars with a large range of ages ($1 - 12.5$ Gyr). Furthermore, SF nuclear discs are mainly hosted by younger bars, whereas NSF nuclear discs are mainly hosted by bars with ages greater than 6.0 Gyr.

The individual results of this galaxy are shown in Fig. 4.3. From the spatial maps, it is clear that R_{kin} (white contour) falls on the V/σ maximum (Gadotti et al., 2020), defining a region of younger stars, and higher SFR than the surroundings. It is also clear that the radius considered in this Chapter (R_{ND} – black contour) encloses the ring of slightly higher SFR. This is the case for most galaxies of our sample. Additionally, the representative ring region is not affected by the SFR of the nuclear disc itself. Following, in the middle panel we can see the SFHs of this galaxy (original MUSE, main disc, and nuclear disc), and the bar age of 10.0 ± 1.5 Gyr. Considering the radial nuclear disc clean results (middle-panel, right), this nuclear disc seems to display younger ages towards the border, with the youngest stars close to R_{kin}, as expected for the inside-out growth scenario. Lastly, in the bottom panel, it is noticeable that stellar population with ages between $2 - 4$ and $4 - 7$ Gyr dominate the mass of the nuclear disc region, comprising about 80% of the total mass in the nuclear disc. In addition, young stars ($0 - 1$ and $1 - 2$ Gyr) are mainly located close to R_{kin}, just outside of it.

NGC 613 – NGC 613 hosts a SF nuclear disc, which is noticeable from the SFR map in Fig. A.1. Considering the mean stellar age spatial map, there is a small region with an older stellar population. Analyzing the dust distribution of this galaxy, this is expected to be an artificial result due to extinction and further improvements on this matter will be performed in the future. In the middle panel, we can see our main results, with the bar age of 3.75 ± 1.50 Gyr. In this case, there seems to be a contamination of older stars in the clean nuclear disc. This can be due to the presence of dust, which can artificially age some stellar populations, or since the representative ring is not as old as the underlying main disc, as discussed in Chapter 2. Additionally, the inside-out growth of the nuclear disc is not clear in the radial analysis for the clean nuclear disc. This can either be a real result or because the clean

nuclear disc still holds contamination of older stars. Considering the radial distribution of the fraction of mass, stellar populations of $2-4$, $4-7$, and $7-10$ Gyr seem to dominate the mass budget, while the youngest stars ($0-1$ Gyr) are either in the very centre or close to R_{kin}. Finally, the high fraction of mass in age-bins older than the bar suggests that the disentanglement was not perfect, and old stellar populations still contaminate the clean nuclear disc, as expected from the independent SFH result.

NGC 1097 – NGC 1097 (Fig. A.2) is the most massive galaxy of our sample (Table 4.1), which hosts a SF nuclear disc, as noticeable from the SFR map. Additionally, the galaxy has strong LINER emissions (Bittner et al., 2020) that were masked for the analysis. From the middle panel, we find a bar age of 3.75 ± 1.50 Gyr and a clear sign of inside-out formation, that is, the mean stellar population age is younger towards the edges of the nuclear disc. Additionally, stellar populations with ages of $2-4$, $4-7$, and $7-10$ Gyr dominate the mass fraction for the nuclear disc, while young stars ($0-1$ and $1-2$ Gyr) are mainly concentrated close to R_{kin}. Furthermore, age bins older than the bar still holds high fractions of mass in the clean nuclear disc, suggesting that the disentanglement was not perfect, as expected from the independent SFH result. Lastly, it is interesting to notice that this galaxy has a companion, NGC 1097A, and clear signs of recent interaction, being a strong candidate for tidally-triggered bar formation studies.

NGC 1300 – NGC 1300 (Fig. A.3) has a NSF nuclear disc, with central AGN-dominated spaxels which were masked. We find a bar age of 8.0 ± 1.5 Gyr and clear signs of inside-out formation. Lastly, the mass in the nuclear disc is dominated by stellar populations with $2-4$, $4-7$, and $7-10$ Gyr, with different gradients. Additionally, the young stars ($0-1$ and $1-2$) are mainly close to R_{kin}, just outside of it.

NGC 1433 – The analysis presented here for NGC 1433 (Fig. A.4) has some differences from Chapter 2. Since this galaxy hosts a nuclear/inner bar (Erwin, 2004; Buta et al., 2015; Bittner et al., 2021), we decided not to mask the central region of it, as opposed to what was done in de Sá-Freitas et al. (2023). Because of that, we find a bar slightly older in this analysis, with an age of 9.0 ± 1.5 Gyr, but still consistent with the previous results, considering the corresponding uncertainties. In addition, the inside-out formation previously reported is still clear. Lastly, the mass in the nuclear disc is mainly composed of stars with ages between $2-4$, $4-7$, and $7-10$ Gyr, with different radial distributions for each group, whereas the young stars are concentrated close to R_{kin}.

NGC 3351 – NGC 3351 (Fig. A.5) is classified as a SF nuclear disc by Bittner et al. (2020), although we do not find strong SFR in our results. We find a bar age of 5.0 ± 1.5 Gyr and a clear sign of inside-out formation. Lastly, the mass budget in the nuclear disc is dominated by a stellar population with ages between $2-4$ and $4-7$ Gyr, with different radial distributions for each group. Additionally, the young stellar populations ($0-1$ and $1-2$ Gyr) are concentrated just outside R_{kin}.

NGC 4303 – NGC 4303 (Fig. A.6) hosts a SF nuclear disc, which is one of the

smallest of the TIMER sample, with $R_{kin} = 210$ pc. We find a bar age of 4.5 ± 1.5 Gyr and no sign of inside-out formation, where the stars across the entire nuclear disc are young. Differently from the others, the mass budget is dominated by young stars, with ages between $1 - 2$ and $2 - 4$ Gyr, about 80% of the nuclear disc mass. Additionally, the youngest starts ($0-1$ Gyr) are located just outside R_{kin}. Lastly, we found two galaxies with redshift differences of 0.000171 and 0.00024 from NGC 4303: SDSS J122154.85+042911.3 and SDSS J122147.59+042938.4, respectively.

NGC 4371 – NGC 4371 (Fig. A.7) is the prof of concept galaxy used in Gadotti et al. (2015), in which the authors derived a minimum bar age of 10.0 Gyr. Since this galaxy has a high-dispersion region in its centre, we decided to mask the central region of $8''$, considering it can be another structure with an independent stellar population (further discussion on this matter can be seen in Section 4.3.1). Because of that, the bar age we derived of 11.0 ± 1.5 Gyr is also considered as a lower limit, but remarkably in agreement with Gadotti et al. (2015). In addition, we find no sign of inside-out formation, given that all stars are very old (ages ≥ 9 Gyr). Lastly, younger stars ($0 - 1$, $1 - 2$, $2 - 4$, and $4 - 7$ Gyr) represent less than 10% of the mass in the nuclear disc.

NGC 4643 – NGC 4643 (Fig. A.8) also has a high-dispersion region in its center ($3''$), which was masked. We find a lower limit for the bar age of 12.5 ± 1.5 Gyr, which is one of the oldest bars in our sample. We find no inside-out formation sign, with all stars older than 8 Gyr, and the fraction of mass is dominated by stellar populations with ages between $10 - 14$ Gyr.

NGC 4981 – As mentioned, we find no bar age for NGC 4981 (Fig. A.9). It is clear from the spatial maps that the resolution for this galaxy is very low, where the Voronoi bins (Cappellari, 2012) are the largest in our sample. Nevertheless, there is a weak sign of inside-out formation for this nuclear disc.

NGC 4984 – We find for the bar an age of 3.75 ± 1.5 Gyr hosted by NGC 4984 (Fig. A.10), which has a SF nuclear disc. For this galaxy, it is clear that the criterion of ND/MD > 1 towards younger ages happens twice. Considering the first crossing happens for ages older than the ones in the MD, and the fact that this galaxy has a lot of dust, we interpreted this older crossing as spurious, considering also it is less significant than the younger crossing. Further analysis and improvement in this case (and others that are similar) are planned for the future. We find a tentative sign of inside-out formation for the clean nuclear disc data, but since there is contamination from older stellar populations, it is not trivial to derive the mean ages. Lastly, the mass budget in the nuclear disc is dominated by stars with ages between $1 - 2$, $2 - 4$, and $4 - 7$ Gyrs.

NGC 5236 – As NGC 4984, NGC 5236 (Fig. A.11) also has two crossing points and is very affected by dust, as can be seen in the mean age spatial map with older stellar populations. For the same reason presented before, we considered the bar age for this galaxy to be 3.5 ± 1.5 Gyr, and improvements in the analysis, especially due to dust

effects, will happen in the future. Additionally, the inside-out formation of this nuclear disc is not as clear, but this can be due to the old stellar population contamination in the nuclear disc SFH. Lastly, the stellar populations that dominate the mass of the nuclear disc are between $2-4$ and $4-7$ Gyr, around 60% of the nuclear disc mass.

NGC 5248 – NGC 5248 (Fig. A.12) is classified as a NSF nuclear disc (Bittner et al., 2020), although in our results it does have a considerable SFR. This galaxy is another case with two crossing points (along with NGC 4984 and NGC 5236), and it is also obscured by dust. For the same argument, we discard the oldest crossing time because it is older than the stellar population of the main disc and can be due to contamination. Additionally, the nuclear disc does seem to have an inside-out growth, although the relation between mean age and radius is not as strong; this can be due to the old stellar population contamination in the nuclear disc SFH. Lastly, stars between $2-4$ Gyr dominate the mass of the nuclear disc, and young stars ($0-1$ and $1-2$ Gyr) are around R_{kin}.

NGC 5728 – NGC 5728 (Fig. A.13) is considered a peculiar nuclear disc (Bittner et al., 2020), mainly because of the strong AGN outflows, which reflects on the high number of spaxels masked in our SFR spatial map. We find a bar age of 10.0 ± 1.5 Gyr, and not a strong sign of inside-out formation of the nuclear disc. Finally, the stellar population that dominates in the nuclear disc regions have ages between $4-7$ and $7-10$ Gyr. Additionally, the youngest stars ($0-1$ Gyr) are concentrated close to R_{kin}. Lastly, there is evidence that NGC 5728 has a nuclear/inner bar (TIMER, in prep.).

NGC 5850 – NGC 5850 (Fig. A.14) hosts a NSF nuclear disc and has an interacting candidate, NGC 5846. Together with NGC 4643, this is one of the oldest bars we find in our sample, with an age of 12.5 ± 1.5 Gyr. Additionally, the inside-out growth is very clear for this galaxy. The young stars with ages between $0-1$ and $1-2$ Gyr represent less than 2% of the mass in the nuclear disc, and the stellar populations with higher fractions of the mass have ages between $4-7$ and $7-10$ Gyr. Lastly, this nuclear disc is reported to host a nuclear/inner bar (e.g., de Lorenzo-Cáceres et al., 2019).

NGC 7140 – NGC 7140 (Fig. A.15) is a NSF nuclear disc with a bar age of 5.5 ± 1.5 Gyr, with no strong indications of inside-out formation. Finally, the stellar population that dominates the mass in the nuclear disc has ages between $2-4$, $4-7$, and $7-10$ Gyr.

NGC 7552 – NGC 7552 (Fig. A.16) is another case with two crossing points and is heavily obscured by dust, as can be noticed as older stellar mean ages in the spatial maps. For the same reasons mentioned before, we considered the oldest crossing point as contamination, either by dust or because the representative ring SFH might not be as old as the real main disc's oldest stellar population. Interestingly, as opposed to all galaxies presented so far, this galaxy has an inverse age radial profile, that is, the oldest stars are on the border of the nuclear disc. This can be a real result or a consequence of the strong obscuring. Lastly, the stars that dominate the mass of this nuclear disc have ages between $0-1$ and $2-4$ Gyr.

Galaxy	Bar age – lower limit	Bar age	Inner/nuclear bar
(1)	(2)	(3)	(4)
IC 1438	–	10.0	Y
NGC 1097	3.75	3.75	N
NGC 1433	–	9.0	Y
NGC 4371	11.0	–	N
NGC 4643	12.5	–	N
NGC 4894	3.25	3.75	N
NGC 5728	–	10.0	Y
NGC 5850	–	12.5	Y
NGC 7755	5.0	11.0	N

Table 4.3: **Multiple nuclear components**. We summarize our analysis for the 9 galaxies which are candidates for having a small classical bulge. The columns are: (1) the galaxy designation; (2) the lower limit measured for bar age; (3) the bar age considering the entire nuclear disc region; (4) the galaxies that possibly host an inner/nuclear bar.

NGC 7755 – The last galaxy of our sample, NGC 7755 (Fig. A.17) is a NSF nuclear disc that has a high-dispersion velocity region in the centre $2''$, which was masked. Due to that, the derived bar age of 5.0 ± 1.5 Gyr, will be considered a lower limit. It is not possible to conclude about inside-out formation, because of the center masking. Finally, the mass is dominated by stellar populations with ages between $2 - 4$ and $4 - 7$ Gyr.

Multiple nuclear components

Although it was reported by the TIMER collaboration an absence of large classical bulges, with high stellar-velocity dispersion in their sample (Bittner et al., 2020), other structures may be present in the centre of the galaxies, co-existing with the nuclear disc. As demonstrated by Erwin et al. (2015), some galaxies can have a smaller classical-bulge, embedded inside the nuclear disc. In this case, the centre of the nuclear disc shows a dispersion-dominated, separate structure. This second structure, if present in our sample, is not accounted for by our methodology, hence, it can contaminate the clean nuclear disc SFH. Furthermore, depending on the formation scenario of this small classical bulge, the stellar populations and SFH might be completely different and not accounted for in the modelled main disc. On the other hand, substructures of the nuclear disc, such as inner/nuclear bars, can also increase the velocity-dispersion, although they are part of the evolution history of the nuclear disc itself. Due to that, one cannot simply mask regions of higher velocity-dispersion assuming it to be an independent structure, and a detailed stellar population diagnosis should be performed.

In our sample of 20 galaxies, 9 displayed a central region with high velocity dispersion; they are IC 1438, NGC 1097, NGC 1433, NGC 4371, NGC 4643, NGC 4984, NGC 5728, NGC 5850, and NGC 7755 (see Table 4.3). Since constructing a detailed diagnosis of substructures is beyond the scope of this work, we decided whether to mask or not these regions case by case. Specially, the decision relied on how much the final bar age was affected. Between these 9 galaxies, 4 have inner/nuclear bars, which are also expected to increase the velocity dispersion; these are IC 1438, NGC 1433, NGC 5728, and NGC 5850. These 4 galaxies did not have the central region masked since, as explained, the inner/nuclear bar is expected to be part of the nuclear disc evolution and share the same SFH. For the rest, we derive two bar ages: centrally masked (lower limit) or not, listed in Table 4.3. Among the 5 remaining galaxies, our results do not vary significantly depending if we mask the centre or not for NGC 1097 and NGC 4984, hence we decided not to mask the central region. For NGC 4371 and NGC 4643, on the other hand, we cannot derive bar ages in the configuration where we do not mask the central region. For that reason, these two galaxies only have lower limit bar ages. Lastly, for NGC 7755, the bar age varies greatly depending if we mask the centre or not ($5 - 11$ Gyr). Because of that, we decided to mask the high velocity dispersion of this galaxy and derive only a lower limit age for this galaxy, since the central region might be occupied by an independent structure. Summarizing, 3 galaxies of our sample have as a final result a lower limit for the bar age; these are NGC 4371, NGC 4643, and NGC 7755.

4.3.2 Dependence of galaxy properties on bar ages

With the preliminary individual results reported in Section 4.3.1, we can, for the first time, investigate how different galaxy properties relate to bar ages, and thus, presumably, how these properties are affected by physical processes connected to bar-driven evolution.

In Fig. 4.5, we investigate how the bar length (Kim et al., 2014; Herrera-Endoqui et al., 2015 – top panel) and the nuclear disc size (bottom panel) correlate to the size of the host galaxy ($R_{25.5}$), separating our analysis between the SF and NSF nuclear discs. For the size of the galaxy, we consider the semi-major axis of the 25.5 mag arc^{-2} isophote, measured in S^{4}G 3.6 μm band (Sheth et al., 2010). We also include the Milky Way and galaxies from Chapter 3. As one can see, the bar length has a strong correlation with the size of the host galaxy. This is reinforced by the Pearson correlation coefficient value of $r = 0.811$ and is statistically confirmed by the value of $p - value < 0.005$. This correlation stands for both sub-samples of SF and NSF nuclear discs, with $p - value - 0.019$ and 0.007, respectively. We performed a similar analysis for the nuclear discs (bottom panel). When it comes to the entire sample (left panel), there is a clear relation between the size of the nuclear disc and the host galaxy, with $r = 0.636$ and $p - value = 0.003$. Considering the SF sample (middle panel), this correlation is stronger, with a remarkable $r = 0.932$ and $p - value = 0.002$. On the other hand, the correlation disappears for the NSF sample, with $r = 0.198$ and $p - value = 0.609$, which indicates that the correlation coefficient is not statistically significant and no conclusions can be made.

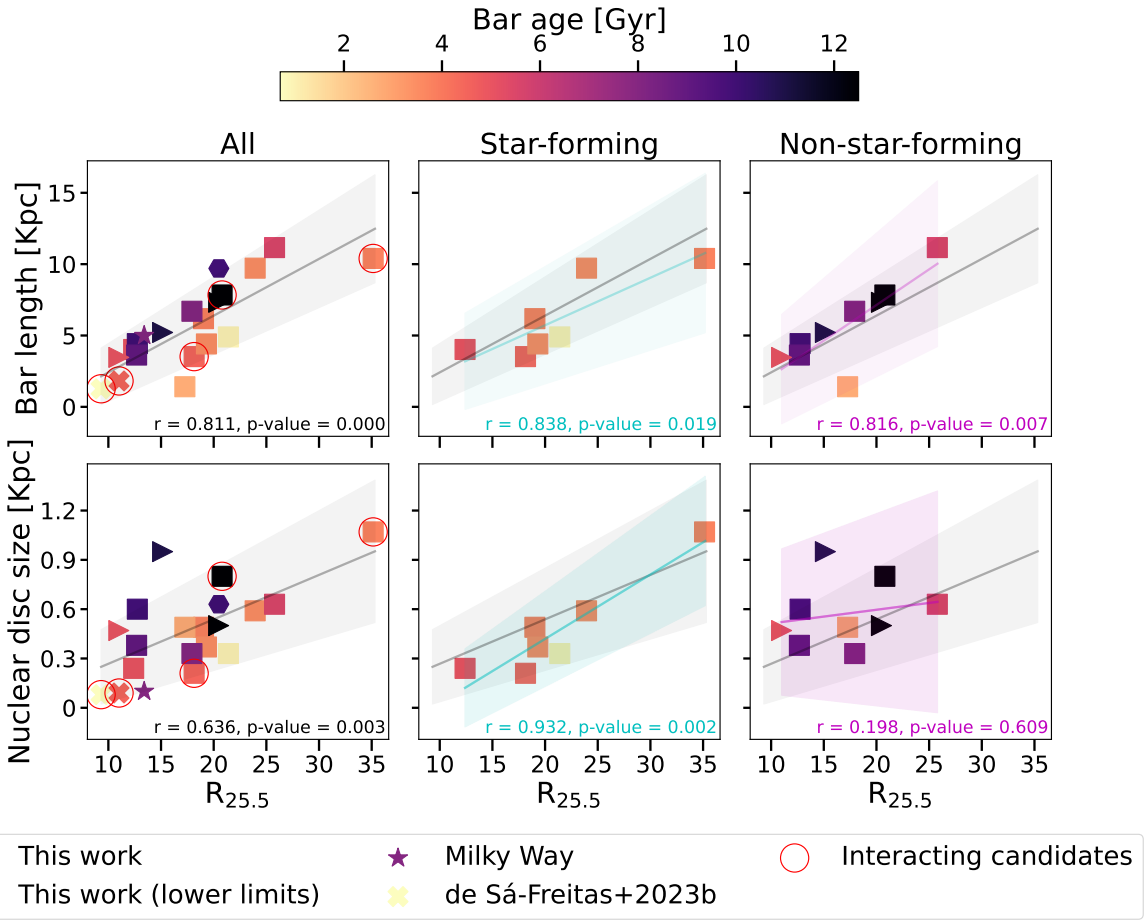

Figure 4.5: Relations between bar length (**top row**) and nuclear disc size (**bottom row**) with the size of the galaxy ($R_{25.5}$), which is the semi-major axis of the outer 25.5 AB mag.arcsec $^{-2}$ isophote from S^{4}G at 3.6μm. We display the complete sample (**left column**), SF (**middle column**), and NSF nuclear discs (**right column**) sub-samples, colour-coded for the derived bar ages, and with corresponding linear fits (solid lines) and $1-\sigma$ intervals (shaded areas). We include galaxies from this work with derived bar ages (squares), with lower limits for bar age (triangles), from Chapter 3 (x's) – NGC 289 and NGC 1566 – and the Milky Way (star). We highlight the galaxies that are possibly interacting in red circles. For all 6 panels, we display the Pearson correlation coefficient and the associated *p-value*. Considering the bar length, we find good correlations with the size of the host galaxy ($r \geq 0.8$), with statistical relevance ($p-value <= 0.05$) independently of the star-formation status of the nuclear disc. On the other hand, considering the nuclear disc size, we find $r \geq 0.6$ and $p-value <= 0.05$ for the entire sample and the SF sub-sample. However, considering the NSF sub-sample, we do not find a correlation between the nuclear disc size and the size of the host galaxy. This indicates that, once there is no gas building up the nuclear disc, its evolution is no longer connected to the bar and the host galaxy.

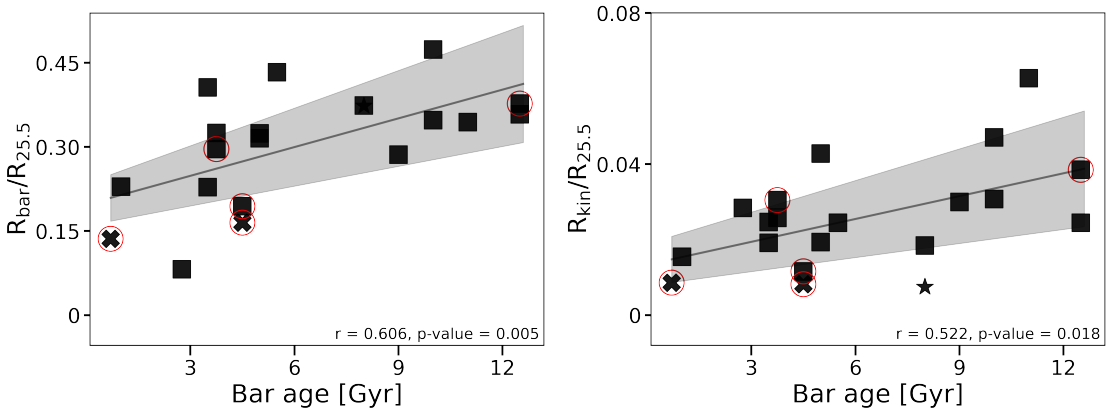

Figure 4.6: We display the relations between normalized bar length ($R_{bar}/R_{25.5}$) and normalized nuclear disc sizes ($R_{ND}/R_{25.5}$) with bar ages. We display the corresponding linear fits (solid black lines) with $1-\sigma$ intervals (shaded gray areas). We included galaxies from this work with bar ages (squares) and lower limits for bar ages (triangle), galaxies from Chapter 3 (x's) – NGC 289 and NGC 1566 – and the Milky Way (star). We highlight the galaxies that are possibly interacting in red circles. We find that, relative to the host galaxy, bar lengths and nuclear disc sizes can grow with time, with r = 0.606 and 0.55, respectively, and $p-values \leq 0.05$ for both cases.

Due to the correlation between the size of the host galaxy with the bar length and the size of the nuclear disc, to investigate the evolution of these structures with the bar age, we consider their normalized size. In other words, the absolute size of the structures might not necessarily reflect an evolution stage. We show in Fig. 4.6 the relations of the normalized bar length (left panel – $R_{bar}/R_{25.5}$) and the normalized nuclear disc size (right – panel $R_{ND}/R_{25.5}$) with respect to the bar age. From this analysis, it is clear that the normalized bar length and nuclear disc size are well correlated to the bar age, with $r = 0.606$ and $r = 0.522$, respectively, and $p-value \leq 0.05$. For the first time, we have an observational indication that these structures, when compared to their host galaxy, can grow with time.

We further investigate how the bar age relates with different galaxy properties such as stellar mass, atomic hydrogen (HI) mass, disc stellar mass, and the light fractions of the disc, bulge, and bar (Disc/Tot, Bulge/Tot, and Bar/Tot), in Fig. 4.7 (see Table 4.1). For the different light fractions, we consider the values derived by Salo et al. (2015), based on photometric models fitting of different components, performed in S^4G images taken in 3.6μ m, which is a good proxy for mass fractions as well. Additionally, we assume as "nuclear disc" what is classified by the authors as "bulge" or "disc 1" – for the cases with two discs in which the first one is the nuclear disc. We display the analysis colour-coded for the SF and NSF sub-samples.

To investigate the downsizing picture, we analyze different properties with respect

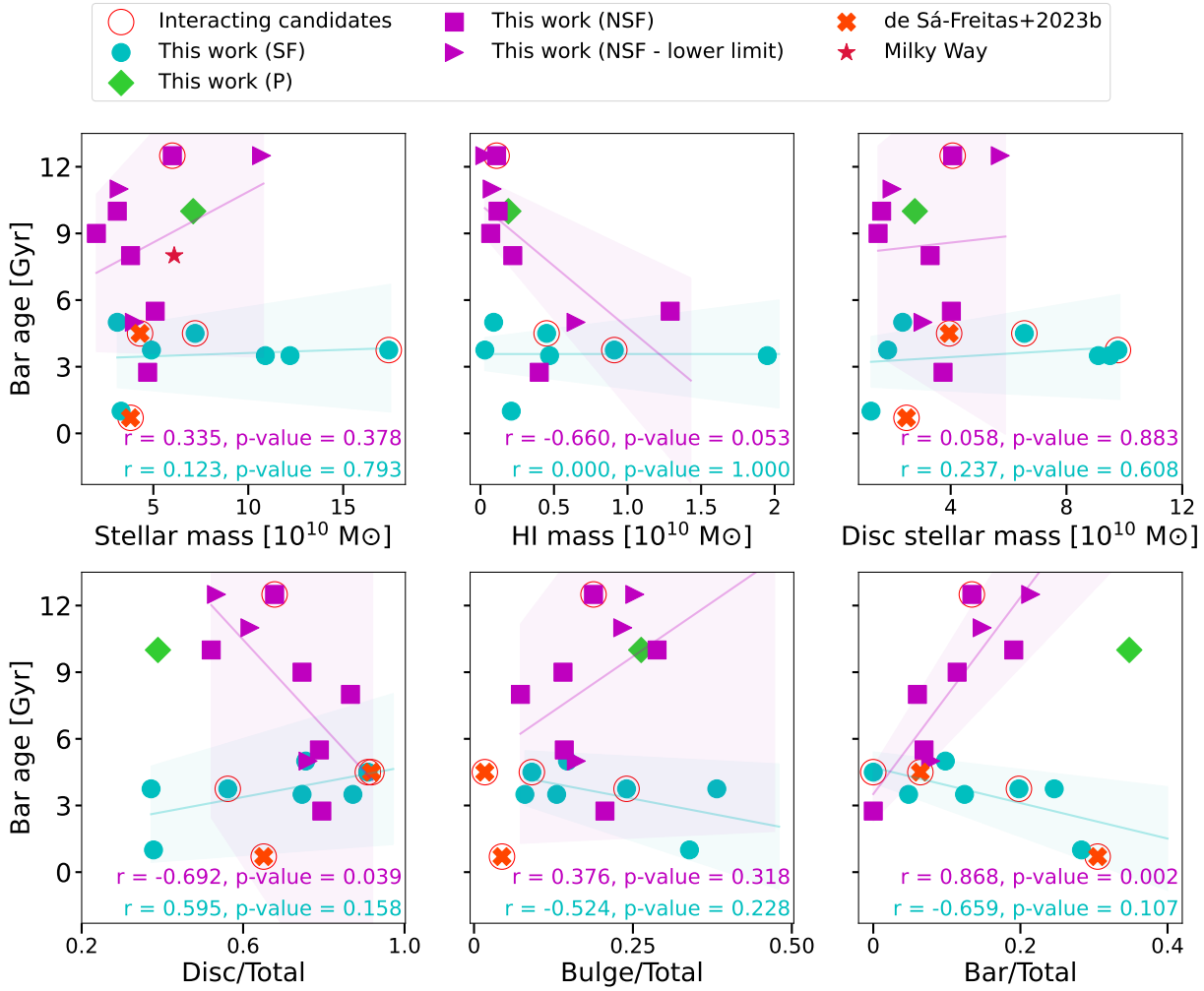

Figure 4.7: We display the bar age dependency with different galaxies properties: stellar mass derived from the S^{4}G 3.6μm images (Sheth et al., 2010 – **top-left**), atomic gas mass derived from the flux absorption at 21-cm (Gadotti et al., 2019 – **top-middle**), disc stellar mass considering the disc/total fraction and the galaxy stellar mass (**top-right**), and the Disc/Total (**bottom-left**), Bulge/Total (**bottom-middle**), and Bar/Total (**bottom-right**) fractions derived in Salo et al. (2015). We include galaxies from this work with derived bar ages (square), with lower limits for bar ages (triangles), from Chapter 3 – NGC 289 and NGC 1566 – and the Milky Way. We highlight possible interactions with red circles and colour-code them separating SF (cyan), NSF (magenta), P (limegreen), Chapter 3 (orange-x), and the Milky Way (red-star). Further, we show the relation between bar age and each property for SF and NSF nuclear discs, together with the associated Pearson correlation coefficient and *p-value*. From the 6 panels, we only find statistically significant ($p - value \leq 0.05$) the (anti-)correlations for the bar age with the Disc/Total and with Bar/Total fractions, and, interestingly, only for the NSF sample.

to bar age in the upper panel of Fig. 4.7. In the downsizing scenario it is expected that the most massive galaxies would have achieved the necessary mass to become self-gravitating first. Since bars only form in discs that have a minimum degree of self-gravitation, older bars would be hosted by the most massive galaxies. Interestingly, when it comes to the dependency of bar age with stellar mass, we find no correlation, for both sub-samples. Furthermore, the SF sub-sample, which has young bars, includes galaxies with a large range of stellar masses ($2 - 17 \times 10^{10} M\odot$). This result indicates that some massive galaxies are still settling and forming bars, in contrast with the downsizing predictions. Considering the HI mass, once again the SF sub-sample shows no correlations. On the other hand, the NSF sub-sample shows a possible anti-correlation ($r = -0.660$) with bar age, with $p - value = 0.053$, close to the commonly used threshold value of $p - value \leq 0.05$. Since the bar shocks the gas in the disc, causing it to inflow and form stars in the nuclear disc, this result shows that, as the bar grows older, less HI gas is available. The third galaxy property is the disc stellar mass. To measure it, we considered the light fraction of the disc (Disc/Tot) and multiplied it by the total stellar mass. For both sub-samples, however, we find no correlation between bar ages and the disc stellar mass, which argues against a pure downsizing scenario.

Furthermore, we investigate how the galaxy substructures' (bulge, disc, bar) light fractions are related to the bar ages in the bottom panel of Fig. 4.7. When it comes to the fractions of disc and bar, the (anti-)correlation is clear for the NSF sub-sample: galaxies with older bars have a lower light fraction in the disc but a larger fraction in the bar. For both cases, the *p-values* have a statistical significance ($p - value \leq 0.05$). On the other hand, considering the *p-values* for these relations, the SF sub-sample does not seem to show any dependency on the fractions. Lastly, the fraction of light in the bulge does not seem to relate to bar age for both sub-samples. This could be a consequence of mixing different structures (nuclear discs and classical bulges) in the same photometric component and more sophisticated photometric decomposition are necessary to improve this analysis.

4.3.3 Gas inflow and the assembly history of nuclear discs

From the individual results (Appendix A), some galaxies display clear radial gradients in mean age within the nuclear disc, that is, the stellar populations get younger towards the outskirts of the nuclear disc. These are: IC 1438, NGC 1097, NGC 1300, NGC 1433, NGC 3351, NGC 4981, NGC 4984, and NGC 5850. Regarding the rest of the sample, the contamination from older stellar population can explain the lack of a clear age gradient. Additionally, when considering the mass fraction for different stellar populations, most galaxies present younger populations peaking their distribution around R_{kin}, especially the ones with current star formation. This is in agreement with the scenario in which nuclear discs are built inside-out (Bittner et al., 2020), where the new gas brought inwards mainly accumulates in the outskirts of the nuclear disc, in the form of nuclear rings.

To further investigate the evolutionary growth of the nuclear disc, we extrapolate

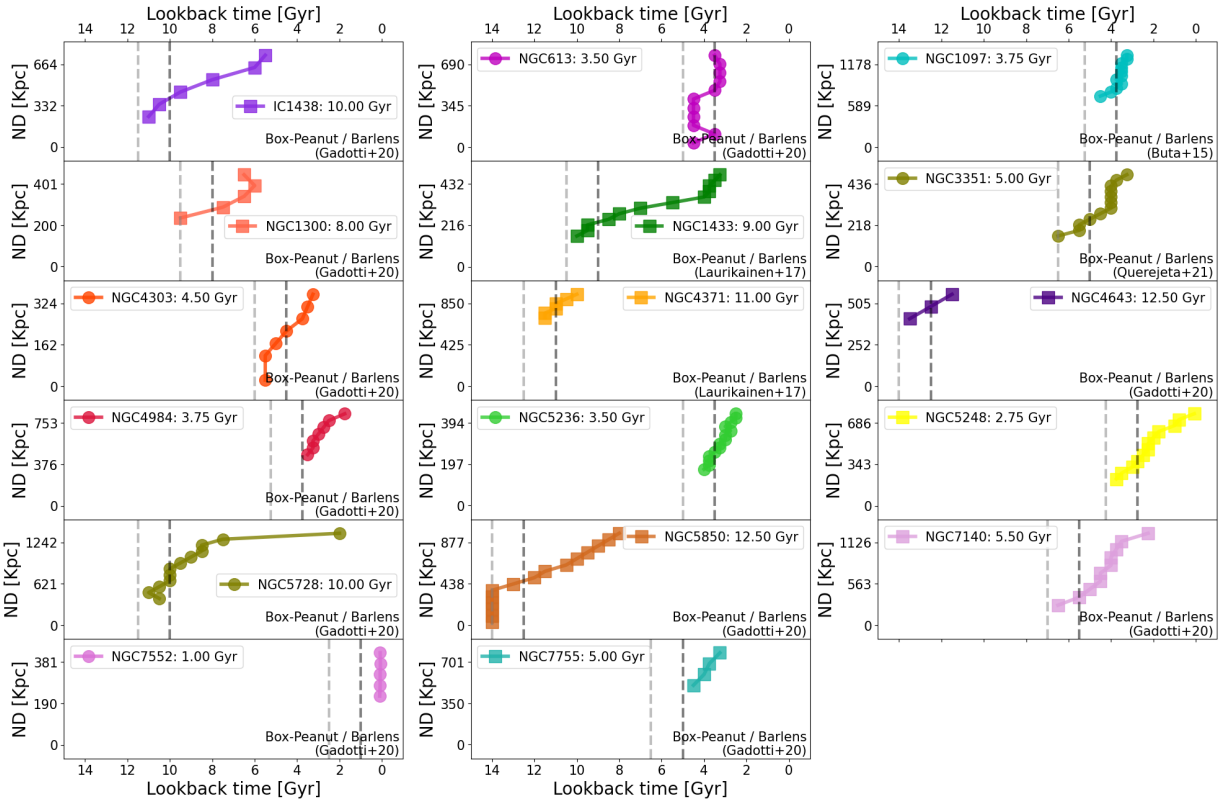

Figure 4.8: **Nuclear disc formation epoch in different radii**. To measure the nuclear disc size for different epochs, we applied our methodology described in Section 4.2 for different radii inside the nuclear disc, as a proxy of "gas inflow time". The SF nuclear discs are shown in circles while the NSF ones in squares. Most of our sample was reported to have a box/peanut bulge or a barlens feature, a sign that the bar has buckled. Additionally, we display the bar age determined through the SFH-based methodology (dashed-dark-grey) and the upper limit for the bar age (dashed-light-grey).

our methodology for different rings inside the structure. Following the same criterion described in Chapter 2, but for different radii in the nuclear disc, we can derive a proxy for "gas inflow time" and measure when the specific part of the nuclear disc was built. With this exercise, we can derive the growth of the nuclear disc as a function of time ("growth rate"), and test whether or not the inside-out scenario applies. It is worth it to point out that we only considered gas inflow times within the bar age and corresponding error measurements, and thus the cases with an inflow time greater than the bar age +1.5 Gyr were not considered reliable. We display the individual results in Fig. 4.8, where a variety of behaviours can be noticed. The majority of the nuclear discs do seem to have grown with time, where for different radii we derive different inflow times, except NGC 7552. This is consistent with the inside-out growth predictions, in which the nuclear disc forms small and, with gas availability, proceeds to growth. However, how small the nuclear disc forms and how it grows with time is linked to the bar and host galaxy properties, as demonstrated in Section 4.3.2.

4.4 Discussion

In this Section, we discuss the impact of our results on galaxy evolution. For the first time, it is possible to analyze how different properties of galaxies change with the aging of bars, and how these observational results compare to theoretical work.

4.4.1 When do galactic discs settle and bars form?

In this Chapter, we derive 17 new bar formation epochs for galaxies in the TIMER survey, deriving the largest sample of nearby galaxies with known bar ages, to the best of our knowledge. Including the galaxies from Chapter 3, we find ages between $\sim 1 - 12.5$ Gyr, which corresponds to redshifts between $1 - 6$. In Section 4.3.1, we display the age distribution (Fig. 4.4) and describe results for each galaxy (see also Appendix A). Since numerical and theoretical work suggest that galaxies can only form a bar once their discs are dynamically settled (at least to a significant extent; Kraljic et al., 2012 and references therein), our result implies that self-gravitating disc galaxies, with relatively low velocity-dispersion, exist since $z \geq 6$. Furthermore, we find galaxies that formed bars relatively recently, with ages below 5 Gyr ($z \leq 0.5$), indicating that this is an ongoing process in the Universe.

When comparing to works that investigate galaxy morphology at high-redshifts (e.g., Shapiro et al., 2008; Schreiber et al., 2009; Epinat et al., 2012; Wisnioski et al., 2015; Rizzo et al., 2020; Lelli et al., 2021; Posses et al., 2023) our results are in good agreement with the scenario in which disc galaxies exist since the Universe was ~ 1 Gyr. Different studies using JWST data find that disc galaxies, with significant rotational support, can be the majority up to $z \sim 8$ (e.g., Ferreira et al., 2022a, 2022b; Nelson et al., 2022; Jacobs et al., 2023). However, many studies demonstrate that high-redshift discs are often thick and turbulent (e.g., Elmegreen & Elmegreen, 2006; Newman et al., 2013), indicating that

these objects are still under great influence of external processes such as minor mergers, and possibly did not yet fully settle their disc. Our results bring a first benchmark of when the transition of the main galaxy evolution driver went from external to internal processes, and when internal/secular evolution arose, at least for our sample. Nevertheless, we would like to point out that our sample is morphologically biased and limited to relatively massive galaxies, and a larger volume-limited sample is necessary to constrain further when this transition happened in the Universe.

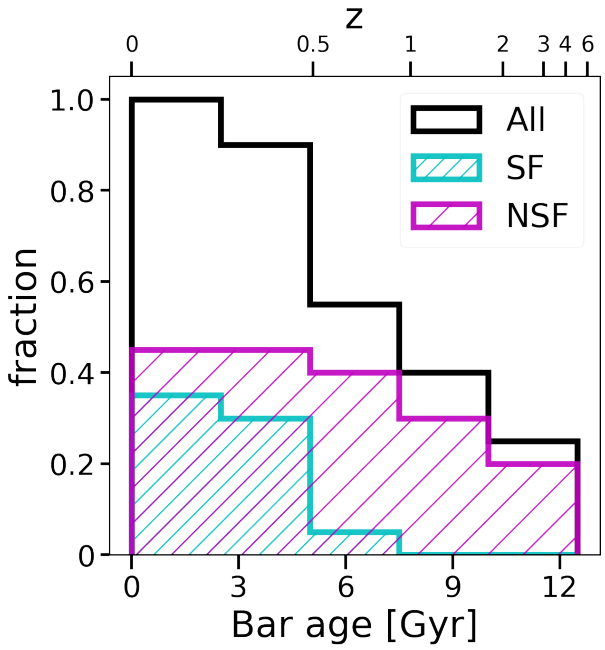

Figure 4.9: Similar to Fig. 4.4, but with a cumulative distribution.

Some simulations that investigate how the bar fraction evolves with time find that bars can exist since $z \approx 6$ (e.g., Kraljic et al., 2012; Rosas-Guevara et al., 2020; Fragkoudi et al., 2020, 2021), which is in good agreement with our results. More specifically, Rosas-Guevara et al. (2020) find, for a TNG50 sample, that 30% of the galaxies are barred at redshift 6, and demonstrate that the discrepancy with observational work at higher-redshifts could result from observational detection limitations. On that aspect, Le Conte et al., (in prep.) derived bar fractions at $1 \leq z \leq 3$ for a JWST sample, finding values between around $7 - 20\%$. The authors also derive bar fractions using HST data for the same sample, finding a decrease in the bar fraction of a factor of $\sim 3{-}4$, confirming the detection limitations from previous works at higher redshifts. To compare how our sample of barred galaxies evolved with time, we reproduce Fig. 4.4 in Fig. 4.9, but now showing the cumulative distributions. Although a direct comparison between these distributions and the evolution of the bar fraction in the Universe cannot be done, albeit their meaning is analogous, it is interesting to see that $\sim 30\%$ of our sample had bars around $z = 6$, in good agreement with Rosas-Guevara et al. (2020). It is also possible to notice a sharp increase in the fraction of bars around $z = 0.5$, following observational findings of Sheth et al. (2008). Nevertheless, we would like to highlight, once again, that a volume-limited sample is necessary to properly constrain this analogous evolution of the bar fraction with time.

Finally, we would like to stress that, although currently bars are understood as robust long-lived structures (e.g., Athanassoula, 2003, 2005; Gadotti et al., 2015; Pérez et al., 2017; de Lorenzo-Cáceres et al., 2019; Fragkoudi et al., 2020; de Sá-Freitas et al., 2023) – that is, old structures that once formed are not easily destroyed – some bars are

still young and were recently formed (e.g., C. de Sá-Freitas, 2023b, in press). This can be extrapolated to the ongoing task of understanding why some galaxies are unbarred. By investigating the properties of galaxies that host young bars, it might be possible to constrain what is preventing some fewer galaxies in the Local Universe to sustain bars and understand if they will form bars at all.

Bar formation and the downsizing scenario

When it comes to disc settling and bar formation, the downsizing scenario (e.g., Cowie et al., 1996; Thomas et al., 2010; Sheth et al., 2012) predicts that the more massive galaxies would host older bars. In other words, the massive galaxies in the Local Universe would have achieved enough mass to dynamically settle their discs first, hence forming their bars first. To test this scenario, we assessed the relation between bar age and a number of relevant galaxy properties in Fig. 4.7, including the current stellar mass, the atomic gas mass, and the current disc stellar mass. We analyzed SF and NSF sub-samples separately, and do not find statistically confirmed correlations between bar ages and different masses, in contradiction with the downsizing scenario predictions. More specifically, in the SF sub-sample, we find galaxies with masses between $2 \leq \mathrm{M}_\star \leq 18 \times 10^{10}\mathrm{M}_\odot$ presenting similar bar ages of ~ 4 Gyr, which indicates that even some massive galaxies formed their bars more recently. Nevertheless, we find a possible anti-correlation between the atomic gas mass with bar age for the NSF sub-sample, with a correlation coefficient of $r = -0.660$ and $p - value = 0.053$, close to the common reliability threshold of $p - value \leq 0.05$. This result can be understood in the context of bar-driven evolution: as the bar forms and funnels gas inwards, less gas is available in the galaxy, resulting in lower values of atomic gas mass in galaxies hosting older bars, consistent with the findings from Fraser-McKelvie et al. (2020).

Erwin (2018) investigates the bar fraction for different masses in a $\mathrm{S}^4\mathrm{G}$ volume-limited sample (Sheth et al., 2010), finding that the fraction of barred galaxies decreases for galaxies with masses greater than $10^{10}\mathrm{M}_\odot$, which is the TIMER sample regime. Considering that bars are robust structures and the downsizing prediction together, one would expect that massive galaxies would form bars first and sustain them until $z = 0$. In other words, the fraction of barred galaxies would increase with mass, which is not observed. This is consistent with our main results, in which we find that the downsizing scenario might not be sufficient to *completely* explain bar formation. Even though achieving enough mass is necessary to dynamically settle the disc, other processes can also be responsible for preventing the formation of the bars. For example, some studies find that fractions of gas in the disc $\geq 10\%$ can suppress or delay the bar formation; similar effects are seen in simulations when the dark matter halo is more massive or kinematically hotter (e.g., Berentzen et al., 2007; Villa-Vargas et al., 2010; Athanassoula et al., 2013). Furthermore, interactions may induce the early formation of a bar or even the formation of a bar in an otherwise bar-stable disc (e.g., Noguchi, 1987; Gerin et al., 1990; Gadotti, 2009; Li et al., 2009; Méndez-Abreu et al., 2013; Łokas et al., 2014; Méndez-Abreu et al., 2023).

This could be the reason for the relatively young bar we find in NGC 1097, for example. This adds complexities to the downsizing picture, which is not necessarily ruled out by our results.

Many different works investigate which physical processes are responsible for the disc formation, that is, the transition between a disordered motion supported galaxy to a rotationally supported low-dispersion object (e.g., Fall & Efstathiou, 1980; Ryden & Gunn, 1987; Okamoto et al., 2005; Brook et al., 2012; Christensen et al., 2016; Stern et al., 2021; Conroy et al., 2022; Hafen et al., 2022; Gurvich et al., 2023; Semenov et al., 2023a, 2023b). Among different possibilities, is the interplay between the circumgalactic medium (CGM) and the interstellar medium (ISM). Stern et al. (2021) argue that, for a FIRE simulation sample of Milky-Way-like galaxies, the virialization of the inner CGM enables the disc formation and settling by cooling flows. This coincides with a transition in the star formation rate from "bursty" to "steady", and the suppression of galactic scale stellar-driven outflows. Furthermore, Semenov et al. (2023a) demonstrate that the disc formation time also depends on how the halos assembled mass (in agreement with Rosas-Guevara et al., 2020) and if destructive mergers took place late-on, which would reset the disc formation process. The authors argue that, for a TNG50 Milky-Way-like sample, late disc formation is associated with mass assemble histories with longer time scales, including significant mergers. Additionally, they show that galaxies with stellar masses $M_\star \geq 10^{10} M_\odot$ tend to form their disc later than the Milky Way, which is expected to have formed the thick disc when the Universe was $\sim 1 - 2$ Gyr. These late disc settling epochs are at odds with the earlier bar formation epochs we find for Milky-Way-mass galaxies, as well as the results from Sanders et al., 2022 and Wylie et al., 2022, which find a bar age for the Milky Way around 8 Gyr. On the other hand, the scenario of disc formation and settling is complex and remains an open question, but it does not seem to necessarily relate to the mass of the galaxy, in agreement with our results. To investigate further the downsizing relation with disc settling, we need to extend our analysis to a volume-limited sample that includes galaxies with lower masses.

4.4.2 Secular evolution and galaxy quenching

Several theoretical, numerical, and observational works find that bars, once formed, affect their host galaxy and drive its evolution (e.g., Lynden-Bell & Kalnajs, 1972; Combes & Gerin, 1985; Ishizuki et al., 1990; Athanassoula, 2003; Sheth et al., 2005; Romero-Gómez et al., 2007; Coelho & Gadotti, 2011; Masters et al., 2012; Di Matteo et al., 2013; Schawinski et al., 2014; Fragkoudi et al., 2016; Haywood et al., 2016; Géron et al., 2021; Rosas-Guevara et al., 2022). When comparing a barred sample with a counter unbarred sample from the SDSS-IV MANGA survey, Fraser-McKelvie et al. (2020) found that barred galaxies peak their star formation history, quench, and form most of their stellar mass first. One important process of bar-driven secular evolution is the funnelling of gas towards the central region, forming the nuclear disc and causing the galaxy quenching – within the reach of the bar (e.g., Masters et al., 2012; Schawinski et al., 2014; Géron et al., 2021).

As demonstrated in Sarzi et al. (2007), the star formation in the nuclear disc can be prolonged, but happen in many bursty episodes, once the gas accumulates enough density to form stars. Due to that, one cannot use the star formation status (SF and NSF) of the nuclear disc as a direct proxy of gas availability in the host galaxy. However, it can be considered a first simplified approach. Considering the differences in bar age distribution between the SF and NSF samples, our results are well aligned with the predictions of secular evolution in the host galaxies. In other words, the nuclear discs that still hold star formation have typically formed later than the ones that do not. This is in line with a scenario in which, once the bar forms, it funnels the available gas inwards, generating a global quench in the galaxy and a starburst in the central region, and this is sustained until the galaxy will no longer have gas left. As a consequence, since there will be no longer gas available, the nuclear disc will quench as well. However, to properly confirm this picture, it is necessary to investigate the gas and star formation rate properties in the entire galaxy.

Lastly, studies find that bars are more likely to form in galaxies that lack gas (e.g., Berentzen et al., 2007; Athanassoula et al., 2013; Seo et al., 2019) that is, galaxies that already started to quench. Since bars also drive quenching in the galaxy, this leads to a difficutly in determining of what took place first: quenching or bar formation. In other words, for a given sample of gas-poor barred galaxies, it is unclear if the bar formed promptly due to the lack of gas or if the quenching was driven by the bar. By investigating in an independent fashion the quenching and bar formation epochs for these galaxies, we will be able to break this degeneracy for the first time.

4.4.3 Bar length evolution and angular momentum exchange.

When it comes to bar evolution, especially bar growth, many studies reach different conclusions. From an observational viewpoint, Kim et al. (2021) analyzed the data from the Cosmic Evolution Survey (COSMOS – Scoville et al., 2007; Koekemoer et al., 2007) and found that the average normalized bar length did not evolve in the past 7 Gyr. This is in agreement with findings from Rosas-Guevara et al. (2022), where the authors found that the bar growth happens at a similar pace to the disc growth for a TNG50 sample, maintaining a fairly constant size relation. On the other hand, Zhao et al. (2020) found for a IllustrisTNG sample (Springel et al., 2018; Pillepich et al., 2018; Marinacci et al., 2018; Naiman et al., 2018; Nelson et al., 2018) that, in the past 6 Gyr, the length of bars increase by a factor of 0.17 dex. Furthermore, Anderson et al. (2022) and Erwin et al. (2023) argue that the presence of "shoulders" – one type of bar profile structure – is evidence of secular bar growth. This is a brief illustration of the lack of agreement on whether or not bars grow in length as they evolve, both in absolute terms or normalised.

Employing our determined bar ages, we can investigate the normalized bar size evolution as in Fig. 4.6 and find an indication that younger bars are smaller than older bars when compared to the size of the galaxy. This is consistent with the picture in which the normalized length of bars increases with their ageing. However, Fragkoudi et at., (in

prep) showed that the picture is not that simple. For an Auriga simulation sample of galaxies, they retrieved the same relation between normalized bar length with bar age. Still, investigating further the evolution of said bars, they found that not every bar has grown with time. The authors demonstrated that bars that formed at higher redshifts ($z \geq 2$) already form large and do not grow, while bars that formed at intermediate redshifts ($z \leq 2$) do grow with time. In other words, the authors retrieve the same relation presented here, but in a scenario in which not all bars have grown. This is in agreement with findings from Peschken & Łokas (2019), where the authors find for an Illustris sample that galaxies tend to form larger at higher redshifts, mainly because they form through interactions and the discs are generally smaller and less stable. That is, with our findings alone we cannot conclude or rule out that the bars of our sample have grown and further individual investigation is necessary. that the same process is happening in these bars. A possible explanation to the different correlations for galaxies in the SF and NSF sub-samples can be devised considering that the bars in the NSF sub-sample are older. It is plausible that the effect is not seen in the galaxies of the SF sub-sample because it is still relatively weak in these galaxies.

Furthermore, Athanassoula (2003) demonstrated that bars can exchange angular momentum by trapping stars from the disc, either in the region of the bar or beyond it. In that scenario, the bar would only increase its length by capturing disc stars from the close neighbourhood. Additionally, as a consequence of trapping new stars, the light fraction of the bar would increase, causing the disc light fraction to decrease, according to Kim et al. (2012). That is, as the bar grows older, more relative light belongs to it when compared to the disc. We investigate this scenario in Fig. 4.7 and find clear (anti-)correlations between bar age and the disc/bar light fractions for the NSF sub-sample, in agreement with these theoretical predictions. Our results reinforce the scenario in which bars exchange angular momentum by capturing stars from the disc. However, we cannot conclude yet if this angular momentum exchange had led to a bar relative growth with time. Lastly, considering the SF sub-sample, we find no statistically confirmed correlations and cannot conclude.

4.4.4 The nuclear disc build-up: hints of a 2-phase history

In Section 4.3.1, we describe in detail the individual analysis for each nuclear disc in the TIMER sample, elucidating how diverse these structures are. Our sample includes a range of sizes, star formation rates, and histories, and stellar population radial, and mass distributions. Furthermore, we investigate how the nuclear disc size relates to its host galaxy, in Fig. 4.5. When it comes to the entire sample, the nuclear disc size is well related to the size of the galaxy, as well as the bar length. This relation indicates that the bar size is inherited by the galaxy disc properties (e.g., Erwin, 2005; Gadotti, 2011; Erwin, 2019; Kim et al., 2021) and can influence the nuclear disc size. Although the physical determining factor of the nuclear disc size is still an open question, many studies show that it is expected to relate to the bar properties (e.g., Shlosman et al., 1989; Athanassoula, 1992a, 1992b;

Knapen, 2005; Comerón et al., 2010; Seo et al., 2019; Gadotti et al., 2020), in agreement with our findings.

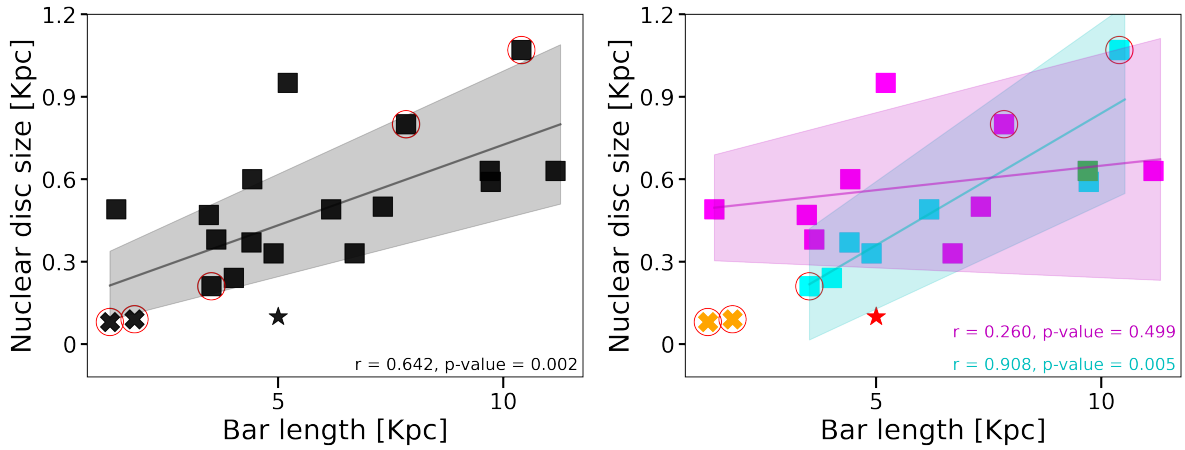

Figure 4.10: Nuclear disc size as a funciton of bar length, colour-coded for the entire TIMER sample (left panel) and separated between SF and NSF sub-sample (right panel). Considering the entire sample, there is a good correlation between the nuclear disc and bar, with a coefficient of $r = 0.642$ and $p - value = 0.002$. On the other hand, analyzing the SF and NSF sub-samples independently, it is possible to see that the correlation only remains for the former and disappears for the latter. This can be an indication of a 2-phase evolution of nuclear discs: bar-built vs. dynamical.

To further illustrate the relation between the bar length and nuclear disc size, we present it in Fig. 4.10 for the entire sample (left panel; see also Gadotti et al., 2020). Considering the SF and NSF sub-samples separately (right panel), it becomes clear that the correlation is not universal, in a similar fashion as the relation between nuclear disc size and galaxy size (Fig. 4.5). While the SF sub-sample is remarkably well correlated with the bar length ($r = 0.908$ and $p - value = 0.005$; as well as with galaxy size), the NSF sub-sample is uncorrelated with it. We interpret it as a hint of a 2-phase evolution of the nuclear disc, and we call the first phase "bar-built" as opposed to the second phase, which we call "dynamical". That is, while the bar is bringing gas inwards, the built-up of the nuclear disc is dependent on the bar and, as a consequence, on the size of the host galaxy as well. However, once the gas inflow is interrupted, the evolution of the nuclear disc and the bar is no longer connected. Hence, the bar proceeds to evolve connected to the host galaxy, but the nuclear disc becomes independent, evolving under the dynamical influence of the central part of the galaxy. In fact, Athanassoula (1992) demonstrated that many different factors can affect the size of the nuclear disc, including the central mass concentration – which does not necessarily depend on the bar properties.

Inside-out formation and growth rate history of nuclear discs

Bittner et al. (2020) put forward the scenario in which nuclear discs grow inside-out, which

is consistent with the simulations of Seo et al. (2019). The authors investigated the TIMER sample and found a radial gradient of the mean stellar age for most nuclear discs, in which the mean stellar population age is younger outwards in the nuclear disc. Additionally, this profile is minimum close to the kinematic radius, measured in Gadotti et al. (2020). We confirm these results in the individual analysis (see Appendix A), after isolating the light from the nuclear disc, finding evidence of an inside-out formation for most objects.

Furthermore, we study the gas inflow history for each nuclear disc in Section 4.3.3 (Fig. 4.8), finding that the majority of the nuclear discs show variations in size with time, agreeing with an inside-out bar-build scenario. The individual slopes in Fig. 4.8 can be considered as the "growth rate" of the nuclear discs, where a flat slope indicates slow or no growth with time, whereas a steep slope indicates fast growth. Since the build-up of the nuclear disc can be linked to the gas inflow – at least in the first, bar-built phase –, the behaviour of the growth rate is an indication of the gas inflow rate.

Analyzing the evolution of the nuclear disc sizes, some galaxies seem to present changes in the growth rate with time. For example, NGC 1433 displays a slow growth at first, followed by a late fast growth from around 5 Gyrs ago. This is true for other galaxies as well. On the other hand, NGC 5236 displays a monotonic growth rate, with no apparent changes. These differences can be due to different reasons or events that can affect the gas inflow towards central parts of the galaxy. For example, the buckling of the bar and the formation of the box/peanut bulge can trigger a late gas inflow (e.g., Pérez et al., 2017), which can be followed by a decrease of gas inflow (e.g., Fragkoudi et al., 2016). This late gas inflow and the change in the properties of the bar can affect the growth of the nuclear disc, accelerating and/or slowing it down. It is interesting that the only two galaxies of our sample that do not show box/peanut bulges also present a monotonic growth of the nuclear disc – although the opposite is not true: some galaxies with a box/peanut bulge also show a monotonic growth. Another possibility is the host galaxy experiencing a minor merger. Depending on the characteristics of this event, the disturbance could also bring gas toward the central region of the galaxy. In fact, our sample includes 5 galaxies with companion candidates, these are: NGC 1097, NGC 4303, NGC 5850 and the two galaxies from Chapter 3, NGC 289, and NGC 1566. In conclusion, with our methodology, we present a new approach to deduce the gas inflow history of the galaxy. Further analysis will allow us to determine which events took place in the galaxy that could explain differences in the growth rate of the nuclear discs.

Double-barred galaxies are old systems

Studies report that $12 - 30\%$ of barred galaxies host a second, inner/nuclear bar (e.g., Erwin, 2004; Buta et al., 2015), with sizes varying between $0.3 - 2.5$ Kpc (de Lorenzo-Cáceres et al., 2020). de Lorenzo-Cáceres et al. (2019 – and references within) argues that there are mainly 2 scenarios to explain the formation of the inner bar. In the first scenario, first a gaseous inner bar would be formed, which would then become a stellar inner bar.

In this case, it is necessary to first form the outer bar (or main bar), bring gas inwards, and then form the inner/nuclear bar. Also, the authors argue that in this scenario the bar would not resemble the main bar, would be constantly destroyed and rebuilt, and, finally, would necessarily be younger than the main bar. In contrast, the second scenario predicts that the inner/nuclear bar would arise from a dynamical instability in the nuclear disc, just as in the formation of the main bar. In this case, the presence of a *stellar* nuclear disc, sustained by cold kinematics, is necessary before the formation of the inner/nuclear bar. In the TIMER team, de Lorenzo-Cáceres et al. (2019), Méndez-Abreu et al. (2019), and Bittner et al. (2021) investigated different aspects of inner/nuclear bars, concluding they share many properties of the outer/main bar, such as buckling (Méndez-Abreu et al., 2019). In fact, Bittner et al. (2021) argue that double-barred systems behave as "galaxies inside galaxies". These findings from the TIMER team suggest that the second scenario of inner/nuclear bar is more likely.

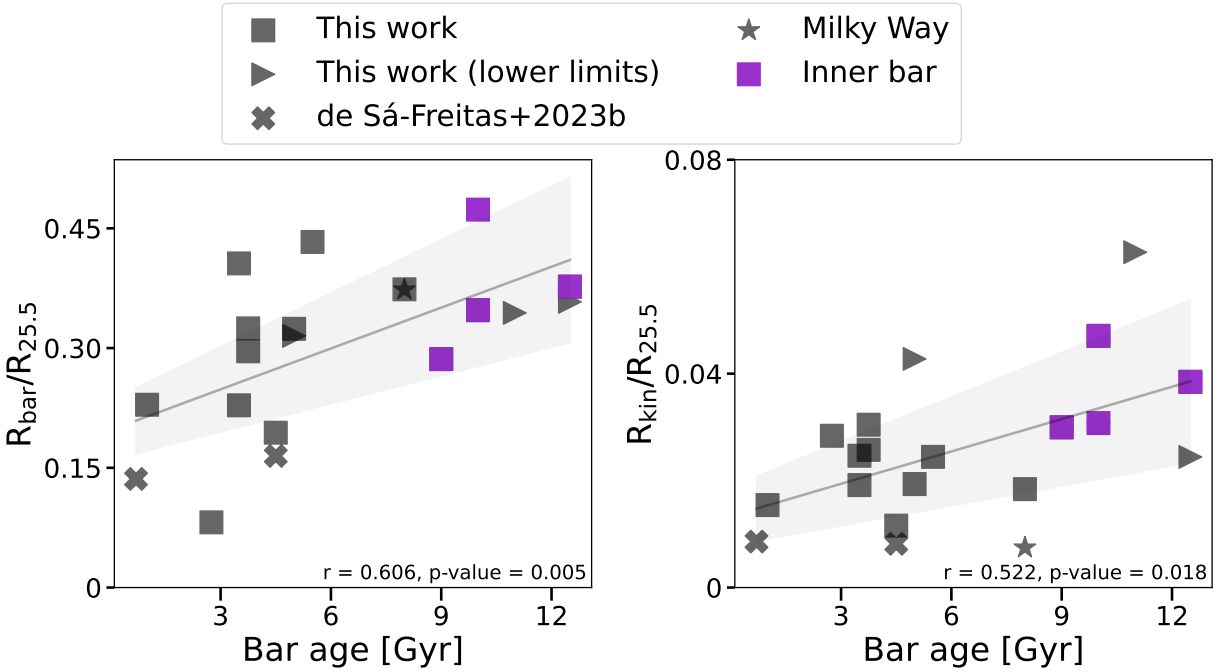

Figure 4.11: Same as Figure 4.6 but highlighting the nuclear discs that were reported to have an inner/nuclear bar (violet-squares). All the nuclear discs that have inner bars are NSF and hosted by older-bar (bar ages $\geq$ 9 Gyrs).

As discussed in Section 4.3.1, 4 of the galaxies in our sample have been reported to host an inner/nuclear bar. We repeat Fig. 4.6 in Fig. 4.11, highlighting the doubled-barred objects, and find they are among the oldest bars of our sample. Our results agree with the scenario in which inner/nuclear bars form from disc instabilities in the nuclear disc, which requires building the mass of the nuclear disc itself, hence longer timescales and older systems. Additionally, studies show that the gas fraction on the main disc can

delay the formation of the main bar (e.g., Berentzen et al., 2007; Athanassoula et al., 2013; Seo et al., 2019). If this is the case also for the inner/nuclear bars, it would be necessary to quench the star formation in the nuclear disc, or at least to consume enough of the gas, to be possible for the inner/nuclear bar to form. Consistent with that, the doubled-barred systems in our sample belong to the NSF sub-sample. Lastly, since the investigation of these systems using spatially resolved spectroscopy is very recent, there are few constraints on timescales for formation or physical limitations to form them, and further efforts are necessary.

4.5 Summary and conclusions

Using a complementary approach for the methodology presented in Chapter 2, in this Chapter we derived the bar ages for most of the TIMER sample. We summarize our findings as follows:

- We present a complementary approach for the methodology in Chapter 3, which takes less computational time. We compared both approaches for the galaxies in Chapters 2 and 3, and find similar results within the estimated errors.

- We derived the bar ages for 17 new galaxies, building the largest sample of barred galaxies for which bar ages are estimated, to be best of our knowledge. We find bar formation epochs between $\sim 1 - 12.5$ Gyr, agreeing with the scenario in which disc galaxies are formed since $z \approx 6$ and the disc settling is an ongoing process in the Universe.

- We find that nuclear discs with star formation are generally hosted by younger bars, while quenched nuclear discs are generally hosted by older bars. This is in agreement with the scenario in which the bar drives the galaxy quenching by bringing gas inwards and consuming it.

- We analysed the bar age in connection to different properties of the nuclear disc, the bar, and the galaxy. Among our main findings we show that galaxies with larger normalised bar and nuclear discs sizes tend to host older bars, which indicates the connected growth of these structures with time. However, simulations demonstrated that the picture might not be as simple and that some bars do not grow with time, but may have formed already long.

- Investigating the fraction of light in different structures (bar, nuclear disc, and galaxy) as a function of bar age, we find indications of angular momentum exchange, where the bar is capturing stars from the main disc, at least for the NSF sub-sample. This is bourne out by a correlation between bar age and the bar-to-total fraction, as well as an anti-correlation between bar age and the disc-to-total fraction.

- For our sample, we find no indications of the downsizing scenario of bar formation.

For example, we find no relation between galaxy or disc stellar mass with bar age. As an interesting example, the most massive galaxy in our sample, NGC 1097, formed its bar only 4 Gyr ago. This suggests that other factors play an important role in bar formation, other than the settling of the main disc. For example, interactions with the environment may affect the signatures of the downsizing picture.

- Analysing the nuclear disc evolution, we find indications of a 2-phase evolution scenario in which, while the bar is bringing gas inwards, the nuclear disc size is connected to the evolution of the bar. However, once there is no longer gas available, the nuclear disc proceeds to evolve – to some extent – independently from the bar. Additionally, deriving the gas inflow history, we find that most nuclear discs follow the inside-out formation scenario and that their growth rate is often not monotonic; this shows that the gas inflow rate along the bar varies with time, which can be the result of different processes, such as the bar buckling and possible interactions with the environment.
- Lastly, we show that double-barred galaxies are usually hosted by older nuclear discs built early by older bars, suggesting, in line with previous results, that longer timescales are required to form inner/nuclear bars.

5

Conclusions and Outlook

In this Chapter, I summarize the work presented in this Thesis, highlighting our main findings and how they impact our current understanding of galaxy evolution from an observational perspective. Additionally, I describe some of the future applications that are only now possible, and which I plan to develop during my ESO-Chile Fellowship, together with the TIMER team.

The task of constraining the processes that drive galaxy evolution in different cosmic epochs remains a challenge. When it comes to morphology at different redshifts, there is a dichotomy: galaxies at high redshifts are usually turbulent while most of the galaxies in the Local Universe present ordered dynamics – which reflects in a disc morphology. In the early Universe, galaxy evolution is mainly driven by the high frequency of interactions and mergers (e.g., Genzel et al., 2008; Law et al., 2009; Oser et al., 2010). These interactions become less frequent with the expansion of the Universe, and galaxies start to settle into more rotationally-supported configurations (Kormendy & Kennicutt, 2004). Even though there are already disc galaxies at intermediate redshifts (e.g., Ferreira et al., 2022a, 2022b, Nelson et al., 2022; Jacobs et al., 2023), these discs are usually thick and present high values of internal dispersion motion, meaning they are still turbulent and unsettled (e.g., Elmegreen & Elmegreen, 2006; Cresci et al., 2009; Neumann et al., 2020). Once the galaxy (partially) settles dynamically, that is, becomes a cold disc with low internal velocity dispersion, it becomes unstable for bar formation, which happens in a short timescale (e.g., Kraljic et al., 2012). Therefore, the presence of the bar is a sign that the disc settled – at least partially – and internal processes are leading the evolution of the galaxy. To understand the moment of transition between external and internal processes leading galaxy evolution, one needs to be able to time the epoch of bar formation for a sizeable sample, which was not possible until recently.

In Chapter 2, we present the first methodology to derive bar formation epochs that is broadly applicable to different objects. The foundation of the methodology is to use bar built structures – in this case, the nuclear disc – to time the formation of the bar itself. The nuclear disc is formed by the bar in relatively short timescales (10^8 Gyr – Athanassoula 1992a,b; Emsellem et al., 2015, Seo et al., 2019; Baba & Kawata, 2020), hence we can consider the formation of the nuclear disc and the bar formation as coeval. In summary, the methodology consists of modelling the light of the main disc by using a representative ring and subtracting it from the central light of the galaxy. With that, we approximately disentangle the central region into contributions of the main and nuclear discs. Applying the same strategy to simulated barred galaxies (see Section 2.2.3 for more details – Fragkoudi & Bieri, in prep.), we found that the most robust criterion to time bar formation is the ratio of the SFHs from the nuclear disc and the main disc. That is, once this ratio is above one for the first time towards younger ages. This criterion reflects the moment when star formation proceeds in the nuclear disc more significantly than in the main underlying disc – as represented in their corresponding spectral properties – and is therefore a working definition of the initial formation of the nuclear disc. By carrying out this exercise, it was possible to conclude that, even if the disentanglement of the light in the central region is not perfect, the ratio between SFHs allows us to time when the bar has formed. We proceeded to apply the methodology in a pilot study on NGC 1433, finding the bar age to be 7.5 Gyr. In addition, we thoroughly investigated sources of errors in our methodology and classify them into two categories: statistical and systematic. The first refers to the noise associated with the observations and the second is the possible dependency of our results on different configurations of the methodology – such as the

galactocentric distance of the representative ring, the light profile employed to model the main disc, different pPXF regularizations, and others. In general, we found that the main source of uncertainties in our results are the systematic choices of configuration, with errors of $^{+1.6}_{-1.1}$ Gyr, and found low statistical errors of $^{+0.2}_{-0.5}$ Gyr – due to the high-signal to noise we achieved. Lastly, considering the isolated SFH of the nuclear disc in different radii, we found evidence supporting an inside-out growth for the nuclear disc, in agreement with different approaches in the literature (e.g., Seo et al., 2019; Bittner et al., 2020).

The inside-out scenario predicts that nuclear discs form small and grow with time. In that scenario, young nuclear discs – hosted by young bars – should be small. In fact, Seo et al. (2019) find for simulated Milky-Way-like galaxies that nuclear discs can form with typical sizes of 40 pc. However, from the observational perspective, kinematically confirmed extragalactic nuclear discs tend to be bigger than 200 pc. In Chapter 3, we present the smallest nuclear discs observed to date, with kinematic confirmation. They are hosted by NGC 289 and NGC 1566 and have sizes of 90 and 77 pc, respectively. Applying the methodology developed in Chapter 2, we find young bars with ages of 4.5 and 0.7 Gyr, respectively. Lastly, these are the first extragalactic nuclear discs with sizes similar to the one hosted by the Milky Way, which has a size of $\sim 200 \pm 50$ pc (e.g., Launhardt et al., 2002, Wegg et al., 2015), although the bars have different ages (see Table 3.2). With these results, we find that not every bar is old and some discs are still settling in the Local Universe.

In Chapter 4, we expand our analysis to all galaxies from the TIMER sample which have a discernible nuclear disc (Gadotti et al. 2019, 2020; Bittner et al., 2020), increasing the known bar ages to a total of 20 galaxies. We also develop a complementary methodology, maintaining the same strategy, but applying it more directly on the SFHs (instead of the additional intermediate steps dealing with the spectra), due to computational time advantages (see Section 4.2 for more details). We find bar ages between $\sim 1 - 12.5$ Gyr, indicating that disc galaxies are settling since $z \approx 6$ and that this is an ongoing process in the Universe. Investigating further aspects of disc settling, we do not find correlations such as that of the bar age with galaxy stellar mass. This is contradicting predictions from the downsizing picture in which the more massive galaxies assembled mass first, so they can form the bar first – considering that the galaxy stellar mass is the most important factor. This is an indication that, although enough mass is necessary to form and sustain a bar, other factors might play a role in delaying or speeding up bar formation. Studies show that destructive mergers can reset the process of settling the disc (e.g., Semenov et al., 2023a; Rosas-Guevara et al., 2022), and gas fraction and dark matter halos play roles in delaying the bar formation as well (e.g., Berentzen et al., 2007; Villa-Vargas et al., 2010; Athanassoula et al., 2013). Furthermore, we find indirect evidence that corroborates the scenario in which bars are quenching their host galaxies. We find that younger bars tend to host nuclear discs with significant star formation, whereas older bars tend to host quenched nuclear discs (SF vs. NSF – Bittner et al., 2020). Focusing on the bar evolution, we find evidence that bars can grow relatively to their bar disc, i.e., we find that older

bars tend to have larger normalised lengths (Fig. 4.6); although Fragkoudi et al., (in prep) showed that the picture might not be as simple and not all bars necessarily grow (some bars may be born already long). Additionally, in Fig. 4.7 we investigate how the fraction of light is enclosed in different galaxy structural components with the ageing of the bar, and find that the bar capture stars as it ages, in agreement with theoretical predictions of the angular momentum exchange between the bar and other structural components (e.g., Athanassoula, 2003; Kim et al., 2016). Lastly, we find indications that nuclear discs have two phases of evolution: "bar-built" and "dynamical". The first takes place while the bar is funneling gas inwards and the size of the nuclear disc is connected to the bar properties. The second happens once there is no longer gas available, and the nuclear disc evolves relatively independently of the bar. Furthermore, we show that we can deduce the gas inflow history onto the nuclear disc and find corroborating evidence that nuclear discs grow inside-out – while there is gas inflow.

The work presented in this Thesis will allow new lines of investigation on secular evolution that were not possible to pursue from the observational point of view so far. Some of the future improvements and applications on which I plan to work during my ESO-Chile Fellowship (2023–2027) will be summarized in the following.

5.1 Further improvements to age-dating bars

This Thesis represents the first developments of our methodology, leaving room for improvements in different aspects. Here, we summarize some of the future work.

- *Comparing spectra- and SFH-based approaches for the entire TIMER sample.* As we discussed in Chapter 4, we developed a complementary methodology to derive bar ages, with the clear advantage of saving computational time. In the timescale necessary to develop this Thesis, we could not further compare both approaches – the strengths and weaknesses of each one. Due to that, one of the first steps to move forward with this work is to compare results from both approaches to the entire TIMER sample, further investigating in which cases they do agree or not.

- *Investigating how different "ingredients" can affect the bar age derivation.* Our methodology relies on the extraction of SFHs from full-fitting spectra. To do that, one has to choose the initial mass function, stellar library (empirical vs. theoretical), isochrone models to follow, and fitting routines, among other "ingredients". Nevertheless, these decisions can affect the final SFHs derived. For example, Bittner et al. (2020) compare derived mean ages from `pPXF` (Cappellari & Emsellem, 2004; Cappellari, 2017) and `STECKMAP` (Ocvirk et al. 2006; **?**) for the same data set, finding differences such as the light-weighted mean age of the old stellar population. Furthermore, Gonçalves et al. (2020) demonstrate that different choices of wavelength range and stellar library can affect the final results. Due to that, we will further investigate how these different ingredients can affect the derived bar age and, especially, if the

relative ages and correlations are sustained. In other words, we would like to test whether or not our results are robust for different approaches to deriving SFHs.

- *Constraining how spatial resolution can limit the bar age measurements.* To properly constrain disc settling in the Universe, one has to derive bar ages for a volume-limited sample, which is not the case for the TIMER sample used in this Thesis. Acquiring high-resolution IFU data for a large sample is not feasible at the moment, since each of the objects in the TIMER survey was observed for around 3600 s. Furthermore, considering other MUSE-VLT surveys with archival data publicly available still do not compose a volume-limited sample with a wide range of masses. Even though large IFU surveys exist, such as the SDSS-IV MaNGA survey[1], their spatial resolution is significantly lower, with average resolution of around 1 Kpc – as opposed to about 100 pc in TIMER. Therefore, it is interesting to investigate how the spatial resolution can affect our results on deriving bar ages. One way of investigating the limit of resolution in which our methodology is still reliable is by degrading the TIMER data to different resolution steps and deriving the corresponding bar ages. With that exercise for the entire sample, we expect to be able to constrain how reliable our methodology is in the case of poor spatial resolution. Once we constrain this limit, we can start to investigate which galaxies from the MaNGA survey could be used in the future to further expand the lines of investigation initiated in this Thesis.

5.2 What happens first: galaxy quenching or bar formation?

Studies with large data sets show that, for fixed mass and morphology, galaxies that host bars are optically redder in comparison to bar-less galaxies (e.g., Masters et al., 2011; Vera et al., 2016; Kruk et al., 2018; Fraser-McKelvie et al., 2020; but see Erwin, 2018). Fraser-McKelvie et al. (2020) demonstrated that, for a large MaNGA sample, this is due to two facts: (*i*) galaxies hosting bars peak their star formation earlier than bar-less galaxies, resulting in on average older stellar populations; (*ii*) barred galaxies are usually more metal-rich. Although there is little doubt that bars affect their host galaxies, it is not clear if these properties are a consequence or cause the presence of the bar. In other words, which one is the cause and which one is the effect?

Observations and simulations show that the presence of the bar causes a redistribution of molecular gas and angular momentum (e.g., Lynden-Bell & Kalnajs, 1972; Combes & Gerin, 1985; Athanassoula, 1992; Athanassoula, 2003; Fragkoudi et al., 2016; Fragkoudi et al., 2017). Along with that, the galaxy starts to decline its star formation rate in regions where the bar has swept the gas, being possible to identify "star formation deserts" (Masters et al., 2012; Schawinski et al., 2014; Haywood et al., 2016; Fraser-McKelvie et al., 2020; Géron et al., 2021). In this scenario; *the presence of the bar would lead to galaxy*

[1]https://www.sdss4.org/surveys/manga/

quenching. On the other hand, simulations also show that gas-less discs are more likely to form bars first and faster (e.g., Berentzen et al., 2007; Athanassoula et al., 2013; Seo et al., 2019). With this, the massive galaxies in the past would start quenching and consuming their molecular gas, which would trigger the bar formation, followed by fast growth and resulting in strong bars hosted by red massive spirals. In this scenario; *the quenching of the galaxy would lead to bar formation.* To assess if either scenario is favoured in nature, it is necessary to time when the bar formed and when the host galaxy started to quench.

In light of the developed methodology presented in this Thesis, we can break this degeneracy for the first time. To do so, I will take advantage of the good quality IFS data from MUSE/VLT already available on the ESO Science Archive Facility (e.g., from TIMER, PHANGS, MAD, and other surveys) and derive their correspondent bar ages. In addition, by deriving SFHs, I plan to develop a multi-diagnostic strategy to map galaxy quenching spatially, for the entire disc. Between possible diagnostic tools, there are (*i*) fraction of mass built in the last 1 Gyr compared to 1 Gyr and 2 Gyr; (*ii*) time when 80% of the stellar mass was built; (*iii*) time since quenching (Werle et al., 2022); (*iv*) star formation rate, and others. With the spatial quenching information and the bar age, I will be able to answer which is the cause and which one is the effect of the interplay between bars and quenching. In addition, I will analyze global and radial trends for the sample, investigating also the relation between bar growth and quenching as a function of radius.

5.3 Why do some galaxies remain barless?

Building the picture of how bars form and evolve is not a trivial task and requires a combined effort from simulations, analytical models, and observations. Today we know that over two-thirds of galaxies host bars in the local Universe (e.g., Eskridge et al., 2000; Menéndez-Delmestre et al., 2007; Sheth et al., 2008; Aguerri et al., 2009; Buta et al., 2015), and most simulations show that bars form quite easily. It can happen either spontaneously once the disc settles (e.g., Toomre, 1964; Combes & Sanders, 1981; Polyachenko, 2013), from early interactions with companion galaxies in the environment (e.g., Noguchi, 1987; Gerin et al., 1989; Miwa & Noguchi, 1998; Peschken & Łokas, 2019; Łokas, 2021), or from interactions with the dark matter halo substructures (e.g., Romano-Díaz et al., 2008). It has become difficult to explain why some galaxies do not host bars in the Local Universe. Additionally, the most recent simulations converge to describe bars as long-lived and robust structures (e.g., Shen & Sellwood, 2004; Athanassoula et al., 2005), and the result from this Thesis corroborate this picture. Therefore, once formed, bars are not easily destroyed. In this context, bar-less disc galaxies probably have never formed or hosted bars. Among possible explanations of delays in bar formation, simulations find that the reasons to delay bar formation can be *central mass concentrations* (CMC – Bournaud & Combes, 2002; Saha & Elmegreen, 2018); *gas-rich discs*, *turbulent discs*, and/or massive dark matter halos (e.g., Athanassoula et al., 2013), but from an observational standpoint it remains unclear why some galaxies do not host bars.

To shed light on this matter, I will investigate the properties of bar-less galaxies and compare them to my previous sample of barred galaxies, especially with galaxies hosting young bars. To investigate the possible explanations listed before, I am going to analyze (*i*) spatially resolved diagnosis for quenching, (*ii*) star formation rates, (*iii*) radial gas content, (*iv*) stellar velocity dispersion, and (*v*) stellar surface densities. In that sense, I will investigate global radial trends with bar age and compare them with bar-less galaxies. Whichever properties are causing the delay in bar formation should be present on bar-less galaxies but not on galaxies hosting young bars.

5.4 Are bars slowing down?

The bar pattern speed ($\Omega_{\rm bar}$) – that is, the angular frequency in which the bar rotates as a solid body around the galaxy centre – is one of the three main properties that describe a bar, along with length and strength. Thus, describing bar evolution includes describing how $\Omega_{\rm bar}$ changes with ageing. However, most theoretical studies and simulations have predictions that differ from the observed measurements in the Local Universe. While the theory generally predicts that bars should slow down with time by interacting with the dark matter halo – due to dynamical friction and angular momentum exchange (e.g., Tremaine & Weinberg, 1984; Debattista & Sellwood, 1998; Debattista & Sellwood, 2000; Athanassoula 2002, 2003; O'Neill & Dubinski, 2003; Holley-Bockelmann et al., 2005) –, observations find that most of the bars in the Local Universe rotate fast (e.g., Debattista & Williams, 2004; Guo et al., 2019; Cuomo et al., 2019; Garma-Oehmichen et al., 2020). Whether this is a problem with theoretical predictions and simulations or with observational measurements is not clear. Recent simulations in the ΛCDM paradigm find diverging results; some studies find that bars slow down in ΛCDM (e.g. Algorry et al., 2017; Peschken & Łokas, 2019, Roshan et al., 2021) while other studies find that bars can remain fast, in agreement with observations (e.g. Fragkoudi et al., 2021). Fragkoudi et al. (2021) find that the proportion of dark matter and baryonic matter can be important to keep bars from slowing down. From the observational perspective, however, it remains challenging to measure $\Omega_{\rm bar}$.

Most of the works that attempt to retrieve the $\Omega_{\rm bar}$ for nearby galaxies rely on the Tremaine-Weinberg method (TW – Tremaine & Weinberg, 1984), which requires the line of sight velocity measured in parallel lines along the major axis of the galaxy. Despite its simplicity, most of the uncertainties rely on deriving proper galaxy and bar measurements – such as inclination, position angle, bar length, etc. Additionally, depending on the tracer used, one can derive different $\Omega_{\rm bar}$ for the same data set (e.g., Williams et al., 2021). Due to that, Tahmasebzadeh et al., (subm.) developed a new approach to derive bar pattern speeds based on dynamical models and observations, fitting observed kinematic data. By applying the methodology derived in Tahmasebzadeh et al. (2022) to NGC 4371, which is a TIMER galaxy, they were able to measure the bar pattern speed independently of the TW method. In future work, they plan to apply the same methodology to the rest of the TIMER sample, as well as other galaxies that have IFU data available. By combining our

efforts with this new approach, and providing bar ages for these galaxies, we can provide a new observational perspective on whether or not bars slow down over time.

5.5 Bar ageing in edge-on galaxies

Chemo-dynamical tracers from the Milky Way show that the Galaxy formed its thick disc when the Universe was around $1-2$ Gyr old (e.g., Belokurov & Kravtsov, 2022; Conroy et al., 2022), and later on settled its thin disc, around ~ 8 Gyr ago (e.g., Haywood et al., 2013; Snaith et al., 2015), coinciding with the Galactic bar epoch of formation (e.g., Wylie et al., 2022; Sanders et al., 2022). From our privileged perspective, we can derive different disc-settling tracers in the Galaxy – such as vertical chemical differentiation –, which was not possible for other galaxies, until recently, due to the insufficient spatial sampling and field of view of IFU instruments prior to MUSE. GECKOS (Generalising Edge-on galaxies and their Chemical bimodalities, Kinematics, and Outflows out to Solar environments – van de Sande et al., 2023) is an unprecedented VLT-MUSE large program survey that includes 35 (near) edge-on galaxies, varying in masses, SFRs and morphology. GECKOS will provide IFU data at high physical spatial resolution for these galaxies. It will thus allow us to constrain galaxy evolution from an edge-on perspective, being suitable for direct comparisons with the Milky Way. Among different possibilities, is deriving the disc settling tracers for barred galaxies and comparing them with our methodology. In the future, I would like to expand the described methodology in this Thesis for these objects, deriving an analogous strategy suitable for edge-on galaxies. This would broaden our perspective on galaxy evolution, allowing us to constrain mass assembly histories and chemical evolution in connection to the thin and thick discs and their possible association with bar ageing. Lastly, the edge-on perspective will bring a unique view of the nuclear disc evolution and the possible 2 phases proposed in this Thesis.

A

Individual results

Camila de Sá-Freitas; and TIMER team

in prep.

In this Appendix, we present in details the individual results for each galaxy from Chapter 4, following Fig. 4.3. We display, for each object, the derived spatial maps of V/σ, mean light-weighted age, and star formation rate, indicating the nuclear disc and representative ring. We also present the star formation histories derived following the methodology presented here (Chapters 2 and 4), with the radial star formation history analysis. Lastly, we investigate how different stellar populations bins dominate the mass in the central region of the galaxy.

---

[2]https://www.eso.org/public/images/potw1212a/
[3]https://www.eso.org/public/spain/images/ngc4303-muse-alma-sbs/?lang
[4]https://noirlab.edu/public/es/images/noao-n5248niksch/?nocache=true

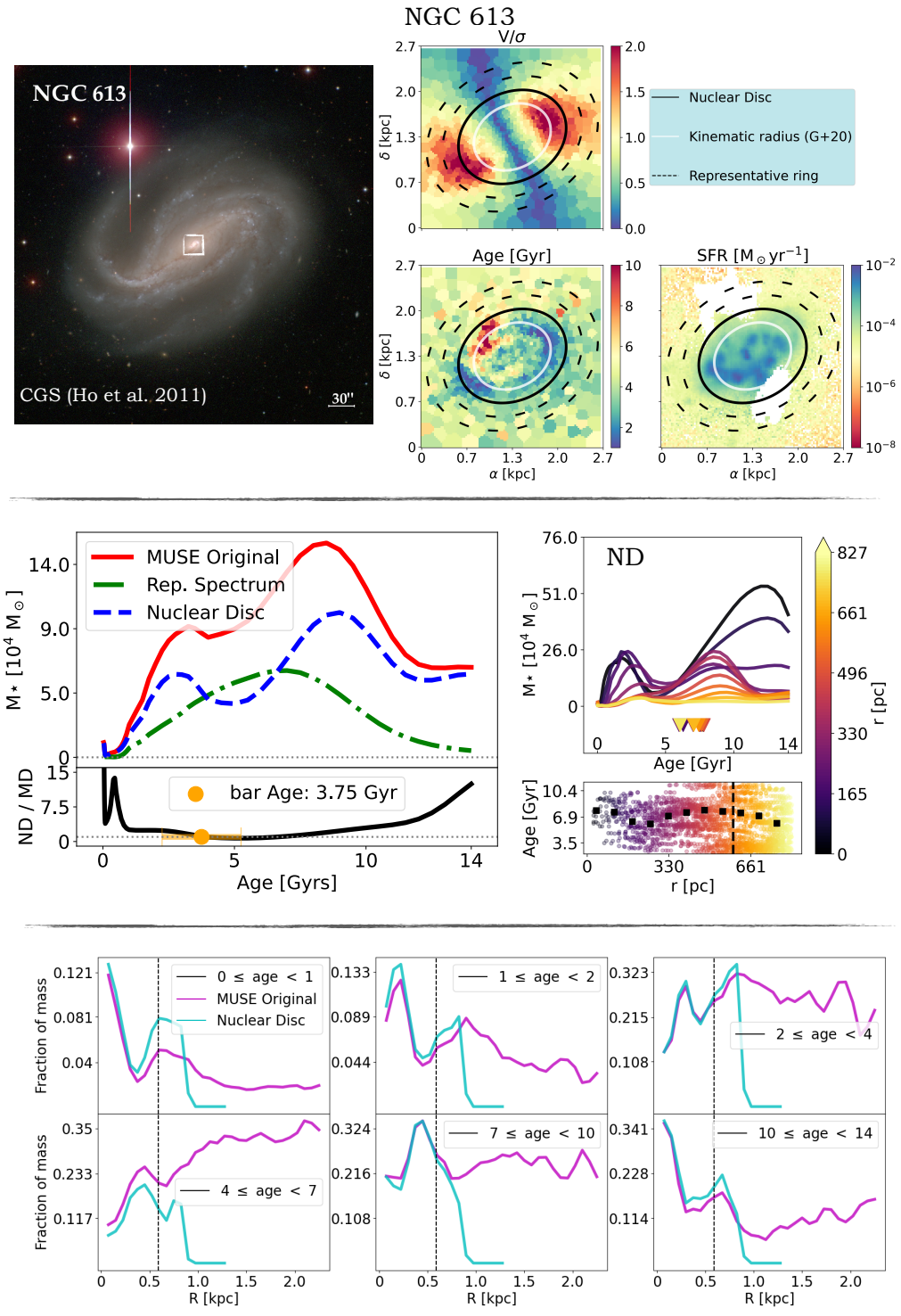

Figure A.1: Same as Fig. 4.3 for NGC 613, but the galaxy image is from CGS (Ho et al., 2011).

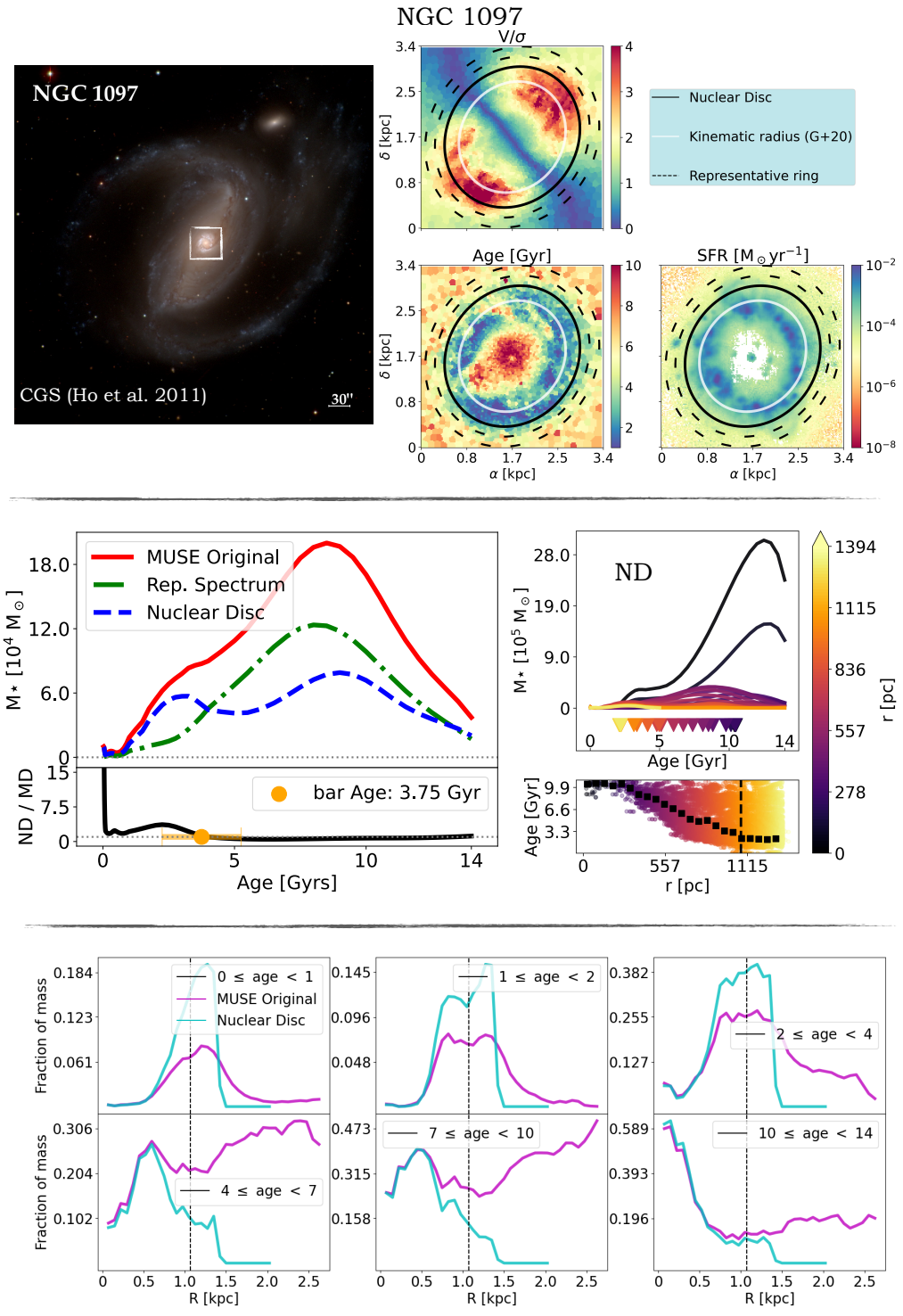

Figure A.2: Same as Fig. 4.3 for NGC 1097, but the galaxy image is from CGS (Ho et al., 2011).

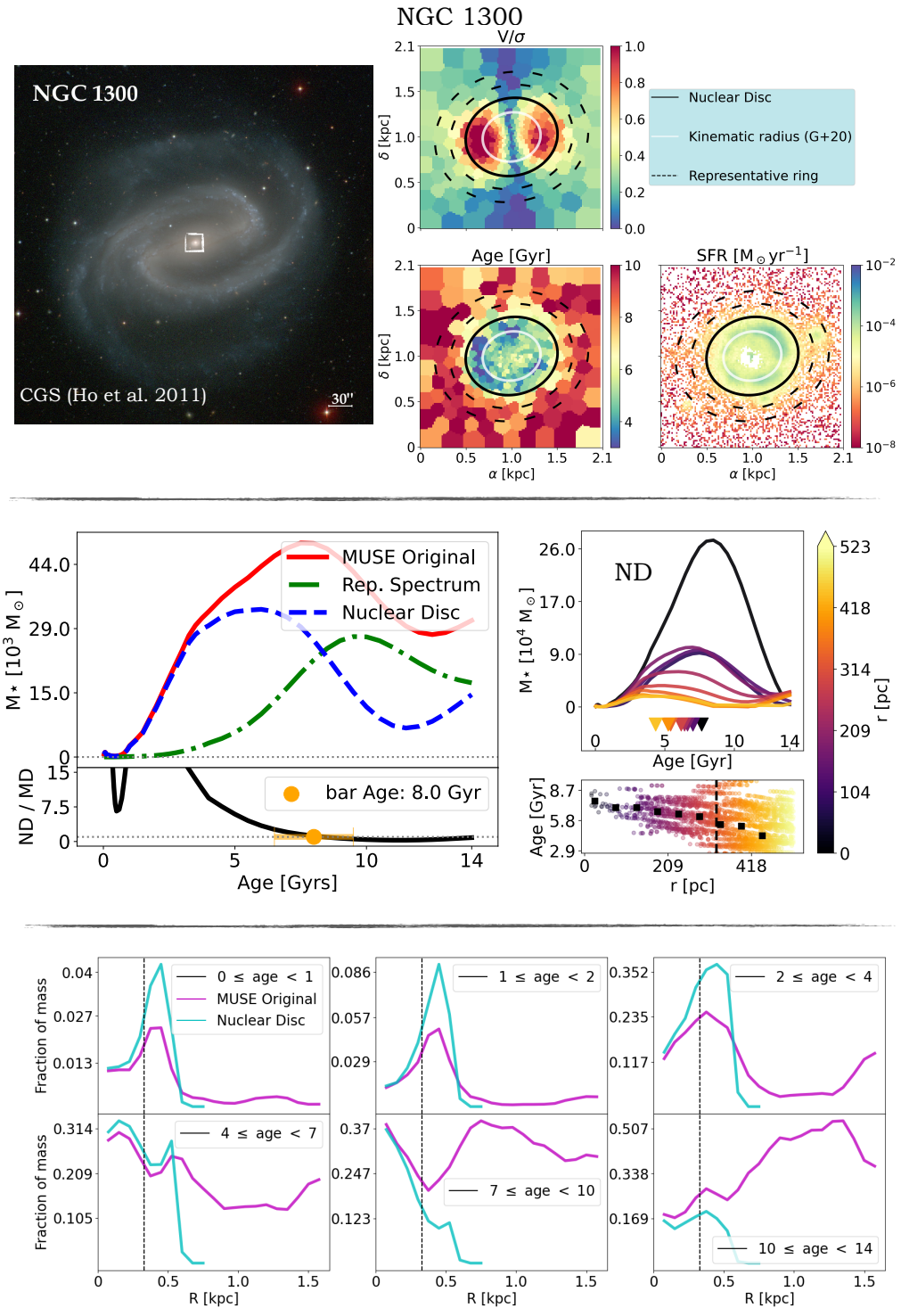

Figure A.3: Same as Fig. 4.3 for NGC 1300, but the galaxy image is from CGS (Ho et al., 2011).

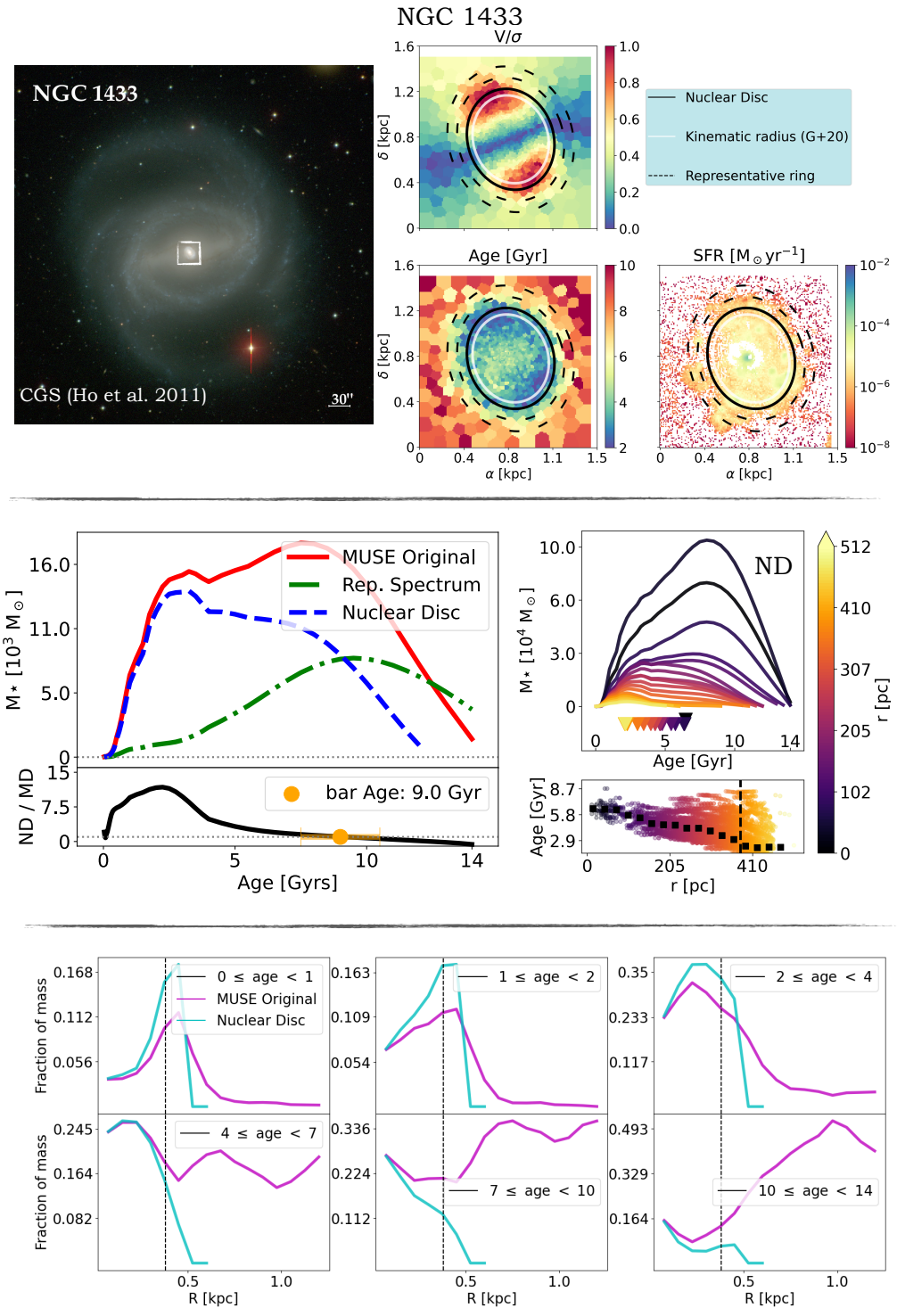

Figure A.4: Same as Fig. 4.3 for NGC 1433, but the galaxy image is from CGS (Ho et al., 2011).

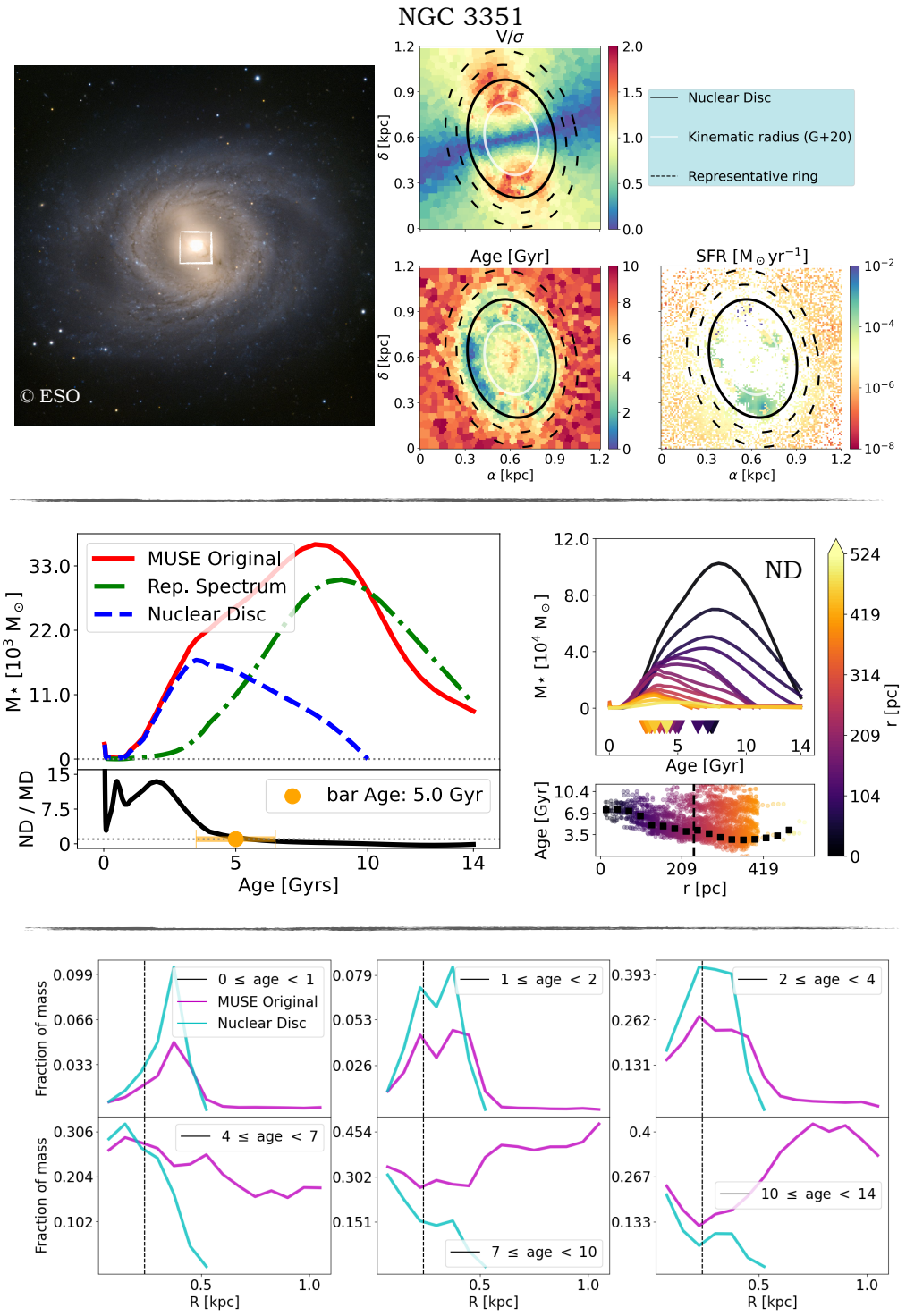

Figure A.5: Same as Fig. 4.3 for NGC 3351, but the galaxy image is from ESO press release[2].

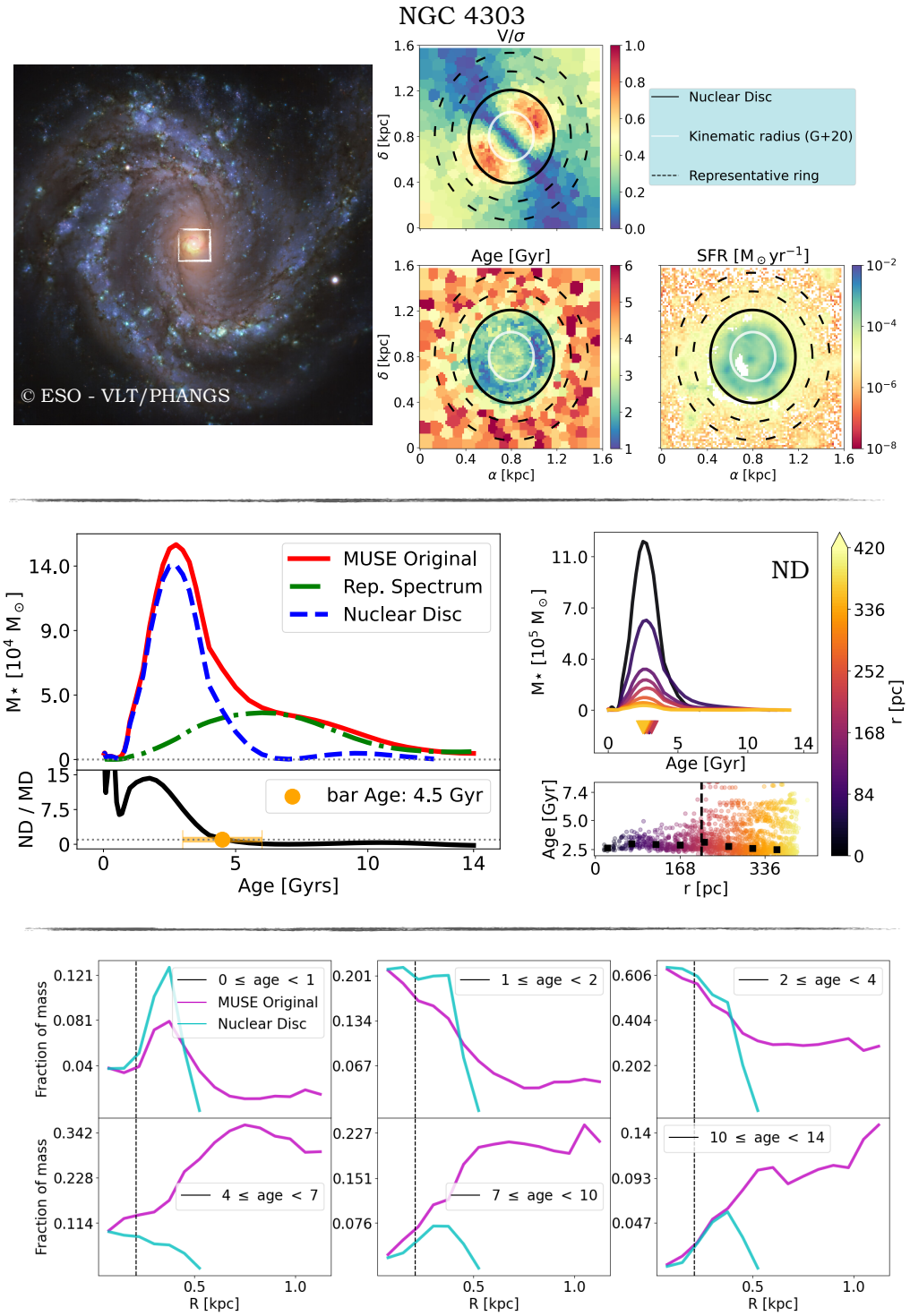

Figure A.6: Same as Fig. 4.3 for NGC 4303, but the galaxy image is from ESO/PHANGS[3].

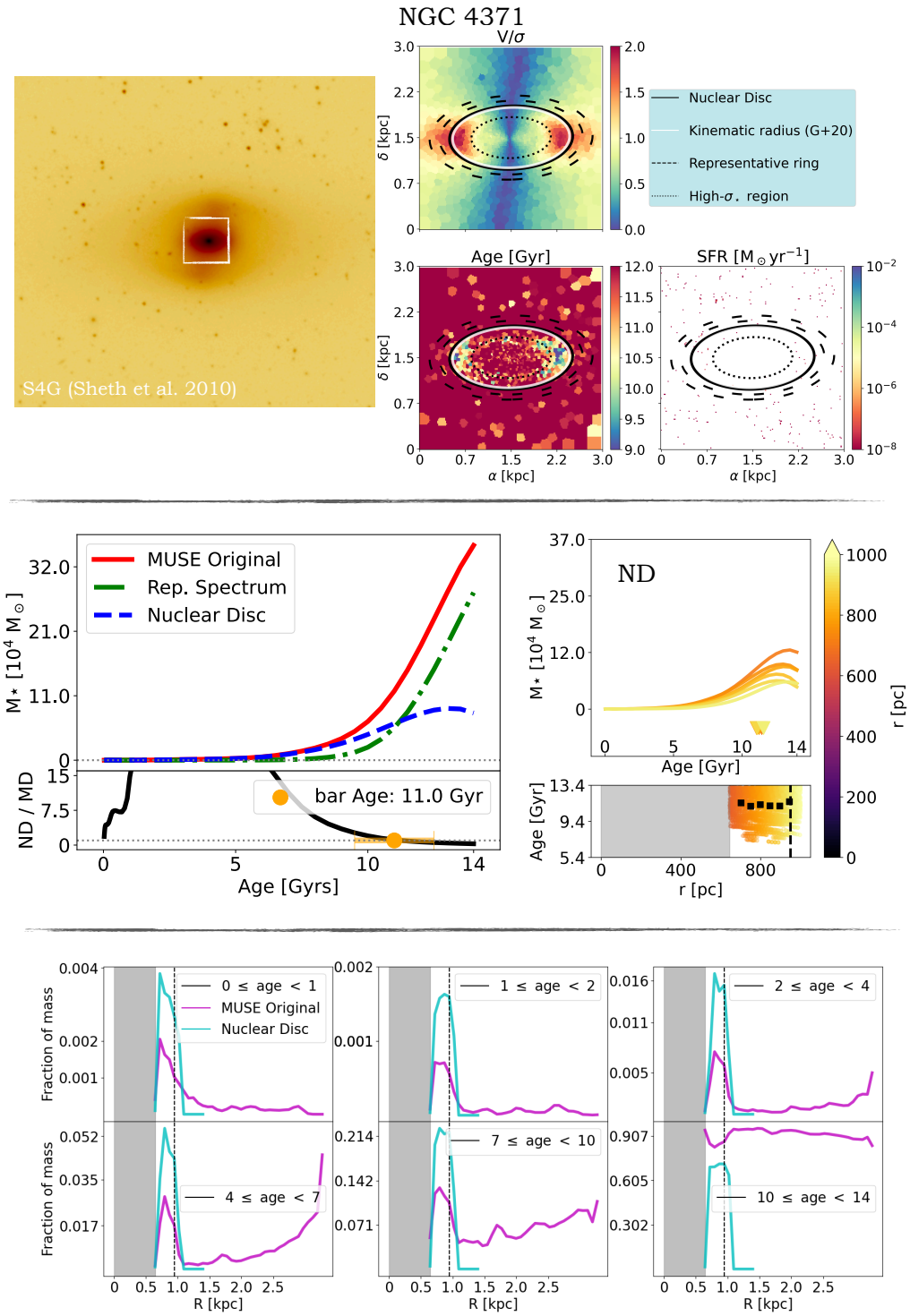

Figure A.7: Same as Fig. 4.3 for NGC 4371.

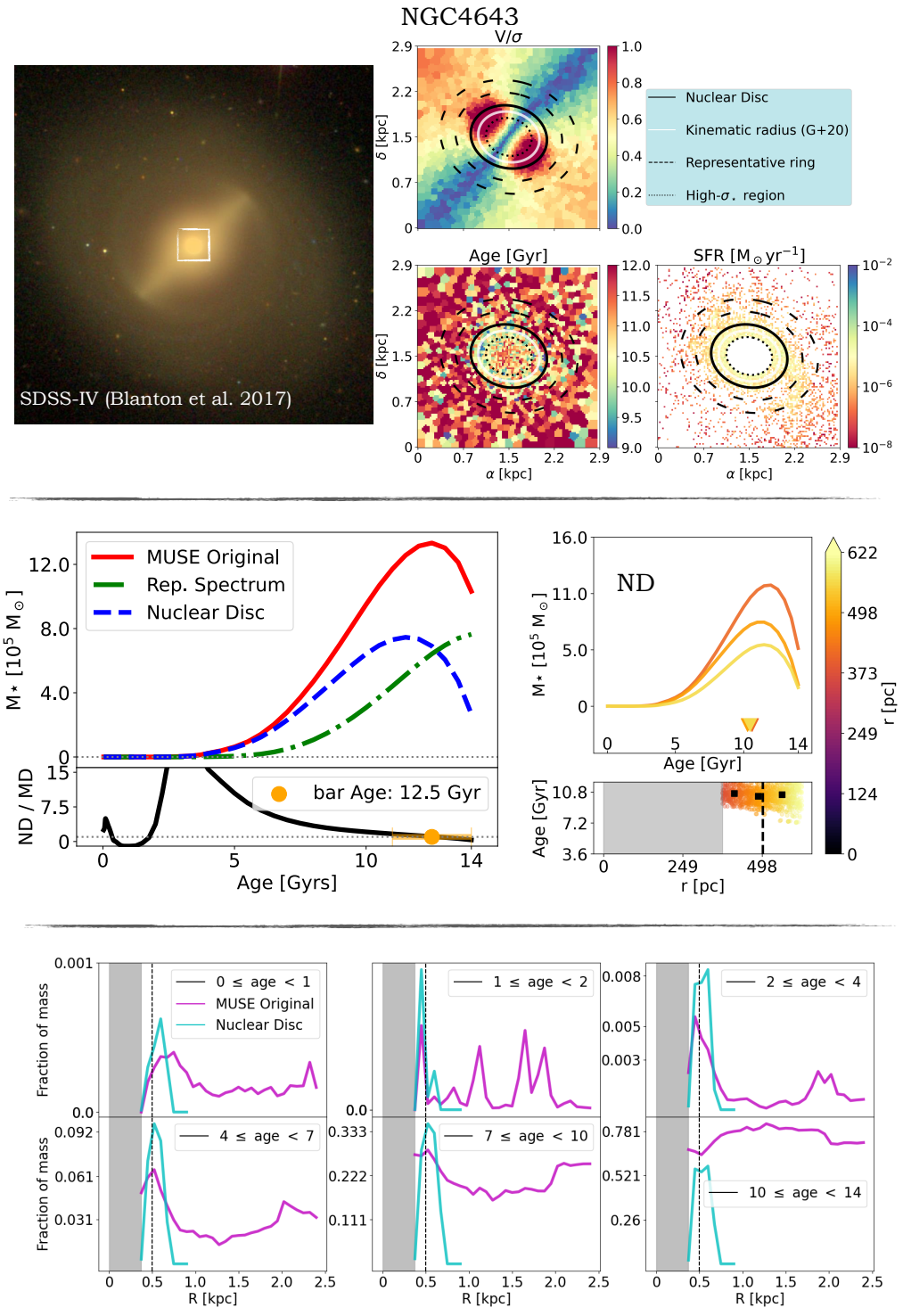

Figure A.8: Same as Fig. 4.3 for NGC 4303, but the galaxy image is from SDSS-IV (Blanton et al., 2017).

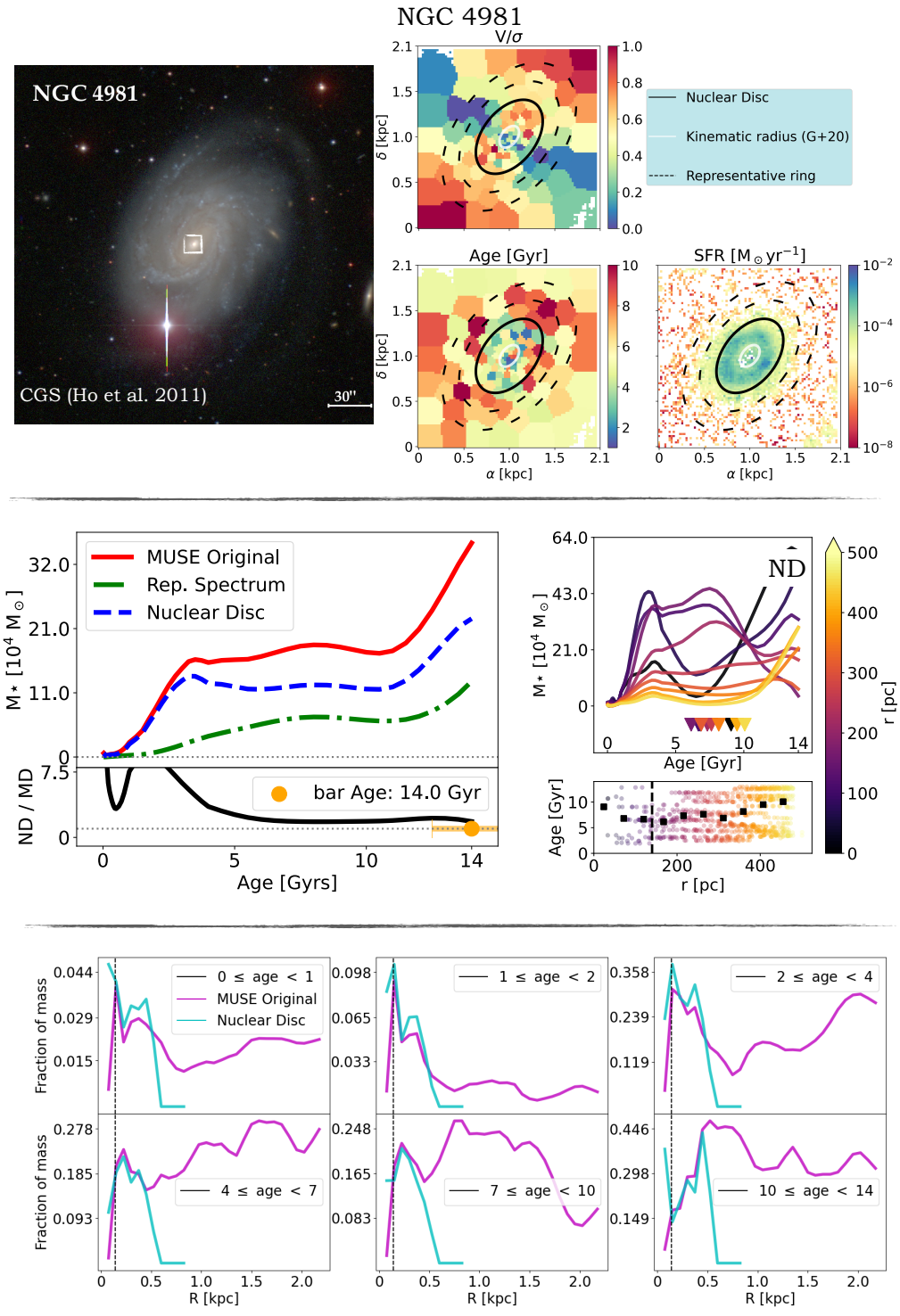

Figure A.9: Same as Fig. 4.3 for NGC 4981, but the galaxy image is from CSG (Ho et al., 2011).

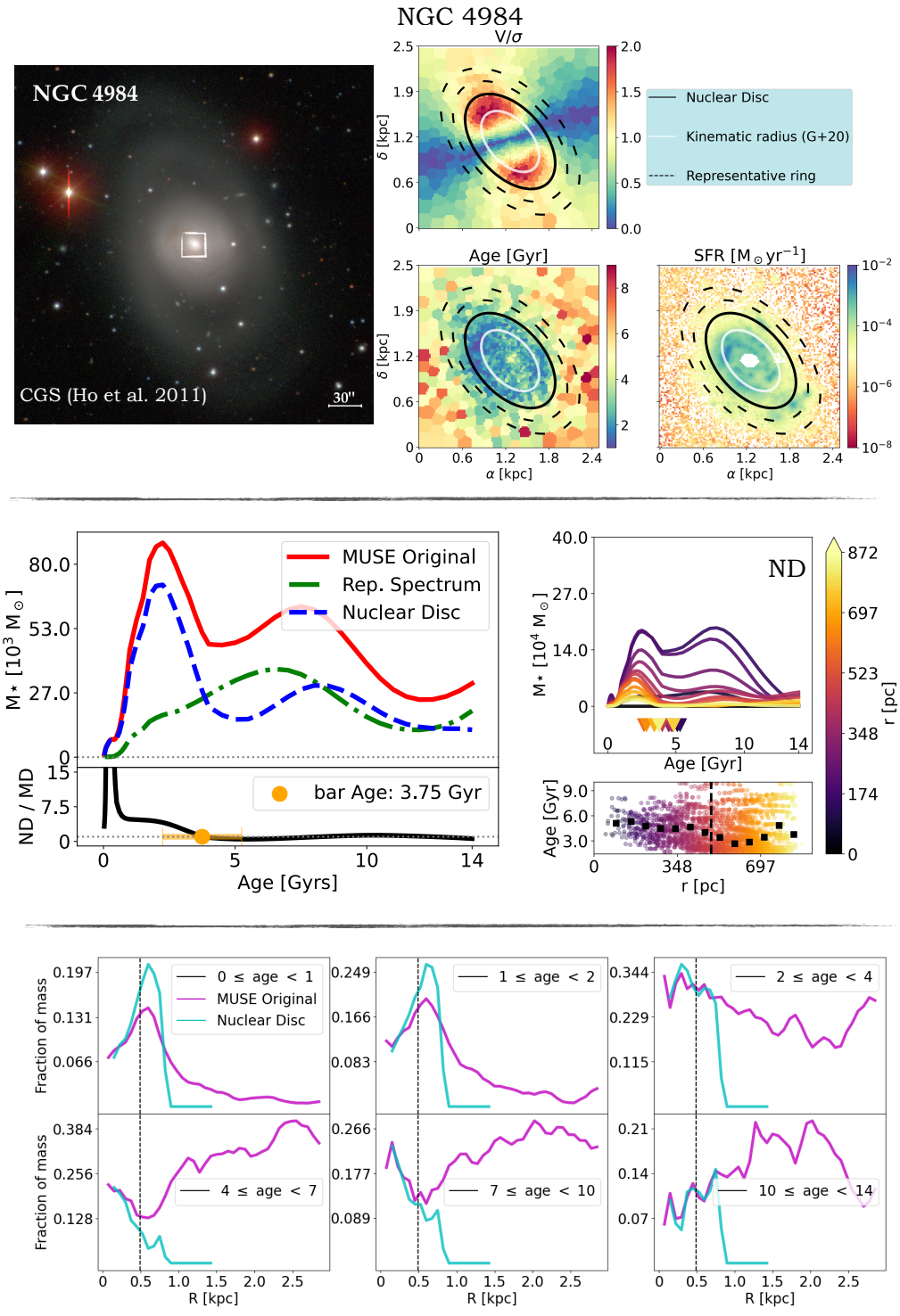

Figure A.10: Same as Fig. 4.3 for NGC 4984, but the galaxy image is from CSG (Ho et al., 2011).

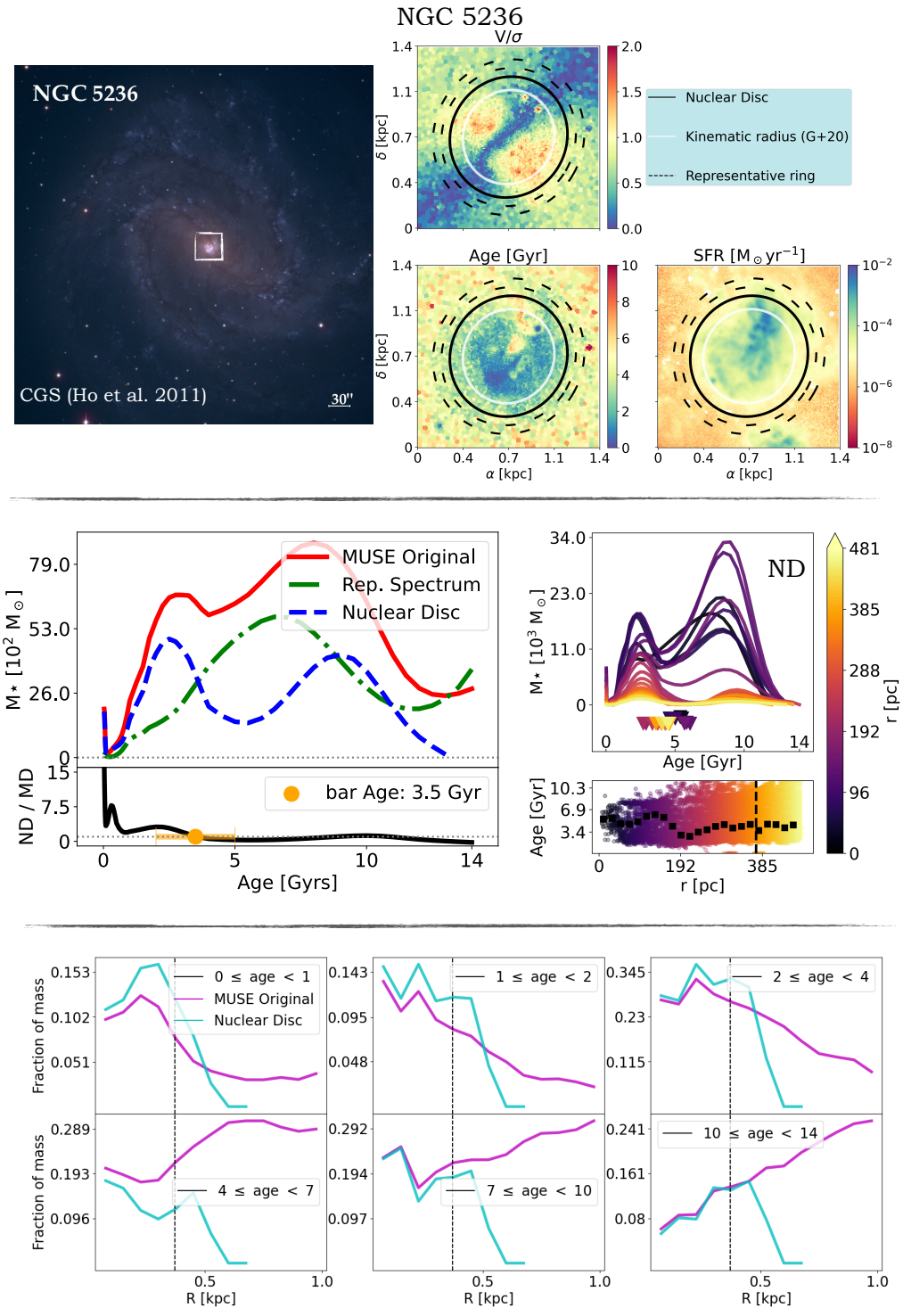

Figure A.11: Same as Fig. 4.3 for NGC 5236, but the galaxy image is from CSG (Ho et al., 2011).

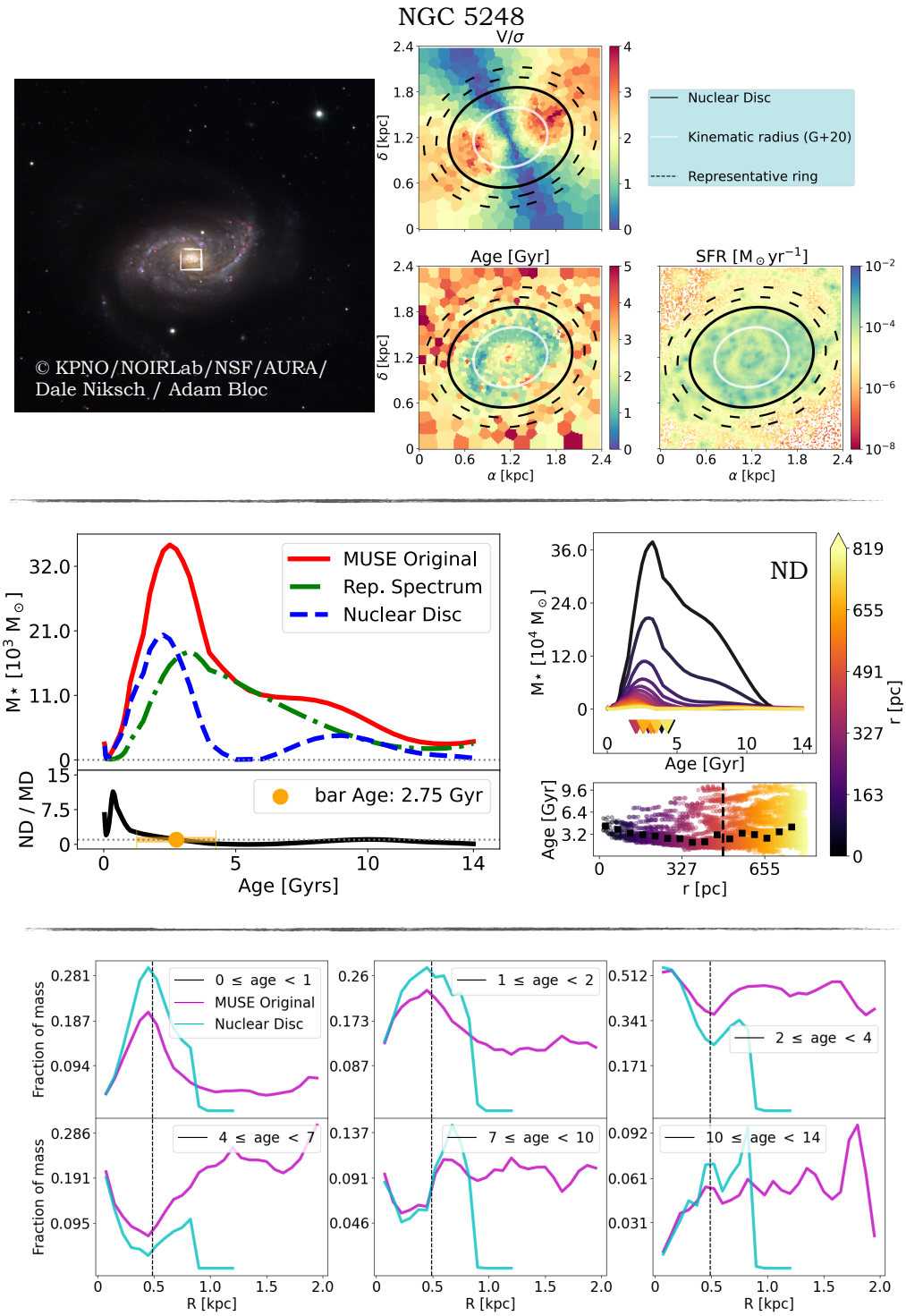

Figure A.12: Same as Fig. 4.3 for NGC 5248, but the galaxy image is from NoirLab+[4].

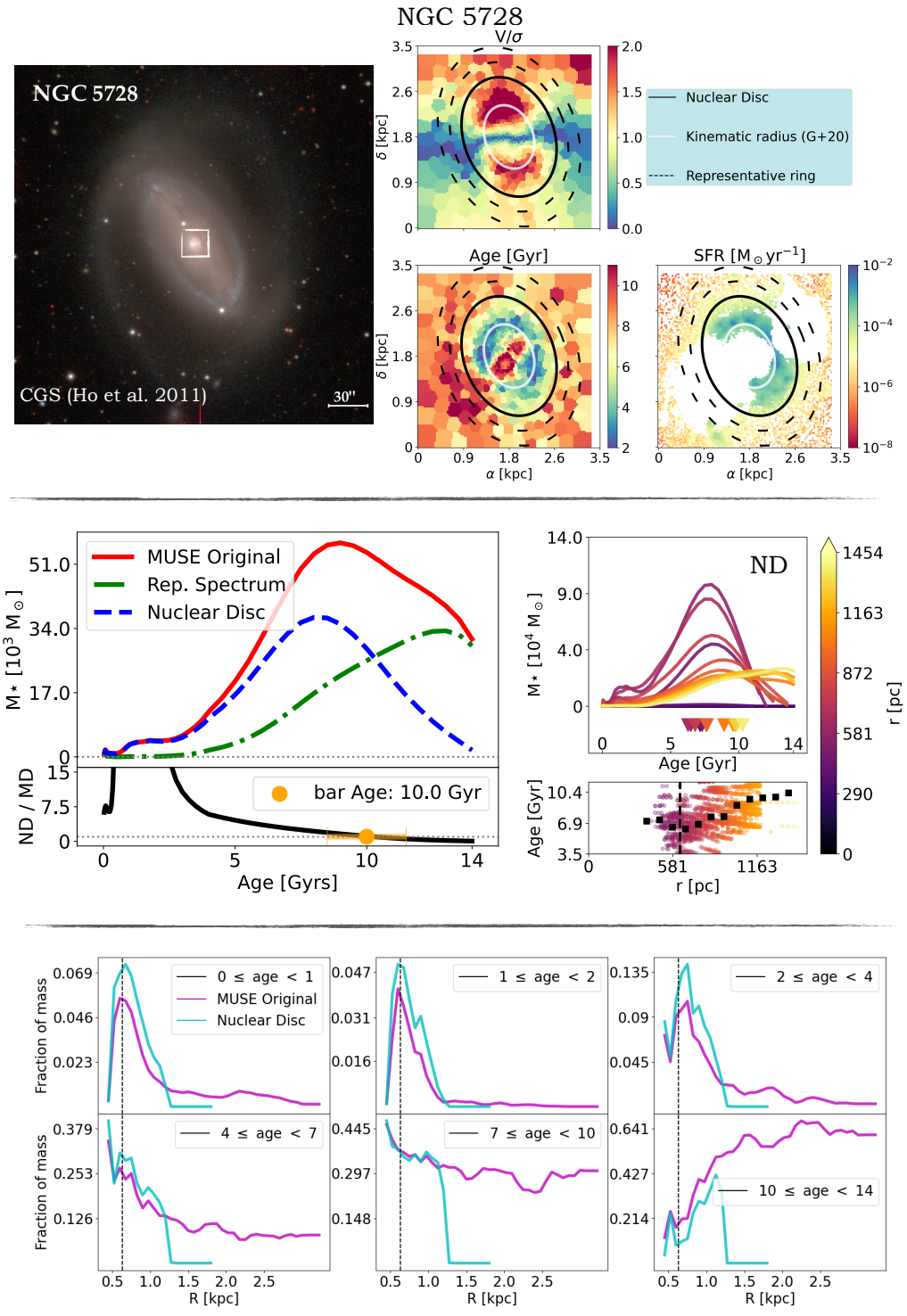

Figure A.13: Same as Fig. 4.3 for NGC 5728, but the galaxy image is from CSG (Ho et al., 2011).

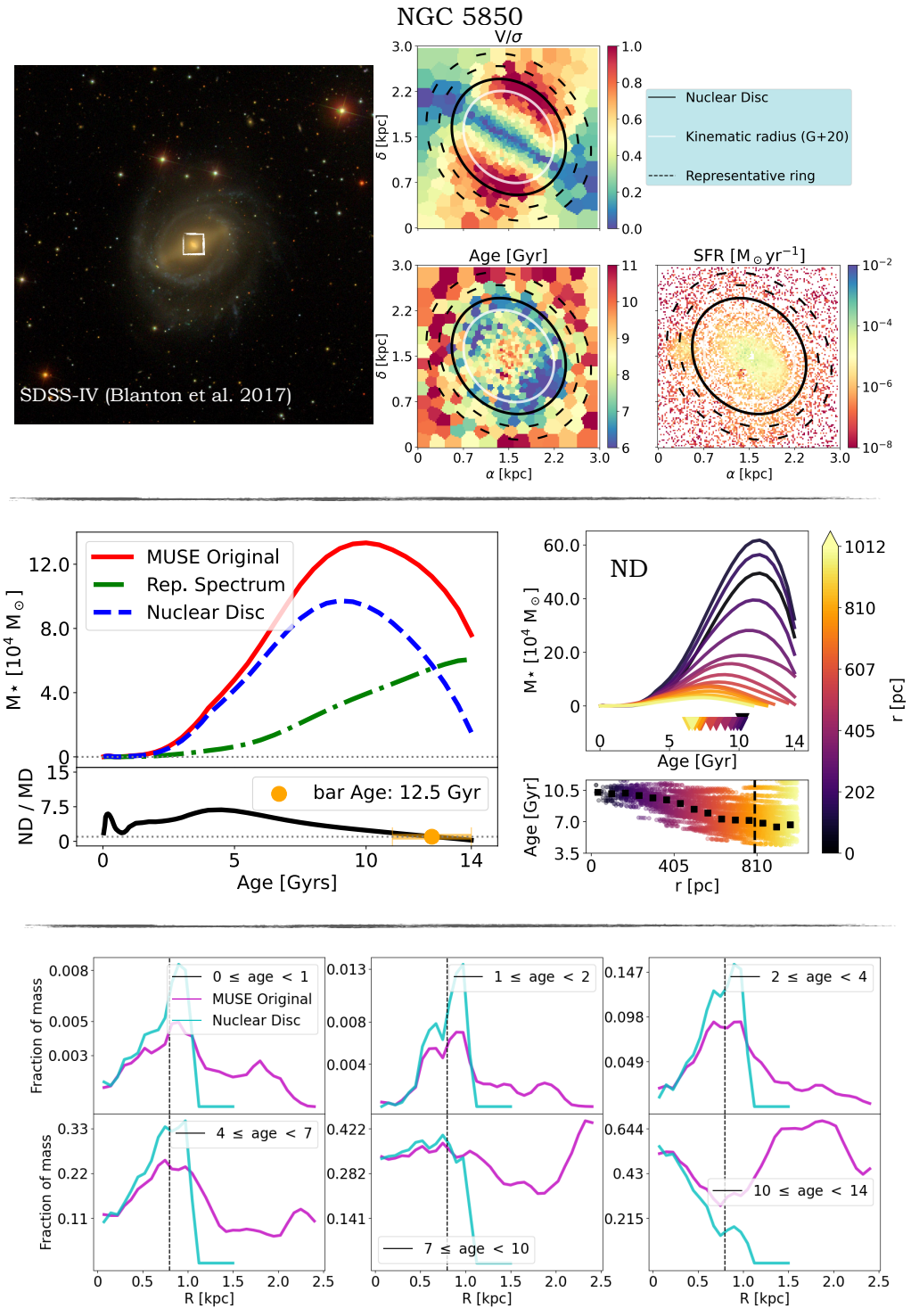

Figure A.14: Same as Fig. 4.3 for NGC 5850, but the galaxy image is from SDSS-IV (Blanton et al., 2017).

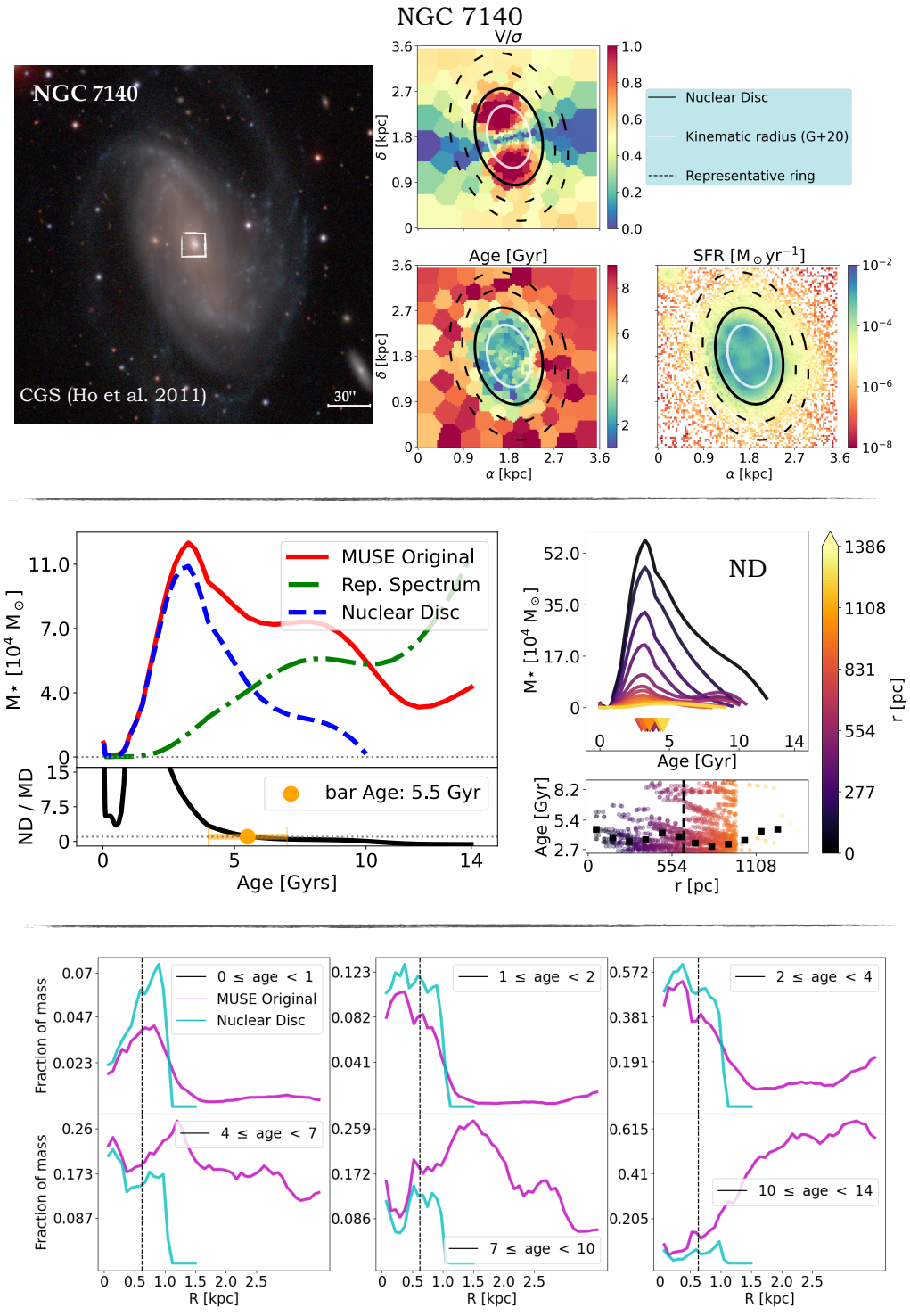

Figure A.15: Same as Fig. 4.3 for NGC 7140, but the galaxy image is from CSG (Ho et al., 2011).

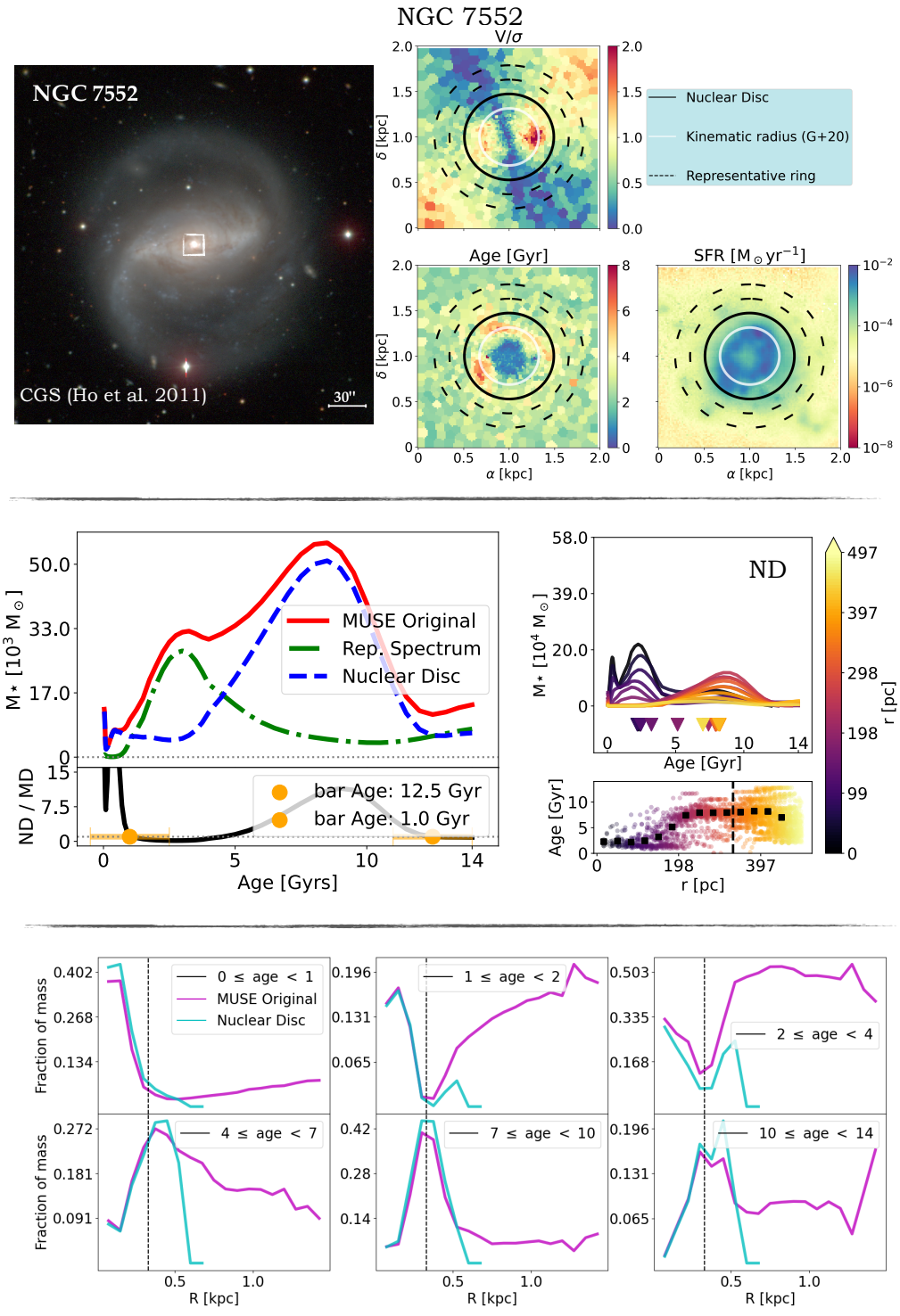

Figure A.16: Same as Fig. 4.3 for NGC 7552, but the galaxy image is from CSG (Ho et al., 2011).

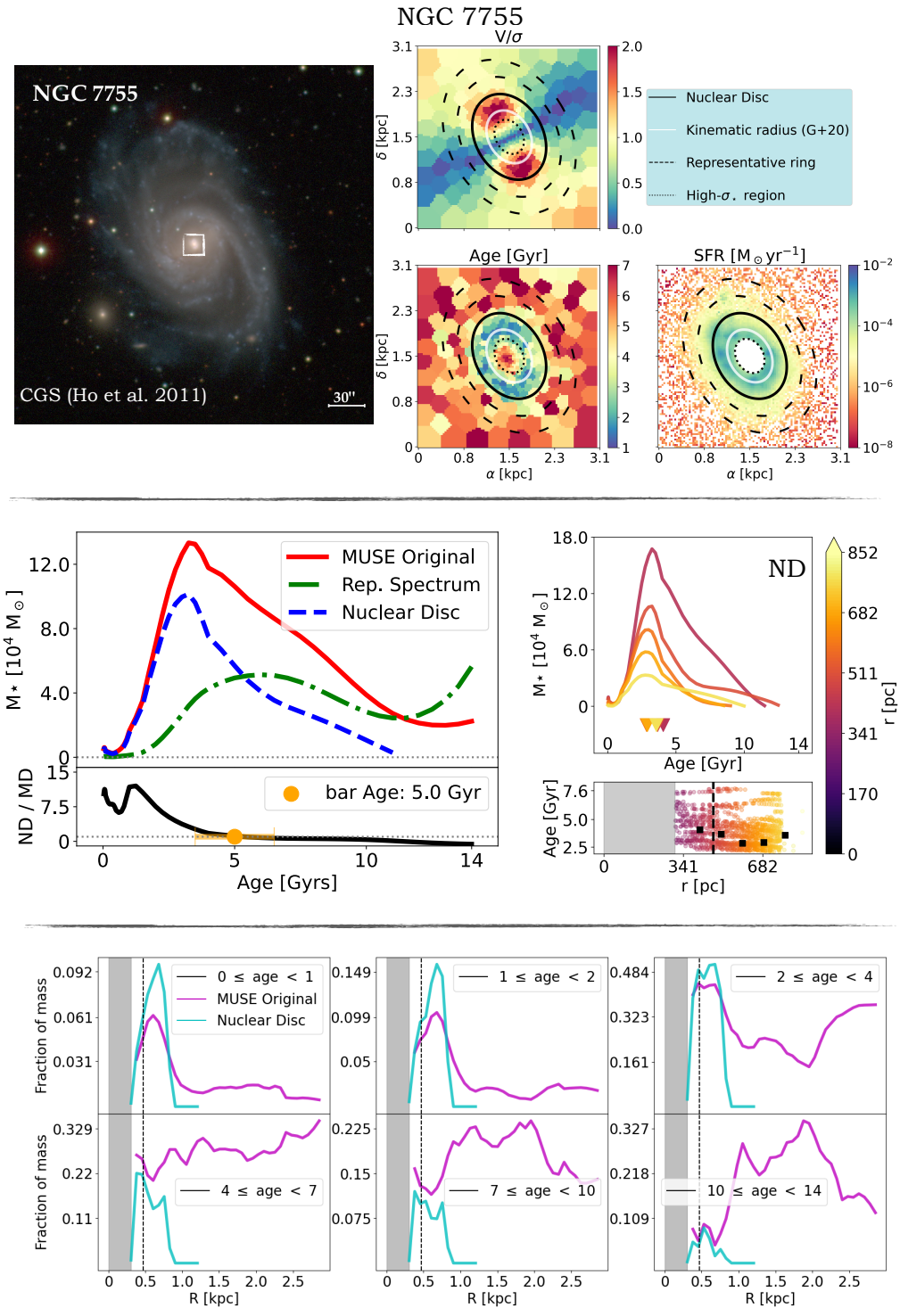

Figure A.17: Same as Fig. 4.3 for NGC 7755, but the galaxy image is from CSG (Ho et al., 2011).

Bibliography

Agertz, O., Teyssier, R., & Moore, B. 2011, Monthly Notices of the Royal Astronomical Society, 410, 1391

Aguerri, J., Beckman, J., & Prieto, M. 1998, The Astronomical Journal, 116, 2136

Aguerri, J., Méndez-Abreu, J., & Corsini, E. 2009, Astronomy & Astrophysics, 495, 491

Aguerri, J., Munoz-Tunón, C., Varela, A., & Prieto, M. 2000, Astronomy and Astrophysics, 361, 841

Algorry, D. G., Navarro, J. F., Abadi, M. G., et al. 2017, Monthly Notices of the Royal Astronomical Society, 469, 1054

Anderson, S. R., Debattista, V. P., Erwin, P., et al. 2022, Monthly Notices of the Royal Astronomical Society, 513, 1642

Arsenault, R. 1989, Astronomy and Astrophysics (ISSN 0004-6361), vol. 217, no. 1-2, June 1989, p. 66-78. Research supported by the European Southern Observatory., 217, 66

Athanassoula, E. 1992, Monthly Notices of the Royal Astronomical Society, 259, 345

Athanassoula, E. 1992a, MNRAS, 259, 328

Athanassoula, E. 1992b, MNRAS, 259, 345

Athanassoula, E. 2002, The Astrophysical Journal, 569, L83

Athanassoula, E. 2005, Monthly Notices of the Royal Astronomical Society, 358, 1477

Athanassoula, E., Lambert, J., & Dehnen, W. 2005, Monthly Notices of the Royal Astronomical Society, 363, 496

Athanassoula, E., Machado, R. E., & Rodionov, S. 2013, Monthly Notices of the Royal Astronomical Society, 429, 1949

Athanassoula, E., Rodionov, S., Peschken, N., & Lambert, J. 2016, The Astrophysical Journal, 821, 90

Athanassoula, L. 2003, Galaxies and Chaos, 313

Audibert, A., Combes, F., García-Burillo, S., et al. 2021, Astronomy & Astrophysics, 656, A60

Aumer, M. & Binney, J. 2017, Monthly Notices of the Royal Astronomical Society, 470, 2113

Baba, J. & Kawata, D. 2020, Monthly Notices of the Royal Astronomical Society, 492, 4500

Baldwin, J. A., Phillips, M. M., & Terlevich, R. 1981, Publications of the Astronomical Society of the Pacific, 93, 5

Barazza, F. D., Jogee, S., & Marinova, I. 2008, The Astrophysical Journal, 675, 1194

Beckman, J. E. & Mahoney, T. J. 1999, Publications of the Astronomical Society of the Pacific, 111, 523

Belokurov, V. & Kravtsov, A. 2022, Monthly Notices of the Royal Astronomical Society, 514, 689

Bendo, G. J. & Joseph, R. D. 2004, The Astronomical Journal, 127, 3338

Berentzen, I., Athanassoula, E., Heller, C., & Fricke, K. 2004, Monthly Notices of the Royal Astronomical Society, 347, 220

Berentzen, I., Shlosman, I., Martinez-Valpuesta, I., & Heller, C. H. 2007, The Astrophysical Journal, 666, 189

Bertola, F. & Capaccioli, M. 1975, Astrophysical Journal, vol. 200, Sept. 1, 1975, pt. 1, p. 439-445., 200, 439

Binney, J. 1981, Monthly Notices of the Royal Astronomical Society, 196, 455

Binney, J. & Tremaine, S. 1987, Princeton, NJ, Princeton University Press, 1987, 747

Binney, J. & Tremaine, S. 2008, Galactic Dynamics 2nd ed. ed J

Bittner, A., de Lorenzo-Cáceres, A., Gadotti, D. A., et al. 2021, Astronomy & Astrophysics, 646, A42

Bittner, A., Falcón-Barroso, J., Nedelchev, B., et al. 2019, Astronomy & Astrophysics, 628, A117

Bittner, A., Sánchez-Blázquez, P., Gadotti, D. A., et al. 2020, Astronomy & Astrophysics, 643, A65

Blanton, M. R., Bershady, M. A., Abolfathi, B., et al. 2017, The Astronomical Journal, 154, 28

Bournaud, F. & Combes, F. 2002, Astronomy & Astrophysics, 392, 83

Bournaud, F., Jog, C., & Combes, F. 2005, Astronomy & Astrophysics, 437, 69

Breda, I., Papaderos, P., & Gomes, J.-M. 2020, Astronomy & Astrophysics, 640, A20

Brook, C. B., Kawata, D., Gibson, B. K., & Flynn, C. 2004, Monthly Notices of the Royal Astronomical Society, 349, 52

Brook, C. B., Stinson, G., Gibson, B. K., et al. 2012, Monthly Notices of the Royal Astronomical Society, 426, 690

Buta, R. 1995, Astrophysical Journal Supplement Series (ISSN 0067-0049), vol. 96, no. 1, p. 39-116, 96, 39

Buta, R. J. & Combes, F. 1996

Buta, R. J., Sheth, K., Athanassoula, E., et al. 2015, The Astrophysical Journal Supplement Series, 217, 32

Buta, R. J., Sheth, K., Regan, M., et al. 2010, The Astrophysical Journal Supplement Series, 190, 147

Cameron, E., Carollo, C. M., Oesch, P., et al. 2010, Monthly Notices of the Royal Astronomical Society, 409, 346

Cappellari, M. 2012, Astrophysics Source Code Library, ascl

Cappellari, M. 2017, Monthly Notices of the Royal Astronomical Society, 466, 798

Cappellari, M. & Copin, Y. 2003, Monthly Notices of the Royal Astronomical Society, 342, 345

Cappellari, M. & Emsellem, E. 2004, Publications of the Astronomical Society of the Pacific, 116, 138

Ceverino, D. & Klypin, A. 2007, Monthly Notices of the Royal Astronomical Society, 379, 1155

Chapelon, S., Contini, T., & Davoust, E. 1999, arXiv preprint astro-ph/9902174

Christensen, C. R., Davé, R., Governato, F., et al. 2016, The Astrophysical Journal, 824, 57

Coelho, P. & Gadotti, D. A. 2011, The Astrophysical Journal Letters, 743, L13

Cole, D. R., Debattista, V. P., Erwin, P., Earp, S. W., & Roškar, R. 2014, Monthly Notices of the Royal Astronomical Society, 445, 3352

Combes, F., Debbasch, F., Friedli, D., & Pfenniger, D. 1990, Astronomy and Astrophysics (ISSN 0004-6361), vol. 233, no. 1, July 1990, p. 82-95. Research supported by the Universite de Geneve and SNSF., 233, 82

Combes, F. & Elmegreen, B. 1993, Astronomy and Astrophysics, Vol. 271, NO. 2/APR, P. 391, 1993, 271, 391

Combes, F. & Gerin, M. 1985, Astronomy and Astrophysics, 150, 327

Combes, F. & Sanders, R. 1981, Astronomy and Astrophysics, 96, 164

Comerón, S., Knapen, J., Beckman, J., et al. 2010, Monthly Notices of the Royal Astronomical Society, 402, 2462

Conroy, C., Weinberg, D. H., Naidu, R. P., et al. 2022, arXiv preprint arXiv:2204.02989

Conselice, C. J., Rajgor, S., & Myers, R. 2008, Monthly Notices of the Royal Astronomical Society, 386, 909

Contopoulos, G. 1980, Astronomy and Astrophysics, vol. 81, no. 1-2, Jan. 1980, p. 198-209., 81, 198

Contopoulos, G. & Grosbol, P. 1989, Astronomy and Astrophysics Review, 1, 261

Contopoulos, G. & Papayannopoulos, T. 1980, Astronomy and Astrophysics, vol. 92, no. 1-2, Dec. 1980, p. 33-46., 92, 33

Cook, M., Barausse, E., Evoli, C., Lapi, A., & Granato, G. 2010, Monthly Notices of the Royal Astronomical Society, 402, 2113

Cowie, L. L., Songaila, A., Hu, E. M., & Cohen, J. 1996, arXiv preprint astro-ph/9606079

Cresci, G., Hicks, E., Genzel, R., et al. 2009, The Astrophysical Journal, 697, 115

Cuomo, V., Corsini, E. M., Aguerri, A. J., & Debattista, V. P. 2019, Proceedings of the International Astronomical Union, 14, 172

Davies, R., Maciejewski, W., Hicks, E., et al. 2014, The Astrophysical Journal, 792, 101

Davis, M., Efstathiou, G., Frenk, C. S., & White, S. D. 1985, Astrophysical Journal, Part 1 (ISSN 0004-637X), vol. 292, May 15, 1985, p. 371-394. Research supported by the Science and Engineering Research Council of England and NASA., 292, 371

de Bernardis, P., Ade, P. A., Bock, J. J., et al. 2000, Nature, 404, 955

de Jong, R. S. 1996, Astronomy and Astrophysics Supplement Series, 118, 557

de Lorenzo-Cáceres, A., Méndez-Abreu, J., Thorne, B., & Costantin, L. 2020, Monthly Notices of the Royal Astronomical Society, 494, 1826

de Lorenzo-Cáceres, A., Sánchez-Blázquez, P., Méndez-Abreu, J., et al. 2019, Monthly Notices of the Royal Astronomical Society, 484, 5296

de Sá-Freitas, C., Fragkoudi, F., Gadotti, D. A., et al. 2023, Astronomy & Astrophysics, 671, A8

De Souza, R. & Dos Anjos, S. 1987, Astronomy and Astrophysics Supplement Series (ISSN 0365-0138), vol. 70, no. 3, Sept. 1987, p. 465-480., 70, 465

De Vaucouleurs, G. 1959, in Astrophysik iv: Sternsysteme/astrophysics iv: Stellar systems (Springer), 275–310

de Vaucouleurs, G., de Vaucouleurs, A., Corwin, Herold G., J., et al. 1991, Third Reference Catalogue of Bright Galaxies

Debattista, V. P., Mayer, L., Carollo, C. M., et al. 2006, The Astrophysical Journal, 645, 209

Debattista, V. P. & Sellwood, J. 1998, The Astrophysical Journal, 493, L5

Debattista, V. P. & Sellwood, J. 2000, The Astrophysical Journal, 543, 704

Debattista, V. P. & Williams, T. 2004, The Astrophysical Journal, 605, 714

Dekel, A., Ceverino, D., et al. 2009, The Astrophysical Journal, 703, 785

Di Matteo, P., Haywood, M., Combes, F., Semelin, B., & Snaith, O. N. 2013, A&A, 553, A102

Di Matteo, P., Haywood, M., Gómez, A., et al. 2014, Astronomy & Astrophysics, 567, A122

Díaz-García, S., Salo, H., Laurikainen, E., & Herrera-Endoqui, M. 2016, A&A, 587, A160

Díaz-García, S., Salo, H., Laurikainen, E., & Herrera-Endoqui, M. 2016, Astronomy & Astrophysics, 587, A160

Eggen, O., Lynden-Bell, D., & Sandage, A. 1962, Astrophysical Journal, vol. 136, p. 748, 136, 748

Ellison, S. L., Nair, P., Patton, D. R., et al. 2011, Monthly Notices of the Royal Astronomical Society, 416, 2182

Elmegreen, B. 1996, in International Astronomical Union Colloquium, Vol. 157, Cambridge University Press, 197–206

Elmegreen, B. G. & Elmegreen, D. M. 1985, Astrophysical Journal, Part 1 (ISSN 0004-637X), vol. 288, Jan. 15, 1985, p. 438-455., 288, 438

Elmegreen, B. G. & Elmegreen, D. M. 2006, The Astrophysical Journal, 650, 644

Elmegreen, D. M., Elmegreen, B. G., Ravindranath, S., & Coe, D. A. 2007, The Astrophysical Journal, 658, 763

Emsellem, E., Renaud, F., Bournaud, F., et al. 2015, Monthly Notices of the Royal Astronomical Society, 446, 2468

Emsellem, E., Schinnerer, E., Santoro, F., et al. 2022, Astronomy & Astrophysics, 659, A191

Epinat, B., Tasca, L., Amram, P., et al. 2012, Astronomy & Astrophysics, 539, A92

Erroz-Ferrer, S., Carollo, C. M., Den Brok, M., et al. 2019, Monthly Notices of the Royal Astronomical Society, 484, 5009

Erwin, P. 2004, Astronomy & Astrophysics, 415, 941

Erwin, P. 2005, Monthly Notices of the Royal Astronomical Society, 364, 283

Erwin, P. 2018, Monthly Notices of the Royal Astronomical Society, 474, 5372

Erwin, P. 2019, Monthly Notices of the Royal Astronomical Society, 489, 3553

Erwin, P. & Debattista, V. P. 2017, Monthly Notices of the Royal Astronomical Society, 468, 2058

Erwin, P., Debattista, V. P., & Anderson, S. R. 2023, Monthly Notices of the Royal Astronomical Society, 524, 3166

Erwin, P., Saglia, R. P., Fabricius, M., et al. 2015, Monthly Notices of the Royal Astronomical Society, 446, 4039

Erwin, P. & Sparke, L. S. 2003, The Astrophysical Journal Supplement Series, 146, 299

Eskridge, P. B., Frogel, J. A., Pogge, R. W., et al. 2000, The Astronomical Journal, 119, 536

Falcón-Barroso, J., Bacon, R., Bureau, M., et al. 2006, Monthly Notices of the Royal Astronomical Society, 369, 529

Falcón-Barroso, J., Peletier, R. F., & Balcells, M. 2002, Monthly Notices of the Royal Astronomical Society, 335, 741

Fall, S. M. & Efstathiou, G. 1980, Monthly Notices of the Royal Astronomical Society, 193, 189

Farouki, R. T. & Shapiro, S. L. 1982, The Astrophysical Journal, 259, 103

Ferreira, L., Adams, N., Conselice, C. J., et al. 2022a, The Astrophysical Journal Letters, 938, L2

Ferreira, L., Conselice, C. J., Sazonova, E., et al. 2022b, arXiv preprint arXiv:2210.01110

Fragkoudi, F., Athanassoula, E., & Bosma, A. 2016, MNRAS, 462, L41

Fragkoudi, F., Athanassoula, E., & Bosma, A. 2016, Monthly Notices of the Royal Astronomical Society: Letters, 462, L41

Fragkoudi, F., Di Matteo, P., Haywood, M., et al. 2017, A&A, 606, A47

Fragkoudi, F., Di Matteo, P., Haywood, M., et al. 2017, Astronomy & Astrophysics, 607, L4

Fragkoudi, F., Di Matteo, P., Haywood, M., et al. 2018, Astronomy & Astrophysics, 616, A180

Fragkoudi, F., Grand, R. J., Pakmor, R., et al. 2020, Monthly Notices of the Royal Astronomical Society, 494, 5936

Fragkoudi, F., Grand, R. J., Pakmor, R., et al. 2021, Astronomy & Astrophysics, 650, L16

Fragkoudi, F., Grand, R. J. J., Pakmor, R., et al. 2020, MNRAS, 494, 5936

Fragkoudi, F., Grand, R. J. J., Pakmor, R., et al. 2021, A&A, 650, L16

Fraser-McKelvie, A., Merrifield, M., Aragón-Salamanca, A., et al. 2020, Monthly Notices of the Royal Astronomical Society, 499, 1116

Friedli, D. & Benz, W. 1993, Astronomy and Astrophysics (ISSN 0004-6361), vol. 268, no. 1, p. 65-85., 268, 65

Gadotti, D. A. 2009, Monthly Notices of the Royal Astronomical Society, 393, 1531

Gadotti, D. A. 2011, MNRAS, 415, 3308

Gadotti, D. A., Bittner, A., Falcón-Barroso, J., et al. 2020, Astronomy & Astrophysics, 643, A14

Gadotti, D. A. & de Souza, R. E. 2005, The Astrophysical Journal, 629, 797

Gadotti, D. A., Sánchez-Blázquez, P., Falcón-Barroso, J., et al. 2019, Monthly Notices of the Royal Astronomical Society, 482, 506

Gadotti, D. A., Seidel, M. K., Sánchez-Blázquez, P., et al. 2015, Astronomy & Astrophysics, 584, A90

Gallo, E., Treu, T., Marshall, P. J., et al. 2010, The Astrophysical Journal, 714, 25

Gao, H., Ho, L. C., Barth, A. J., & Li, Z.-Y. 2019, The Astrophysical Journal Supplement Series, 244, 34

Garland, I. L., Fahey, M. J., Simmons, B. D., et al. 2023, Monthly Notices of the Royal Astronomical Society, 522, 211

Garma-Oehmichen, L., Cano-Díaz, M., Hernández-Toledo, H., et al. 2020, Monthly Notices of the Royal Astronomical Society, 491, 3655

Garma-Oehmichen, L., Hernández-Toledo, H., Aquino-Ortíz, E., et al. 2022, Monthly Notices of the Royal Astronomical Society, 517, 5660

Garnavich, P. M., Kirshner, R. P., Challis, P., et al. 1998, The Astrophysical Journal, 493, L53

Genzel, R., Burkert, A., Bouché, N., et al. 2008, The Astrophysical Journal, 687, 59

Gerhard, O. E. 1981, Monthly Notices of the Royal Astronomical Society, 197, 179

Gerin, M., Combes, F., & Athanassoula, E. 1989, Dynamics of Astrophysical Discs, 219

Gerin, M., Combes, F., & Athanassoula, E. 1990, Astronomy and Astrophysics, 230, 37

Géron, T., Smethurst, R. J., Lintott, C., et al. 2021, Monthly Notices of the Royal Astronomical Society, 507, 4389

Ghosh, S. & Di Matteo, P. 2023, arXiv preprint arXiv:2308.10948

Ghosh, S., Fragkoudi, F., Di Matteo, P., & Saha, K. 2023, Astronomy & Astrophysics, 674, A128

Ghosh, S., Saha, K., Di Matteo, P., & Combes, F. 2021, Monthly Notices of the Royal Astronomical Society, 502, 3085

Gilmore, G., Wyse, R. F., & Kuijken, K. 1989, Annual review of astronomy and astrophysics, 27, 555

Gonçalves, G., Coelho, P., Schiavon, R., & Usher, C. 2020, Monthly Notices of the Royal Astronomical Society, 499, 2327

Gott III, J. R. & Thuan, T. X. 1976, Astrophysical Journal, vol. 204, Mar. 15, 1976, pt. 1, p. 649-667., 204, 649

Goz, D., Monaco, P., Murante, G., & Curir, A. 2015, Monthly Notices of the Royal Astronomical Society, 447, 1774

Guo, R., Mao, S., Athanassoula, E., et al. 2019, Monthly Notices of the Royal Astronomical Society, 482, 1733

Guo, Y., Ferguson, H. C., Bell, E. F., et al. 2015, The Astrophysical Journal, 800, 39

Guo, Y., Jogee, S., Finkelstein, S. L., et al. 2023, The Astrophysical Journal Letters, 945, L10

Gurvich, A. B., Stern, J., Faucher-Giguère, C.-A., et al. 2023, Monthly Notices of the Royal Astronomical Society, 519, 2598

Hafen, Z., Stern, J., Bullock, J., et al. 2022, Monthly Notices of the Royal Astronomical Society, 514, 5056

Haines, C., Pereira, M., Smith, G. P., et al. 2015, The Astrophysical Journal, 806, 101

Halle, A., Di Matteo, P., Haywood, M., & Combes, F. 2015, Astronomy & Astrophysics, 578, A58

Halle, A., Di Matteo, P., Haywood, M., & Combes, F. 2015, A&A, 578, A58

Haywood, M., Di Matteo, P., Lehnert, M. D., Katz, D., & Gómez, A. 2013, Astronomy & Astrophysics, 560, A109

Haywood, M., Di Matteo, P., Snaith, O., & Lehnert, M. 2015, Astronomy & Astrophysics, 579, A5

Haywood, M., Lehnert, M., Di Matteo, P., et al. 2016, Astronomy & Astrophysics, 589, A66

Heller, C. H. & Shlosman, I. 1994, Astrophysical Journal, Part 1 (ISSN 0004-637X), vol. 424, no. 1, p. 84-105, 424, 84

Hernquist, L. 1993, Astrophysical Journal, Part 1 (ISSN 0004-637X), vol. 409, no. 2, p. 548-562., 409, 548

Herrera-Endoqui, M., Díaz-García, S., Laurikainen, E., & Salo, H. 2015, Astronomy & Astrophysics, 582, A86

Ho, L. C., Filippenko, A. V., & Sargent, W. L. 1997, The Astrophysical Journal, 487, 591

Ho, L. C., Li, Z.-Y., Barth, A. J., Seigar, M. S., & Peng, C. Y. 2011, The Astrophysical Journal Supplement Series, 197, 21

Hohl, F. 1971, Astrophysical Journal, vol. 168, p. 343, 168, 343

Holley-Bockelmann, K., Weinberg, M., & Katz, N. 2005, Monthly Notices of the Royal Astronomical Society, 363, 991

Hopkins, P. F. & Quataert, E. 2010, Monthly Notices of the Royal Astronomical Society, 407, 1529

Howard, C. D., Rich, R. M., Clarkson, W., et al. 2009, The Astrophysical Journal, 702, L153

Hubble, E. P. 1925, Pop. Astr.; Vol. 33; Page 252-255, 33

Hubble, E. P. 1926, ApJ, 64, 321

Hubble, E. P. 1936, Realm of the Nebulae

Illingworth, G. 1977, Astrophysical Journal, Part 2-Letters to the Editor, vol. 218, Dec. 1, 1977, p. L43-L47., 218, L43

Ishizuki, S., Kawabe, R., Ishiguro, M., et al. 1990, Nature, 344, 224

Jacobs, C., Glazebrook, K., Calabrò, A., et al. 2023, The Astrophysical Journal Letters, 948, L13

Kalnajs, A. J. 1976, Astrophysical Journal, Vol. 205, pp. 751-761 (1976)., 205, 751

Katz, N. 1992, Astrophysical Journal, Part 1 (ISSN 0004-637X), vol. 391, no. 2, June 1, 1992, p. 502-517. Research supported by Pittsburgh Supercomputing Center., 391, 502

Kendall, S., Clarke, C., & Kennicutt Jr, R. 2015, Monthly Notices of the Royal Astronomical Society, 446, 4155

Kennedy, R., Bamford, S. P., Baldry, I., et al. 2015, Monthly Notices of the Royal Astronomical Society, 454, 806

Kim, T., Athanassoula, E., Sheth, K., et al. 2021, The Astrophysical Journal, 922, 196

Kim, T., Gadotti, D. A., Athanassoula, E., et al. 2016, Monthly Notices of the Royal Astronomical Society, 462, 3430

Kim, T., Gadotti, D. A., Sheth, K., et al. 2014, The Astrophysical Journal, 782, 64

Kim, T., Sheth, K., Gadotti, D. A., et al. 2015, The Astrophysical Journal, 799, 99

Kim, W.-T., Seo, W.-Y., & Kim, Y. 2012, The Astrophysical Journal, 758, 14

Kimm, T. & Cen, R. 2014, ApJ, 788, 121

Kimm, T., Cen, R., Devriendt, J., Dubois, Y., & Slyz, A. 2015, MNRAS, 451, 2900

Knapen, J. 2005, Astronomy & Astrophysics, 429, 141

Knapen, J. H. 2005, A&A, 429, 141

Koekemoer, A. M., Aussel, H., Calzetti, D., et al. 2007, The Astrophysical Journal Supplement Series, 172, 196

Kolcu, T., Maciejewski, W., Gadotti, D. A., et al. 2023, Monthly Notices of the Royal Astronomical Society, stad1896

Kormendy, J. & Kennicutt, R. C. 2004, Annu. Rev. Astron. Astrophys., 42, 603

Kraljic, K., Bournaud, F., & Martig, M. 2012, The Astrophysical Journal, 757, 60

Kroupa, P. 2001, Monthly Notices of the Royal Astronomical Society, 322, 231

Kruk, S. J., Lintott, C. J., Bamford, S. P., et al. 2018, Monthly Notices of the Royal Astronomical Society, 473, 4731

Kruk, S. J., Lintott, C. J., Simmons, B. D., et al. 2017, Monthly Notices of the Royal Astronomical Society, 469, 3363

Kuchinski, L., Freedman, W., Madore, B. F., et al. 2000, The Astrophysical Journal Supplement Series, 131, 441

Lang, M., Holley-Bockelmann, K., & Sinha, M. 2014, The Astrophysical Journal Letters, 790, L33

Larson, R. B. 1974, Monthly Notices of the Royal Astronomical Society, 166, 585

Larson, R. B. 1975, Monthly Notices of the Royal Astronomical Society, 173, 671

Larson, R. B. 1976, Monthly Notices of the Royal Astronomical Society, 176, 31

Lauger, S., Burgarella, D., & Buat, V. 2005, Astronomy & Astrophysics, 434, 77

Launhardt, R., Zylka, R., & Mezger, P. 2002, Astronomy & Astrophysics, 384, 112

Laurikainen, E., Salo, H., Buta, R., Knapen, J., & Comerón, S. 2010, Monthly Notices of the Royal Astronomical Society, 405, 1089

Laurikainen, E., Salo, H., & Rautiainen, P. 2002, Monthly Notices of the Royal Astronomical Society, 331, 880

Law, D. R., Steidel, C. C., Erb, D. K., et al. 2009, The Astrophysical Journal, 697, 2057

Lelli, F., Di Teodoro, E. M., Fraternali, F., et al. 2021, Science, 371, 713

Lelli, F., Zhang, Z.-Y., Bisbas, T. G., et al. 2023, arXiv preprint arXiv:2302.00030

Leroy, A. K., Schinnerer, E., Hughes, A., et al. 2021, The Astrophysical Journal Supplement Series, 257, 43

Li, C., Gadotti, D. A., Mao, S., & Kauffmann, G. 2009, Monthly Notices of the Royal Astronomical Society, 397, 726

Licquia, T. C. & Newman, J. A. 2015, The Astrophysical Journal, 806, 96

Lin, L.-H., Wang, H.-H., Hsieh, P.-Y., et al. 2013, The Astrophysical Journal, 771, 8

Łokas, E., Athanassoula, E., Debattista, V. P., et al. 2014, Monthly Notices of the Royal Astronomical Society, 445, 1339

Łokas, E. L. 2018, The Astrophysical Journal, 857, 6

Łokas, E. L. 2021, Astronomy & Astrophysics, 647, A143

Łokas, E. L., Ebrová, I., Del Pino, A., et al. 2016, The Astrophysical Journal, 826, 227

Łokas, E. L., Semczuk, M., Gajda, G., & D'Onghia, E. 2015, The Astrophysical Journal, 810, 100

López-Cobá, C., Sánchez, S. F., Lin, L., et al. 2022, The Astrophysical Journal, 939, 40

Lucey, M., Pearson, S., Hunt, J. A., et al. 2023, Monthly Notices of the Royal Astronomical Society, 520, 4779

Lütticke, R., Dettmar, R.-J., & Pohlen, M. 2000, Astronomy and Astrophysics Supplement Series, 145, 405

Lynden-Bell, D. & Kalnajs, A. 1972, Monthly Notices of the Royal Astronomical Society, 157, 1

Maia, M., Da Costa, L., & Latham, D. W. 1989, The Astrophysical Journal Supplement Series, 69, 809

Marinacci, F., Vogelsberger, M., Pakmor, R., et al. 2018, Monthly Notices of the Royal Astronomical Society, 480, 5113

Martig, M., Pinna, F., Falcón-Barroso, J., et al. 2021, Monthly Notices of the Royal Astronomical Society, 508, 2458

Martin, P. 1995, Astronomical Journal v. 109, p. 2428, 109, 2428

Martin, P. & Roy, J.-R. 1995, The Astrophysical Journal, Part 1 (ISSN 0004-637X), vol. 445, no. 1, p. 161-172, 445, 161

Martinet, L. & Friedli, D. 1997, arXiv preprint astro-ph/9701091

Martinez-Valpuesta, I., Shlosman, I., & Heller, C. 2006, The Astrophysical Journal, 637, 214

Masters, K. L., Krawczyk, C., Shamsi, S., et al. 2021, Monthly Notices of the Royal Astronomical Society, 507, 3923

Masters, K. L., Nichol, R. C., Haynes, M. P., et al. 2012, Monthly Notices of the Royal Astronomical Society, 424, 2180

Masters, K. L., Nichol, R. C., Hoyle, B., et al. 2011, Monthly Notices of the Royal Astronomical Society, 411, 2026

McDermid, R. M., Alatalo, K., Blitz, L., et al. 2015, Monthly Notices of the Royal Astronomical Society, 448, 3484

Melvin, T., Masters, K., Lintott, C., et al. 2014, Monthly Notices of the Royal Astronomical Society, 438, 2882

Méndez-Abreu, J., Aguerri, J. A., Falcón-Barroso, J., et al. 2018, Monthly Notices of the Royal Astronomical Society, 474, 1307

Méndez-Abreu, J., Corsini, E., Debattista, V. P., et al. 2008, The Astrophysical Journal, 679, L73

Méndez-Abreu, J., Costantin, L., & Kruk, S. 2023, arXiv preprint arXiv:2307.02898

Méndez-Abreu, J., de Lorenzo-Cáceres, A., Gadotti, D., et al. 2019, Monthly Notices of the Royal Astronomical Society: Letters, 482, L118

Méndez-Abreu, J., García, M., Eliche-Moral, M., et al. 2013, Highlights of Spanish Astrophysics VII, 660

Méndez-Abreu, J., Sánchez-Janssen, R., & Aguerri, J. 2010, The Astrophysical Journal Letters, 711, L61

Méndez-Abreu, J., Sánchez-Janssen, R., Aguerri, J., Corsini, E., & Zarattini, S. 2012, The Astrophysical Journal Letters, 761, L6

Menéndez-Delmestre, K., Sheth, K., Schinnerer, E., Jarrett, T. H., & Scoville, N. Z. 2007, The Astrophysical Journal, 657, 790

Miwa, T. & Noguchi, M. 1998, The Astrophysical Journal, 499, 149

Moles, M., Marquez, I., & Perez, E. 1995, Astrophysical Journal, Part 1 (ISSN 0004-637X), vol. 438, no. 2, p. 604-609, 438, 604

Morgan, W. 1958, Publications of the Astronomical Society of the Pacific, 70, 364

Muñoz-Mateos, J. C., Sheth, K., De Paz, A. G., et al. 2013, The Astrophysical Journal, 771, 59

Muñoz-Mateos, J. C., Sheth, K., Regan, M., et al. 2015, The Astrophysical Journal Supplement Series, 219, 3

Munoz-Tunón, C., Caon, N., & Aguerri, J. A. L. 2004, The Astronomical Journal, 127, 58

Naab, T., Johansson, P. H., & Ostriker, J. P. 2009, The Astrophysical Journal, 699, L178

Naab, T., Oser, L., Emsellem, E., et al. 2014, Monthly Notices of the Royal Astronomical Society, 444, 3357

Naiman, J. P., Pillepich, A., Springel, V., et al. 2018, Monthly Notices of the Royal Astronomical Society, 477, 1206

Nair, P. B. & Abraham, R. G. 2010, The Astrophysical Journal Letters, 714, L260

Navarro, J. F. & Benz, W. 1991, Astrophysical Journal, Part 1 (ISSN 0004-637X), vol. 380, Oct. 20, 1991, p. 320-329. Research supported by SNSF and CONICET., 380, 320

Navarro, J. F., Frenk, C. S., & White, S. D. M. 1997, ApJ, 490, 493

Navarro, J. F. & White, S. D. 1994, Monthly Notices of the Royal Astronomical Society, 267, 401

Neeleman, M., Prochaska, J. X., Kanekar, N., & Rafelski, M. 2020, Nature, 581, 269

Nelson, D., Pillepich, A., Springel, V., et al. 2018, Monthly Notices of the Royal Astronomical Society, 475, 624

Nelson, E. J., Suess, K. A., Bezanson, R., et al. 2022, arXiv preprint arXiv:2208.01630

Ness, M., Freeman, K., Athanassoula, E., et al. 2013, Monthly Notices of the Royal Astronomical Society, 430, 836

Ness, M., Freeman, K., Athanassoula, E., et al. 2012, The Astrophysical Journal, 756, 22

Ness, M. & Lang, D. 2016, The Astronomical Journal, 152, 14

Neumann, J., Fragkoudi, F., Pérez, I., et al. 2020, Astronomy & Astrophysics, 637, A56

Newman, S. F., Genzel, R., Schreiber, N. M. F., et al. 2013, The Astrophysical Journal, 767, 104

Noguchi, M. 1987, Monthly Notices of the Royal Astronomical Society, 228, 635

Nogueira-Cavalcante, J., Gonçalves, T., Menéndez-Delmestre, K., & Sheth, K. 2018, Monthly Notices of the Royal Astronomical Society, 473, 1346

Ocvirk, P., Pichon, C., Lançon, A., & Thiébaut, E. 2006, Monthly Notices of the Royal Astronomical Society, 365, 74

Okamoto, T., Eke, V. R., Frenk, C. S., & Jenkins, A. 2005, Monthly Notices of the Royal Astronomical Society, 363, 1299

Okamoto, T., Isoe, M., & Habe, A. 2015, Publications of the Astronomical Society of Japan, 67, 63

O'Neill, J. & Dubinski, J. 2003, Monthly Notices of the Royal Astronomical Society, 346, 251

Oser, L., Ostriker, J. P., Naab, T., Johansson, P. H., & Burkert, A. 2010, The Astrophysical Journal, 725, 2312

Ostriker, J. P. & Peebles, P. J. 1973, The Astrophysical Journal, 186, 467

Papaderos, P., Breda, I., Humphrey, A., et al. 2022, A&A, 658, A74

Pérez, I., Martínez-Valpuesta, I., Ruiz-Lara, T., et al. 2017, Monthly Notices of the Royal Astronomical Society: Letters, 470, L122

Perlmutter, S., Aldering, G., Goldhaber, G., et al. 1999, The Astrophysical Journal, 517, 565

Perret, V. 2016, DICE: Disk Initial Conditions Environment, Astrophysics Source Code Library, record ascl:1607.002

Perret, V., Renaud, F., Epinat, B., et al. 2014, A&A, 562, A1

Peschken, N. & Łokas, E. L. 2019, Monthly Notices of the Royal Astronomical Society, 483, 2721

Petersen, M. S., Weinberg, M. D., & Katz, N. 2023, arXiv preprint arXiv:2305.13366

Pfenniger, D. & Friedli, D. 1991, Astronomy and Astrophysics (ISSN 0004-6361), vol. 252, no. 1, Dec. 1991, p. 75-93. Research supported by Observatoire de Geneve and SNSF., 252, 75

Pfenniger, D. & Norman, C. 1990, Astrophysical Journal, Part 1 (ISSN 0004-637X), vol. 363, Nov. 10, 1990, p. 391-410. Research supported by SNSF., 363, 391

Pietrinferni, A., Cassisi, S., Salaris, M., & Castelli, F. 2004, The Astrophysical Journal, 612, 168

Pietrinferni, A., Cassisi, S., Salaris, M., & Castelli, F. 2006, The Astrophysical Journal, 642, 797

Pietrinferni, A., Cassisi, S., Salaris, M., & Hidalgo, S. 2013, Astronomy & Astrophysics, 558, A46

Pietrinferni, A., Cassisi, S., Salaris, M., Percival, S., & Ferguson, J. W. 2009, The Astrophysical Journal, 697, 275

Pillepich, A., Nelson, D., Hernquist, L., et al. 2018, Monthly Notices of the Royal Astronomical Society, 475, 648

Pinna, F., Falcón-Barroso, J., Martig, M., et al. 2019, Astronomy & Astrophysics, 625, A95

Polyachenko, E. 2013, Astronomy Letters, 39, 72

Posses, A., Aravena, M., González-López, J., et al. 2023, Astronomy & Astrophysics, 669, A46

Prieto, M., Lopez, J., Varela, A., Munoz-Tunon, C., & Gottesman, S. 1996, in International Astronomical Union Colloquium, Vol. 157, Cambridge University Press, 480–482

Regan, M. W. & Elmegreen, D. M. 1997, The Astronomical Journal, v. 114, p. 965., 114, 965

Renaud, F., Agertz, O., Read, J. I., et al. 2021, Monthly Notices of the Royal Astronomical Society, 503, 5846

Rix, H.-W., Chandra, V., Andrae, R., et al. 2022, The Astrophysical Journal, 941, 45

Rizzo, F., Vegetti, S., Powell, D., et al. 2020, Nature, 584, 201

Roberts, M. S. & Haynes, M. P. 1994, Annual Review of Astronomy and Astrophysics, 32, 115

Romano-Díaz, E., Shlosman, I., Heller, C., & Hoffman, Y. 2008, The Astrophysical Journal, 687, L13

Romero-Gómez, M., Athanassoula, E., Masdemont, J. J., & García-Gómez, C. 2007, A&A, 472, 63

Rosas-Guevara, Y., Bonoli, S., Dotti, M., et al. 2022, Monthly Notices of the Royal Astronomical Society, 512, 5339

Rosas-Guevara, Y., Bonoli, S., Dotti, M., et al. 2020, Monthly Notices of the Royal Astronomical Society, 491, 2547

Rosas-Guevara, Y., Bonoli, S., Dotti, M., et al. 2020, MNRAS, 491, 2547

Roshan, M., Ghafourian, N., Kashfi, T., et al. 2021, Monthly Notices of the Royal Astronomical Society, 508, 926

Ryden, B. S. & Gunn, J. E. 1987, Astrophysical Journal, Part 1 (ISSN 0004-637X), vol. 318, July 1, 1987, p. 15-31. Research supported by the John D. and Catherine T. MacArthur Foundation., 318, 15

Saha, K. & Elmegreen, B. 2018, The Astrophysical Journal, 858, 24

Salo, H., Laurikainen, E., Laine, J., et al. 2015, The Astrophysical Journal Supplement Series, 219, 4

Sánchez, S., Kennicutt, R., De Paz, A. G., et al. 2012, Astronomy & Astrophysics, 538, A8

Sanchez-Blazquez, P., Ocvirk, P., Gibson, B. K., Pérez, I., & Peletier, R. F. 2011, Monthly Notices of the Royal Astronomical Society, 415, 709

Sandage, A. 1961, The Hubble atlas of galaxies, Vol. 618 (Carnegie Institution of Washington Washington, DC)

Sandage, A., Freeman, K. C., & Stokes, N. 1970, Astrophysical Journal, vol. 160, p. 831, 160, 831

Sanders, J. L., Matsunaga, N., Kawata, D., et al. 2022, Monthly Notices of the Royal Astronomical Society, 517, 257

Sarzi, M., Allard, E., Knapen, J., & Mazzuca, L. 2007, Monthly Notices of the Royal Astronomical Society, 380, 949

Sarzi, M., Falcón-Barroso, J., Davies, R. L., et al. 2006, Monthly Notices of the Royal Astronomical Society, 366, 1151

Sarzi, M., Iodice, E., Coccato, L., et al. 2018, Astronomy & Astrophysics, 616, A121

Schawinski, K., Urry, C. M., Simmons, B. D., et al. 2014, Monthly Notices of the Royal Astronomical Society, 440, 889

Schreiber, N. F., Genzel, R., Bouché, N., et al. 2009, The Astrophysical Journal, 706, 1364

Schreiber, N. F., Genzel, R., Lehnert, M. D., et al. 2006, The Astrophysical Journal, 645, 1062

Scoville, N., Abraham, R., Aussel, H., et al. 2007, The Astrophysical Journal Supplement Series, 172, 38

Sellwood, J. 2014, Reviews of Modern Physics, 86, 1

Semenov, V. A., Conroy, C., Chandra, V., Hernquist, L., & Nelson, D. 2023a, arXiv preprint arXiv:2306.09398

Semenov, V. A., Conroy, C., Chandra, V., Hernquist, L., & Nelson, D. 2023b, arXiv preprint arXiv:2306.13125

Seo, W.-Y., Kim, W.-T., Kwak, S., et al. 2019, The Astrophysical Journal, 872, 5

Shapiro, K. L., Genzel, R., Schreiber, N. M. F., et al. 2008, The Astrophysical Journal, 682, 231

Shen, J., Rich, R. M., Kormendy, J., et al. 2010, The Astrophysical Journal Letters, 720, L72

Shen, J. & Sellwood, J. 2004, The Astrophysical Journal, 604, 614

Sheth, K., Elmegreen, D. M., Elmegreen, B. G., et al. 2008, The Astrophysical Journal, 675, 1141

Sheth, K., Melbourne, J., Elmegreen, D. M., et al. 2012, The Astrophysical Journal, 758, 136

Sheth, K., Regan, M., Hinz, J. L., et al. 2010, Publications of the Astronomical Society of the Pacific, 122, 1397

Sheth, K., Regan, M. W., Scoville, N. Z., & Strubbe, L. E. 2003, The Astrophysical Journal, 592, L13

Sheth, K., Vogel, S. N., Regan, M. W., Thornley, M. D., & Teuben, P. J. 2005, The Astrophysical Journal, 632, 217

Shlosman, I., Frank, J., & Begelman, M. C. 1989, Nature, 338, 45

Silva-Lima, L. A., Martins, L. P., Coelho, P. R., & Gadotti, D. A. 2022, Astronomy & Astrophysics, 661, A105

Simien, F. & De Vaucouleurs, G. 1986, Astrophysical Journal, Part 1 (ISSN 0004-637X), vol. 302, March 15, 1986, p. 564-578., 302, 564

Simkin, S., Su, H., & Schwarz, M. 1980, Astrophysical Journal, Part 1, vol. 237, Apr. 15, 1980, p. 404-413., 237, 404

Simmons, B. D., Melvin, T., Lintott, C., et al. 2014, Monthly Notices of the Royal Astronomical Society, 445, 3466

Skokos, C., Patsis, P., & Athanassoula, E. 2002, Monthly Notices of the Royal Astronomical Society, 333, 847

Smit, R., Bouwens, R. J., Carniani, S., et al. 2018, Nature, 553, 178

Snaith, O., Haywood, M., Di Matteo, P., et al. 2015, Astronomy & Astrophysics, 578, A87

Snaith, O. N., Haywood, M., Di Matteo, P., et al. 2014, The Astrophysical Journal Letters, 781, L31

Sommer-Larsen, J., Gelato, S., & Vedel, H. 1999, The Astrophysical Journal, 519, 501

Sormani, M. C., Magorrian, J., Nogueras-Lara, F., et al. 2020, Monthly Notices of the Royal Astronomical Society, 499, 7

Sormani, M. C., Sanders, J. L., Fritz, T. K., et al. 2022, Monthly Notices of the Royal Astronomical Society, 512, 1857

Sormani, M. C., Sobacchi, E., Fragkoudi, F., et al. 2018, Monthly Notices of the Royal Astronomical Society, 481, 2

Springel, V., Di Matteo, T., & Hernquist, L. 2005, The Astrophysical Journal Letters, 620, L79

Springel, V., Pakmor, R., Pillepich, A., et al. 2018, Monthly Notices of the Royal Astronomical Society, 475, 676

Stern, J., Faucher-Giguère, C.-A., Fielding, D., et al. 2021, The Astrophysical Journal, 911, 88

Tahmasebzadeh, B., Zhu, L., Shen, J., Gerhard, O., & van de Ven, G. 2022, The Astrophysical Journal, 941, 109

Teyssier, R. 2002, A&A, 385, 337

Thomas, D., Maraston, C., Schawinski, K., Sarzi, M., & Silk, J. 2010, Monthly Notices of the Royal Astronomical Society, 404, 1775

Toomre, A. 1963, Astrophysical Journal, vol. 138, p. 385, 138, 385

Toomre, A. 1964, The Astrophysical Journal, 139, 1217

Toomre, A. 1977, in Evolution of Galaxies and Stellar Populations, 401

Toomre, A. & Toomre, J. 1972, Astrophysical Journal, Vol. 178, pp. 623-666 (1972), 178, 623

Tremaine, S. & Weinberg, M. D. 1984, The Astrophysical Journal, 282, L5

van de Sande, J., Fraser-McKelvie, A., Fisher, D., et al. 2023, arXiv preprint arXiv:2306.00059

van den Bergh, S. 1960, The Astrophysical Journal, 131, 558

Van Der Marel, R. P. & Franx, M. 1993, The Astrophysical Journal, 407, 525

Vazdekis, A., Coelho, P., Cassisi, S., et al. 2015, Monthly Notices of the Royal Astronomical Society, 449, 1177

Vazdekis, A., Koleva, M., Ricciardelli, E., Röck, B., & Falcón-Barroso, J. 2016, Monthly Notices of the Royal Astronomical Society, 463, 3409

Vera, M., Alonso, S., & Coldwell, G. 2016, Astronomy & Astrophysics, 595, A63

Vika, M., Vulcani, B., Bamford, S. P., Häußler, B., & Rojas, A. L. 2015, Astronomy & Astrophysics, 577, A97

Villa-Vargas, J., Shlosman, I., & Heller, C. 2010, The Astrophysical Journal, 719, 1470

Wegg, C. & Gerhard, O. 2013, Monthly Notices of the Royal Astronomical Society, 435, 1874

Wegg, C., Gerhard, O., & Portail, M. 2015, Monthly Notices of the Royal Astronomical Society, 450, 4050

Weiland, J., Arendt, R., Berriman, G., et al. 1994, Astrophysical Journal, Part 2-Letters (ISSN 0004-637X), vol. 425, no. 2, p. L81-L84, 425, L81

Werle, A., Poggianti, B., Moretti, A., et al. 2022, The Astrophysical Journal, 930, 43

White, S. D. & Frenk, C. S. 1991, Astrophysical Journal, Part 1 (ISSN 0004-637X), vol. 379, Sept. 20, 1991, p. 52-79. Research supported by NASA, NSF, and SERC., 379, 52

White, S. D. & Rees, M. J. 1978, Monthly Notices of the Royal Astronomical Society, 183, 341

Williams, T. G., Schinnerer, E., Emsellem, E., et al. 2021, The Astronomical Journal, 161, 185

Wisnioski, E., Schreiber, N. F., Wuyts, S., et al. 2015, The Astrophysical Journal, 799, 209

Wozniak, H., Friedli, D., Martinet, L., Martin, P., & Bratschi, P. 1995, Astronomy and Astrophysics Supplement Series, 111, 115

Wylie, S. M., Clarke, J. P., & Gerhard, O. E. 2022, Astronomy & Astrophysics, 659, A80

Zana, T., Dotti, M., Capelo, P. R., et al. 2018, Monthly Notices of the Royal Astronomical Society, 479, 5214

Zee, W.-B. G., Paudel, S., Moon, J.-S., & Yoon, S.-J. 2023, The Astrophysical Journal, 949, 91

Zhao, D., Du, M., Ho, L. C., Debattista, V. P., & Shi, J. 2020, The Astrophysical Journal, 904, 170

Zhu, L., van de Ven, G., Méndez-Abreu, J., & Obreja, A. 2018, Monthly Notices of the Royal Astronomical Society, 479, 945

Zou, Y., Shen, J., Bureau, M., & Li, Z.-Y. 2019, The Astrophysical Journal, 884, 23

Danksagung

Danke.